



Doctoral Thesis

Development of constitutive models for the accurate simulation of advanced polymer-based composites under complex loading states

Ivan Ruiz Cózar

2024



Doctoral Thesis

Development of constitutive models for the accurate simulation of advanced polymer-based composites under complex loading states

Ivan Ruiz Cózar

2024

Doctoral Program in Technology

Advisors:

Dr. Pere Maimí Vert
Universitat de Girona

Dr. Emilio V. González Juan
Universitat de Girona

Dr. Fermin E. Otero Gruer
Universitat Politècnica de Catalunya

Thesis submitted to the Universitat de Girona for the degree of Doctor of
Philosophy

Ivan Ruiz Cózar

Development of constitutive models for the accurate simulation of advanced polymer-based composites under complex loading states

Doctoral Thesis, 2024

Doctoral Program in Technology

Advisors:

Dr. Pere Maimí Vert

Dr. Emilio V. González Juan

Dr. Fermin E. Otero Gruer

Universitat de Girona

AMADE Research Group

Escola Politècnica Superior

Dept. d'Enginyeria Mecànica i de la Construcció Industrial

Carrer Universitat de Girona, 4. Campus de Montilivi

17003 Girona

“Knowledge will make you be free.

— Socrates

(Greek philosopher from Athens)

“Luck is what happens when preparation meets opportunity.

— Seneca

(Roman philosopher)

“Everything we hear is an opinion, not a fact. Everything we see is a perspective, not the truth.

— Marco Aurelio

(Roman emperor)

“The beauty of pain, not only is it temporary... is it tells you when you begin to give enough of yourself in pursuit of your dreams. If the work hasn't hurt or cost you anything, or at least made you uncomfortable, then I'm sorry to be the one to tell you but you're not working hard enough, or sacrificing all that you could to be all you can be.

— Arnold Schwarzenegger

(seven-time Mr. Olympia,

actor, businessman,

38th governor of California...)

Preface

The work contained in this Ph.D. thesis was conducted in the AMADE Research Group (Escola Politècnica Superior, Dept. d'Enginyeria Mecànica i de la Construcció Industrial, Universitat de Girona, Spain). The thesis was carried out with predoctoral Grant 2019FI_B_01117 from the Catalan government. This work has been conducted within the framework of VITAL project. This work has also received funding from the Clean Sky 2 Joint Undertaking (JU) under grant agreement No. 864723 (TREAL). The JU receives support from the European Union's Horizon 2020 research and innovation programme and the Clean Sky 2 JU members other than the Union. Additionally, the present work has received funding from the Clean Sky 2 Joint Undertaking (JU) under grant agreements No. 886519 (BEDYN).

Acknowledgements

En primer lloc, m'agradaria agrair als meus directors de tesi el seu suport i ajuda, Dr. Pere Maimí Vert, Dr. Emilio V. González Juan i Dr. Fermín E. Otero Gruer. Aquesta tesi ha sigut una feina d'equip que sense vosaltres no hagués estat possible. Hem fet una molt bona feina. Vull agrair tot el coneixement que meu transmès, el temps que meu dedicat, les hores de discussió i anàlisi que hem tingut. Ha estat un plaer treballar amb vosaltres i m'heu facilitat molt la feina. Sempre heu estat disposats a dedicar-me el temps que he necessitat. I would also like to thank Dr. Pedro P. Camanho and Dr. Stephanie Miot for their time, their comments have helped to improve this work.

En segon lloc vull agrair el suport i guia que ha sigut el Dr. Albert Turon Travesa en el meu transcurs a AMADE. Si avui estic defensant aquesta tesi, en part és gràcies a tu. Encara recordo la trucada que vam tenir on et vaig preguntar si podia fer la tesi doctoral amb vosaltres. En aquell moment no vas dubtar i em vas oferir diferents opcions. A més, en aquestes darreres setmanes m'has ajudat a trobar un lloc per poder fer una estada de postdoc a l'estrange. Gràcies.

Vull fer una menció especial al Dr. Oriol Vallmajó Martín, vam començar al mateix temps aquest camí tan especial que és fer una tesi doctoral. Encara recordo aquell viatge que vam fer a Porto per definir els nostres temes de tesi (no direm que va passar aquell matí en aquella presentació). Gràcies pel temps que m'has dedicat i les hores d'anàlisi (Explícit/Implícit, true strain, B-basis value...).

També vull agrair a tots els membres del grup de recerca AMADE el seu suport durant tots aquests anys. L'ambient de feina durant aquests anys ha sigut immillorable. Vull agrair a tots els membres del laboratori el seu suport i la seva disponibilitat a resoldre qualsevol dubte. També vull fer menció de l'ambient que hi ha a la sala de doctorands, vull agrair a tots els doctorands l'ambient que heu creat. Sempre recordaré aquella nit del congrés del MATCOMP'21, va ser una conversa de qualitat. I want to thank the ping-pong team for their time, those hours learning and playing ping-pong have been a lot of fun. También quiero agradecer a Pablo Martin Villaroel Marquina las horas de debate y conversación que tuvimos durante el confinamiento.

Quiero agradecer a mi familia la ayuda que me ha prestado durante este tiempo. Ha habido momentos difíciles, pero sé que habéis estado a mi lado ayudándome. Ahora vienen nuevos retos y sé que me apoyareis en todo, como siempre lo habéis hecho, gracias.

Aquestes són les darreres paraules que estic escrivint de la meva tesi. Ara es tanca una etapa de la meva vida per donar pas a una de nova.

Declaration



UNIVERSITAT POLITÈCNICA
DE CATALUNYA
BARCELONATECH

Dr. Pere Maimí Vert, Professor Titular at Universitat de Girona,

Dr. Emilio V. González Juan, Professor Agregat at Universitat de Girona,

and

Dr. Fermin E. Otero Gruer, Professor Lector at Universitat Politècnica de Catalunya,

hereby CERTIFY that:

The work entitled *Development of constitutive models for the accurate simulation of advanced polymer-based composites under complex loading states*, submitted for the doctoral degree by Ivan Ruiz Cózar, has been conducted under our supervision and that it fulfils the requirements for the *International Mention*.

Dr. Pere Maimí Vert
Universitat de Girona

Dr. Emilio V. González Juan
Universitat de Girona

Dr. Fermin E. Otero Gruer
Universitat Politècnica de Catalunya

Girona, 2024

Contents

Preface	i
Acknowledgements	ii
Declaration	iv
List of Acronyms	x
List of Symbols	xi
List of Figures	xvi
List of Tables	xxiii
List of Codes	xxiv
List of Algorithms	xxv
Abstract	xxvi
Resum	xxix
Resumen	xxxii
1 Introduction	1
1.1 Contextual background	1
1.2 Motivation	4
1.3 Objectives	5
1.4 Methodology	5
1.5 Research dissemination	7
2 Elastoplastic damage model	11
2.1 Constitutive model	13
2.1.1 Modelling Plasticity	16
2.1.2 Modelling Damage Evolution	19
2.2 Input model parameters	24
2.3 Implementation	26
2.4 Numerical predictions	30

2.4.1	Off-axis tests	35
2.4.2	Open-hole tensile and compressive tests	39
3	Enhanced elastoplastic damage model	42
3.1	Formulation	44
3.2	Constitutive model implementation	45
3.3	Numerical predictions	50
3.3.1	Longitudinal tensile test	51
3.3.2	Open-hole tensile and compressive tests	52
3.3.3	Open-hole compressive test with quasi-isotropic laminate	53
3.3.4	Open-hole compressive test at 0°	57
3.3.5	Open-hole compressive test at 90°	59
4	Transverse Poisson's ratios	65
4.1	Material and methods	67
4.1.1	Transverse tensile test	67
4.1.2	Transverse compressive test	69
4.1.3	Instrumentation and data reduction	71
4.2	Results and discussion	74
5	Failure envelope shape definition	84
5.1	Calibration of the envelope shape coefficients	85
5.2	Bounds of the envelope shape coefficients	88
5.3	Influence of the failure envelope on the failure strength of filled-hole compressive laminates	91
5.3.1	Experimental campaign	91
5.3.2	Finite element modelling strategy	92
5.3.3	Failure envelopes definition	96
5.3.4	Results and discussion	97
6	Complex simulations under multiaxial loading conditions	105
6.1	End-notched flexure test	105
6.2	Four-point bending tests using L-shaped specimens	108
6.3	Single-lap shear composite bolted joint tests	112
7	Viscoelastic-viscoplastic viscodamage constitutive model	119
7.1	Constitutive model	122
7.1.1	Modelling Viscoelasticity	123
7.1.2	Modelling Viscoplasticity	126

7.1.3	Modelling Viscodamage	127
7.2	Thermodynamic consistency of the viscoelastic-viscoplastic viscodamage model	128
7.2.1	Thermodynamic consistency of the viscoelastic energy dissipated . .	129
7.2.2	Thermodynamic consistency of the viscoplastic energy dissipated . .	130
7.2.3	Thermodynamic consistency of the viscodamage energy dissipated . .	131
7.2.4	Thermodynamic restrictions of the material properties	134
7.3	Numerical predictions	134
7.3.1	Calibration of the strengths under dynamic conditions	135
7.3.2	Gauss-point level tests	136
7.3.3	Off-axis compressive tests	140
8	Numerical limitations of the constitutive model	145
8.1	Infinitesimal Strain theory	145
8.1.1	Rigid body rotation virtual test	145
8.1.2	Simple longitudinal shear virtual test	147
8.2	Friction effects	150
9	Conclusions	154
9.1	Concluding remarks	154
9.2	Perspectives and future work	159
Appendices		162
A	Determination of the parameters of the plastic flow potential function	163
B	Damage variables	167
B.1	Longitudinal damage variable d_ℓ	167
B.1.1	Longitudinal tensile damage variable $d_{\ell T}$	167
B.1.2	Longitudinal compressive damage variable $d_{\ell C}$	171
B.2	Transverse damage variable d_t	173
B.3	Transverse shear damage variable d_{st}	173
B.4	Longitudinal shear damage variable $d_{s\ell}$	175
C	Calculus of the increment of the consistency parameter of the plasticity model	
$(\Delta\gamma_{(n+1)}^{(k)})$		179
C.1	Derivatives as a function of σ	181
C.2	Derivatives as a function of \mathbb{K}	182
C.3	Derivatives as a function of \mathbb{L}	184

C.4	Derivatives as a function of \mathbb{M}	185
C.5	Numerical-analytical comparison of $\Delta\gamma$	185
D	Vector product in Fortran	189
E	Prevent division by zero in Fortran	193
F	Critical characteristic element length	195
F.1	Critical characteristic length for a linear softening law	196
F.2	Critical characteristic length for a bilinear softening law	197
F.3	Critical characteristic length IM7/8522 unidirectional prepreg system	198
G	Verification of the implementation of the constitutive model	200
G.1	Plasticity modelling	200
G.2	Damage modelling using the original model	205
G.3	Damage modelling using the enhanced model	211
H	Positive semi-definite matrix	215
I	Strain-crack opening displacement relationship	217
Bibliography		220

List of Acronyms

FE	finite element
CFRP	carbon fibre-reinforced polymer
FRP	fibre-reinforced polymer
CDM	continuum damage mechanics
3D	three-dimensional
C/C-SiC	carbon fibre reinforced carbon-silicon carbide
VUMAT	user material Fortran subroutine used in Abaqus/Explicit solver
C3D8R	Eight-node 3D solid finite element with reduced integration used in Abaqus
OHT	open-hole tensile
OHC	open-hole compressive
ASTM	American Society for Testing and Materials
CAI	compression after impact
DIC	digital image correlation
PEEK	poly-ether-ether-ketone
FHC	filled-hole compressive
AITM	Airbus' internal test method
DENT	double edge notched tensile
DENC	double edge notched compressive
ENF	end-notched flexural
SLS	single-lap shear
1D	one-dimensional

List of Symbols

Capital Latin letters

A_{DIC}	DIC area analysed
A	Generic matrix in Appendix D
A, B	Generic matrices in Appendix H
C_e	Elasticity tensor
C_{ve}	Maxwell elasticity tensor
E	Young's modulus in Appendix I
E_t	Bulk elastic modulus in the isotropic plane
E₁₁	Longitudinal Young's modulus
E₂₂	Transverse Young's modulus
E	Green-Lagrange strain tensor
E_{DIC_{ij}}	Experimental error of the DIC equipment
E_{SG}	Error from the strain gauge equipment
E_{rand}	Random experimental error
E_{std}	Standard experimental error
E_{ν_{23}}	Experimental uncertainty of ν_{23}
E_{ν_{23C}}	Experimental uncertainty of ν_{23C}
E_{ν_{23T}}	Experimental uncertainty of ν_{23T}
F_N	Activation function in direction N
F	Deformation gradient tensor
G_t	Shear elastic modulus in the isotropic plane
G₁₂	Longitudinal shear Young's modulus
H	Compliance tensor
K, M	Tensors with the coefficients of the non-linear terms of ϕ^p
L_s	Doubler length of the metallic part in the single-shear bolted joint test
L	Tensor with the coefficients of the linear term of ϕ^p
N_{px}	Number of pixels of the analysed area with the DIC equipment
R	Residual in Newton-Raphson algorithm at Gauss-point level
S_L	Longitudinal shear strength
S_{LP}	Longitudinal shear yield stress
S_T	Transverse shear strength
S_{ε_{ij}^{DIC}}	Sample standard deviation of the strain field from the DIC equipment
U₁₁	Total displacement applied in Chapter 8

W	Complementary Gibbs free-energy density function
W_s	Width of the specimen in the single-shear bolted joint test
X_C	Longitudinal compressive strength
X_T	Longitudinal tensile strength
Y_C	Transverse compressive strength
Y_{CB}	Biaxial transverse compressive strength
Y_{CP}	Transverse compressive yield stress
Y_T	Transverse tensile strength
Y_{TB}	Biaxial transverse tensile strength
Y_{TP}	Transverse tensile yield stress

Small Latin letters

$a_{i_s M}$	Slope of the corresponding softening law
$b_{i_s M}$	Intercept of the corresponding softening law
\mathbf{b}, \mathbf{c}	Generic vector in Appendix D
d_M	Damage variable in direction M
dS_{11}	Initial length in Chapter 8
ds_{11}	Final length in Chapter 8
e_s	Eccentricity of the hole in the single-shear bolted joint test
f_{X_C}	Parameter to define the shape of the longitudinal compressive softening law
$f_{X_C} \mathcal{G}_{X_C}$	Longitudinal compressive fracture toughness
$f_{X_T}, f_{\mathcal{G}_{X_T}}$	Parameters to define the shape of the longitudinal tensile softening law
l_M^*	Characteristic element length in direction M
m	Coefficient of the non-linear terms of ϕ^p in Voigt notation
r_N	Elastic threshold domain in direction N
t	Time discretisation of the FE explicit solver
tol	Tolerance
u	Displacement
\vec{v}	Generic vector in Appendix H
$z_{\alpha/2}$	Confidence range of the standard experimental error

Greek letters

α_0	Fracture plane angle
β^{vp}	Rate sensitivity viscoplastic parameter
Γ	Viscoelastic relaxation tensor
γ	Consistency parameter of the implementation of plasticity

γ^{ve}	Uniaxial viscoelastic parameter
$\bar{\gamma}^{ve}$	Viscoelastic parameter
$\boldsymbol{\varepsilon}$	Strain tensor
$\bar{\boldsymbol{\varepsilon}}^{ve}$	Equivalent viscoelastic strain tensor
$\bar{\boldsymbol{\varepsilon}}^p$	Equivalent plastic strain
η_ℓ	Longitudinal matrix friction coefficient
$\eta_t, \eta_t^q, \eta_{s\ell}, \eta_{s\ell}^q$	Failure envelope shape coefficients
η^{vd}	Viscodamage parameter
η^{vp}	Viscoplastic parameter
θ	Fibre orientation
κ_M	Coefficient of the M damage variable
λ	Plastic multiplier parameter
$\mu_t, \mu_{s\ell}$	Failure envelope shape coefficients
$\mu_{tp}, \mu_{s\ell p}$	Plastic envelope shape coefficients
ν_{12}	Longitudinal shear Poisson's ratio
ν_{23}	Transverse shear Poisson's ratio
ν_{122}^p	Ratio of $-\varepsilon_{22}^p/\varepsilon_{12}^p$ under longitudinal shear loading conditions
ν_{23C}^p	Plastic transverse shear Poisson's ratio in compression
ν_{23T}^p	Plastic transverse shear Poisson's ratio in tension
Ξ	Mechanical energy dissipated per unit volume
$\boldsymbol{\sigma}$	Stress tensor
$\sigma_\ell, p_t, \tau_t, \tau_\ell$	Stress invariants
σ_u	Strength
τ^{ve}	Viscoelastic relaxation time parameter
ϕ_N	Loading function of the damage variable in direction N
$\phi_{\ell C}^{qs}$	Longitudinal compressive viscodamage norm in Chapter 7
ϕ_t^{qs}	Transverse viscodamage norm in Chapter 7
ϕ^p	Yield function
φ^p	Plastic potential function
Ψ	Helmholtz free-energy density function
ψ	Rotation angle in Chapter 8
$\omega_{i_s M}$	Crack opening of the cohesive law in direction M of the segment i_s
ω_{ij}	Crack opening displacement
Ω_{DIC}	DIC area domain

Others

\mathcal{G}_{S_L}	Longitudinal shear fracture toughness
\mathcal{G}_{X_T}	Longitudinal tensile fracture toughness
\mathcal{G}_{Y_C}	Transverse compressive fracture toughness
\mathcal{G}_{Y_T}	Transverse tensile fracture toughness

Operators

$\partial_x(f)$	Partial derivative of function f with respect to x
$d_x(f)$	Derivative of function f with respect to x
$\langle \cdot \rangle$	McCauley operator

Indices, superscripts and brackets

$(\cdot)_C$	Refers to compression
$(\cdot)_c$	Refers to critical
$(\cdot)_{i_i}$	Index of the segment of softening law
$(\cdot)_{ij}$	Cartesian components
$(\cdot)_\ell$	Refers to longitudinal direction
$(\cdot)_{px}$	Refers to a pixel of the DIC equipment
$(\cdot)_s$	Refers to shear direction
$(\cdot)_T$	Refers to tension
$(\cdot)_t$	Refers to transverse direction
$(\cdot)_{vol}$	Volumetric part of a quantity
$(\cdot)_\psi$	Refers to a rotation with respect to ψ
$(\cdot)_{(n+1)}$	Data in the current integration time
$(\cdot)^c$	Cracking part of a quantity
$(\cdot)^{cor}$	Quantity in the Corotational coordinate system
$(\cdot)^d$	Refers to the degraded part of a quantity due to damage
$(\cdot)^{DIC}$	Refers to the DIC equipment
$(\cdot)^{dyn}$	Dynamic part of a quantity
$(\cdot)^e$	Elastic part of a quantity
$(\cdot)^G$	Global coordinate system
$(\cdot)^i$	Inelastic part of a quantity
$(\cdot)^p$	Plastic part of a quantity
$(\cdot)^{pr}$	Predictor of the damage modelling
$(\cdot)^{tr}$	Trial quantity in elastic predictor step
$(\cdot)^v$	Viscous part of a quantity

$(\cdot)^{ve}$	Viscoelastic part of a quantity
$(\cdot)^{vp}$	Viscoplastic part of a quantity
$(\cdot)^{(k+1)}$	Counter of Newton-Raphson steps
$\hat{(\cdot)}$	Refers to the potential parameters of the potential plastic function
$\tilde{(\cdot)}$	Refers to the effective stress domain
$\check{(\cdot)}$	Refers to the predictor stress domain
$\bar{(\cdot)}$	Average of quantity in Chapter 4

List of Figures

1.1	Schematic representation of the length scales employed in the finite element models.	2
1.2	Schematic representation of the discretisation of the different meso-mechanical analyses of finite element models.	4
2.1	Schematic representation of uniaxial stress vs. strain curve response at the Gauss-point level.	14
2.2	Schematic representation of yield stresses vs. equivalent plastic strain curve.	17
2.3	Schematic representation of the failure envelope in the effective stress space.	21
2.4	Stress vs. crack opening displacement (ω_{ij}) curve of each softening law.	23
2.5	Schematic representation of the meshes and the applied boundary conditions used in the: (a) off-axis simulations, and (b) open-hole simulations. θ is the fibre angle orientation.	31
2.6	Plastic and failure envelopes of the IM7/8552 unidirectional prepreg system.	34
2.7	Yield stress vs. equivalent plastic strain curves of the M7/8552 unidirectional prepreg system [124].	35
2.8	Numerical-experimental comparison of the remote stress vs. axial strain curves of the off-axis compressive tests performed by Koerber et al. [8].	37
2.9	Failure envelope for the $\tilde{\sigma}_{22} - \tilde{\sigma}_{12}$ effective stress space with different values of S_L .	38
2.10	Numerical-experimental comparison of the fracture planes obtained from the off-axis compressive tests performed by Koerber et al. [9].	38
2.11	Numerical-experimental comparison of the remote stress vs. axial strain curves of the off-axis tensile tests performed by Koerber et al. [9].	39
2.12	Numerical-experimental comparison of the remote failure strength of the open-hole tensile and compressive tests measured by Camanho et al. [114] and by Bessa [129], respectively.	40
3.1	Longitudinal virtual tensile test at the Gauss-point level using a CDM model using the effective stress tensor.	43
3.2	Schematic representation of the numerical implementation of the enhanced constitutive model at the Gauss-point level when a pure transverse tensile test is applied.	46

3.3	Schematic representation of the numerical implementation of the enhanced constitutive model at the Gauss-point level when a pure transverse tensile test is applied.	47
3.4	Schematic representation of the boundary conditions applied in the open-hole compressive virtual test. θ is the fibre angle orientation.	51
3.5	Longitudinal virtual tensile test at the Gauss-point level using the enhanced constitutive model.	52
3.6	Numerical-experimental comparison of the remote failure strength of the open-hole tensile and compressive tests.	53
3.7	Numerical-experimental comparison of the remote stress vs. axial strain curves of the open-hole compressive test performed by Wisnom et al. [139]. .	54
3.8	Numerical-experimental comparison of the onset of failure at 98% of the remote failure load from the quasi-isotropic laminate in the open-hole compressive test.	55
3.9	Numerical-experimental comparison of the external failure pattern after the remote failure load from the quasi-isotropic laminate in the open-hole compressive test.	56
3.10	Predicted failure mechanism evolution of the quasi-isotropic laminate in an open-hole compressive test using the enhanced model.	57
3.11	Predicted remote stress vs. axial strain curves from the open-hole compressive test with $[0]_8$	58
3.12	Numerical-experimental comparison of the failure pattern at the remote failure load from the open-hole compressive test with all 8 plies at 0°	59
3.13	Predicted external failure patterns after the remote failure load of the $[0]_8$ laminate in an open-hole compressive test using: a) the enhanced model; and b) the original model.	59
3.14	Predicted remote stress vs. axial strain curves from the open-hole compressive test with $[90]_8$	60
3.15	Predicted failure mechanism at the remote failure strength of the $[90]_8$ laminate in an open-hole compressive test using: a) enhanced model; and b) original model.	61
3.16	Predicted failure pattern when 2.25% of the axial strain is applied from the open-hole compressive test with all 8 plies at 90°	63
4.1	Experimental setup of the transverse tensile (a) and compressive (b) tests. .	68
4.2	Schematic representation of: a) and c) transverse tensile test, and b) and d) transverse compressive test.	69

4.3	Schematic representation of load vs. time curve of the transverse compressive test.	70
4.4	Schematic representation of the procedure to measure the elastic (a) and plastic (b) transverse Poisson's ratios in compression.	72
4.5	Lateral strain field from the transverse tensile (a) and compressive (b) tests using the DIC equipment at $\text{abs}(\bar{\varepsilon}_{22}^{DIC}) \approx 0.5\%$	76
4.6	Stress vs. strain curve obtained from the transverse compressive (left) and tensile (right) tests using the average strain from the two strain gauges.	77
4.7	Goodness-of-fit plot of the DIC axial strain vs. average strain measured from the two strain gauges from the transverse tensile test.	77
4.8	Elastic transverse Poisson's ratio in tension vs. DIC elastic axial strain curve.	78
4.9	Goodness-of-fit plot of the DIC axial strain vs. average strain measured from the strain gauges from the transverse compressive test.	79
4.10	Elastic transverse Poisson's ratio in compression vs. DIC elastic axial strain curve.	80
4.11	Stress vs. strain curve from the transverse compressive test (a) and elastic transverse Poisson's ratio in compression vs. DIC elastic axial strain from different loading cycles (b).	80
4.12	Plastic transverse Poisson's ratio in compression vs. DIC plastic axial strain curve measured from the transverse compressive test.	81
5.1	Schematic representation of the failure envelope for the $\tilde{\sigma}_{22} - \tilde{\sigma}_{33}$ effective stress space with discontinuity.	89
5.2	Schematic representation of the failure envelope for the $\tilde{\sigma}_{11} - \tilde{\sigma}_{12}$ effective stress space with discontinuity.	90
5.3	Schematic representation of the finite element models using in the filled-hole compressive tests.	94
5.4	Schematic representation of the failure envelopes for the effective stress space at the onset of damage.	97
5.5	Normalised strength for each FHC configuration and for each failure envelope. Results are all normalised by the experimental average strength of FI-24np.	98
5.6	Comparison of the failure mechanisms, at the onset of damage, with each failure envelope for the QI-W25 configuration.	100
5.7	Comparison of the failure pattern between the experiments and FE model for three different configurations.	103
6.1	Schematic representation of the assembly of the end-notched flexure finite element model.	106

6.2	Schematic representation of the applied boundary conditions of the end-notched flexure finite element model.	107
6.3	Numerical-experimental comparison of reaction force vs. cross-head displacement of the end-notched flexure test carried out by Jiménez and Miravete [206].	107
6.4	Numerical-experimental comparison of the end-notched flexure test carried out by Jiménez and Miravete [206].	108
6.5	Dimensions of the four-point bending test on L-shaped specimens.	109
6.6	Schematic representation of the applied boundary conditions of the four-point bending finite element model with a L-shaped specimen.	110
6.7	Numerical-experimental comparison of the four-point bending test using L-shaped specimens with the quasi-isotropic laminate (25/50/25) (left) and the highly disoriented laminate (11/67/22) (right) carried out by Airbus. The reaction force is normalised with respect to its experimental average value. .	111
6.8	Numerical-experimental comparison of the external failure pattern at the peak load from the quasi-isotropic laminate (25/50/25): a) experimental data, and b) numerical results. d_t is damage variable associated to the mode-I matrix cracking.	112
6.9	Numerical-experimental comparison of the external failure pattern at the peak load from the highly disoriented laminate (11/67/22): a) experimental data, and b) numerical results. d_t is damage variable associated to the mode-I matrix cracking.	112
6.10	Geometry and dimensions of the single-shear bolted joints. All dimensions are in mm.	113
6.11	Schematic representation of the mesh and boundary conditions applied on the single-lap shear FE model.	115
6.12	Predicted results of the SLS-Net configuration.	116
6.13	Predicted results of the SLS-Bearing configuration.	117
7.1	Schematic representation of uniaxial stress vs. strain curve response at the Gauss-point level.	123
7.2	Schematic representation of the 1D rheological scheme of the proposed constitutive model.	123
7.3	Schematic representation of a transverse tensile test to measure the relaxation time of the Newtonian dashpot of the Maxwell element.	126
7.4	Simple longitudinal shear virtual test at the Gauss-point level at two different strain rate conditions.	138

7.5	Relaxation virtual test under simple longitudinal shear loading conditions at the Gauss-point level.	139
7.6	Comparison between the relaxation test and the monotonically increasing tests at different strain rates applying simple longitudinal shear loading conditions.	140
7.7	Schematic representation of the boundary conditions (a), and the displacement vs. time curves applied to the dynamic tests in the off-axis compressive tests [8] (b).	141
7.8	Numerical-experimental comparison of the remote stress vs. axial strain curves of the off-axis compressive tests performed by Koerber et al. [8].	143
8.1	Comparison of the longitudinal strain from the Infinitesimal Strain theory with that obtained from Green-Lagrange strain tensor (Finite Strain theory) when a rotation and a small longitudinal displacement is applied.	146
8.2	Schematic representation of the deformed shape of unidirectional FRP laminates under longitudinal shear conditions.	148
8.3	Simple longitudinal shear virtual test.	149
8.4	A schematic representation of the stress vs. crack opening displacement curve under longitudinal shear loading conditions for different compressive loads. .	151
8.5	Comparison of the predicted stress vs. cross-head displacement curve of the SLS-Bearing configuration obtained using both the enhanced model and the enhanced model with friction effects.	152
B.1	Softening law in the longitudinal tensile direction.	169
B.2	Softening law in the longitudinal compressive direction.	171
B.3	Stress vs. crack opening displacement curve of the softening law in: a) transverse tensile direction and b) longitudinal shear direction.	174
C.1	Maximum relative error between the analytical solution of $\Delta\gamma$ and its numerical approximation.	187
F.1	Schematic representation of a stress vs. strain curve behaviour using a linear softening law with two different characteristic element lengths.	195
F.2	Schematic representation of a stress vs. strain curve behaviour using a linear softening law with three different characteristic element lengths.	196
F.3	Schematic representation of a stress vs. strain curve behaviour using a bilinear softening law with the critical length of the: a) first segment and b) second segment.	197

G.1	The stress vs. strain curve obtained from a longitudinal compressive virtual test. The cross indicates the longitudinal compressive strength X_C .	201
G.2	The stress vs. strain curve obtained from a longitudinal tensile virtual test. The cross indicates the longitudinal tensile strength X_T .	202
G.3	The stress vs. equivalent strain curve ($\bar{\varepsilon}^p$) obtained from transverse compressive virtual tests.	202
G.4	The stress vs. equivalent strain curve ($\bar{\varepsilon}^p$) obtained from transverse tensile virtual tests.	203
G.5	The stress vs. equivalent strain curve ($\bar{\varepsilon}^p$) obtained from biaxial transverse compressive virtual tests.	203
G.6	The stress vs. equivalent strain curve ($\bar{\varepsilon}^p$) obtained from biaxial transverse tensile virtual tests.	203
G.7	The stress vs. equivalent strain curve ($\bar{\varepsilon}^p$) obtained from longitudinal shear virtual tests.	204
G.8	The stress vs. equivalent strain curve ($\bar{\varepsilon}^p$) obtained from transverse shear virtual tests.	204
G.9	The stress vs. strain curve obtained from a longitudinal compressive virtual test using the original constitutive model proposed in Chapter 2.	206
G.10	The stress vs. strain curve obtained from a longitudinal tensile virtual test using the original constitutive model proposed in Chapter 2.	207
G.11	The stress vs. strain curve obtained from transverse compressive virtual tests using the original constitutive model proposed in Chapter 2.	208
G.12	The stress vs. strain curve obtained from transverse tensile virtual tests using the original constitutive model proposed in Chapter 2.	208
G.13	The stress vs. strain curve obtained from biaxial transverse compressive virtual tests using the original constitutive model proposed in Chapter 2.	209
G.14	The stress vs. strain curve obtained from biaxial transverse tensile virtual tests using the original constitutive model proposed in Chapter 2.	209
G.15	The stress vs. strain curve obtained from longitudinal shear virtual tests using the original constitutive model proposed in Chapter 2.	210
G.16	The stress vs. strain curve obtained from transverse shear virtual tests using the original constitutive model proposed in Chapter 2.	210
G.17	The stress vs. strain curve obtained from a longitudinal compressive virtual test using the enhanced constitutive model proposed in Chapter 3.	212
G.18	The stress vs. strain curve obtained from a longitudinal tensile virtual test using the enhanced constitutive model proposed in Chapter 3.	212

G.19	The stress vs. strain curve obtained from transverse compressive virtual tests using the enhanced constitutive model proposed in Chapter 3.	213
I.1	Schematic representation of a crack band in a continuum damage model. . .	218

List of Tables

2.1	Standardised tests to determine the model input parameters. Other standard procedures may also be employed.	25
2.2	Comparison of the number of elements and nodes with different finite element modelling approaches.	31
2.3	Model input parameters for the IM7/8552 unidirectional prepreg system. . .	33
4.1	Accuracy of the equipment used in the experimental tests.	75
4.2	Transverse Poisson's ratio obtained from the corresponding linear regression analysis of $\bar{\varepsilon}_{33}^{DIC}$ vs. $\bar{\varepsilon}_{22}^{DIC}$	82
5.1	Configurations of the filled-hole compressive tests analysed.	92
5.2	Tests carried out to determine the model input parameters for the carbon/e-poxy unidirectional prepreg system used.	93
6.1	Material properties for steel and titanium alloy.	110
6.2	Dimensions of the single-lap shear tests [201].	114
7.1	Modelling strategies used in the literature to address the dynamic effects in CFRP laminates.	121
7.2	Dynamic model input parameters for a unidirectional IM7/8552 prepreg system.	135
F.1	Critical characteristic element length to prevent the snap-back effect in each direction.	198
G.1	Virtual tests performed to verify the implementation of the plasticity model in a user material subroutine.	201
G.2	Virtual tests performed to verify the implementation of the damage model in a user material subroutine using the original constitutive model.	205
G.3	Virtual tests performed to verify the implementation of the damage model in a user material subroutine using the enhanced constitutive model.	211

List of Codes

D.1	Fortran code of the traditional algorithm of the product between a matrix and a vector ($\mathbf{c} = \mathbf{Ab}$)	189
D.2	Fortran code of the suggested algorithm by Cowell and Christopher [113] of the product between a matrix and a vector ($\mathbf{c} = \mathbf{Ab}$). The code is available at: https://github.com/IR-Cozar/Vector-product-in-Fortran	190
E.1	Fortran code to prevent a division by zero. The code is available at: https://github.com/IR-Cozar/Prevent-a-division-by-zero	193

List of Algorithms

1	Algorithm of the proposed constitutive model at time $t_{(n+1)}$	29
2	Algorithm of the enhanced constitutive model at time $t_{(n+1)}$	49
3	Algorithm of the damage modelling based on the finite strain theory at time $t_{(n+1)}$	150
4	Algorithm in each statement of the above Fortran code (Algorithm D.1). . .	190
5	Algorithm in each statement of the improved Fortran code (Algorithm D.2). .	191

Abstract

In recent decades, several meso-scale computational models have been developed for predicting the failure evolution and strength of composite materials. Nevertheless, the complex failure mechanisms of composites pose a formidable challenge to the development of models capable of consistently reproducing its mechanical response under different loading case scenarios. Furthermore, the lack of standardised multiaxial tests has hindered consensus on failure envelopes and criteria for composites. In this thesis, a new 3D elastoplastic damage model is then proposed to predict the plastic deformation and the progressive failure of unidirectional laminated composite materials at the meso-scale level.

A new plastic yield function and a new non-associative flow rule are proposed to properly define the evolution of the plastic strains. The transverse plastic Poisson's ratio and the volumetric plastic strains can be then imposed. The proposed model is developed under the continuum damage mechanics and the thermodynamics of irreversible process framework. The damage evolution laws are defined to account for the failure mechanisms on both longitudinal and transverse directions. The plastic yield function and the failure criteria can be adjusted by setting two and six input model parameters (envelope shape coefficients), respectively, to account for the mechanical behaviour of the material being analysed. Off-axis compressive and tensile tests with different ply orientations and high plastic dependency are used to demonstrate the ability of the model to capture the plastic response and the onset of damage as well as the fracture planes. In addition, a numerical-experimental comparison of open-hole compressive and tensile tests with different dimensions are carried out to demonstrate the capabilities of the model to predict the failure strength. Good agreement is obtained between the numerical and experimental data.

Spurious damage modes in continuum damage mechanics models for transversally isotropic materials which use the effective stress tensor can be generated when large strains occur. A new methodology to prevent this phenomenon is developed in the present thesis. The longitudinal damage activation functions are based on the effective stress tensor. However, nominal stresses are used on the transverse damage activation function. The proposed method can be straightforwardly implemented on previously-developed constitutive models which use effective stress tensor, and an explicit implementation of the proposed constitutive model is presented. The enhancement of the predicted failure mechanisms obtained from the present constitutive model, with respect to models which use effective stress tensor, is

then demonstrated. The proposed constitutive model presents a good agreement of the predicted failure pattern obtained from open-hole experimental tests, as well as on the predicted failure strength.

Guidelines are provided on how to characterise the input material parameters of the proposed model. In this line, a new methodology to measure the transverse Poisson's ratios in fibre-reinforced polymer composite materials is developed. Transverse tensile and transverse compressive standardised tests are instrumented using digital image correlation equipment to measure the strain field on the through-the-thickness surface of the specimens. A thermoplastic-based composite material is used to describe the proposed methodology. The elastic transverse Poisson's ratio exhibits a different behaviour in tension than in compression, its value being greater in compression than in tension. Assuming no plastic strain in the longitudinal direction, the plastic transverse Poisson's ratio in compression suggests no volumetric plastic strains for small axial plastic strains. However, plastic dilatancy is observed when the amount of compressive plastic axial strain increases.

The influence of the failure envelope shape coefficients on the failure strength prediction of filled-hole compressive laminates is analysed. The analysis is carried out using different geometries, stacking sequences, preloads, etc. The findings indicate a large effect of the failure envelope shape on both the predicted failure strength of filled-hole compressive laminates and developed failure mechanisms. Therefore, the correct adjustment of the failure criteria can be as relevant as defining accurately the model input parameters. These results emphasise the importance of accurately establishing failure envelope, rather than overemphasising the development of complex models.

The capabilities of the constitutive model to predict the mechanical response of carbon fibre-reinforcement polymer laminates under complex loading conditions is demonstrated by performing several numerical-experimental comparisons. Apart from the accurate predictions in the off-axis and open-hole tests, there is good agreement between the numerical results and the experimental data in end-notched flexural test, four-point bending tests using L-shaped specimens and single-lap shear composite bolted joint tests. These tests have been analysed because they are tests in which the non-uniform out-of-plane stress states are developed, and they are challenging problems due to the combination of different failure mechanisms.

The constitutive model is extended to account for the viscous effects due to dynamic loading conditions. A novel 3D viscoelastic-viscoplastic and viscodamage constitutive model is proposed. The viscoelastic response is modelled using the generalised Maxwell model and an overstress model is employed to address the viscoplastic strain. The onset of

viscodamage mechanisms is based on experimental expressions, and their propagation is considered to ensure the correct dissipation of the corresponding energy. The mechanical response of the present constitutive model under pure longitudinal shear loading conditions at different strain rates is presented. The higher the strain rate is, the stiffer the response in the viscoelastic and viscoplastic region is. Additionally, the onset of viscodamage increases with high strain rate. Off-axis compressive experimental data at two different strain rates are employed to demonstrate the capabilities of the present model, and good predictions are obtained.

Resum

En les darreres dècades, diferents models computacionals a nivell meso s'han desenvolupat per predir l'evolució de la fractura i la resistència dels materials compostos. No obstant, els mecanismes de falla dels compostos són complexos i això fa que sigui un gran repte desenvolupar models capaços de reproduir el seu comportament sota diferents estats de càrrega de manera consistent. A més, la falta d'assajos multiaxials estandarditzats ha dificultat el consens sobre les evolvents i criteris de falla dels material compostos. En aquesta tesi s'ha proposat un nou model elastoplàstic amb dany en tres dimensions per predir la deformació plàstica i el dany progressiu dels laminats unidireccionals de material compost a l'escala meso.

Una nova funció de fluència plàstica i una nova regla de fluència no associada es proposen per definir correctament l'evolució de les deformacions plàstiques. Aleshores, es poden imposar el coeficient de Poisson transversal plàstic i les deformacions plàstiques volumètriques. El model proposat es basa en la mecànica del dany continu i la termodinàmica de processos irreversibles. Les lleis d'evolució del dany s'han definit per tenir en compte els mecanismes de falla en la direcció longitudinal i transversal. La funció de fluència plàstica i els criteris de falla es poden ajustar mitjançant dos i sis paràmetres d'entrada del model (coeficients de forma de les evolvents), respectivament, per considerar el comportament mecànic del material que està analitzant. S'utilitzen assajos de compressió i tracció “off-axis” amb diferents orientacions de les capes i una alta dependència plàstica per demostrar la capacitat del model per captar la resposta plàstica, l'inici del dany i també els plans de falla. A més, es realitza una comparació numèric-experimental d'assajos a compressió i tracció en provetes amb un forat amb diferents dimensions per demostrar la capacitat del model de predir la seva resistència. S'obté una bona concordança entre les dades numèriques i les experimentals.

Quan hi ha grans deformacions, es poden generar modes de dany espuris en el models basats en la mecànica del dany continu per materials transversalment isotòpics els quals utilitzen el tensor de tensions efectives. En aquesta tesi es desenvolupa una nova metodologia per prevenir aquest fenomen. Les funcions d'activació del dany longitudinal estan basades en les tensions efectives. En canvi, s'utilitzen les tensions nominals a la funció d'activació del dany transversal. El mètode proposat es pot implementar directament en els models constitutius que s'han desenvolupat prèviament utilitzant les tensions efectives i es presenta una implementació explícita del model constitutiu proposat. A continuació, es mostra la millora en la prediccio dels mecanismes de falla obtinguda amb el model constitutiu

presentat, respecte a models que utilitzen el tensor de tensions efectives. El model constitutiu proposat mostra una bona concordança amb el patró de falla extern obtingut a partir d'assajos experimentals amb provetes foradades i també en la prediccio de la seva resistència.

Es proporcionen pautes per caracteritzar els paràmetres d'entrada del model proposat. En aquesta línia, es desenvolupa una nova metodologia per mesurar els coeficients de Poisson transversal en materials compostos polimèrics reforçats amb fibra. S'instrumentalitzen assajos normalitzats de tracció i de compressió transversals mitjançant un equip de correlació digital d'imatges per mesurar el camp de deformacions a través de l'espessor de la superfície de les provetes. S'utilitza un material compost amb base termoplàstica per descriure la metodologia proposada. El coeficient de Poisson transversal mostra un comportament diferent a tracció que a compressió, sent el seu valor més gran a compressió que a tracció. Assumint que no hi ha deformació plàstiques en la direcció longitudinal, no hi ha deformacions plàstiques volumètriques segons el coeficient de Poisson transversal plàstic a compressió. En canvi, s'observa dilatància plàstica quan la deformació axial transversal a compressió augmenta.

S'analitza la influència dels coeficients de forma de l'evolvent de falla sobre la prediccio de la resistència en provetes a compressió amb un forat i un cargol. L'anàlisi es realitza utilitzant diferents geometries, seqüències d'apilament, precàrregues, etc. Els resultats indiquen que hi ha un gran efecte de la forma de l'evolvent de falla sobre la prediccions de la resistència i el desenvolupament dels mecanismes de falla en les provetes analitzades. Aleshores, el correcte ajustament dels criteris de falla pot ser tan important com definir amb precisió els paràmetres d'entrada del model. Aquest resultats subratllen la importància d'establir amb precisió les evolents de falla, en lloc de focalitzar-se en desenvolupar models complexos.

Les capacitats del model constitutiu per predir la resposta mecànica de laminats polimèrics reforçats amb de fibra de carboni sota condicions de càrrega complexes es demostren realitzant diferents comparacions numèric-experimentals. A més de les bones prediccions obtingudes als assajos "off-axis" i amb les provetes foradades, hi ha una bona concordança entre els resultat numèrics i les dades experimental en assajos a flexió amb una entalla a l'extrem, en assajos a flexió a quatre punts utilitzant provetes en forma de "L" i en assajos d'unions cargolades sotmeses a tallant. Aquest assajos han sigut analitzats perquè són assajos on hi ha estats de tensions no uniformes fora del pla i són un gran repte degut a què hi ha la combinació de diferents mecanismes de falla.

El model constitutiu s'ha ampliat per tenir en compte els efectes viscosos degut a condicions dinàmiques. S'ha proposat un nou model viscoelàstic viscoplàstic amb dany viscós en tres

dimensions. La resposta viscoelàstica s'ha modelat utilitzant el model de Maxwell generalitzat i s'ha utilitzat un model de sobretensió per modelar les deformacions viscoplàstiques. La iniciació dels mecanismes dany viscós es basa en expressions experimentals i la seva propagació té en compte la correcta dissipació de l'energia corresponent. Es presenta la resposta mecànica del model constitutiu proposat sota estats de càrrega longitudinals a tallant a diferents velocitats de deformació. A l'augmentar la velocitat de deformació, augmenta la rigidesa en els règims viscoelàstic i viscoplàstics. A més, la iniciació del dany viscós augmenta a l'augmentar la velocitat de deformació. S'utilitzen assajos “off-axis” a compressió per demostrar les capacitats predictores del model proposat.

Resumen

En las últimas décadas, diferentes modelos computacionales a nivel meso se han desarrollado para predecir la evolución de la fractura y la resistencia de los materiales compuestos. No obstante, los mecanismos de falla de los compuestos son complejos i esto hace que sea un gran reto desarrollar modelos capaces de reproducir su comportamiento bajo diferentes estados de carga de manera consistente. Además, la falta de ensayos mutiaxiales normalizados ha dificultado el consenso sobre las envolventes y los criterios de fallo de los materiales compuestos. En esta tesis se propone un nuevo modelo de daño elastoplástico en 3D para predecir la deformación plástica y el fallo progresivo de los laminados unidireccionales de materiales compuesto a escala meso.

Una nueva función de fluencia plástica y una nueva regla de fluencia no asociada se proponen para definir correctamente la evolución de las deformaciones plásticas. Entonces, se pueden imponer el coeficiente de Poisson transversal plástico y las deformaciones plásticas volumétricas. El modelo propuesto se basa en la mecánica del daño continuo y la termodinámica de procesos irreversibles. Las leyes de evolución del daño se han definido para tener en cuenta los mecanismos de falla en la dirección longitudinal y transversal. La función de fluencia plástica y los criterios de falla pueden ajustarse mediante dos y seis parámetros de entrada del modelo (coeficientes de forma de las envolventes), respectivamente, para considerar el comportamiento mecánico del material que está analizando. Se utilizan ensayos de compresión y tracción "off-axis" con diferentes orientaciones de las capas y una alta dependencia plástica para demostrar la capacidad del modelo para captar la respuesta plástica, el inicio del daño y también los planos de falla. Además, se realiza una comparación numérico-experimental de ensayos a compresión y tracción en probetas con un agujero con distintas dimensiones para demostrar la capacidad del modelo de predecir su resistencia. Se obtiene una buena concordancia entre los datos numéricos y experimentales.

Cuando existen grandes deformaciones, se pueden generar modos de daño espurios en los modelos basados en la mecánica del daño continuo por materiales transversalmente isotrópicos que utilizan el tensor de tensiones efectivas. En esta tesis se desarrolla una nueva metodología para prevenir ese fenómeno. Las funciones de activación del daño longitudinal están basadas en las tensiones efectivas. Sin embargo, se utilizan las tensiones nominales en la función de activación del daño transversal. El método propuesto puede implementarse directamente en los modelos constitutivos que se han desarrollado previamente utilizando las tensiones efectivas y se presenta una implementación explícita del modelo constitutivo

propuesto. A continuación, se muestra la mejora en la predicción de los mecanismos de falla obtenida con el modelo constitutivo presentado respecto a modelos que utilizan el tensor de tensiones efectivas. El modelo constitutivo propuesto muestra una buena concordancia con el patrón de falla externo obtenido a partir de ensayos experimentales con probetas agujereadas y también en la predicción de su resistencia.

Se proporcionan pautas para caracterizar los parámetros de entrada del modelo propuesto. En esta línea, se desarrolla una nueva metodología para medir los coeficientes de Poisson transversal en materiales compuestos poliméricos reforzados con fibra. Se instrumentalizan ensayos normalizados de tracción y compresión transversales mediante un equipo de correlación digital de imágenes para medir el campo de deformaciones a través del espesor de la superficie de las probetas. Se utiliza un material compuesto de base termoplástica para describir la metodología propuesta. El coeficiente de Poisson transversal muestra un comportamiento diferente a tracción que a compresión, siendo su mayor valor a compresión que a tracción. Asumiendo que no existe deformación plástica en la dirección longitudinal, no hay deformaciones plásticas volumétricas según el coeficiente de Poisson transversal plástico a compresión. Sin embargo, se observa dilatación plástica cuando la deformación axial transversal a compresión aumenta.

Se analiza la influencia de los coeficientes de forma de la envolvente de falla sobre la predicción de la resistencia en probetas a compresión con un agujero y un tornillo. El análisis se realiza utilizando diferentes geometrías, secuencias de apilado, precargas, etc. Los resultados indican que existe un gran efecto de la forma de la envolvente de falla sobre las predicciones de la resistencia y el desarrollo de los mecanismos de falla en las probetas analizadas. Entonces, el correcto ajuste de los criterios de falla puede ser tan importante como definir con precisión los parámetros de entrada del modelo. Estos resultados subrayan la importancia de establecer con precisión las evolventes de falla, en lugar de focalizarse a desarrollar modelos complejos.

Las capacidades del modelo constitutivo para predecir la respuesta mecánica de laminados poliméricos reforzados con fibra de carbono bajo condiciones de carga complejas se demuestran realizando diferentes comparaciones numérico-experimentales. Además de las buenas predicciones obtenidas en los ensayos “off-axis” y con las probetas agujereadas, existe una buena concordancia entre los resultados numéricos y los datos experimental en ensayos a flexión con una muesca en el extremo, en ensayos a flexión a cuatro puntos utilizando probetas en forma de “L” y en ensayos de uniones atornilladas sometidas a cortante. Estos ensayos han sido analizados porque son ensayos donde existen estados de tensiones

no uniformes fuera del plano y son un gran reto debido a que existe la combinación de diferentes mecanismos de falla.

El modelo constitutivo se ha extendido para tener en cuenta los efectos viscosos debido a condiciones dinámicas. Se ha propuesto un nuevo modelo viscoelástico viscoplástico con daño viscoso en tres dimensiones. La respuesta viscoelástica se ha moldeado utilizando el modelo de Maxwell generalizado y se ha utilizado un modelo de sobretensión para modelar las deformaciones viscoplásticas. La iniciación de los mecanismos de daño viscoso se basa en expresiones experimentales y su propagación tiene en cuenta la correcta disipación de la energía correspondiente. Se presenta la respuesta mecánica del modelo constitutivo propuesto bajo estados de carga longitudinales a cortante a distintas velocidades de deformación. Al aumentar la velocidad de deformación, aumenta la rigidez en los regímenes viscoelástico y viscoplásticos. Además, la iniciación del daño viscoso aumenta al aumentar la velocidad de deformación. Se utilizan ensayos “off-axis” a compresión para demostrar las capacidades de predicción del modelo propuesto.

Introduction

1.1 Contextual background

Composite materials are defined as a combination of materials with different constituents. They do not fuse or dissolve into each other and can usually be physically identified. The structure of composites consists of two components: i) matrix and ii) reinforcement. In addition, the region between these two components is known as the interface. The reinforcement constituent is surrounded by the matrix component, resulting in superior properties of both materials [1]. Matrices can be divided into three main groups: i) metallic, ii) ceramic, and iii) polymeric, while the reinforcements can be made of different material: glass, carbon, aramid, etc. [2, 3]; and geometries: particles, short fibres, long fibres, etc. The present thesis focuses on unidirectional plies of polymer-based composite materials reinforced with long carbon fibres.

Carbon fibre-reinforced polymer (CFRP) laminates are the combination of multiple CFRP laminae tailored to withstand the appropriate external loads, improving the stiffness and strength of a single laminae [4]. They can fail due to various interacting failure mechanisms such as fibre failure, matrix cracking and delamination, due to the heterogeneity of the material and its complex mechanical behaviour [5]. Fibre failure under tensile loading occurs on a plane perpendicular to the longitudinal axis, whereas compressive fibre failure is due to the collapse of the fibres and promotes shear kinking and matrix damage [6, 7]. Matrix cracking occurs in the resin, accounting for fibre-matrix debonding or voids. Delamination between layers can be promoted by interlaminar stresses that can develop at the free edges or due to curvature areas, as well as out-of-plane loading conditions such as impacts, etc. In addition, CFRP components exhibit non-linearity due to plastic deformation, which causes stress redistribution and affects the onset of failure mechanisms. The directions governed by the matrix can show significant plastic deformation [8–10]. Furthermore, the mechanical behaviour of CFRPs depends on the hydrostatic pressure in both plastic and damage stages [11, 12].

The use of CFRP laminates in the aircraft component manufacturing has increased in the recent years due to its high stiffness and strength, low density and high fatigue resistance [1, 13, 14]. CFRPs are widely employed in major-load bearing structures and replace older aircraft structures which were made of aluminium. In addition, CFRP laminates are used in the automotive sector to reduce the pollutant emissions through weight reduction of

vehicles, thereby improving energy efficiency in both internal combustion engine vehicles [14–16] and electric vehicles [17–20].

The certification requirements for composite structures in the civil aircraft sector require long and expensive test campaigns. For instance, during the airworthiness certification process, all critical loading scenarios and associated failure modes must be considered: environmental effects, material and manufacturing variability, defects, and service damage during maintenance [21]. The building block approach is a method often used to support the certification process. This approach involves different levels of testing from coupon level to component level (the complete full scale product) [2, 21, 22]. Experimental testing is then combined with analysis techniques to achieve a good balance between the cost and reliability of CFRP structural designs.

Finite element (FE) models with appropriate constitutive models can be used to model the mechanical behaviour of fibre-reinforced polymer (FRP) structures. The FE modelling approach for FRPs can be divided into different length scales from lower to higher as [23]: micro-mechanical, meso-mechanical and macro-mechanical, see Fig. 1.1. Macro-mechanical analyses use shell elements to model FRP laminates with many integration points through-the-thickness as the number of plies in the laminate [24–26]. As a result, the analyses are limited to plane stress states, but are very efficient in terms of computational time [27]. They are often employed to predict the behaviour of large structures, but also for preliminary design and optimisation processes [28–32].

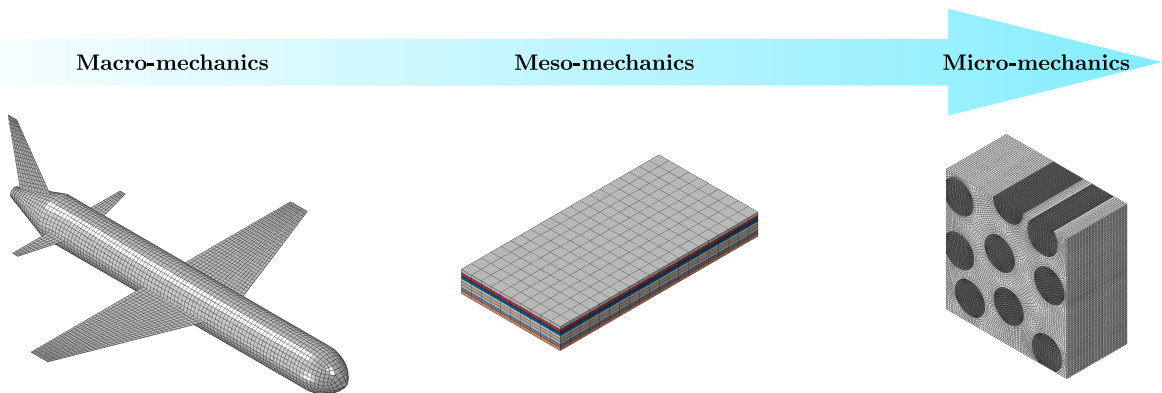


Figure 1.1.: Schematic representation of the length scales employed in the finite element models.

In the other extreme, micro-mechanical analyses model the constituents (fibres and matrix) providing detailed information of the deformation and fracture processes of FRP laminates [33]. No simplifications or assumptions are required as in the higher length scales. However, FE models at this scale are generally limited to small representative volumes due to the high computational time, and are not suitable for application at the coupon or structural

level. They are usually employed to design the material itself [34–37] and analyse the effect of defect of FRPs [38–46].

Each laminae of FRP laminates is explicitly modelled at the meso-scale level. Therefore, the laminate is constructed by stacking each ply with the appropriate fibre orientation. The intralaminar behaviour of each layer can be then modelled by assuming that the FRP plies behave as a transversely isotropic homogeneous material within the continuum damage mechanics (CDM) framework [5, 47–52]. In addition, the interface behaviour between the plies can be considered using cohesive zone models [53–56].

The CDM theory was originally proposed by Kachanov [57] and Rabotnov et al. [58] for creep analysis of metals. The CDM is based on the general framework of thermodynamics of irreversible processes with internal state variables [59]. The constitutive equations of the material are modelled as a continuum. The deformation is described by the strain field variable, while the distribution of internal forces is described by the stress field. Under certain loading conditions, the material starts to degrade and is modelled it by a continuum field in CDM. Therefore, a discontinuity (a crack) is modelled by continuous variables [60]. The elastic material properties are degraded by the internal damage variables.

Meso-mechanical models can be categorised according to their discretisation [61] (see Fig. 1.2 from left to right): i) fully continuum model without interface elements, ii) continuum model for intralaminar damage with cohesive elements to model delamination, iii) continuum model in the fibre direction with cohesive elements to capture matrix cracking and delamination and iv) fully discretised model with cohesive elements to capture fibre failure, matrix cracking and delamination. Regardless of the level of discretisation, all continuum damage models have three common parts: i) the undamaged state which can be linear, elasto-plastic, visco-elastic, etc.; ii) the onset of damage; and iii) the damage propagation modelling. This thesis focuses on the modelling of CFRP laminates at the meso-scale level.

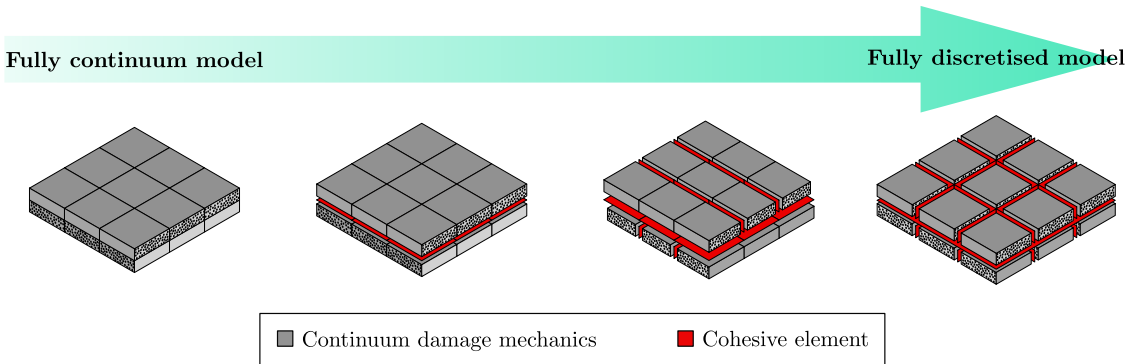


Figure 1.2.: Schematic representation of the discretisation of the different meso-mechanical analyses of finite element models. Note that the dots are the schematic representation of the fibres, but the fibres are not explicitly modelled.

1.2 Motivation

CFRP structures can fail due to various interacting failure mechanisms. As a consequence, extensive experimental test campaigns are necessary for designing and certifying composite parts [2]. The development of accurate modelling and simulation approaches to support design and certification processes is an ongoing topic. This will allow experimental test campaigns to be replaced or complemented by virtual testing, thereby reducing the time of the design process and the final cost of CFRP structures.

Often, the load-carrying capacity of FRP structures does not suddenly drop when the onset of damage occurs in a specific region. The structure can support additional load before collapsing completely. Therefore, it is important to quantify the initial failure as well as its development and progression. Additionally, FRP laminates can exhibit plastic deformation under loading states governed by the matrix, such as under transverse shear loading scenarios. Plastic deformation can produce stress redistribution that affects the failure of FRP laminates. Other important aspect to consider is the influence of dynamic loading on the mechanical response of FRPs, as the loading rate effects can be significant in impact loading scenarios. Moreover, the effect of the 3D stress states on the failure mechanisms is significant such as in curved FRP laminates, bolted composite joints with clamping pressure, etc. These factors, among others, make predicting the mechanical response of FRPs a challenging task.

Different methods to predict the failure response of FRP laminates under complex loading conditions have been carried out in the literature. The world wide failure exercises [62–67] evaluated the predictive ability of each method by comparing its predictions with experimental data. The comparison demonstrated that none of the theories considered successfully predicted properly all the analysed aspects: the onset of damage, laminate

strength, crack density, large deformation, etc. [62, 66, 68]. Several constitutive models have been proposed for FRP structures in the literature. However, no single model has been consolidated as a reference. There is no single 3D constitutive model presented in the literature that combines plastic modelling, failure modelling (onset and progressive model), and considers the dynamic loading effects of FRPs. Additionally, the models that partially account for these aspects have not been fully validated.

1.3 Objectives

The main objective of the thesis is to develop a high-fidelity model to predict the plastic deformation and fracture of FRP laminates under dynamic loading conditions. This main objective is addressed through the following sub-objectives:

1. To develop a constitutive model to predict the plastic deformation and fracture of FRP laminates under quasi-static loading conditions.
2. To implement the constitutive model in a subroutine to be used with a FE commercial solver.
3. To verify the implementation of the constitutive model.
4. To carry out an extensive numerical-experimental comparison to analyse the capabilities of the model to predict the mechanical response of FRPs.
5. To extend the quasi-static model to predict the plastic deformation and fracture of FRP laminates under dynamic loading conditions.

1.4 Methodology

As a starting point, a state-of-art of constitutive models proposed in the literature to predict the plastic deformation and fracture of FRP laminates at the meso-scale level is conducted. An existing 3D damage model is selected and extended to also predict plastic deformation in [Chapter 2](#). A new yield function and a non-associative flow rule are proposed. Then, a new implementation is also proposed to combine plastic and damage modelling. The algorithm is implemented in a user-defined material in Fortran subroutine to be used in a commercial FE software. The capabilities of the proposed model to predict the plastic deformation and fracture of FRP laminates are also demonstrated through numerical-experimental comparisons under different loading states. A scientific article has already been published based on this work.

After, the proposed constitutive model is enhanced to improve the prediction of the failure mechanisms after the onset of damage. The new formulation and its implementation are described in [Chapter 3](#). The new model is also implemented in a user material Fortran subroutine and verified. A comparison is carried out between the predictions of the enhanced model and those of the original model to demonstrate the improvements. Furthermore, a numerical-experimental comparison is conducted. Another scientific article has already been published based on this work.

Most of the model input parameters can be characterised using standardised tests or experimental methodologies proposed in the literature. Only the methodology to measure the transverse Poisson's ratio and the shape of the failure envelope in some stress spaces are not clearly defined with standard tests. Therefore, a new methodology is proposed to measure the transverse Poisson's ratio in [Chapter 4](#), and a numerical analysis is conducted to determine the effect of the failure envelope on the failure strength in [Chapter 5](#).

From the new proposed methodology, the transverse Poisson's ratio can be measured experimentally in both the elastic and plastic regions. Experimental tests are carried out using a CFRP thermoplastic-based composite material to demonstrate the ability of the proposed methodology. Finally, the experimental data are presented and analysed. This work is also summarised in a scientific article and has already been published.

The influence of the selected failure criterion on the failure strength of FRP laminates under 3D loading conditions is investigated. In this analysis, different failure criterion are defined in the longitudinal vs. transverse stress space. The numerical results are compared to experimental data highlighting the significant influence of the failure criterion on the failure predictions. This analysis is also summarised in a scientific article already published.

The enhanced constitutive model is evaluated under different complex 3D loading conditions in [Chapter 6](#). Numerical-experimental comparisons of different loading cases are conducted. The FE modelling strategy of each case is described, and the results are analysed.

The enhanced constitutive model is then extended to account for visco effects due to dynamic loading conditions in [Chapter 7](#). The new model is described, implemented in a user material Fortran subroutine, and verified. Finally, a numerical-experimental comparison is performed and analysed. This viscous constitutive model is also described in scientific article already accepted for publication.

Different numerical limitations of the proposed constitutive model are analysed in [Chapter 8](#). Firstly, some aspects of the use of the Infinitesimal Strain theory are presented and analysed.

The results obtained from the Infinitesimal Strain theory are then compared with those obtained from the Finite Strain theory. Additionally, a potential influence of the friction effects in the constitutive model is presented.

The thesis concludes by proposing future work to further improve the proposed constitutive model in [Chapter 9](#). The concluding remarks summarise the work done. Additionally, detailed descriptions of previously mentioned milestones are presented in different appendices.

1.5 Research dissemination

The work included in this thesis resulted in the following scientific publications:

- i. **I.R. Cózar**, F. Otero, P. Maimí, E.V. González, S. Miot, A. Turon, and P.P. Camanho. A three-dimensional plastic-damage model for polymer composite materials. *Composites Part A: Applied Science and Manufacturing* (2022), 163, 107198. DOI: <https://doi.org/10.1016/j.compositesa.2022.107198>
ISSN: 1359-835X, Impact Factor: 8.7, ranked 4/35 in the category of *Materials Science, Composites* (1st quartile)¹.
- ii. **I.R. Cózar**, F. Otero, P. Maimí, E.V. González, A. Turon, and P.P. Camanho. An enhanced constitutive model to predict plastic deformation and multiple failure mechanisms in fibre-reinforced polymer composite materials. *Composite Structures* (2024), 330, 117696. DOI: <https://doi.org/10.1016/j.compstruct.2023.117696>
ISSN: 0263-8223, Impact Factor: 6.3, ranked 6/35 in the category of *Materials Science, Composites* (1st quartile)¹.
- iii. **I.R. Cózar**, J.J. Arbeláez-Toro, P. Maimí, F. Otero, E.V. González, A. Turon, and P.P. Camanho. A novel methodology to measure the transverse Poisson's ratio in the elastic and plastic regions for composite materials. *Composites Part B: Engineering* (2024), 272, 111098. DOI: <https://doi.org/10.1016/j.compositesb.2023.111098>
ISSN: 1359-8368, Impact Factor: 13.1, ranked 1/35 in the category of *Materials Science, Composites* (1st quartile)¹.
- iv. **I.R. Cózar**, J.M. Guerrero, P. Maimí, A. Arteiro, S. García-Rodríguez, M. Herman and A. Turon. (2024). Influence of unidirectional composite failure envelope shape on predicting compressive failure of a laminate with a filled-hole. *Composites Part B: Engineering*, 276. DOI: <https://doi.org/10.1016/j.compositesb.2024.111352>

ISSN: 1359-8368, Impact Factor: 13.1, ranked 1/35 in the category of *Materials Science, Composites* (1st quartile)¹.

- v. **I.R. Cózar**, P. Maimí, E.V. González, P.P. Camanho and F. Otero. A three-dimensional viscoelastic-viscoplastic and viscodamage constitutive model for unidirectional fibre-reinforced polymer laminates. *Composites Science and Technology*, 110634. DOI: <https://doi.org/10.1016/j.compscitech.2024.110634>

ISSN: 0266-3538, Impact Factor: 9.1, ranked 5/35 in the category of *Materials Science, Composites* (1st quartile)¹.

Additionally, the work presented in this thesis has been disseminated in the following conferences:

- i **I.R. Cózar**, P. Maimí, F. Otero, E.V. González, P.P. Camanho, S. Miot and A. Turon. A novel plasticity-damage constitutive model for unidirectional long fibre reinforced polymer. In: *Composites 2021 - 8th ECCOMAS thematic conference on the mechanical response of composite*. Online event, 2021. International conference: Oral presentation.
- ii **I.R. Cózar**, E.V. González, P. Maimí, F. Otero, P.P. Camanho and A. Turon. Development of analytical and computational methods to predict the mechanical behavior of thermoplastic-based composite materials. In: *The Vth conference of predoctoral researchers*. Online event, 2021. Doctoral School of the Universitat de Girona, internal conference: Oral presentation.
- iii **I.R. Cózar**, P. Maimí, F. Otero, E.V. González, P.P. Camanho, S. Miot and A. Turon. A novel plasticity-damage constitutive model for unidirectional long fibre reinforced. In: *MATCOMP'21 - XIV Congreso nacional de materiales compuestos*. Sevilla, Spain 2022. Asociación española de materiales compuestos, national conference: Oral presentation.
- iv **S.M. García-Rodríguez**, M. Herman, J.-L. Leon-Dufour, M. Kaminski, I.R. Cózar, F. Laurin, A. Turon, C. Fagiano. Progressive failure analysis of filled hole and bearing composite laminate bolted joints. In: *11th International Conference on Composites Testing and Model Identification*. Girona, Spain 2023. International conference: Oral presentation.
- v **I.R. Cózar**, F. Otero, P. Maimí, E.V. González, A. Turon and P.P. Camanho. An enhanced 3D elastoplastic-damage constitutive model for fibre-reinforced polymer

composite materials. In: *Composites 2023 - The 9th ECCOMAS thematic conference on the mechanical response of composites*. Trapani, Italy 2023. International conference: Oral presentation.

vi **I.R. Cózar**, J.M. Guerrero, P. Maimí, A. Arteiro, S. García-Rodríguez, M. Herman, A. Turon and F. Otero. Influence of the failure criteria on the failure strength prediction of filled-hole compressive tests using carbon fibre reinforced polymer laminates. In: *NewFrac Conference - New computational strategies for fracture*. Porto, Portugal 2024. International conference: Oral presentation.

Elastoplastic damage model

In recent decades, several meso-mechanical models have been developed to predict the failure evolution and strength of FRP laminates [5, 51, 52]. However, the complex mechanical behaviour of FRPs presents a major challenge in developing a model capable of consistently reproducing different loading conditions, from in-plane to complex 3D conditions [62, 66, 68]. As previously explained, the fracture of FRPs are governed by the combination of different failure mechanisms. Furthermore, the plastic deformation of the FRP structures under certain loading conditions causes stress redistribution, which affects the failure mechanisms. All these phenomena need to be taken into account by formulating advanced constitutive models to accurately predict the mechanical response of FRP structures.

Out-of-plane stresses are insignificant when laminated composite materials are used in thin structures where in-plane stresses dominate the stress state away from free edges. However, FRP laminates are used in complex geometries where it is critical to capture the effects of out-of-plane stresses [69]. Therefore, 3D material models are needed to capture the inelastic deformation and fracture behaviour in out-of-plane stress states (e.g. shear yielding and the fracture strengths affected by the hydrostatic pressure [11, 12], three-dimensional (3D) stress state effects on the failure of pressure vessels [70], three-point bending tests to predict the out-of-plane tensile strength [71], bolted composite joints with clamping pressure, in impact tests, in curved structures, etc.), but also under the in-plane stress states (e.g. tests with in-plane boundary conditions where interface damage plays a relevant role).

Plasticity models combined with continuum damage mechanics formulations are often used to predict the non-linear mechanical response of FRP laminates. Chen et al. [72] developed an elastoplastic damage model to predict the mechanical response of a unidirectional FRP laminate by assuming plane stress conditions. The plasticity model was based on the model presented by Sun and Chen [73]. An isotropic yield function and an associative flow rule were used. The damage model was based on the Hashin's failure criteria with three damage variables to capture: fibre failure, matrix cracking due to a pure transverse load, and longitudinal shear stiffness degradation from fibre failure and matrix cracking. The damage evolution was described with exponential softening laws. The onset of damage was validated by comparing the numerical failure predictions with the failure strength from open-hole tensile tests. In general, good predictions were found, although the relative error was higher than 15% for 4 of the 17 cases studied. In addition, an in-plane shear

test was simulated. The results showed a good prediction of the plastic strain but an under-prediction of the failure strength.

Hoffarth et al. [74] proposed an elastoplastic damage model to predict the mechanical behaviour of a unidirectional FRP laminate under impact load. The yield function of the plasticity model was defined using the Tsai-Wu composite failure criterion [75]. A new non-associative flow rule was proposed to define the evolution of the plastic strains. The onset and propagation of damage were based on the work of Matzenmiller et al. [76]. The authors compared the out-of-plane displacement vs. time curve obtained from an impact test with the numerical predictions. The predicted curve accurately captured the positive and negative peak displacement values of the first cycle and the displacement profile around the first peak. However, the peak displacements were overestimated for the subsequent cycles.

Xie et al. [77] presented an elastoplastic damage model to describe the mechanical response of a carbon fibre reinforced carbon-silicon carbide (C/C-SiC) composite material in-plane stress conditions. The authors proposed a new yield function as a function of the in-plane stresses and the material properties, and an associative flow rule was used. Three damage variables were used to degrade the in-plane elastic material properties. The evolution of each damage variable was defined using exponential functions. The material model was validated by comparing the plastic response to the one obtained from experimental data. Off-axis tensile and in-plane shear curves were predicted with a good agreement with the experimental data, and the plastic deformations were correctly predicted. In addition, the load-displacement, load-plastic strain and load-strain predicted curves from a single open-hole tensile test were compared to the corresponding experimental data. Again, the material model properly captured the plastic response.

Holthusen et al. [78] developed a constitutive model for unidirectional fibre composite materials. The plasticity model was based on the Von Mises yield criterion with an associative flow rule. Three damage variables were used: two associated with the fibre (tension and compression damage) and one for the matrix. The authors showed the simulated response of the material under cyclic uniaxial tensile-compressive loading and the interaction between the fibre and matrix damage. Open-hole virtual tests were also performed with different conditions on the material model (enabling/disabling plasticity and damage).

Chen et al. [10] proposed an elastoplastic damage model to describe the plastic hardening response and damage evolution. The modified Drucker-Prager yield criterion proposed by Cho et al. [79] was employed to account for the deviatoric and dilatational plastic

deformation. In addition, the authors added a term in the yield function to prevent compressive stresses from generating shear yielding based on the work of Daniel [80]. An associative flow rule was used. The damage activation functions was based on the Puck failure criteria [81, 82]. Exponential damage laws were used to model the degradation of the elastic material properties in the principal directions. The model was validated by simulating off-axis compressive and tensile tests. The comparison with the experimental test showed good agreement of the stress vs. strain curves and the failure strengths.

From the previous literature observations, there is a need to develop an elastoplastic damage model using: a plastic flow rule to capture the plastic dilatancy or contractility, a 3D material model to account for out-of-plane loading conditions, and an extensive comparison of the numerical predictions with experimental data. Therefore, the objective of this chapter is to develop a reliable constitutive model to predict the plastic deformation and the progressive failure of FRPs at the meso-scale level. The constitutive model is described in [Section 2.1](#) and the characterisation of the input model properties in [Section 2.2](#). The numerical implementation of the model is described in [Section 2.3](#). The capabilities of the model are demonstrated by comparing the numerical results with experimental data from off-axis compressive and tensile tests and open-hole compressive and tensile (OHC and OHT, respectively) tests. [Section 2.4](#) presents a detailed comparison of the stress vs. strain curves, the failure strength and the fracture planes.

2.1 Constitutive model

The proposed material model is developed within the framework of the Infinitesimal Strain theory. The strain tensor is composed as

$$\boldsymbol{\varepsilon} = \boldsymbol{\varepsilon}^e + \boldsymbol{\varepsilon}^p, \quad (2.1)$$

where $\boldsymbol{\varepsilon}^e$ is the elastic strain tensor (it includes cracking strains) and $\boldsymbol{\varepsilon}^p$ is plastic strain tensor.

For homogenised composite materials, plasticity is not considered in the longitudinal direction. The model describes a purely elastic response before the onset of damage in the longitudinal direction, [Fig. 2.1a](#). However, an elastic behaviour until the onset of plasticity in the directions governed by the matrix is assumed. Then, the plastic strains can grow until a matrix crack is started. After that, the damage develops without increasing the plastic strains at the Gauss-point level, see [Fig. 2.1b](#).

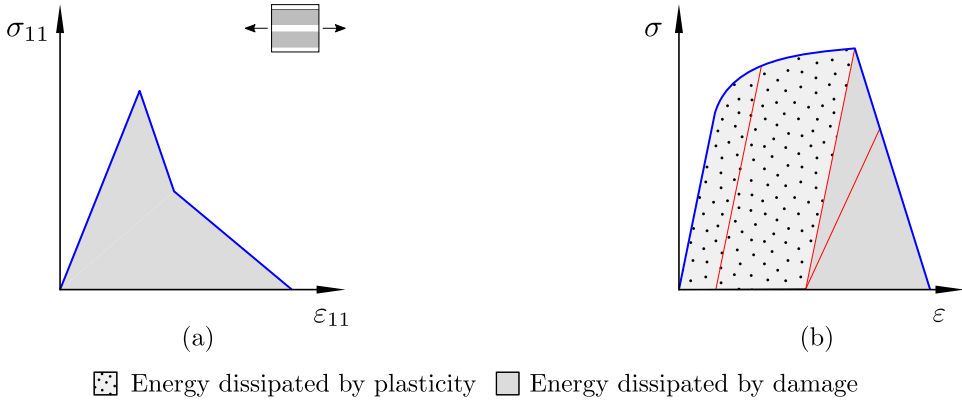


Figure 2.1.: Schematic representation of uniaxial stress vs. strain curve response at the Gauss-point level: a) in the longitudinal direction, and b) in the directions governed by the matrix.

A new plasticity model is proposed and combined with a damage model (see Fig. 2.1b). Several failure criteria have been proposed in the literature such as maximum stress/strain criterion, Hashin's criterion, LaRC, Puck's criterion [82–85], etc. As evidenced by the world wide failure exercises [63–67], there is no a single failure criteria that can consistently reproduce the experimental data. For this reason, the damage model developed by Quintanas-Corominas et al. [86] is used in the proposed constitutive model of this thesis, since this damage modelling allows the failure criteria to be modified as a function of six input model parameters. Therefore, the failure envelope can be adjusted according to the behaviour of the material being studied, rather than having a fixed failure criteria as seen in other models.

The complementary Gibbs free-energy density function (W) proposed by Quintanas-Corominas et al. [86] is then used. The model depends on four of the five invariants of the stress tensor (σ) at a rotation with respect to the longitudinal axis: the longitudinal stress σ_ℓ (fibre dominant direction); the transverse hydrostatic pressure p_t ; τ_ℓ and τ_t which are related with the longitudinal shear stress and the transverse shear stress, respectively. The function W is defined as

$$W := \frac{\sigma_\ell^2}{2(1-d_\ell)E_{11}} - \frac{2\nu_{12}\sigma_\ell p_t}{E_{11}} + \frac{p_t^2}{2(1-d_t)E_t} + \frac{\tau_t^2}{2(1-d_{st})G_t} + \frac{\tau_\ell^2}{2(1-d_{s\ell})G_{12}} + \boldsymbol{\sigma}^T \boldsymbol{\varepsilon}^p, \quad (2.2)$$

where E_{11} is the longitudinal elastic modulus, ν_{12} is the longitudinal Poisson's ratio and G_{12} is the longitudinal shear elastic modulus. E_t and G_t are the bulk and shear elastic stiffness in the transverse isotropic plane, respectively, which are defined as

$$E_t := \frac{E_{22}}{2(1-\nu_{23})}, \quad (2.3)$$

and

$$G_t := \frac{E_{22}}{2(1 + \nu_{23})}, \quad (2.4)$$

where E_{22} is the transverse elastic modulus and ν_{23} is the transverse Poisson's ratio. The stress invariants are defined as

$$\sigma_\ell = \sigma_{11}, \quad (2.5)$$

$$p_t = \frac{\sigma_{22} + \sigma_{33}}{2}, \quad (2.6)$$

$$\tau_\ell = \sqrt{\sigma_{12}^2 + \sigma_{13}^2} \quad (2.7)$$

and

$$\tau_t = \frac{\sqrt{(\sigma_{22} - \sigma_{33})^2 + 4\sigma_{23}^2}}{2}, \quad (2.8)$$

where σ_{ij} are the Cartesian components of the stress tensor ($\boldsymbol{\sigma}$). The scalar variables $d_{M=\ell,t,s\ell,st}$ describe the damage state in the corresponding direction. The subscript ℓ refers to longitudinal (fibre), t refers to transverse (matrix) and s refers to shear. The material is undamaged for $d_M = 0$, is damaged for $0 < d_M \leq 1$, and is fully damaged for $d_M = 1$.

The strain tensor is obtained from the Clausius-Duhem inequality [47, 87] as the derivative of W with respect to the mechanical stresses as

$$\boldsymbol{\varepsilon} = \frac{\partial W}{\partial \boldsymbol{\sigma}} = \mathbb{H}\boldsymbol{\sigma} + \boldsymbol{\varepsilon}^p, \quad (2.9)$$

where \mathbb{H} is the compliance tensor and can be expressed in Voigt Notation as

$$\mathbb{H} = \begin{bmatrix} \mathbb{H}_{11} & \mathbb{H}_{12} & \mathbb{H}_{12} & 0 & 0 & 0 \\ \mathbb{H}_{12} & \mathbb{H}_{22} & \mathbb{H}_{23} & 0 & 0 & 0 \\ \mathbb{H}_{12} & \mathbb{H}_{23} & \mathbb{H}_{22} & 0 & 0 & 0 \\ 0 & 0 & 0 & \mathbb{H}_{44} & 0 & 0 \\ 0 & 0 & 0 & 0 & \mathbb{H}_{55} & 0 \\ 0 & 0 & 0 & 0 & 0 & \mathbb{H}_{55} \end{bmatrix} \quad (2.10)$$

with:

$$\begin{aligned}
\mathbb{H}_{11} &= \frac{1}{(1-d_\ell)E_{11}} \\
\mathbb{H}_{12} &= -\frac{\nu_{12}}{E_{11}} \\
\mathbb{H}_{22} &= \frac{1}{4(1-d_t)E_t} + \frac{1}{4(1-d_{st})G_t} \\
\mathbb{H}_{23} &= \frac{1}{4(1-d_t)E_t} - \frac{1}{4(1-d_{st})G_t} \\
\mathbb{H}_{44} &= \frac{1}{(1-d_{st})G_t} \\
\mathbb{H}_{55} &= \frac{1}{(1-d_{s\ell})G_{12}}.
\end{aligned} \tag{2.11}$$

2.1.1 Modelling Plasticity

A scalar function is proposed as the yield function, which depends on the stress invariants, and the equivalent plastic strain $\bar{\varepsilon}^p$ since the yield stresses (Y_{TP} , Y_{CP} and S_{LP}) are defined as a function of $\bar{\varepsilon}^p$, see Fig. 2.2. The yield function is developed from the transverse loading function proposed by Quintanas-Corominas et al. [86], because it is a convex function homogeneous of degree one. In addition, the function allows different shapes of the yield surface to be defined. Furthermore, a single function is used for defining a closed plastic envelope instead of using multiple equations as formulated in other models (e.g. using one for compression and one for tension depending on the transverse hydrostatic pressure [9]). Therefore, the yield function reads

$$\begin{aligned}
\phi^p(\boldsymbol{\sigma}, \bar{\varepsilon}^p) := & \sqrt{\left(\frac{Y_{CP} + Y_{TP}}{Y_{CP}Y_{TP}}\right)^2 \frac{\tau_t^2 + \mu_{tp}p_t^2}{1 + \mu_{tp}} + \left(\frac{\mu_{s\ell p}}{S_{LP}}\tau_\ell\right)^2} \\
& + \frac{Y_{CP} - Y_{TP}}{Y_{CP}Y_{TP}}p_t + \frac{1 - \mu_{s\ell p}}{S_{LP}}\tau_\ell - 1 \leq 0,
\end{aligned} \tag{2.12}$$

where Y_{TP} and Y_{CP} are the transverse tensile and compressive yield stresses, respectively, and S_{LP} is the longitudinal shear yield stress. $\mu_{s\ell p}$ and μ_{tp} are the plastic envelope shape coefficients, see Fig. 2.3a and b replacing the damage parameters by the corresponding plastic parameters, e.g. Y_T by Y_{TP} .

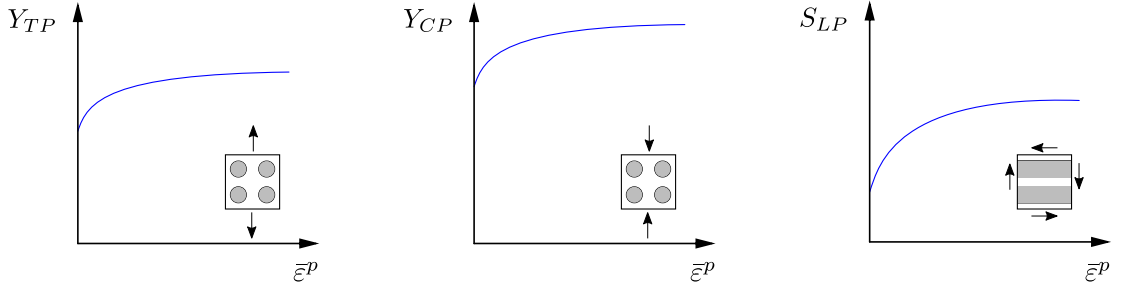


Figure 2.2.: Schematic representation of yield stresses vs. equivalent plastic strain curve.

The yield function of Eq. (2.12) allows to control the activation of the yielding for uniaxial loads in the transverse direction in tension and in compression, as well as for longitudinal shear loading states by means of the corresponding yield stresses. Furthermore, the plasticity can be activated under other transverse loading conditions controlled by μ_{tp} and $\mu_{s\ell p}$. For example, shear yielding in the longitudinal or transverse direction is affected by the transverse hydrostatic pressure as observed in [11, 12]: the higher the transverse compressive hydrostatic is, the higher the shear yielding is.

The evolution of the equivalent plastic strain rate is defined as

$$\dot{\varepsilon}^p := \sqrt{\frac{1}{2} \|\dot{\varepsilon}^p\|}, \quad (2.13)$$

where $\dot{\varepsilon}^p$ is the plastic strain rate.

The mechanical behaviour of FRP laminates depend on the transverse hydrostatic pressure [11, 12]. This dependence requires the use of elastoplastic material models with a non-associative flow rule to properly capture the plastic dilatancy or contractility. This allows the volumetric plastic strains and the plastic Poisson's ratios to be imposed. Therefore, a non-associative flow rule is applied in the proposed model, and the evolution of the plastic strains is defined by the gradient of the potential function φ^p , see Eq. (2.21). The plastic strain rate is defined as

$$\dot{\varepsilon}^p := \lambda \frac{\partial \varphi^p}{\partial \sigma}, \quad (2.14)$$

where λ is the plastic multiplier parameter [88]. The loading-unloading conditions are applied using the following Kuhn-Tucker conditions to calculate λ :

$$\phi^p \leq 0, \quad \lambda \geq 0. \quad (2.15)$$

Therefore, under plastic loading $\phi^p = 0$ and $\lambda > 0$, and for unloading $\phi^p < 0$ and $\lambda = 0$. Hence,

$$\dot{\phi}^p \lambda = 0. \quad (2.16)$$

These conditions can be summarised in the consistency condition as

$$\dot{\phi}^p \lambda = 0. \quad (2.17)$$

The plastic multiplier parameter λ can be calculated in case of plastic loading ($\dot{\phi}^p = 0$ and $\lambda > 0$) imposing the following condition

$$\dot{\phi}^p = \frac{\partial \phi^p}{\partial \boldsymbol{\sigma}} \dot{\boldsymbol{\sigma}} + \frac{\partial \phi^p}{\partial \bar{\varepsilon}^p} \dot{\bar{\varepsilon}}^p = 0. \quad (2.18)$$

Inserting Eqs. (2.13) and (2.14) in the previous conditions yields

$$\dot{\phi}^p = \frac{\partial \phi^p}{\partial \boldsymbol{\sigma}} \mathbb{C}_e \left(\dot{\boldsymbol{\varepsilon}} - \lambda \frac{\partial \varphi^p}{\partial \boldsymbol{\sigma}} \right) + \frac{\partial \phi^p}{\partial \bar{\varepsilon}^p} \lambda \sqrt{\frac{1}{2} \left\| \frac{\partial \varphi^p}{\partial \boldsymbol{\sigma}} \right\|^2} = 0, \quad (2.19)$$

and the plastic multiplier parameter yields

$$\lambda = \frac{\partial_{\boldsymbol{\sigma}}(\phi^p) \mathbb{C}_e \dot{\boldsymbol{\varepsilon}}}{\partial_{\boldsymbol{\sigma}}(\phi^p) \mathbb{C}_e \partial_{\boldsymbol{\sigma}}(\varphi^p) - \sqrt{\frac{1}{2} \partial_{\bar{\varepsilon}^p}(\phi^p) \left\| \partial_{\boldsymbol{\sigma}}(\varphi^p) \right\|^2}}. \quad (2.20)$$

Finally, the plastic potential function is defined as

$$\begin{aligned} \varphi^p(\boldsymbol{\sigma}) := & \sqrt{\left(\frac{\hat{Y}_{CP} + \hat{Y}_{TP}}{\hat{Y}_{TP} \hat{Y}_{CP}} \right)^2 \frac{\tau_t^2 + \hat{\mu}_{tp} p_t^2}{1 + \hat{\mu}_{tp}} + \left(\frac{\hat{\mu}_{s\ell p}}{\hat{S}_{LP}} \tau_\ell \right)^2} \\ & + \frac{\hat{Y}_{CP} - \hat{Y}_{TP}}{\hat{Y}_{TP} \hat{Y}_{CP}} p_t + \frac{1 - \hat{\mu}_{s\ell p}}{\hat{S}_{LP}} \tau_\ell - 1. \end{aligned} \quad (2.21)$$

Eq. (2.21) has the same form as the yield function but each yield stress and plastic envelope shape coefficients are replaced by the corresponding plastic potential parameters. Hence, a one degree homogenous and convex function is used for φ^p . The plastic potential stresses \hat{Y}_{TP} , \hat{Y}_{CP} and \hat{S}_{LP} and the plastic potential envelope shape coefficients $\hat{\mu}_{tp}$ and $\hat{\mu}_{s\ell p}$ are defined as constant parameters. They do not have a physical meaning, they are used to control the plastic dilatancy or contractility in the plastic zone (these parameters define the direction of the plastic flow). For this reason, only the ratios between them are relevant and not their absolute values. Note that, if the plastic potential parameters are set equal to the yield parameters, the plasticity would be modelled using an associative flow rule.

The plastic dilatancy or contractility can be defined using three plastic Poisson's ratios: ν_{23T}^p and ν_{23C}^p are the transverse tensile and compressive plastic Poisson's ratios, respectively, and $\nu_{122}^p := -\frac{\varepsilon_{22}^p}{\varepsilon_{12}^p}$. They can be measured by three tests: pure transverse tensile test (ν_{23T}^p), pure transverse compressive test (ν_{23C}^p) and pure longitudinal shear test (ν_{122}^p). It should be noted that, these tests are also used to adjust the yield function. Hence, the total number of tests required to calibrate the plasticity input parameters does not increase.

The procedure to obtain the plastic potential ratios as a function of the plastic Poisson's ratios is explained in detail in [Appendix A](#). They are defined as

$$\begin{aligned}\frac{\hat{Y}_{CP}}{\hat{Y}_{TP}} &= \frac{\nu_{23C}^p + 1}{\nu_{23T}^p + 1} \\ \frac{\hat{S}_{LP}}{\hat{Y}_{TP}} &= \frac{2\nu_{122}^p(\nu_{23C}^p + 1)}{\nu_{23T}^p - \nu_{23C}^p} \\ \hat{\mu}_{tp} &= \frac{1 - \nu_{23C}^p \nu_{23T}^p}{(\nu_{23C}^p + 1)(\nu_{23T}^p + 1)} \\ \hat{\mu}_{s\ell p} &\in \mathbf{R}.\end{aligned}\tag{2.22}$$

However, if there is no volumetric plastic strains ($\nu_{23T}^p = \nu_{23C}^p = 1$ and $\nu_{122}^p = 0$), the plastic potential relationships are simplified to

$$\begin{aligned}\frac{\hat{Y}_{CP}}{\hat{Y}_{TP}} &= 1 \\ \hat{S}_{LP} &\in \mathbf{R} \\ \hat{\mu}_{tp} &= 0 \\ \hat{\mu}_{s\ell p} &\in \mathbf{R}.\end{aligned}\tag{2.23}$$

2.1.2 Modelling Damage Evolution

As explained before, CDM theory is often employed in conjunction with FE models to predict crack initiation and propagation in FRP laminates [5, 51, 52]. CDM models represent a crack by introducing damage variables (d_M) in the corresponding terms of the elasticity tensor ($\mathbb{C}_e(d_M) = \mathbb{H}^{-1}$) to obtain the stress tensor ($\boldsymbol{\sigma}$) as a function of the elastic strain tensor ($\boldsymbol{\varepsilon}^e$),

$$\boldsymbol{\sigma} = \mathbb{C}_e(d_M)\boldsymbol{\varepsilon}^e.\tag{2.24}$$

Therefore, the non-linear response due to cracking is obtained without explicitly modelling it in the FE discretisation (the FE mesh).

In the proposed constitutive model, the evolution of the damage is based on the model developed by Quintanas-Corominas et al. [86]. The model is based on the Crack Band model proposed by Bažant and Oh [89] to ensure the proper energy dissipation when the crack propagates. The degradation of the elastic properties is modelled by four softening laws: $d_\ell(r_{\ell T}, r_{\ell C})$ is associated to the first stress invariant σ_ℓ and model the longitudinal failure in tension ($\sigma_\ell > 0$) and in compression ($\sigma_\ell < 0$); $d_t(r_t)$ is related to the mode-I matrix cracking associated to the second stress invariant p_t ; $d_{st}(r_t)$ describes the mode-II matrix cracking associated to the third stress invariant τ_t ; and $d_{s\ell}(r_t, r_{\ell T})$ is linked to the longitudinal tensile and matrix damage mechanisms associated to the stress invariant τ_ℓ .

The terms of \mathbb{C}_e are often modified according to the corresponding d_M obtained from a failure criterion. For example, Maimí et al. [49] modelled a longitudinal crack resulting from tensile stresses by reducing the longitudinal Young's modulus as a function of a damage variable obtained from the non-interactive maximum strain failure criterion. The authors evaluated the failure criterion using the effective stress tensor $(\tilde{\boldsymbol{\sigma}})$. This framework was introduced by Lemaitre [90] and is based on the *hypothesis of Strain Equivalence* [90, 91]. The hypothesis considers that the strain associated to a damaged stress state $(\boldsymbol{\sigma})$ is equivalent to the strain associated with its effective stress state (undamaged stress state, $\tilde{\boldsymbol{\sigma}}$). The effective stress tensor can be calculated as a function of the elastic material properties and $\boldsymbol{\varepsilon}^e$ as

$$\tilde{\boldsymbol{\sigma}} = \mathbb{C}_e(d_M = 0)\boldsymbol{\varepsilon}^e, \quad (2.25)$$

and is widely used to evaluate the failure criteria in CDM models [47, 49, 52, 72, 76, 86, 92–95]. In the proposed model, three loading functions as a function of $\tilde{\boldsymbol{\sigma}}$ are employed to consider the previously explained damage mechanisms: $\phi_{\ell T}$ for the fibre breakage and pull-out, $\phi_{\ell C}$ for the fibre kinking and crushing, and ϕ_t for the matrix cracking. They read

$$\phi_{\ell T} := \frac{\tilde{\sigma}_\ell - 2v_{12}\tilde{p}_t}{X_T}, \quad (2.26)$$

$$\phi_{\ell C} := \frac{1}{X_C} \left(\sqrt{\tilde{\sigma}_\ell^2 + \eta_t^q \tilde{p}_t^2 + \eta_{s\ell}^q \tilde{\tau}_\ell^2} + \eta_t \tilde{p}_t + \eta_{s\ell} \tilde{\tau}_\ell \right), \quad (2.27)$$

and

$$\phi_t := \sqrt{\left(\frac{Y_C + Y_T}{Y_T Y_C}\right)^2 \frac{\tilde{\tau}_t^2 + \mu_t \tilde{p}_t^2}{1 + \mu_t} + \left(\frac{\mu_{s\ell} \tilde{\tau}_\ell}{S_L}\right)^2} + \frac{Y_C - Y_T}{Y_T Y_C} \tilde{p}_t + \frac{1 - \mu_{s\ell}}{S_L} \tilde{\tau}_\ell, \quad (2.28)$$

where X_T and X_C are the longitudinal tensile and compressive strengths, respectively; Y_T and Y_C are the transverse tensile and compressive strengths, respectively; and S_L is the longitudinal shear strength. The effective stress invariants $\tilde{\sigma}_\ell$, \tilde{p}_t , $\tilde{\tau}_\ell$ and $\tilde{\tau}_t$ are obtained by evaluating Eqs. (2.5)–(2.8) with $\tilde{\sigma}$. The failure envelope shape coefficients: η_t and η_t^q are related to the transverse hydrostatic pressure and the longitudinal compressive strength; $\eta_{s\ell}$ and $\eta_{s\ell}^q$ are associated to the longitudinal compressive and longitudinal shear strengths; μ_t is governed by the transverse shear and transverse biaxial strengths; and $\mu_{s\ell}$ is linked to the transverse and longitudinal shear strengths, see Fig. 2.3.

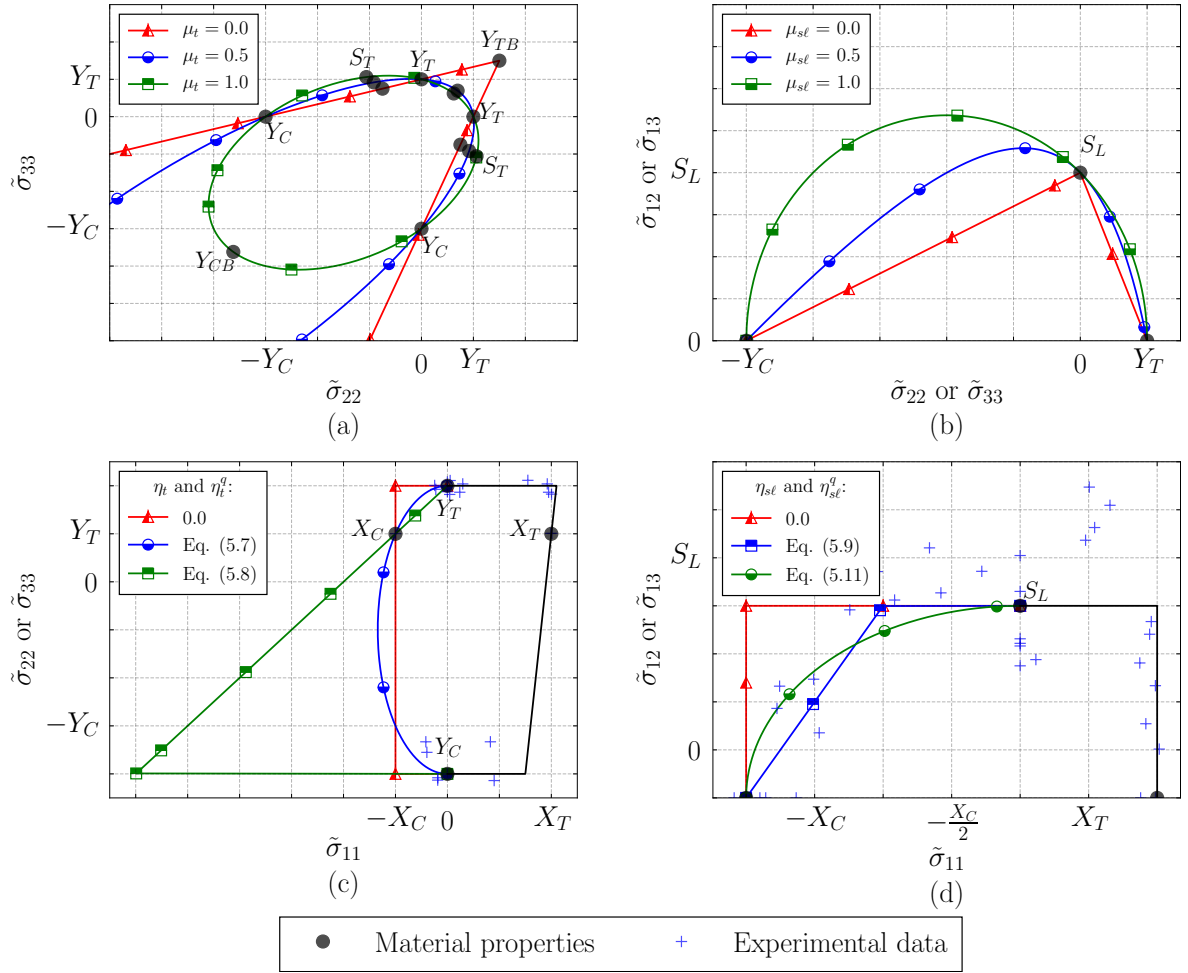


Figure 2.3.: Schematic representation of the failure envelope in the effective stress space: a) $\tilde{\sigma}_{22} - \tilde{\sigma}_{33}$, b) $\tilde{\sigma}_{22} - \tilde{\sigma}_{12}$, c) $\tilde{\sigma}_{11} - \tilde{\sigma}_{22}$, and d) $\tilde{\sigma}_{11} - \tilde{\sigma}_{12}$. Note that, b) and d) are symmetric with respect to their X-axis. The experimental data in c) from Welsh et al. [96] is used to propose Eq. (5.7), and d) from Soden et al. [97] for Eq. (5.9), see Section 5.1.

Damage activation functions based on effective stresses (or strains) can be expressed as

$$F_N := \phi_N - r_N \leq 0, \quad (2.29)$$

where r_N is the corresponding elastic domain threshold (an internal damage variable) related to a damage mechanism $N = \ell T, \ell C, t$. The corresponding elastic domain threshold is calculated by integrating its corresponding loading function with respect to time applying the Kuhn-Tucker relations [47]. They can be explicitly integrated as

$$r_N = \max \left(1, \max_{s \in [0, t]} \left(\phi_N^s \right) \right), \quad (2.30)$$

since the loading functions are defined only as a function of the strain tensor.

The evolution of d_M is defined as a function of r_N in [Appendix B](#). The longitudinal damage variable d_ℓ is defined as

$$d_\ell := d_{\ell T} \frac{\langle \sigma_\ell \rangle}{|\sigma_\ell|} + d_{\ell C} \frac{\langle -\sigma_\ell \rangle}{|\sigma_\ell|}, \quad (2.31)$$

where $\langle x \rangle = (x + |x|)/2$ is the McCauley operator. Therefore, if the first stress invariant is positive ($\sigma_\ell > 0$), then $d_\ell = d_{\ell T}$, otherwise $d_\ell = d_{\ell C}$. This allows a different longitudinal damage evolution in tension than in compression. The procedure to calculate both the longitudinal tensile and compressive damage variables as a function of $r_{\ell T}$ and $r_{\ell C}$, respectively, is described in detail in [Appendix B.1](#). The calibration of $d_{\ell T}$ and $d_{\ell C}$ can be achieved through the use of X_T and X_C obtained from longitudinal tensile and compressive tests, respectively, according to the standards [98, 99]. Additionally, the tensile and compressive fracture toughnesses (\mathcal{G}_{X_T} and $f_{\mathcal{G}_{X_C}} \mathcal{G}_{X_C}$, respectively) can be obtained from the methodology proposed by Ortega et al. [100], as well as the shape of the longitudinal softening laws.

The softening law in the longitudinal tensile direction $d_{\ell T}$ is defined using a bilinear law, in the same way as in [101, 102]. The first segment is defined with a large drop stress due to the fibre breakage followed by a large tail related to the fibre pull-out, see [Fig. 2.4a](#). The damage variable in the longitudinal compressive direction $d_{\ell C}$ is also defined using a bilinear softening law, in the same way as [101, 102]. The first segment defines the onset of kink-band using a large drop followed by an horizontal asymptote related to kink-band broadening and frictional contact, see [Fig. 2.4b](#).

The degradation of the matrix stiffness due to mode-I matrix cracking is assumed to be equivalent to that generated by mode-II matrix cracking when the crack opens ($p_t > 0 \rightarrow d_t = d_{st}$). However, there is no degradation of the matrix stiffness in mode-I when the crack closes ($p_t < 0 \rightarrow d_t = 0$). Therefore, the transverse damage variable d_t is defined

equal to the transverse shear damage variable d_{st} when the second invariant p_t is positive, and equal to zero when the second invariant is negative,

$$d_t := d_{st} \frac{\langle p_t \rangle}{|p_t|}. \quad (2.32)$$

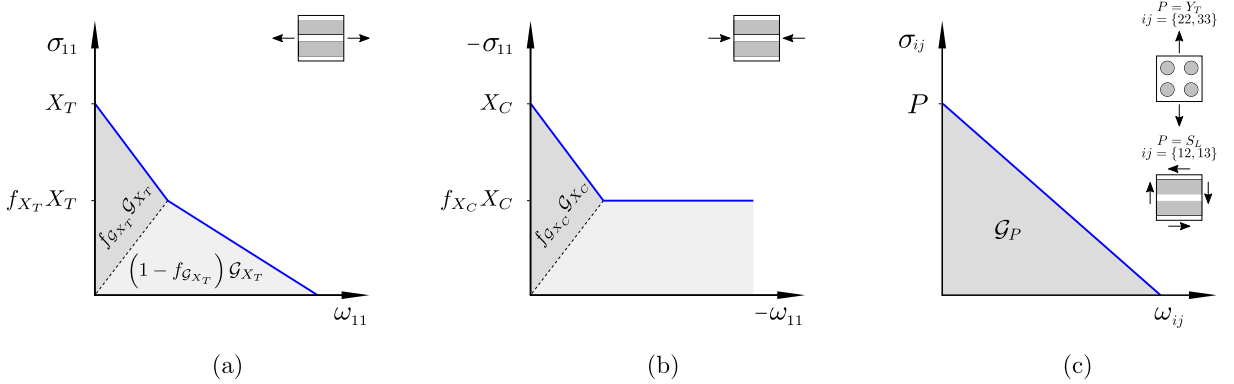


Figure 2.4.: Stress vs. crack opening displacement (ω_{ij}) curve of the softening law in: a) the longitudinal tensile direction, b) the longitudinal compressive direction, and c) the directions governed by the matrix.

The damage variable d_{st} is defined assuming a linear softening law (Fig. 2.4c) and is established as a function of the elastic domain threshold r_t in Appendix B.3. This damage variable can be calibrated from a transverse tensile standard test [98] for determining Y_T . Additionally, the mode-I intralaminar fracture toughness (\mathcal{G}_{Y_T}) can be assumed equal to the mode-I interlaminar fracture toughness of a unidirectional laminate that can be obtained by a double cantilever beam standard test [103].

The stiffness degradation in the longitudinal shear direction is introduced by $d_{s\ell}$, which is defined as a function of the longitudinal shear effective stresses ($\tilde{\sigma}_{12}$ and $\tilde{\sigma}_{13}$), but also due to the longitudinal tensile effective stress ($\tilde{\sigma}_{11}$). The proposed $d_{s\ell}$ is defined as

$$d_{s\ell} := 1 - (1 - d_{s\ell^*})(1 - d_{\ell T}), \quad (2.33)$$

where $d_{s\ell^*}$ is the damage variable presented in Appendix B.4 and is related to the longitudinal shear effective stresses. The calibration of $d_{s\ell^*}$ can be carried out with either a longitudinal shear standard test [104] or a V-notched rail shear standard test [105] for determining S_L . Additionally, the mode-II intralaminar fracture toughness (\mathcal{G}_{S_L}) can be assumed equal to the mode-II interlaminar fracture toughness of a unidirectional laminate that can be obtained by a calibrated end-loaded split standard test [106].

2.2 Input model parameters

The input model parameters of the proposed constitutive model can be divided into three groups: (i) elastic material properties, (ii) plasticity modelling inputs, and (iii) damage modelling inputs. Most of these parameters can be measured or fitted directly from standardised tests, see [Table 2.1](#). However, there are no standardised tests for determining the transverse Poisson's ratios and the shape coefficients of the plastic and failure envelopes. The input model parameters can be obtained from seven different types of tests with different configurations (stacking sequences, sizes, etc.), in exception of the shape coefficients of the envelopes and ν_{122}^p .

A new methodology for measuring the transverse Poisson's ratio from standardised tests using a supplementary data acquisition system and a data reduction method is described in [Chapter 4](#). The definition of the envelope shape coefficients and their bounds are presented in [Chapter 5](#). Additionally, the effect of η_t and η_t^q on the failure strength prediction of filled-hole compressive (FHC) tests is analysed.

Table 2.1.: Standardised tests to determine the model input parameters. Other standard procedures may also be employed.

	Description	Symbol	Test
Elastic	Longitudinal Young's modulus	E_{11}	Longitudinal tensile test (ASTM D3039) [98]
	Transverse Young's modulus	E_{22}	Transverse tensile test (ASTM D3039) [98]
	Longitudinal shear's modulus	G_{12}	Longitudinal shear tensile test (ASTM D3518) [104]
	Longitudinal Poisson's ratio	ν_{12}	Longitudinal tensile test (ASTM D3039) [98]
	Transverse Poisson's ratio	ν_{23}	Transverse tensile test (ASTM D3039) [98] [†]
Plastic	Transverse tensile yield stress curve	Y_{TP}	Transverse tensile test (ASTM D3039) [98] ^{††}
	Transverse compressive yield stress curve	Y_{CP}	Transverse compressive test (ASTM D6641) [99] ^{††}
	Longitudinal shear yield stress curve	S_{LP}	V-notched rail shear test (ASTM D7078) [105] ^{††}
	Transverse plastic Poisson's ratio in tension	ν_{23T}^p	Longitudinal shear tensile test (ASTM D3518) [104] ^{††}
	Transverse plastic Poisson's ratio in compression	ν_{23C}^p	Transverse tensile test (ASTM D3039) [98] [†]
Damage	Longitudinal tensile strength	X_T	Transverse compressive test (ASTM D6641) [99] ^{††}
	Longitudinal tensile fracture toughness	\mathcal{G}_{X_T}	Compact tensile test [100]
	Shape of the longitudinal tensile softening law	f_{X_T} and $f_{\mathcal{G}_{X_T}}$	Double end notched tensile test [107]
	Longitudinal compressive strength	X_C	Compact tensile test [100]
	Longitudinal compressive fracture toughness	$f_{\mathcal{G}_{X_C}} \mathcal{G}_{X_C}$	Double end notched tensile test [107] [*]
	Shape of the longitudinal compressive softening law	f_{X_C}	Longitudinal compressive test (ASTM D6641) [99]
	Transverse tensile strength	Y_T	Compact compressive test [100]
	Transverse tensile fracture toughness	\mathcal{G}_{Y_T}	Double end notched compressive test [108] [*]
	Transverse compressive strength	Y_C	Transverse tensile test (ASTM D3039) [98]
	Longitudinal shear strength	S_L	Mode-I interlaminar fracture toughness test (ASTM D5528/ISO 15034) [103, 109] [‡]
	Longitudinal shear fracture toughness	\mathcal{G}_{S_L}	Transverse compressive test (ASTM D6641) [99]
			V-notched rail shear test (ASTM D7078) [105]
			Longitudinal shear tensile test (ASTM D3518) [104]
			Mode-II interlaminar fracture toughness test (ASTM D7905/ISO 15114) [106, 110] [‡]

[†] Using a digital image correlation acquisition system with an additional data reduction method, see [Chapter 4](#).

^{††} Assuming no damage occurs until the specimen fails, the plastic strain can then be calculated by subtracting the elastic strain, as the ratio of stress to Young's modulus, from the total strain.

^{*} Inversely identified using finite element simulations.

[‡] Assuming that the intralaminar fracture toughness is equivalent to the interlaminar fracture toughness.

2.3 Implementation

The constitutive model presented in [Section 2.1](#) is solved at the Gauss-point level using an explicit FE solver. The evolution of the plasticity internal variables ($\boldsymbol{\varepsilon}^p$ and $\bar{\boldsymbol{\varepsilon}}^p$) is discretised in time using the Backward Euler integration scheme and the operator split method: (i) an initial elastic predictor step, and (ii) a posterior plastic corrector step. However, the evolution of the internal damage variables (r_N) is carried out by integrating r_N into time using [Eq. \(2.30\)](#), therefore, they can be explicitly solved.

The algorithm of the material model time discretisation ($t_{(n+1)}$) is presented in this section. The known data with respect to the previous increment of the time ($t_{(n)}$) are the current total strain tensor at the end of the increment ($\boldsymbol{\varepsilon}_{(n+1)}$) and the internal variables at the beginning of the increment ($\boldsymbol{\varepsilon}_{(n)}^p$, $\bar{\boldsymbol{\varepsilon}}_{(n)}^p$ and $r_{N(n)}$).

Firstly, the damage model is evaluated to determine if the damage variables associated with the matrix cracking (d_t , $d_{s\ell}$ and d_{st}) are activated in the current time interval. If they are greater than zero, plasticity does not develop. However, if the matrix is undamaged ($d_t = d_{s\ell} = d_{st} = 0$), plasticity can evolve, see [Fig. 2.1b](#). It is possible that the initiation of the matrix damage and an increase of the plastic strain tensor occur at the same time interval. In this case, the model assumes that the strain increment is only due to damage instead of damage and plasticity. This assumption produces a negligible error in the results, because very small time increments are used in simulations with explicit solver.

Secondly, if the matrix is undamaged, the model calculates the increment of the plastic strains. For that, the elastic trial stress tensor is obtained by assuming that there is no increase in the plastic strain tensor in the current time step ($\boldsymbol{\sigma}_{(n+1)}^{tr} = \boldsymbol{\sigma}_{(n+1)} (\Delta \boldsymbol{\varepsilon}_{(n+1)}^p = 0)$). Then, the yield function is evaluated with $\boldsymbol{\sigma}_{(n+1)}^{tr}$ and $\bar{\boldsymbol{\varepsilon}}_{(n)}^p$. If the yield function is less than tol (in this case, the bound is defined using a tolerance tol), there are no increment of plastic strains in the current time interval. However, if the yield function is greater than tol , the plastic strains increase in the current time interval. Therefore, the equivalent plastic strain that meets the condition in [Eq. \(2.12\)](#) must be found.

The Backward Euler algorithm at $t_{(n+1)}$ is applied to update the evolution of the plasticity equations with $\gamma_{(n+1)} = \lambda_{(n+1)}(t_{(n+1)} - t_{(n)})$, where $\gamma_{(n+1)}$ is the consistency parameter. Therefore, the evolution of the plasticity equations read

$$\begin{aligned}\boldsymbol{\varepsilon}_{(n+1)}^p &= \boldsymbol{\varepsilon}_{(n)}^p + \gamma_{(n+1)} \frac{\partial \varphi^p}{\partial \boldsymbol{\sigma}_{(n+1)}} \\ \boldsymbol{\sigma}_{(n+1)} &= \boldsymbol{\sigma}_{(n+1)}^{tr} - \gamma_{(n+1)} \mathbb{C}_e \frac{\partial \varphi^p}{\partial \boldsymbol{\sigma}_{(n+1)}} \\ \bar{\boldsymbol{\varepsilon}}_{(n+1)}^p &= \bar{\boldsymbol{\varepsilon}}_{(n)}^p + \gamma_{(n+1)} \sqrt{\frac{1}{2}} \left\| \frac{\partial \varphi^p}{\partial \boldsymbol{\sigma}_{(n+1)}} \right\|.\end{aligned}\quad (2.34)$$

The yield function condition from Eq. (2.12) gives an algebraic constraint that has to be fulfilled at the end of the current time step ($\phi_{(n+1)}^p(\boldsymbol{\sigma}_{(n+1)}, \bar{\boldsymbol{\varepsilon}}_{(n+1)}^p) = 0$). This condition is solved with the Newton-Raphson method for $\gamma_{(n+1)}$. The residual equation is developed in a Taylor-series and linearised as

$$\text{Lin}[R_{(n+1)}] = \phi_{(n+1)}^p + \frac{d\phi^p}{d\gamma_{(n+1)}} \Delta\gamma_{(n+1)} = 0. \quad (2.35)$$

Therefore, the linearisation of the residual is solved for the increment of the consistency parameter as

$$\Delta\gamma_{(n+1)} = -\frac{\phi_{(n+1)}^p}{\frac{d\phi^p}{d\gamma_{(n+1)}}}. \quad (2.36)$$

The analytical calculation of $\Delta\gamma_{(n+1)}$ is outlined in Appendix C. Additionally, a comparison between the numerical and analytical solutions has been conducted. The findings exhibit no significant difference in resolving Eq. (2.36) or computational time between the two approaches when the suitable numerical perturbation is used. Therefore, the numerical approximation of $\partial_\gamma(\phi^p)$ is used to calculate $\Delta\gamma$, as its implementation algorithm is simpler than the analytical one.

Finally, the evolution of the plasticity internal variables is evaluated with the general convex cutting-plane algorithm presented by Simo and Springer [88]. Algorithm 1 summarises the workflow to implement the proposed constitutive model using an explicit solver in a non-linear FE framework. The constitutive model is implemented in a user material Fortran subroutine (VUMAT) to be used with the FE Abaqus/Explicit solver [111]. The implementation carried out using a VUMAT subroutine is verified to determine that the Fortran code accurately represents the proposed constitutive model [112].

The user material subroutine has been developed taking into account several considerations for reducing the computational time for the constitutive model calculation. All constant scalar, vector and matrix values of the constitutive model are calculated at the beginning of the FE simulation and stored in memory. Consequently, they are evaluated only once, rather than repeating it at every time interval. Additionally, the approach to calculate the vector product proposed by Cowell and Christopher [113] is implemented. The proposed approach consists into reorganise the traditional loop to reduce its number of iterations and, then its computational time, see [Appendix D](#). Others aspects have also been considered: avoid "if" conditions in loops and prioritise calculation with vectors instead of scalars.

Dividing by zero should be avoided to prevent numerical errors. In some cases, manipulating the expressions alone may suffice. However, certain operations require a specific evaluation to prevent this issue. [Appendix E](#) presents a Fortran function to prevent this numerical error.

Algorithm 1: Algorithm of the proposed constitutive model at time $t_{(n+1)}$

Input:

total strain tensor at $t_{(n+1)}$: $\boldsymbol{\varepsilon}_{(n+1)}$
 internal variables at $t_{(n+1)}$: $\boldsymbol{\varepsilon}^p_{(n)}, \bar{\boldsymbol{\varepsilon}}^p_{(n)}, r_{\ell T_{(n)}}, r_{\ell C_{(n)}}, r_{t_{(n)}}$

Initialisation:

Local Newton-Raphson iteration: $k = 0$

Effective stress tensor: $\tilde{\boldsymbol{\sigma}} = \mathbb{C}_{e0}(\boldsymbol{\varepsilon}_{(n+1)} - \boldsymbol{\varepsilon}^p_{(n)})$

Effective stress invariants in Eqs. (2.5)–(2.8)

Loading functions in Eqs. (2.26)–(2.28)

Elastic domain threshold in Eq. (2.30)

Damage variables in Eqs. (2.31)–(2.33)

Elastic predictor: $\boldsymbol{\sigma}_{(n+1)}^{tr} = \mathbb{C}_e(\boldsymbol{\varepsilon}_{(n+1)} - \boldsymbol{\varepsilon}^p_{(n)})$

1 if $d_t = 0$ and $d_{st} = 0$ and $d_{sl} = 0$ then

Yield stresses: $Y_{CP}(\bar{\boldsymbol{\varepsilon}}^p_{(n)})$, $Y_{TP}(\bar{\boldsymbol{\varepsilon}}^p_{(n)})$ and $S_{LP}(\bar{\boldsymbol{\varepsilon}}^p_{(n)})$

Yield function in Eq. (2.12): $\phi_{(n+1)}^p$

General convex cutting-plane algorithm (return-mapping):

2 $\boldsymbol{\sigma}_{(n+1)}^{(k)} = \boldsymbol{\sigma}_{(n+1)}^{tr}$

3 $\phi_{(n+1)}^{p(k+1)} = \phi_{(n+1)}^p$

4 **while** $\phi_{(n+1)}^{p(k+1)} > tol$ **do**

Derivative of the plastic potential function with respect to the stress tensor:

$$\partial_{\boldsymbol{\sigma}_{(n+1)}^{(k)}} (\varphi^p)$$

Increment of the consistency parameter in Eq. (2.36): $\Delta\gamma_{(n+1)}^{(k)}$

Update the plastic strain tensor: $\boldsymbol{\varepsilon}_{(n+1)}^{p(k+1)} = \boldsymbol{\varepsilon}_{(n+1)}^{p(k)} + \Delta\gamma_{(n+1)}^{(k)} \partial_{\boldsymbol{\sigma}_{(n+1)}^{(k)}} (\varphi^p)$

Update the stress tensor: $\boldsymbol{\sigma}_{(n+1)}^{(k+1)} = \boldsymbol{\sigma}_{(n+1)}^{(k)} - \Delta\gamma_{(n+1)}^{(k)} \mathbb{C}_e \partial_{\boldsymbol{\sigma}_{(n+1)}^{(k)}} (\varphi^p)$

Update the equivalent plastic strain: $\bar{\boldsymbol{\varepsilon}}_{(n+1)}^{p(k+1)} = \bar{\boldsymbol{\varepsilon}}_{(n+1)}^{p(k)} + \Delta\gamma_{(n+1)}^{(k)} \sqrt{\frac{1}{2}} \left\| \partial_{\boldsymbol{\sigma}_{(n+1)}^{(k)}} (\varphi^p) \right\|$

Update yield stresses: $Y_{CP}(\bar{\boldsymbol{\varepsilon}}_{(n+1)}^{p(k+1)})$, $Y_{TP}(\bar{\boldsymbol{\varepsilon}}_{(n+1)}^{p(k+1)})$ and $S_{LP}(\bar{\boldsymbol{\varepsilon}}_{(n+1)}^{p(k+1)})$

Yield function in Eq. (2.12): $\phi_{(n+1)}^{p(k+1)}$

5 $k = k + 1$

6 **end**

7 **end**

2.4 Numerical predictions

Four cases are used to demonstrate the capabilities of the material model to predict not only the plastic deformation of composite materials, but also the onset and propagation of damage. Off-axis compressive and tensile tests with different ply orientations and high plastic dependency are used to demonstrate the ability of the model to capture the plastic response in [Section 2.4.1](#). In addition, they are selected to demonstrate the capabilities of the model to predict the onset of damage as well as the fracture planes when the failure mechanisms are matrix dominated. OHT and OHC tests are used to present the potential of the model to predict the failure strength when the failure mechanisms are fibre dominated [114], see [Section 2.4.2](#).

The FE results using the Abaqus/Explicit solver [111] are compared to the corresponding experimental data. 3D eight-node C3D8R solid elements with reduced integration are used. For all the simulations presented in this thesis, 3D eight-node C3D8R solid elements with reduced integration are used. The C3D8R solid elements are widely used in FE simulations with constitutive models based on the Crack Band model [89], such as open-hole and filled-hole test [115], low velocity impact and compression after impact (CAI) test [116], single-lap bolted joints [117–119], composite pressure vessels [120], etc. Reduced integration elements are used to alleviate the overstiffness of the elements away from the hole due to their high aspect ratio [121]. Reduced integration elements also allow to reduce the computational time compare with the full integration elements.

The in-plane mesh element size is defined less or equal to 0.24 mm around the areas where damage is expected to occur, in order to prevent snap-back of the constitutive softening laws for each failure mode [101]. In this case, the in-plane mesh element size is approximately defined four times smaller than the critical one (0.99 mm in the transverse direction), see [Appendix F](#). In addition, elastic elements are defined in the regions where the damage is not expected to occur in order to reduce the computational time in the open-hole specimens, see [Fig. 2.5b](#).

Three elements through-the-thickness of each ply are used. In the literature, the most common practise is to use a single element per ply instead. However, with a single element through-the-thickness per ply, in-situ strengths are employed to compensate the deficiency in the out-of-plane discretisation, which implies to increase the transverse strengths (Y_C , Y_T and S_L). Consequently, the critical element size drastically decreases since the damage model regularises the fracture toughness with respect to the characteristic element size [89], see [Appendix F](#). The use of three elements through-the-thickness of each ply allows to better discretise the out-of-plane kinematics of the laminate compared with

using a single element. Therefore, no in-situ strengths [122] are used in the proposed FE modelling strategy.

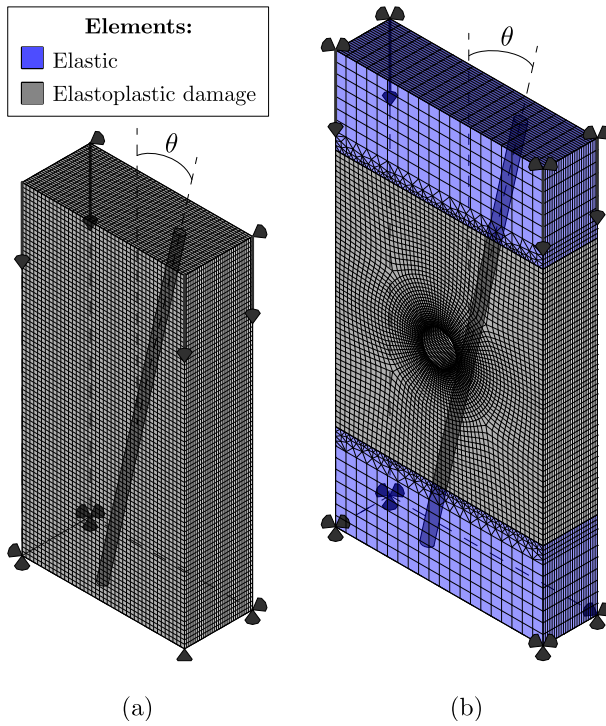


Figure 2.5.: Schematic representation of the meshes and the applied boundary conditions used in the: (a) off-axis simulations, and (b) open-hole simulations. θ is the fibre angle orientation.

As a reference, Table 2.2 presents the difference in the number of elements and nodes from an off-axis FE model as well as from an open-hole model. The dimensions of the off-axis specimen are 10 mm \times 20 mm with 32 plies, and those of the open-hole are 30 mm \times 20 mm and a hole diameter of 5 mm with 32 plies. The mesh element size of each case in Table 2.2 is defined equal to one third of the critical one, the FE meshes are presented in Fig. 2.5. The critical element size is reduced more than 4.5 times when the in-situ strengths are used increasing drastically the total computational time.

Table 2.2.: Comparison of the number of elements and nodes with different finite element modelling approaches.

	Off-axis FE model		Open-hole FE model	
Number of elements per ply	3	1	3	1
In-situ strengths	No	Yes	No	Yes
Critical element size (mm)	0.99	0.20	0.99	0.20
Mesh element size (mm)	0.33	0.05	0.33	0.05
Number of elements	187 488	2 560 000	215 136	1 001 928
Number of nodes	198 656	2 659 833	219 146	1 003 050

The off-axis specimen with three elements per ply results in approximately 14 times fewer elements than using a single element per ply, and approximately 4 times fewer in the open-hole specimen. Therefore, the proposed FE modelling approach is more efficient in terms of computational time than using a single element through-the-thickness per ply with in-situ strength. In addition, cohesive elements are not included between the ply interfaces to model delamination in the proposed FE modelling strategy. Instead, the presence of three elements per ply allows the model predicts failure patterns similar to delamination in the vicinity between the plies. This approach also helps to reduce further the computational resources. Furthermore, the use of three elements through-the-thickness per ply mitigate the hourglass effect, since through-the-thickness kinematics is much better described.

In all loading cases, the laminates are manufactured using a CFRP system, IM7/8552 unidirectional prepreg system with a nominal thickness of 0.131 mm [114]. [Table 2.3](#) summarises the model input parameters. The failure envelope shape coefficients are those reported in [86], see [Fig. 2.6](#). They were obtained by fitting the failure criteria previously developed by Camanho et al. [123], which were developed by combining experimental data and micro-mechanical models for the selected material in this work. The plastic envelope shape coefficients are fitted from the yield surface developed by Vogler et al. [124], see [Fig. 2.7](#). In addition, the plastic yield-equivalent plastic strain relationships are obtained from [124].

Table 2.3.: Model input parameters for the IM7/8552 unidirectional prepreg system.

	Symbol	Value	Unit	Source
Elastic	E_{11}	171420.00	MPa	[114]
	E_{22}	9080.00	MPa	[114]
	G_{12}	5290.00	MPa	[114]
	ν_{12}	0.32	-	[114]
	ν_{23}	0.45	-	Assumed
Plastic	$Y_{CP}(\bar{\varepsilon}^p)$	curve		[124]
	$Y_{TP}(\bar{\varepsilon}^p)$	curve		[124]
	$S_{LP}(\bar{\varepsilon}^p)$	curve		[124]
	μ_{tp}	0.47	-	Adjusted in Section 2.4
	$\mu_{s\ell p}$	1.00	-	Adjusted in Section 2.4
	ν_{23T}^p	1.00	-	[124]
	ν_{23C}^p	1.00	-	[124]
Damage	ν_{122}^p	0.00	-	[124]
	X_T	2323.50	MPa	[125]
	$f_{X_T} X_T$	464.70	MPa	[86]
	\mathcal{G}_{X_T}	97.80	N/mm	[126]
	$f_{\mathcal{G}_{X_T}} \mathcal{G}_{X_T}$	48.90	N/mm	[86]
	X_C	1017.50	MPa	[125]
	$f_{X_C} X_C$	203.50	MPa	[86]
	$f_{\mathcal{G}_{X_C}} \mathcal{G}_{X_C}$	26.58	N/mm	[86]
	Y_T	62.30	MPa	[114]
	\mathcal{G}_{Y_T}	0.28	N/mm	[114]
	Y_C	253.70	MPa	[86]
	S_L	92.30	MPa	[114]
	\mathcal{G}_{S_L}	0.80	N/mm	[114]
	μ_t	0.90	-	[86]
	$\mu_{s\ell}$	1.00	-	[86]
	$\eta_{s\ell}$	9.50	-	[86]
	$\eta_{s\ell}^q$	0.00	-	[86]
	η_t	12.00	-	[86]
	η_t^q	350.00	-	[86]

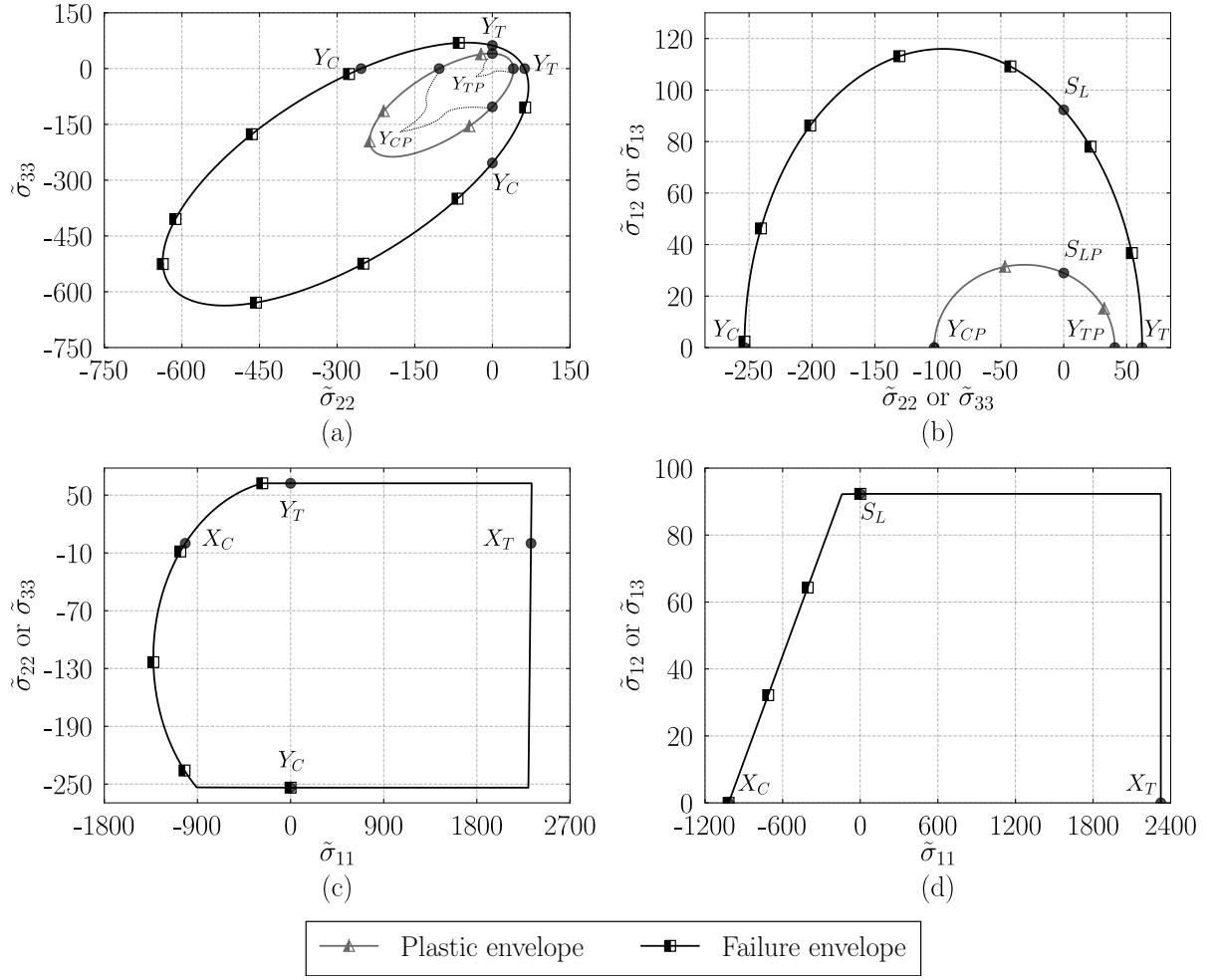


Figure 2.6.: Plastic and failure envelopes of the IM7/8552 unidirectional prepreg system for the effective stress space: a) $\tilde{\sigma}_{22} - \tilde{\sigma}_{33}$, b) $\tilde{\sigma}_{22} - \tilde{\sigma}_{12}$, c) $\tilde{\sigma}_{11} - \tilde{\sigma}_{22}$, and d) $\tilde{\sigma}_{11} - \tilde{\sigma}_{12}$. Note that, b) and d) are symmetric with respect to their X-axis.

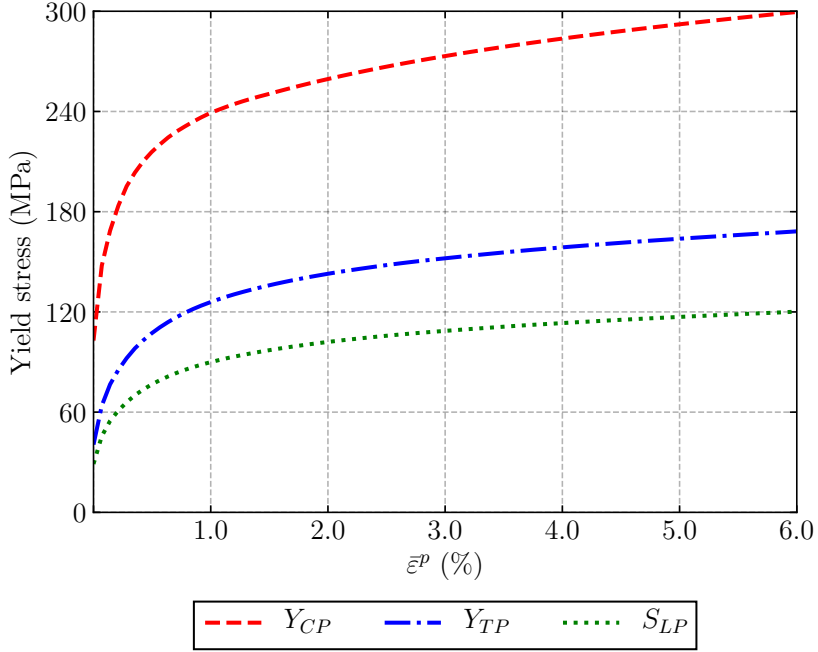


Figure 2.7.: Yield stress vs. equivalent plastic strain curves of the M7/8552 unidirectional prepreg system [124].

The transverse Poisson's ratio (ν_{23}) is assumed considering the value from [127] ($\nu_{23} = 0.45$), where the same polymer with different carbon fibre was used. The effect of ν_{23} on the numerical results is analysed. Different virtual tests are carried out with $\nu_{23} = \{0.3, 0.35, 0.40, 0.45\}$: off-axis compressive virtual tests with a fibre orientation of 30° and another at 75° , and OHT test with a hole diameter equal to 8 mm and OHC test with a diameter of 2 mm. No significant differences are found neither in the failure strength (the higher coefficient of variation from the numerical results is less than 0.4%) nor in the strains at the failure strength (the higher coefficient of variation is less than 2.5%) and in the stress vs. strain curves.

2.4.1 Off-axis tests

The off-axis compressive tests carried out by Koerber et al. [8] with the fibre angle orientations $\theta = 15^\circ, 30^\circ, 45^\circ, 60^\circ, 75^\circ$ and 90° are simulated. The in-plane dimensions of the specimens are 10 mm \times 20 mm with 32 plies. In the numerical model, only the vertical displacements are fixed at the ends of the specimens, and vertical displacement is applied on the top face at low velocity to avoid dynamic effects during the simulation. Additional boundary conditions are defined to avoid rigid body motions, see Fig. 2.5a.

The stress vs. axial strain curves from the numerical simulations are compared to the experimental data in Fig. 2.8. The predicted failure strength of the specimens is in very

good agreement with the test data at $\theta = 15^\circ, 30^\circ, 75^\circ$ and 90° . However, failure strength is underestimated at $\theta = 45^\circ$ and 60° . An explanation is that the experimental data are out of the failure envelope, see Fig. 2.9. To obtain more accurate predictions, ϕ_t could be modified to fit the experimental data. Additionally, the value of μ_{sl} can be adjusted to improve the agreement with the experimental data. In this case, this value has been fixed at one to be consistent with the definition of the shape coefficients reported by Quintanas-Corominas et al. [86] ($\mu_{sl} = 1$). Moreover, three material properties are required to define the failure envelope: Y_C , Y_T and S_L , where the latter can be experimentally estimated using different methods. Camanho et al. [114] estimated S_L using the ASTM D 3518/3518M-94 test standard [104]. Therefore, S_L was estimated from an in-plane shear test using a $[\pm 45^\circ]$ laminate when 5% of the axial strain is reached (it is not physically measured). However, Koerber et al. [8] estimated S_L by decomposing the failure strength into the transverse normal stress and shear stress in the material direction from off-axis compressive tests at $\theta = 15^\circ$ and 30° [128]. Consequently, there are discrepancies when setting S_L , hence, the value can be adjusted within a range ($S_L = [92.3, 99.9]$ MPa) to improve the failure strength predictions. In this study, S_L is defined from Camanho et al. [114], to be also consistent with the definition of the input damage parameters of the composite material coming from the same work. In addition, it should be mentioned that a small discrepancies in the failure strength produces a large disagreement in the ultimate axial strain.

A good accuracy of the predicted plastic deformation with respect to the experimental data are obtained, except at $\theta = 60^\circ$ where the hardening response is slightly underpredicted. This numerical-experimental discrepancy at $\theta = 60^\circ$ is because the yield surface does not properly fit the experimental data at that orientation, similar to the failure envelope at $\theta = 45^\circ$ and 60° in Fig. 2.9.

The predicted fracture planes are compared to those experimentally obtained in Fig. 2.10, where the fully damaged elements are represented with a dark transparent colour. The predicted fracture planes are in good agreement with the experimental data reported, except for $\theta = 15^\circ$. For this orientation, the damage growth is consistent with the experimental data until the peak load, then the fracture angle suddenly changes. The prediction of the fracture planes for $\theta = 15^\circ$ can be improved by orienting the mesh with the fibre angle. For the rest orientations, the model is able to predict the in-plane fracture angle (which is clearly visible at $\theta = 30^\circ$) but also the out-of-plane fracture angle (which is clearly visible at $\theta = 75^\circ$).

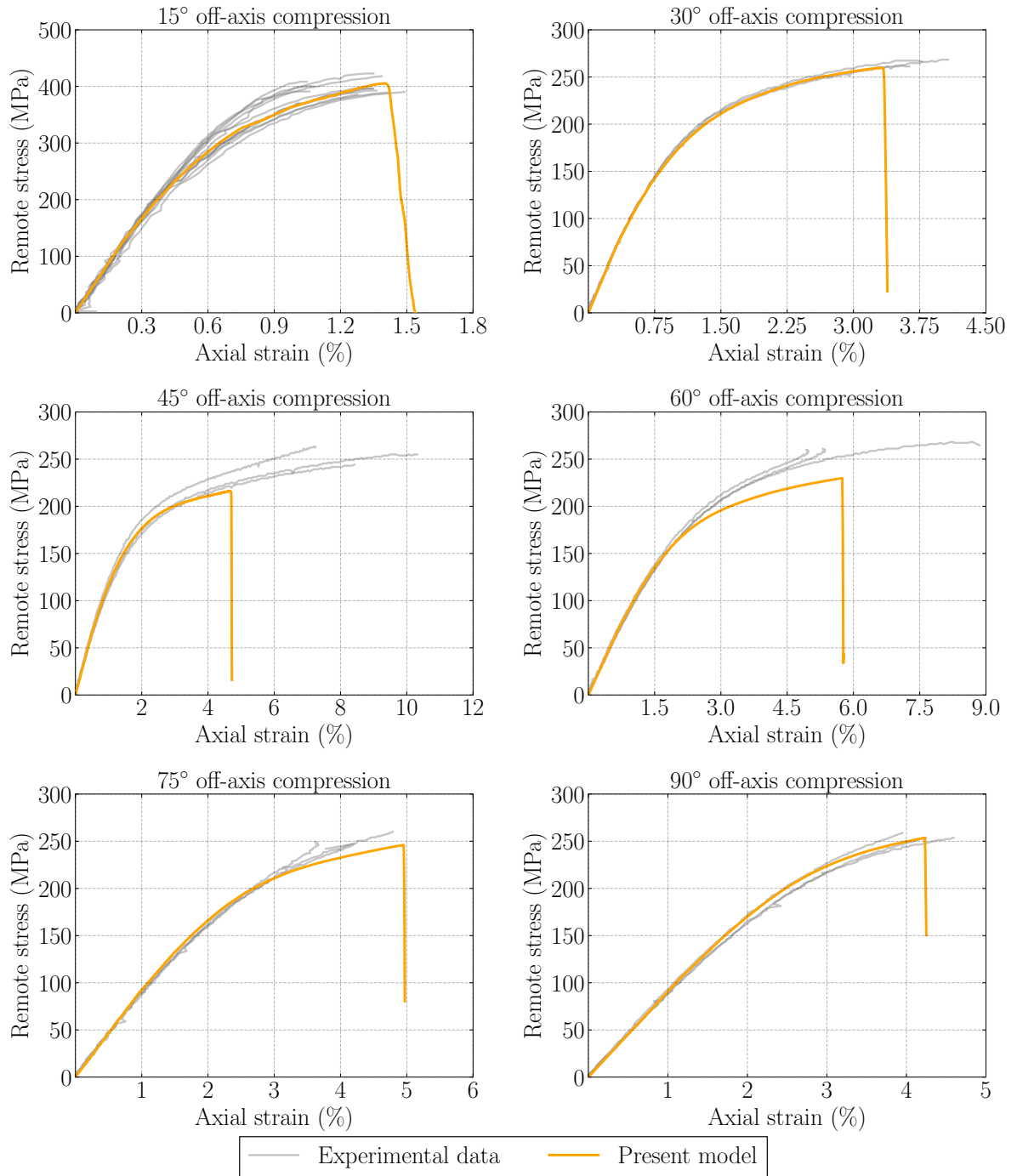


Figure 2.8.: Numerical-experimental comparison of the remote stress vs. axial strain curves of the off-axis compressive tests performed by Koerber et al. [8].

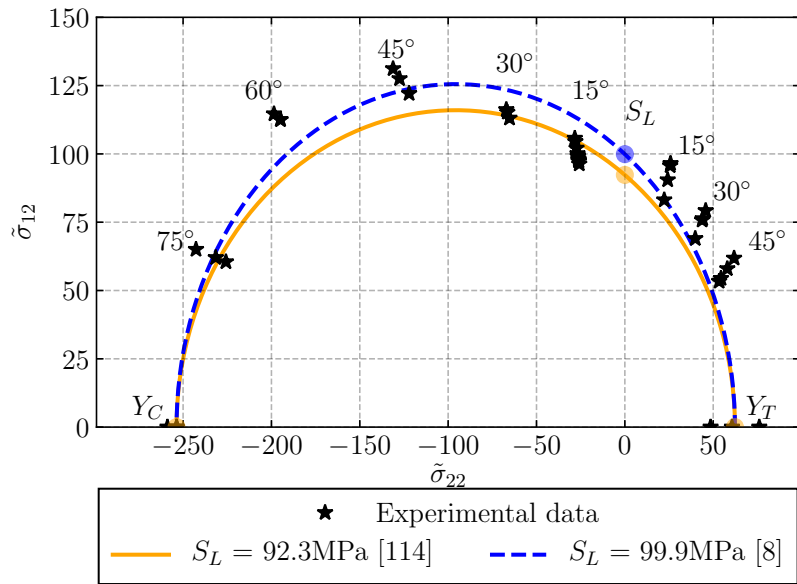


Figure 2.9.: Failure envelope for the $\tilde{\sigma}_{22} - \tilde{\sigma}_{12}$ effective stress space with S_L from Camanho et al. [114] and with S_L from Koerber et al. [8], and compressive and tensile experimental data from Koerber et al. [8] and Koerber et al. [9], respectively.

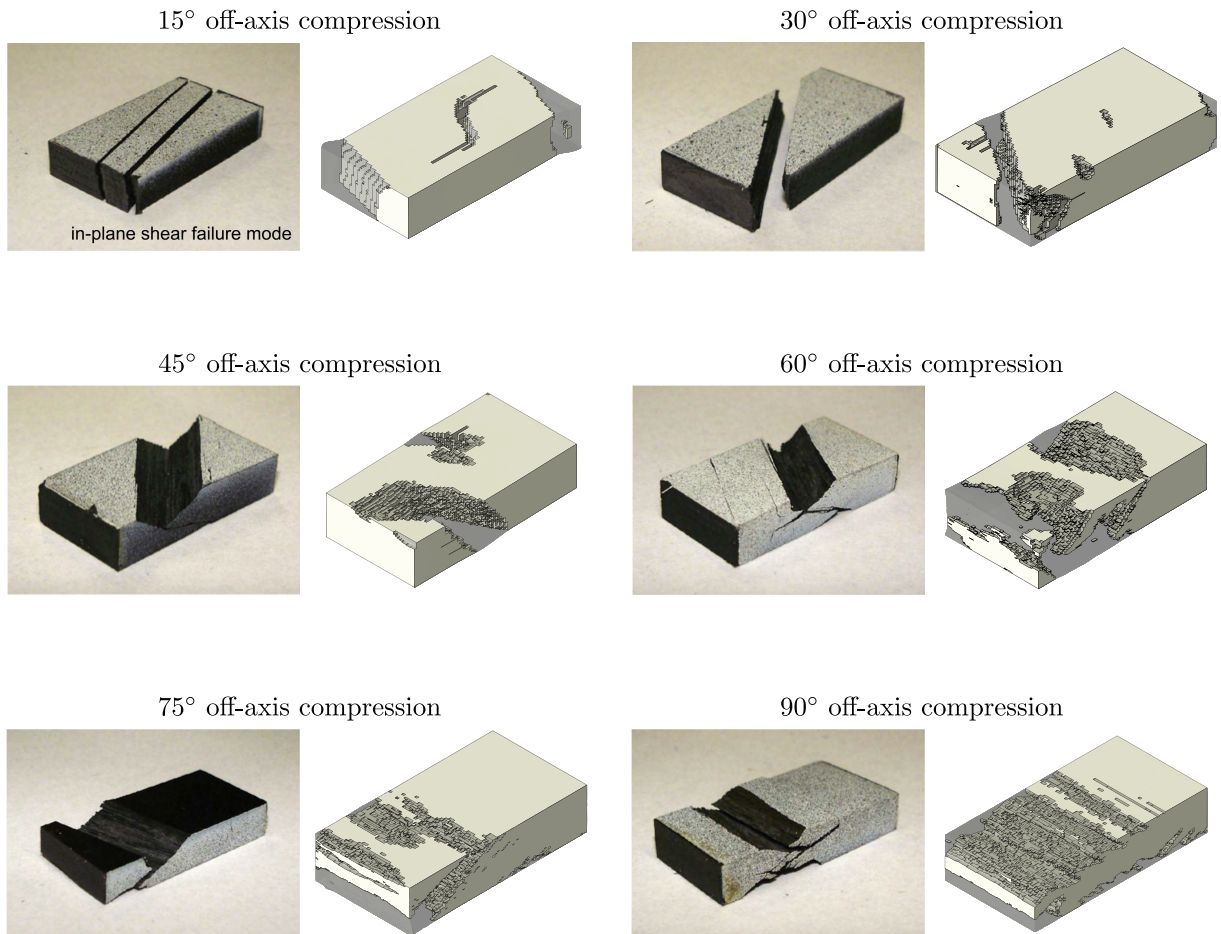


Figure 2.10.: Numerical-experimental comparison of the fracture planes obtained from the off-axis compressive tests performed by Koerber et al. [9].

The comparison between the numerical and experimental data from off-axis tensile tests performed by Koerber et al. [9] is carried out. The in-plane dimensions of the specimens for $\theta = 15^\circ$ are 8 mm \times 72 mm and for $\theta = 30^\circ, 45^\circ$ and 90° are 8 mm \times 62 mm, and they are made with 12 plies. The same boundary conditions as the previous simulations are used applying tension instead of compression, see Fig. 2.5a. Good correlation between the numerical and experimental data for the plastic deformation is obtained, see Fig. 2.11. However, the numerical model underpredicted the failure strength for $\theta = 15^\circ, 30^\circ$ and 45° , since the experimental data are outside the failure envelope, see Fig. 2.9.

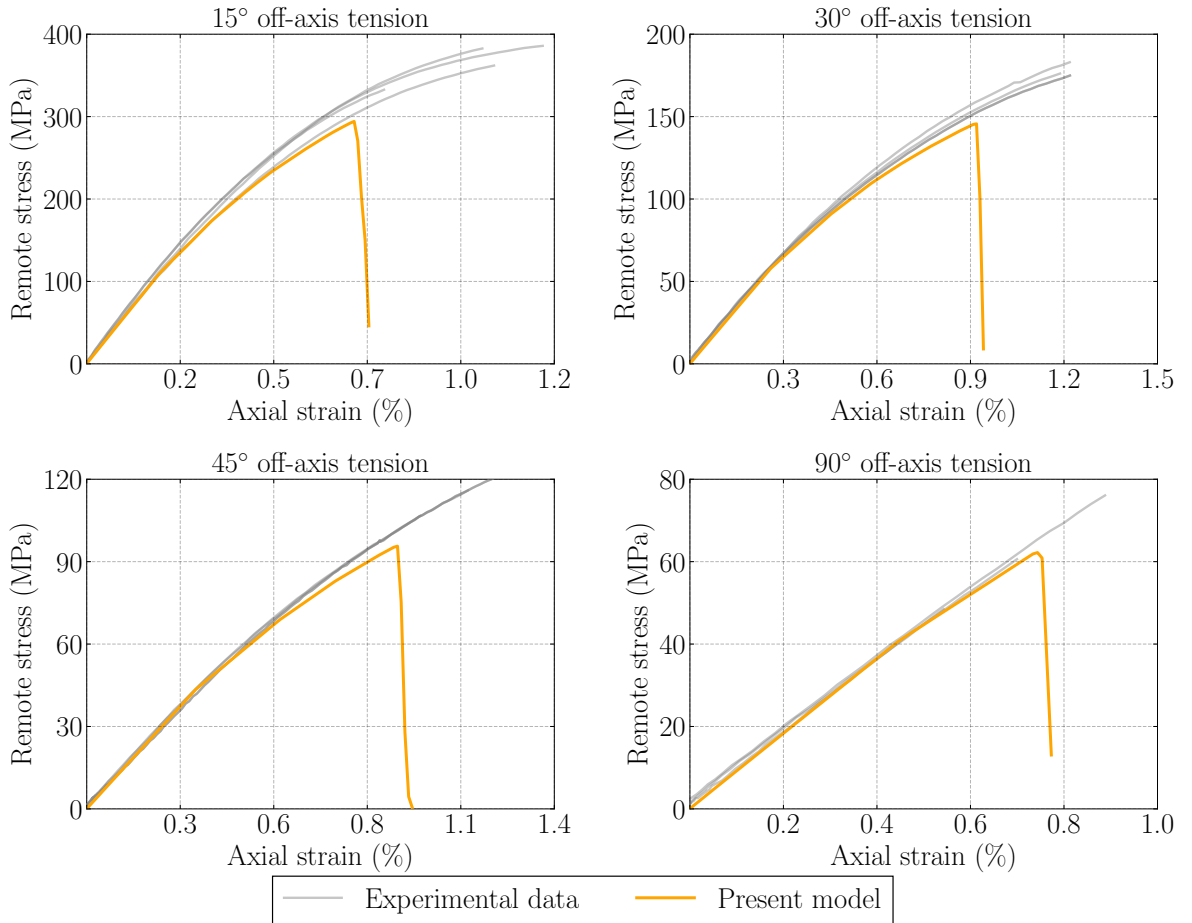


Figure 2.11.: Numerical-experimental comparison of the remote stress vs. axial strain curves of the off-axis tensile tests performed by Koerber et al. [9].

2.4.2 Open-hole tensile and compressive tests

The experimental data from the OHT and OHC tests carried out by Camanho et al. [114] and by Bessa [129], respectively, are used to further evaluate the accuracy of the proposed constitutive model. The hole diameters used in the tests were: 2 mm, 4 mm, 6 mm and 8 mm in tension, and 2 mm, 3 mm, 4 mm and 5 mm in compression. The in-plane dimensions were defined using a width-to-diameter ratio equals to 6 and the laminate

thickness with a stacking sequence of $[90/0/\pm 45]_{3S}$. Vertical displacement is applied on the top face at low velocity to avoid dynamic effects during the simulation. Additionally, the ends of the virtual specimens are clamped to reproduce the boundary conditions of the tests, see Fig. 2.5b.

The predicted remote failure strengths are compared to the experimental data in Fig. 2.12. The numerical results for the tensile tests are within the experimentally measured dispersion, except the test with a hole diameter equal to 2 mm where a relative error of 2.8% is obtained. The numerical results of the compressive simulations with small hole diameters (2 mm and 3 mm) are within the experimental data scatter, but for higher hole diameters (4 mm and 5 mm) overpredictions are obtained (the highest relative error is 1.9%).

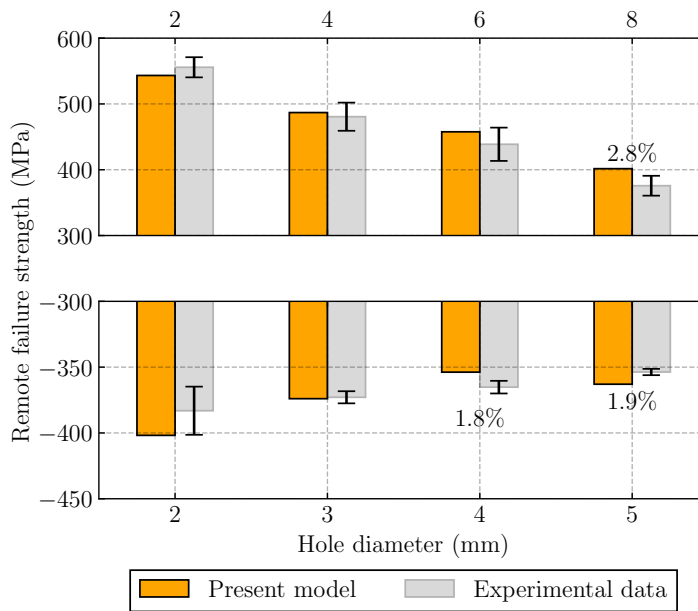


Figure 2.12: Numerical-experimental comparison of the remote failure strength of the open-hole tensile and compressive tests measured by Camanho et al. [114] and by Bessa [129], respectively. The error bars denote the standard deviation of the experimental data and the values are the relative error between the numerical result and experimental data.

The influence of the plasticity on the numerical results of the OHC tests with hole diameters equal to 2 mm and 3 mm is analysed, since the rest of the configurations have a large dependence on the longitudinal direction where the plasticity is not considered, see the experimental data reported by Camanho et al. [122]. Similar remote failure strengths are obtained whether or not plasticity is enabled in the constitutive model (difference in failure strength is less than 5%). However, enabling plasticity significantly influences the ultimate strain (difference in ultimate strain is within 11% and 13%). The smallest ultimate strains are obtained when plasticity is disabled.

Enhanced elastoplastic damage model

One of the main advantages of using $\tilde{\sigma}$ in CDM models is to develop a constitutive model efficient in terms of computational time. The elastic material properties (i.e., $\mathbb{C}_e(d_M = 0)$) and ε^e are the known data in CDM models with $\tilde{\sigma}$ while evaluating the failure criteria. Therefore, the damage only depends on the strain tensor and can be explicitly found, see [Section 2.3](#). However, an iterative implicit solution for the damage variables should be employed in CDM models which use σ to evaluate the failure criteria [123, 130–132], then the computational time increases.

The use of $\tilde{\sigma}$ in evaluating failure criteria can induce the activation of damage variables corresponding to failure mechanisms that should not occur [133]. A large elastic strain in a particular direction due to damage produces a large effective stress in that direction, but also large effective stresses in other directions may be generated. This phenomenon is observed in the pure longitudinal and transverse directions of $\tilde{\sigma}$, due to the coupling of the strains by the Poisson's ratios. For example, a uniaxial loading in the longitudinal direction activates damage variables associated to the longitudinal direction (d_ℓ). In this case, this longitudinal damage also produces effective stresses in the pure transverse directions,

$$\tilde{\sigma}_{22} = \tilde{\sigma}_{33} = \frac{E_{11}E_{22}\nu_{12}}{E_{11}(1-\nu_{23}) - 2E_{22}\nu_{12}^2} d_\ell \varepsilon_{11}^e. \quad (3.1)$$

Hence, damage variables associated to the transverse directions can be activated despite the nominal stresses being null ($\sigma_{22} = \sigma_{33} = 0$), see [Fig. 3.1](#). Consequently, spurious damage can be generated in the transverse directions. This event is a general limitation of constitutive models which use $\tilde{\sigma}$. This phenomenon can be observed in the literature constitutive models [49, 86, 92, 93, 95].

Matzenmiller et al. [76] proposed a damage model to describe the mechanical behaviour of FRP laminates based on the CDM theory. The model describes four failure mechanisms: i) fibre failure due to traction; ii) fibre buckling and kinking due to compression; iii) matrix cracking under transverse tension and shearing; and iv) matrix cracking under transverse compression and shearing. Each failure mechanism listed above is associated with a failure criterion as a function of $\tilde{\sigma}$ and its corresponding damage variable. The authors avoided the coupling of the components of $\tilde{\sigma}$ when the damage is achieved by degrading the Poisson's ratios as a function of the corresponding damage variable. These relationships

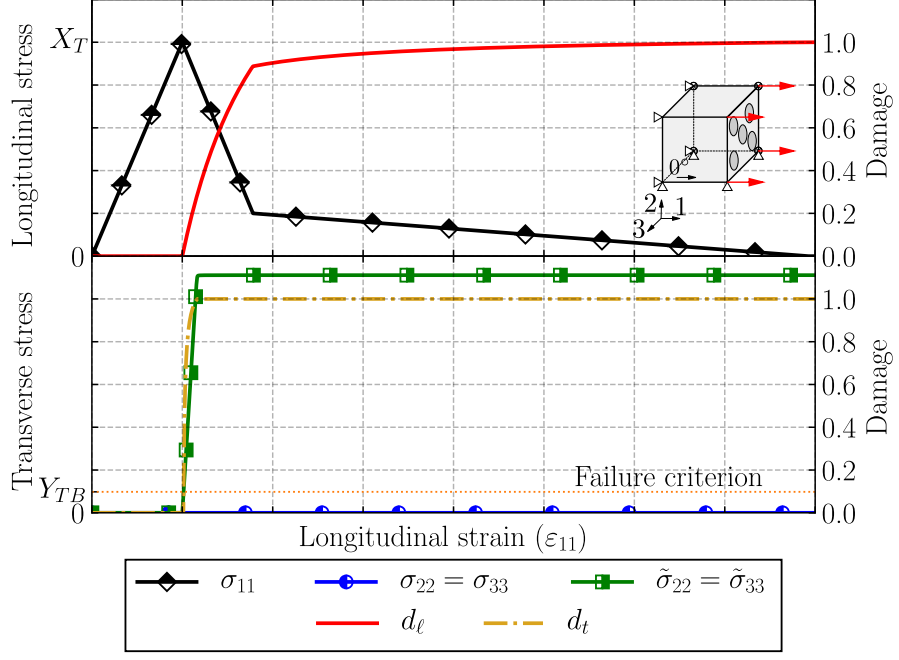


Figure 3.1.: Longitudinal virtual tensile test at the Gauss-point level using a CDM model using the $\tilde{\sigma}$, where d_ℓ and d_t are the damage variables associated to the longitudinal and transverse direction, respectively, X_T is the longitudinal tensile strength and Y_{TB} is the biaxial transverse tensile strength. Longitudinal response (top) and transverse response (bottom).

were assumed from experimental evidence. This procedure allows the components of $\tilde{\sigma}$ to be decoupled when damage occurs. Hence, the Poisson's ratios are a function of the damage variables that are unknown while $\tilde{\sigma}$ must be calculated. Therefore, an iterative algorithm should be implemented to solve the model [134], thus increasing the computational time. In addition, the solution presented by Matzenmiller et al. [76] cannot be straightforwardly implemented in the previously developed constitutive models which use $\tilde{\sigma}$ (e.g. the evolution of the damage variables must be redefined).

The main objective of this chapter is to present an improved approach to avoid spurious damage in CDM models which use $\tilde{\sigma}$ due to large strains caused by damage in other directions. The solution presented here can be explicitly implemented in existing CDM models that have already been developed using $\tilde{\sigma}$ [49, 86, 92, 93, 95] and linked with an explicit FE solver. The constitutive model presented in the previous chapter (original model) is used as a baseline to demonstrate how the formulation of existing CDM model can be modified to avoid spurious damage modes developing.

The formulation of the new proposed constitutive model is presented in Section 3.1 and its implementation in a FE explicit solver in Section 3.2. A pure longitudinal virtual test at the Gauss-point level presented in Section 3.3 demonstrates that no spurious damage is

found in the new proposed constitutive model (enhanced model). In addition, OHC tests with a multidirectional laminate and with unidirectional laminates are used to explain and demonstrate the improvements in the failure patterns predicted by the enhanced model.

3.1 Formulation

The previous formulation can produce spurious damage, as explained before. That is clearly presented in Fig. 3.1 where a large ε_{11}^e generates transverse effective stresses (due to d_ℓ) and, then spurious transverse damage. This phenomenon cannot be observed for the longitudinal tensile damage because $\phi_{\ell T}$ in Eq. (2.26) only depends on ε_{11}^e , since a non-interacting maximum allowable strain criteria is employed. However, this event can arise at $\phi_{\ell C}$ (from Eq. (2.27)) since longitudinal compressive failure mechanisms are promoted by matrix cracking in FRP laminates. Longitudinal compressive failure is promoted by fibre collapse as a result of shear kinking (due to small initial fibre misalignments) and matrix cracking [135, 136]. In addition, the transverse failure directly affects the longitudinal compressive stiffness since the matrix is not capable of containing the fibres promoting fibre microbuckling.

In FRPs, the onset of a crack in any direction governed by the matrix is reached with less stress compared with the stress required to initiate a crack in the pure longitudinal direction. Therefore, the longitudinal damage variables do not usually experience the spurious damage phenomenon previously discussed. Based on the previous observations, ϕ_t (see Eq. (2.28)) is modified as a function of the nominal stress tensor instead of the effective stress tensor. Therefore, ϕ_t is not affected by pure longitudinal loading conditions. The damage activation function defined in Eq. (2.29) is rewritten for the transverse direction as

$$F_t := \phi_t - 1 \leq 0, \quad (3.2)$$

and the transverse loading function as ($\boldsymbol{\sigma}$ instead of $\tilde{\boldsymbol{\sigma}}$ in Eq. (2.28))

$$\phi_t := \sqrt{\left(\frac{Y_C^d + Y_T^d}{Y_T^d Y_C^d}\right)^2 \frac{\tau_t^2 + \mu_t p_t^2}{1 + \mu_t} + \left(\frac{\mu_{s\ell}}{S_L^d} \tau_\ell\right)^2} + \frac{Y_C^d - Y_T^d}{Y_T^d Y_C^d} p_t + \frac{1 - \mu_{s\ell}}{S_L^d} \tau_\ell, \quad (3.3)$$

where the index $(\cdot)^d$ in strengths refers to them being from the material currently damaged. Therefore, these strengths must be defined as a function of the corresponding damage variable (current strengths) since the loading function is evaluated with the nominal stress tensor. Otherwise, only the onset of damage and not the evolution of the damage would be captured. For example, in a pure transverse tensile test $\sigma_{22} = Y_T$ is only in the onset of damage, after that $\sigma_{22} < Y_T$. The current strengths are obtained assuming linear softening

laws for the transverse damage variables as in [Chapter 2](#) (see [Fig. 2.4c](#)) and applying: pure transverse compressive state stress conditions for $Y_C^d(d_{st})$; pure transverse tensile state stress conditions for $Y_T^d(d_{st})$; and pure longitudinal shear state stress conditions for $S_L^d(d_{s\ell^*})$. They read

$$Y_C^d = \frac{4Y_C \mathcal{G}_{Y_C} E_{22} (1 - d_{st})}{4\mathcal{G}_{Y_C} E_{22} (1 - d_{st}) + l_t^* (\nu_{23} - 1) (Y_C d_{st})^2 + 2Y_C^2 l_t^* d_{st}}, \quad (3.4)$$

$$Y_T^d = \frac{2Y_T \mathcal{G}_{Y_T} E_{22} (1 - d_{st})}{2\mathcal{G}_{Y_T} E_{22} (1 - d_{st}) + Y_T^2 l_t^* d_{st}}, \quad (3.5)$$

and

$$S_L^d = \frac{2\mathcal{G}_{S_L} S_L G_{12} (1 - d_{s\ell^*})}{2\mathcal{G}_{S_L} G_{12} (1 - d_{s\ell^*}) + S_L^2 l_s^* d_{s\ell^*}}, \quad (3.6)$$

where l_t^* and l_s^* are the characteristic element length at the transverse and longitudinal shear directions, respectively.

3.2 Constitutive model implementation

The implementation of the constitutive model presented in this chapter (enhanced model) for an explicit FE solver at the Gauss-point level is explained below. The damage variable corresponding to the longitudinal direction (d_ℓ) is explicitly obtained as in the original model, since the same damage activation functions ([Eq. \(2.29\)](#)) are used. However, the damage variables corresponding to the transverse direction (d_{st} and $d_{s\ell^*}$) must be obtained from the transverse damage activation function in [Eq. \(3.2\)](#).

FE models with explicit solvers use very small increments of the strain tensor, especially for FRPs. Therefore, the variation of the stress tensor and of the internal variables is very small between each increment of the strain tensor. The implementation algorithm presented here is based on the fact that the solution at time $t_{(n+1)}$ is close to solution at the converged solution at the previous time interval ($t_{(n)}$).

The schematic representation of the modelled damage for a pure transverse tensile test at the Gauss-point level is presented in [Fig. 3.2](#); note that the displayed strain increment is high for the sake of the algorithm explanation. Firstly, the elastic-plastic behaviour is considered without damage (see [Fig. 3.2a](#)). Then, the onset of matrix crack is observed and, therefore, no further development of plasticity will evolve. From point 0 to 1 in

Fig. 3.2b, a predictor stress tensor ($\check{\sigma}$) is calculated using \mathbb{C}_e as a function of the damage variables of the previous time interval ($d_{M_{(n)}}$) as

$$\check{\sigma}_{(n+1)} := \mathbb{C}_e(d_{M_{(n)}})\epsilon_{(n+1)}^e. \quad (3.7)$$

Therefore, the predicted and effective stress tensors are the same when the material is undamaged ($d_{M_{(n)}} = 0 \rightarrow \check{\sigma} = \tilde{\sigma}$). However, if the Gauss-point is damaged at the previous time interval, the predicted and effective stress tensors are not the same ($d_{M_{(n)}} > 0 \rightarrow \check{\sigma} \neq \tilde{\sigma}$), see **Fig. 3.2c** from points 1 to 2. After that, $\phi_{t_{(n+1)}}$ is evaluated as a function of $\check{\sigma}(d_{M_{(n)}})$ and the current transverse strengths from Eqs. (3.4)–(3.6) with $d_{M_{(n)}} \left(Y_C^d(d_{st_{(n)}}), Y_T^d(d_{st_{(n)}}) \text{ and } S_L^d(d_{s\ell^*(n)}) \right)$.

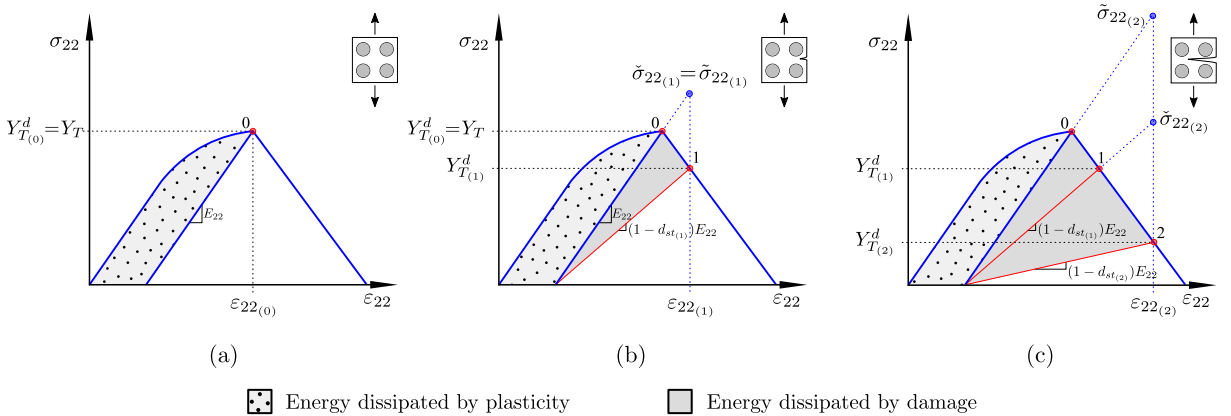


Figure 3.2.: Schematic representation of the numerical implementation of the enhanced constitutive model at the Gauss-point level when a pure transverse tensile test is applied: a) undamaged stress state; b) onset of a matrix crack; and c) propagation of a matrix crack.

A new internal transverse damage variable (r_t) is introduced to account for the history of the transverse damage, then d_{st} and $d_{s\ell^*}$ are obtained as a function of r_t . When the transverse damage evolves, the imposed condition by Eq. (3.2) is achieved by linearising F_t as

$$F_{t_{(n+1)}} + \frac{\partial F_{t_{(n+1)}}}{\partial r_{t_{(n+1)}}} \Delta r_{t_{(n+1)}} = 0. \quad (3.8)$$

Considering that Eq. (3.3) satisfies

$$\frac{\partial F_{t_{(n+1)}}}{\partial r_{t_{(n+1)}}} \approx -\frac{1}{r_{t_{(n)}}}, \quad (3.9)$$

and by introducing Eq. (3.9) in Eq. (3.8), the internal transverse damage variable at the current time yields

$$r_{t_{(n+1)}} = \phi_{t_{(n+1)}} r_{t_{(n)}}. \quad (3.10)$$

Finally, to guarantee that r_t monotonically increases, then

$$r_{t_{(n+1)}} = \max \left(r_{t_{(n)}}, \phi_{t_{(n+1)}} r_{t_{(n)}} \right), \quad (3.11)$$

where the initial r_t must be defined equal to 1. The residue from the first iteration is negligible when FE explicit solver is employed.

In summary, the implementation is based on the approach applied in the constitutive model presented in Chapter 2 with $\tilde{\sigma}$. The main difference is that F_t is evaluated with the damaged material properties and the applied stress tensor. The graphical comparison of the proposed implementation method with the one used in constitutive models with $\tilde{\sigma}$ under a pure transverse tensile loading state is presented in Fig. 3.3. The current predictor stress tensor ($\check{\sigma}_{(n+1)}$) is equal to the effective stress tensor calculated by degrading the corresponding stiffness using $d_{M_{(n)}}$ ($\tilde{\sigma}_{(n+1)}(\mathbb{C}_e(d_{M_{(n)}}))$). Similar behaviour is obtained when the transverse internal damage variable r_t is compared. Therefore, the evolution of the transverse damage variables as a function of r_t yields the one in constitutive models with $\tilde{\sigma}$. The transverse damage is guaranteed to increase since $r_{t_{(n+1)}}$ in Eq. (3.11) always increases and the transverse damage variables as a function of $r_{t_{(n+1)}}$ are monotonically increasing functions.

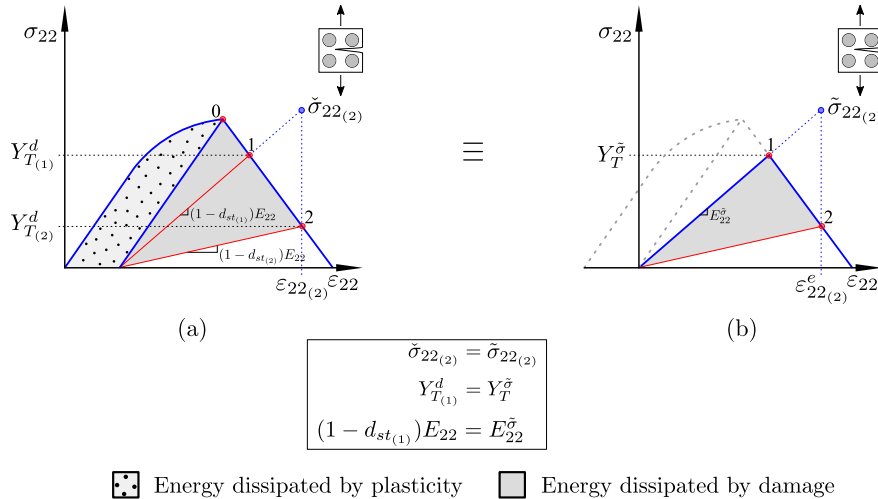


Figure 3.3.: Schematic representation of the numerical implementation of the enhanced constitutive model at the Gauss-point level when a pure transverse tensile test is applied: a) proposed implementation; b) equivalent implementation using the effective stress tensor and damaged material properties.

The longitudinal elastic domain thresholds ($\phi_{\ell T}, \phi_{\ell C}$) are explicitly obtained from Eq. (2.30). All damage variables (longitudinal and transversal) are obtained from the expressions presented in the original model using the strengths from the undamaged material, see

[Appendix B](#). The return mapping for the plasticity modelling and its coupling with the damage modelling presented in [Section 2.3](#) are employed here. [Algorithm 2](#) summarises the workflow to implement the constitutive model at the Gauss-point level using an explicit solver in a non-linear FE framework. The enhanced constitutive model is implemented in a user material Fortran subroutine (VUMAT) to be used with the Abaqus/Explicit solver [137], and its implementation is verified as the previous model using the loading cases presented in [Appendix G](#).

Algorithm 2: Algorithm of the enhanced constitutive model at time $t_{(n+1)}$

Input:

Total strain tensor at $t_{(n+1)}$: $\boldsymbol{\varepsilon}_{(n+1)}$
 Internal variables at $t_{(n+1)}$: $\boldsymbol{\varepsilon}_{(n)}^p, \bar{\boldsymbol{\varepsilon}}_{(n)}^p, r_{\ell T_{(n)}}, r_{\ell C_{(n)}}, r_{t_{(n)}}$

Initialisation:

Local Newton-Raphson iteration: $k = 0$

Effective stress tensor: $\tilde{\boldsymbol{\sigma}} = \mathbb{C}_e(d_M = 0)(\boldsymbol{\varepsilon}_{(n+1)} - \boldsymbol{\varepsilon}_{(n)}^p)$

Effective stress invariants using $\tilde{\boldsymbol{\sigma}}$ in Eqs. (2.5)–(2.8)

Stress tensor of the damage predictor: $\check{\boldsymbol{\sigma}} = \mathbb{C}_e(d_{M_{(n)}})(\boldsymbol{\varepsilon}_{(n+1)} - \boldsymbol{\varepsilon}_{(n)}^p)$

Stress invariants of the damage predictor using $\check{\boldsymbol{\sigma}}$ in Eqs. (2.5)–(2.8)

Update the transverse strengths as a function of $d_{M_{(n)}}$ in Eqs. (3.4)–(3.6)

Loading functions in Eqs. (2.26), (2.27) and (3.3): $\phi_{\ell T}(\tilde{\boldsymbol{\sigma}}), \phi_{\ell C}(\tilde{\boldsymbol{\sigma}})$ and $\phi_t(\check{\boldsymbol{\sigma}})$

Internal damage variables in Eqs. (2.30) and (3.11)

Damage variables from the original model: $d_{M_{(n+1)}}$

Elastic predictor: $\boldsymbol{\sigma}_{(n+1)}^{tr} = \mathbb{C}_e(d_{M_{(n+1)}})(\boldsymbol{\varepsilon}_{(n+1)} - \boldsymbol{\varepsilon}_{(n)}^p)$

1 **if** $d_t = 0$ and $d_{st} = 0$ and $d_{sl} = 0$ **then**

Yield stresses: $Y_{CP}(\bar{\boldsymbol{\varepsilon}}_{(n)}^p), Y_{TP}(\bar{\boldsymbol{\varepsilon}}_{(n)}^p)$ and $S_{LP}(\bar{\boldsymbol{\varepsilon}}_{(n)}^p)$

Yield function in Eq. (2.12): $\phi_{(n+1)}^p$

General convex cutting-plane algorithm (return-mapping):

$$\boldsymbol{\sigma}_{(n+1)}^{(k)} = \boldsymbol{\sigma}_{(n+1)}^{tr}$$

$$\phi_{(n+1)}^{p(k+1)} = \phi_{(n+1)}^p$$

4 **while** $\phi_{(n+1)}^{p(k+1)} > tol$ **do**

Derivative of the plastic potential function with respect to the stress tensor:

$$\partial_{\boldsymbol{\sigma}_{(n+1)}^{(k)}} (\varphi^p)$$

Increment of the consistency parameter: $\Delta\gamma_{(n+1)}^{(k)} = -\frac{\phi_{(n+1)}^p}{\frac{d\phi_{(n+1)}^p}{d\gamma_{(n+1)}}}$

Update the plastic strain tensor: $\boldsymbol{\varepsilon}_{(n+1)}^{p(k+1)} = \boldsymbol{\varepsilon}_{(n+1)}^{p(k)} + \Delta\gamma_{(n+1)}^{(k)} \partial_{\boldsymbol{\sigma}_{(n+1)}^{(k)}} (\varphi^p)$

Update the stress tensor: $\boldsymbol{\sigma}_{(n+1)}^{(k+1)} = \boldsymbol{\sigma}_{(n+1)}^{(k)} - \Delta\gamma_{(n+1)}^{(k)} \mathbb{C}_e \partial_{\boldsymbol{\sigma}_{(n+1)}^{(k)}} (\varphi^p)$

Update the equivalent plastic strain: $\bar{\boldsymbol{\varepsilon}}_{(n+1)}^{p(k+1)} = \bar{\boldsymbol{\varepsilon}}_{(n+1)}^{p(k)} + \Delta\gamma_{(n+1)}^{(k)} \sqrt{\frac{1}{2}} \left\| \partial_{\boldsymbol{\sigma}_{(n+1)}^{(k)}} (\varphi^p) \right\|$

Update yield stresses: $Y_{CP}(\bar{\boldsymbol{\varepsilon}}_{(n+1)}^{p(k+1)}), Y_{TP}(\bar{\boldsymbol{\varepsilon}}_{(n+1)}^{p(k+1)})$ and $S_{LP}(\bar{\boldsymbol{\varepsilon}}_{(n+1)}^{p(k+1)})$

Yield function in Eq. (2.12): $\phi_{(n+1)}^{p(k+1)}$

5 $k = k + 1$

6 **end**

7 **end**

3.3 Numerical predictions

The improvement of the formulation presented in this chapter (enhanced model) is demonstrated by comparing its predictions with those obtained by the previous model presented in [Chapter 2](#) (original model, which is a CDM model based on $\tilde{\sigma}$). A longitudinal virtual tensile test at Gauss-point level is performed in [Section 3.3.1](#). The stresses and damage variables vs. strain curves of the longitudinal and transverse direction are presented. The numerical-experimental comparison of the remote failure strengths of open-hole tests carried out in [Section 2.4.2](#) is extended with the predictions from the enhanced model. Next, an OHC virtual test is conducted using a quasi-isotropic laminate with both the original and enhanced models and the results are compared with experimental data in [Section 3.3.3](#). This comparison is used to analyse the impact of the enhanced model on the predictions (failure strength and failure pattern). After that, an OHC virtual test using a unidirectional stacking sequence at 0° is presented in [Section 3.3.4](#), since the failure strength of OHC tests in quasi-isotropic laminates is governed by the plies at 0° . This comparison can help to explain the possible discrepancies on the predicted failure strength obtained from each model in the quasi-isotropic laminate. Finally, another OHC virtual test using a unidirectional stacking sequence at 90° is performed in [Section 3.3.5](#). This last comparison can help to explain the possible discrepancies on the predicted failure pattern in the quasi-isotropic laminate.

The FE modelling strategy used in [Section 2.4](#) is employed to predict the strength of the OHT and OHC tests of [Section 3.3.2](#) (geometries, discretization of the FE meshes, boundary conditions, etc.). For the rest of the simulations, the mesh element size is defined approximately equal to 0.1 mm to prevent snap-back of the constitutive softening laws for each failure mode around the regions where damage is expected in the open-hole tests. In this case, the in-plane mesh element size is defined approximately ten times smaller than the critical one [101] (0.99 mm in the transverse direction, see [Appendix F](#)) to enhance the predictability of failure patterns of each configuration. In addition, three elements through-the-thickness of each ply are used.

The same CFRP system employed in [Chapter 2](#) is used in this chapter, IM7/8552 unidirectional prepreg system. Therefore, the material properties presented in [Section 2.4](#) are used. Additionally, the fracture toughness in the transverse compressive direction (\mathcal{G}_{Y_C}) is adjusted to fit the experimental data. This material property (\mathcal{G}_{Y_C}) is not employed in the original model. The OHC test presented in [Section 2.4.2](#) with a hole diameter of 3 mm is selected to adjust \mathcal{G}_{Y_C} . The FE modelling strategy used in the fit analysis also follows the one presented in [Section 2.4](#). The relative error between the numerical and

average experimental values of the remote failure strength is equal to 0.18%. Finally, the value of \mathcal{G}_{Y_C} is set equal to 2.8 N/mm.

The boundary conditions presented in Fig. 3.4 are applied in the open-hole virtual tests, except for the FE models of Section 3.3.2. The displacement on the upper face of the specimens is applied at low velocity to avoid dynamic effects, while the remaining degrees of freedom of this face are constrained. Furthermore, all degrees of freedom on the bottom face of the specimens are constrained. In addition, the out-of-plane displacement on the front and back faces are fixed in the virtual test of Section 3.3.4 in accordance with Seon et al. [138], who used a support to prevent buckling during experimental tests.

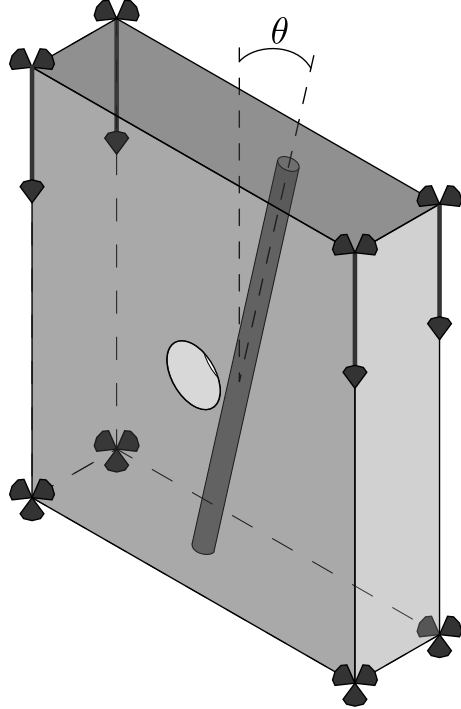


Figure 3.4.: Schematic representation of the boundary conditions applied in the open-hole compressive virtual test. θ is the fibre angle orientation.

3.3.1 Longitudinal tensile test

A pure longitudinal virtual tensile test is carried out using the enhanced constitutive model at the Gauss-point level. The longitudinal stress vs. strain curve follows the imposed softening law in the tensile direction (bilinear softening curve) and the evolution of $d_{s\ell}$ is equal to $d_{\ell T}$ due to the definition of Eq. (2.33) since $d_{s\ell^*}(\phi_t = 0) = 0$, see Fig. 3.5. However, the transverse damage variables are equal to zero ($d_t = d_{st} = d_{s\ell^*} = 0$) since the stresses in the transverse directions are equal to zero and, therefore, $\phi_t = 0$.

The comparison of Fig. 3.1 with Fig. 3.5 demonstrates that the CDM which use $\tilde{\sigma}$ can generate spurious damage in the transverse direction when a pure tensile loading condition is

applied. However, the enhanced model avoids transverse damage variables being activated when the Gauss-point is not loaded in the transverse direction ($p_t = \tau_\ell = \tau_t = 0$).

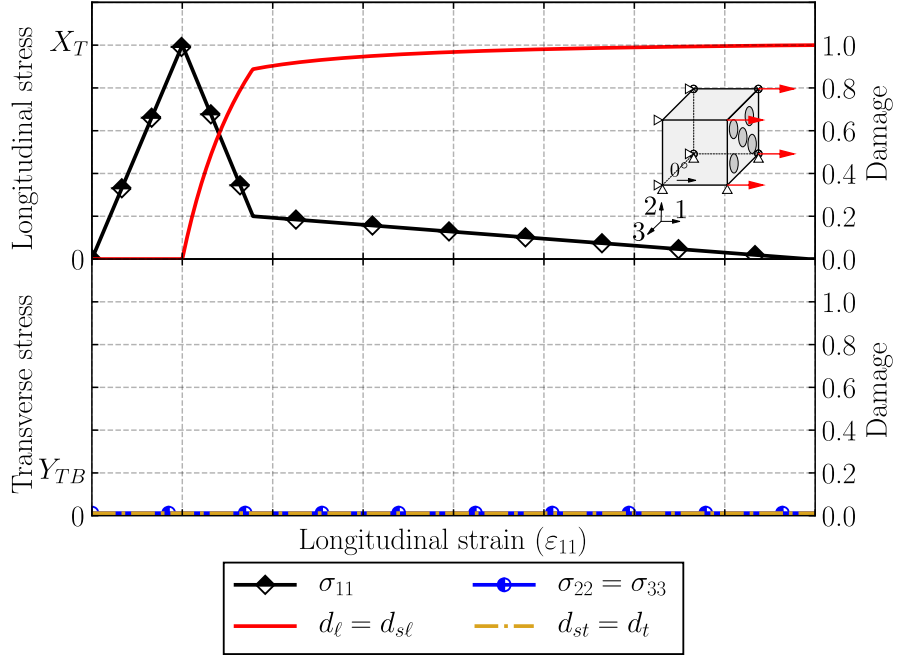


Figure 3.5.: Longitudinal virtual tensile test at the Gauss-point level using the enhanced constitutive model, where Y_{TB} is the biaxial transverse tensile strength. Longitudinal response (top) and transverse response (bottom).

3.3.2 Open-hole tensile and compressive tests

The numerical results of the original model are compared to the experimental data from OHT and OHC tests in [Section 2.4.2](#), and the comparison is extended to the proposed constitutive model described in this chapter (enhanced model). The same FE modelling strategy as the aforementioned section is used with the enhanced constitutive model. The remote failure strengths predicted are then compared to the experimental data in [Fig. 3.6](#). The predictions of the enhanced model are comparable to those of the original constitutive model, apart from with respect to larger hole diameters (8 mm under tension and 4 mm and 5 mm under compression). For these cases, the relative error of the remote failure strength between the numerical and experimental results has decreased; from 2.8% to 0.7% under tension. The relative error decreases under compression in the configuration with a hole diameter equal to 4 mm from 1.8% to 1.3%. Additionally, the prediction of the enhanced model is within the scatter of the experimental data for the hole diameter of 5 mm.

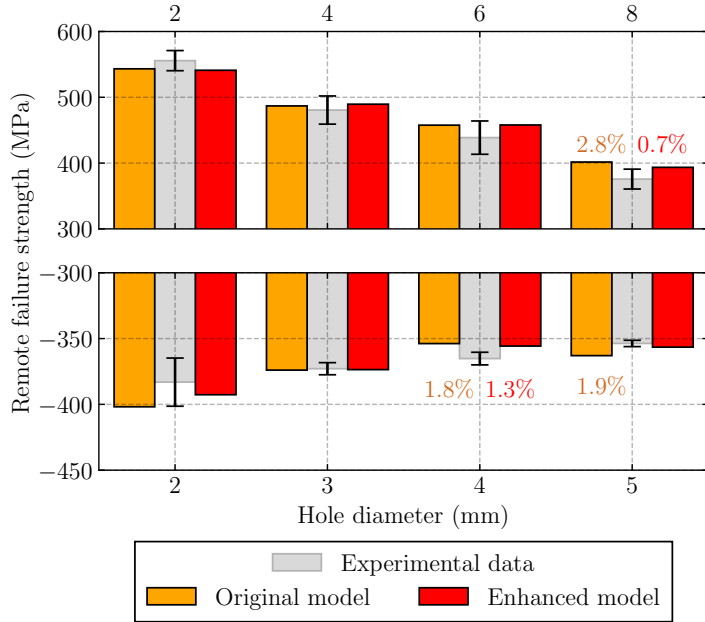


Figure 3.6.: Numerical-experimental comparison of the remote failure strength of the open-hole tensile and compressive tests measured by Camanho et al. [114] and by Bessa [129], respectively. The error bars denote the standard deviation of the experimental data and the values are the relative error between the numerical result and experimental data.

3.3.3 Open-hole compressive test with quasi-isotropic laminate

The OHC test in a quasi-isotropic laminate $[45/90/-45/0]_{4s}$ with a diameter of 6.35 mm carried out by Wisnom et al. [139] is used in this section. The remote stress vs. strain curve obtained from the enhanced model matches the one obtained by the original model until the onset of damage, see Fig. 3.7. After that, the evolution of the curves are significantly different. It would be expected that the original model which use $\tilde{\sigma}$ suddenly drops when the failure strength is reached since the longitudinal damage generates spurious transverse damage. However, the remote stress vs. strain curve gradually decreases after the failure strength from the original model. This behaviour is explained in Fig. 3.9c, the failure from the original model is developed in a larger area in comparison with the results from the enhanced model because the spurious damage is extended in the whole specimen. Therefore, the model with $\tilde{\sigma}$ dissipated more energy due to damage than the enhanced model.

The remote stress obtained from the enhanced model suddenly drops after the remote failure strength since the damage is localised at the midplane of the specimen (see Fig. 3.9b). In addition, the comparison of predicted remote failure strength using the enhanced model and the original model with the average value from the experimental tests is in very good agreement. The relative error between the remote failure strength from the enhanced

model and the average experimental data are equal to 0.32%, and 1.15% from original model. The grey area in Fig. 3.7 represents the experimental error of the remote failure strength by assuming a level of confidence equal to 95%. Therefore, the predicted remote failure strength from both models are within the expected dispersion of the experimental data.

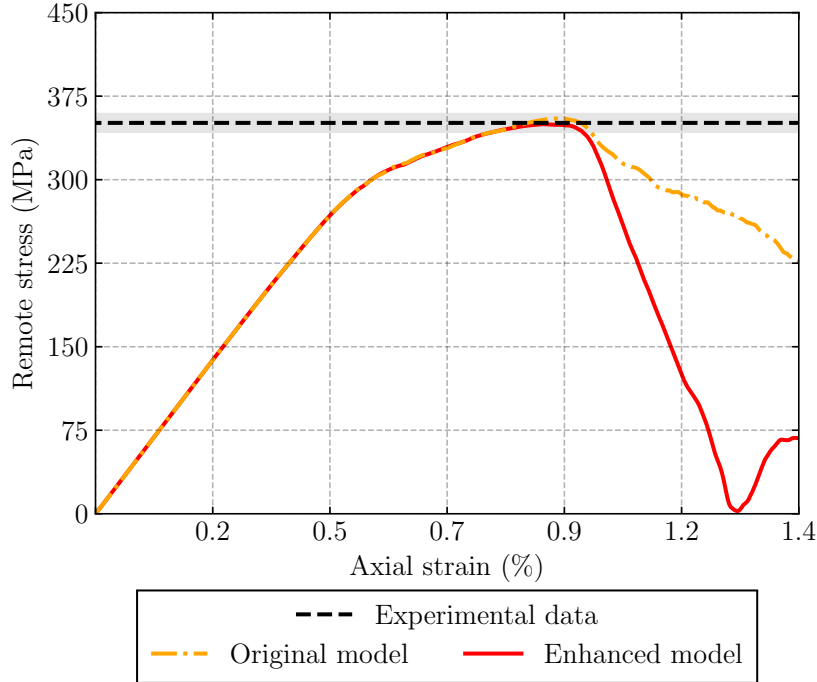


Figure 3.7.: Numerical-experimental comparison of the remote stress vs. axial strain curves of the open-hole compressive test performed by Wisnom et al. [139]. The grey area represents the experimental error of the remote failure strength by assuming a level of confidence equal to 95%.

Fig. 3.8 compares the predicted external failure pattern with the experimental data at 98% of the remote failure load. Only the comparison of $d_{s\ell}$ with the experimental data are presented since the external failure patterns of d_{st} is approximately equal to $d_{s\ell}$ and no fully-damaged elements are found in d_ℓ and d_t . The initiation of the failure patterns from both constitutive models are in good agreement with the experimental data. In all cases, failure starts in two separate zones around the hole edge with similar in-plane angles.

The predicted failure external patterns after the peak load are compared to the experimental data in Fig. 3.9. Only the transverse damage variable d_{st} is presented since the failure pattern of $d_{s\ell}$ is approximately equal to d_{st} and negligible failure is found in d_t . The brittle failure mechanism observed in the experimental data are properly captured by the enhanced constitutive model. The predicted failure pattern is in good agreement with the fracture straight across the laminate and the out-of-plane fracture plane observed in

the experimental data, see Fig. 3.9a and b. However, the failure pattern predicted by the original constitutive model is not in agreement with the experimental data, see Fig. 3.9a and c. Similar behaviour is observed at the remote peak load, the damage is localised around the hole in a fracture straight across the laminate in the enhanced model. However, the failure pattern suddenly grows from the hole to either direction in the original model.

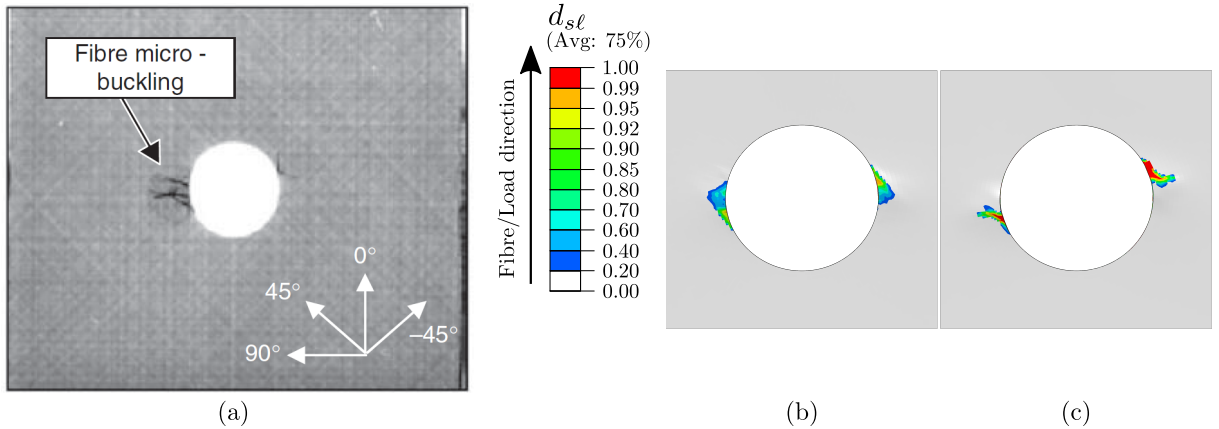


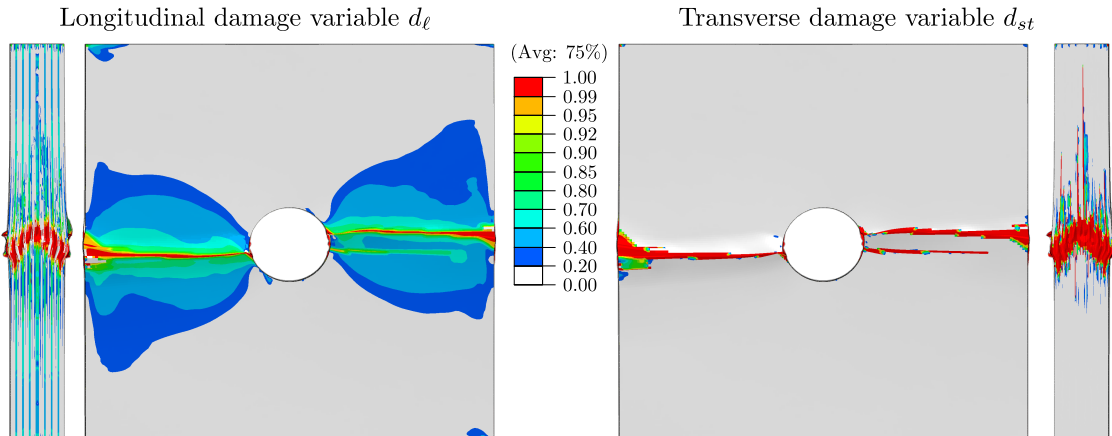
Figure 3.8: Numerical-experimental comparison of the onset of failure at 98% of the remote failure load from the quasi-isotropic laminate in the open-hole compressive test: a) experimental data from [139]; b) numerical results from the enhanced model; and c) numerical results from the original model.

The localisation of the damage in OHC specimens with multidirectional laminates always initiates at the hole edges in the outer 0° plies at about 75÷85% of the failure strength [140–145]. This phenomenon is predicted by the enhanced model, most of the energy dissipated from the longitudinal failure mechanism at 75% of the failure strength is observed at the outer 0° plies, see Fig. 3.10b. A negligible failure is found in the rest of the layers at 75% of the remote failure load.

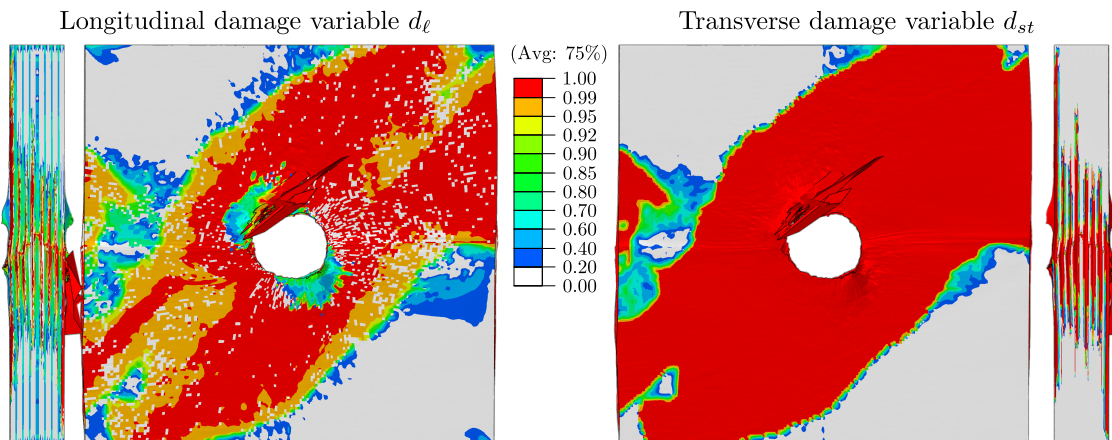
The main failure mechanism in OHC specimens is the fibre microbuckling in the 0° plies, which promotes delamination between the off-axis and 0° plies at the hole edges [140–145]. In the FE models, there are three elements through-the-thickness of each ply and d_t refers to the mode-I matrix cracking. In addition, despite not having specific elements to model delamination as cohesive elements on the ply interfaces, the elements located on the 0° midplane layer in contact with those from the -45° layer show the typical delaminated failure pattern. After that, the delamination grows in that interface, see Fig. 3.10c.



(a)



(b)



(c)

Figure 3.9.: Numerical-experimental comparison of the external failure pattern after the remote failure load from the quasi-isotropic laminate in the open-hole compressive test: a) experimental data from Wisnom et al. [139]; b) numerical results from the enhanced model; and c) numerical results from the original model.

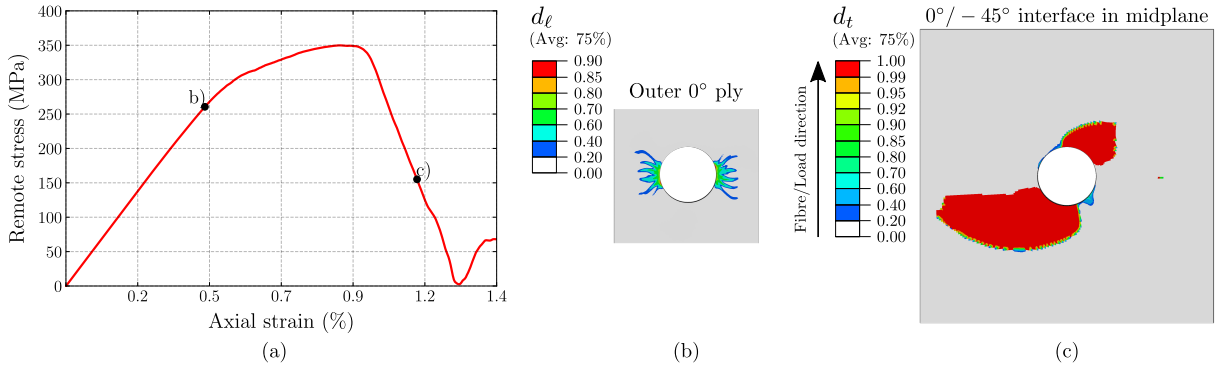


Figure 3.10: Predicted failure mechanism evolution of the quasi-isotropic laminate in an open-hole compressive test using the enhanced model: a) predicted remote stress vs. strain curve; b) longitudinal failure pattern of 0° outer ply at 75% of the failure strength; and c) failure pattern of 0° / -45° interface in the midplane of the specimen after the failure strength.

The discrepancies on the failure pattern predicted by the original model with the pattern experimentally obtained does not have significant influence on the failure strength in OHC quasi-isotropic laminates. However, these discrepancies can take an important influence in damage-tolerance design. In the aeronautical and aerospace industry, a composite structure is designed to be able to sustain loads even with damage [146]. For example, in a CAI test, firstly the specimen is impacted and different damage mechanisms are then produced: matrix cracking, fibres fractures and delamination [101]. After that, the specimen is loaded in compression until failure. In the CAI test, the residual strength depends on the local buckling and the propagation of the impacted-induced failure mechanisms previously described [147, 148]. Hence, a good prediction of the failure pattern in the impact test is required to properly predict the CAI strength. The CAI strength decreases when the delaminated area increases [101, 102, 149]. Therefore, if the delaminated area is not properly predicted, the constitutive model cannot capture the CAI strength.

3.3.4 Open-hole compressive test at 0°

As previously mentioned, the failure strength in OHC tests of multidirectional laminates is governed by the 0° layers [140–145]. For this reason, an OHC virtual test with all plies aligned with respect to the load direction is used to explain the agreement of the predicted failure strength from the enhanced and original models in Fig. 3.7. In addition, the OHC test carried out by Seon et al. [138] is employed to compare the predicted onset failure pattern. The hole diameter of the specimen used in the virtual tests is equal to 6.35 mm and the in-plane dimensions are 12.8 mm \times 25.6 mm as defined in [138], and eight plies at 0° with respect to the loading direction are used (as in Section 3.3.3).

The comparison of the remote stress vs. strain curve obtained from both the enhanced and original models is performed in Fig. 3.11. Good agreement between both predicted curves is found until the remote failure strength. After that, the curves differently drop and, finally, the stress stabilises around 100 MPa in both cases. This observation could explain the agreement in the predicted failure strength from OHC specimens with quasi-isotropic laminates. The failure strength in quasi-isotropic laminates is governed by 0° layers and no significant discrepancies in the predicted remote failure strength from both models with 0° unidirectional laminates are obtained.

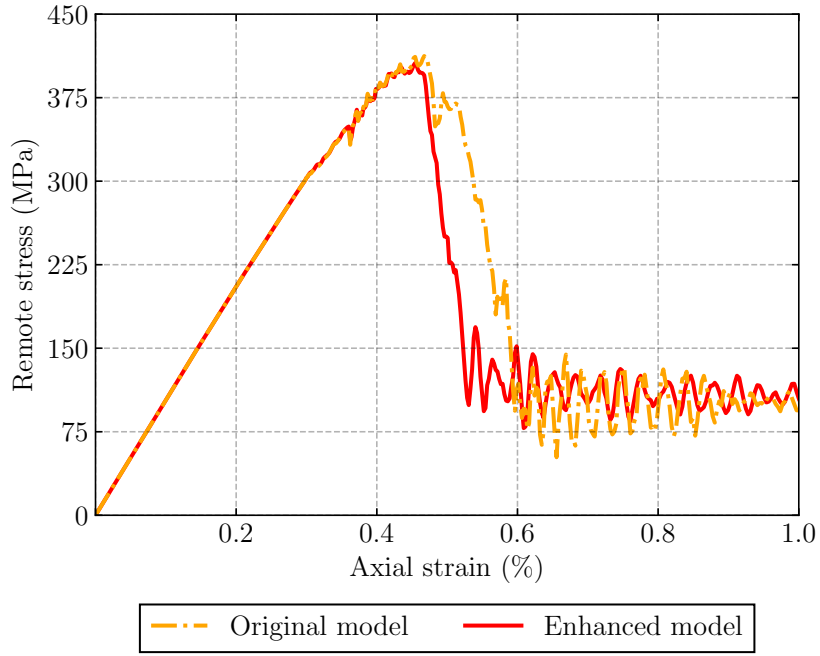


Figure 3.11: Predicted remote stress vs. axial strain curves from the open-hole compressive test with $[0]_8$.

Fig. 3.12 compares the external predicted failure pattern at the remote failure strength with the experimental data reported by Seon et al. [138]. A matrix crack is observed in all cases (the experimental data and the numerical predictions). Good agreement is found on the failure mechanism between the predictions and the experimental data. In contrast, the predicted failure patterns obtained after the failure load from both models are significantly different, see Fig. 3.13. The cracks predicted after the failure load by the enhanced model grow with an inclination from the hole edge to the lateral edges (Fig. 3.13a), whereas the cracks predicted by the original model grow horizontally, see Fig. 3.13b. That can explain the discrepancies obtained in the failure pattern of the quasi-isotropic laminate in Fig. 3.9.

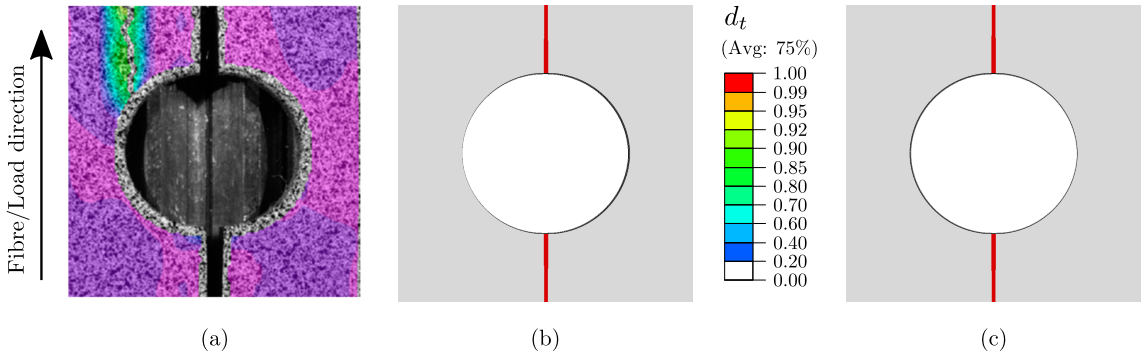


Figure 3.12.: Numerical-experimental comparison of the failure pattern at the remote failure load from the $[0]_8$ laminate in the open-hole compressive test: a) experimental data from Seon et al. [138]; b) numerical results from the enhanced model; and c) numerical results from the original model.

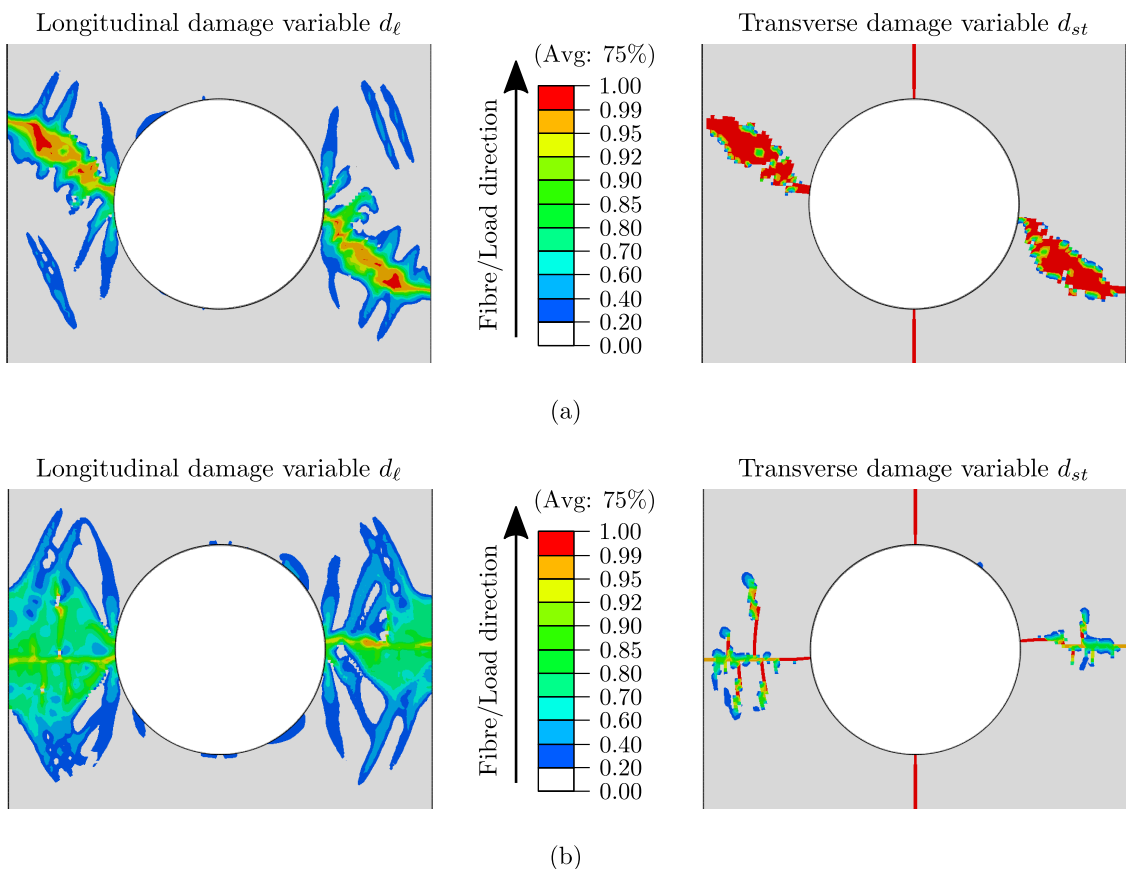


Figure 3.13.: Predicted external failure patterns after the remote failure load of the $[0]_8$ laminate in an open-hole compressive test using: a) the enhanced model; and b) the original model.

3.3.5 Open-hole compressive test at 90°

OHC virtual tests at 90° are carried out to better understand the discrepancies obtained in the predicted failure pattern from the quasi-isotropic laminate in Section 3.3.3. The dimensions of the specimen are $31.75 \text{ mm} \times 31.75 \text{ mm}$, the hole diameter is defined equal to 6.35 mm and eight plies at 90° with respect to the load direction.

The remote stress vs. strain curve predicted from the enhanced model match the one obtained from the original model until the remote failure strength of the latter model is reached, see Fig. 3.14. After that, the results from the original model are unstable and very large values of the remote load are obtained. However, the remote stress vs. strain curve predicted by the enhanced model increases until the failure strength and, after that, suddenly decreases until 0 MPa. The percent difference between the predicted remote failure strength obtained by each model is 10.65%. This difference does not have a significant impact on the predicted remote stress vs. strain curve until the failure strength of an OHC virtual test with a multidirectional laminate, since they are dominated by the 0° layers.

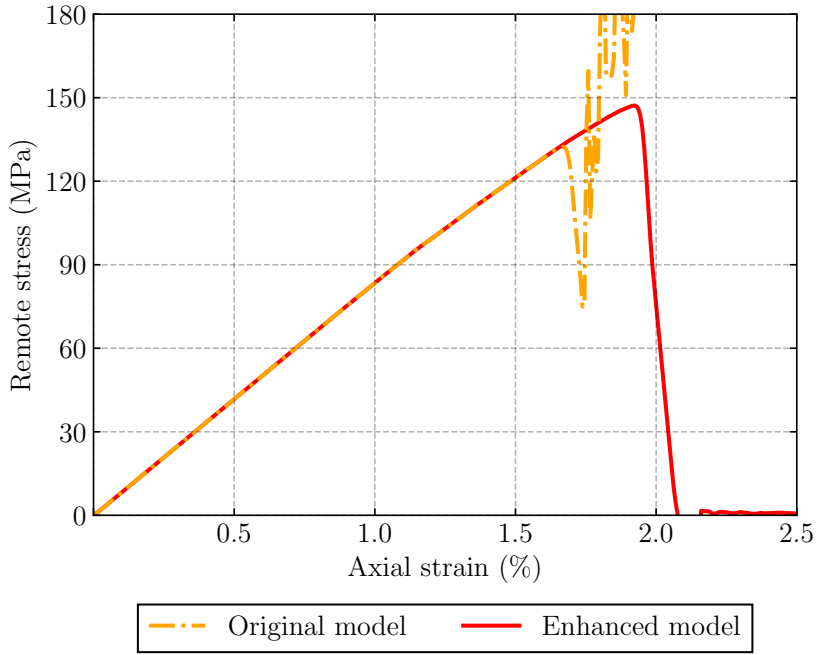


Figure 3.14: Predicted remote stress vs. axial strain curves from the open-hole compressive test with [90]8.

The external failure patterns predicted by the original model at the remote failure strength is significantly different from those obtained with the enhanced model, see Fig. 3.15. In the enhanced model, two matrix cracks are localised at the midplane of the specimen at the hole edge, and they are horizontally propagated to the specimen edge, see Fig. 3.15a. However, the original model not only predicts two matrix cracks at the hole edge growing in the horizontal direction, but also in the vertical direction, see Fig. 3.15b. In addition, the fibre failure predicted by the enhanced model is negligible, but fully-damaged elements in the longitudinal direction are found in the predictions from the original model.

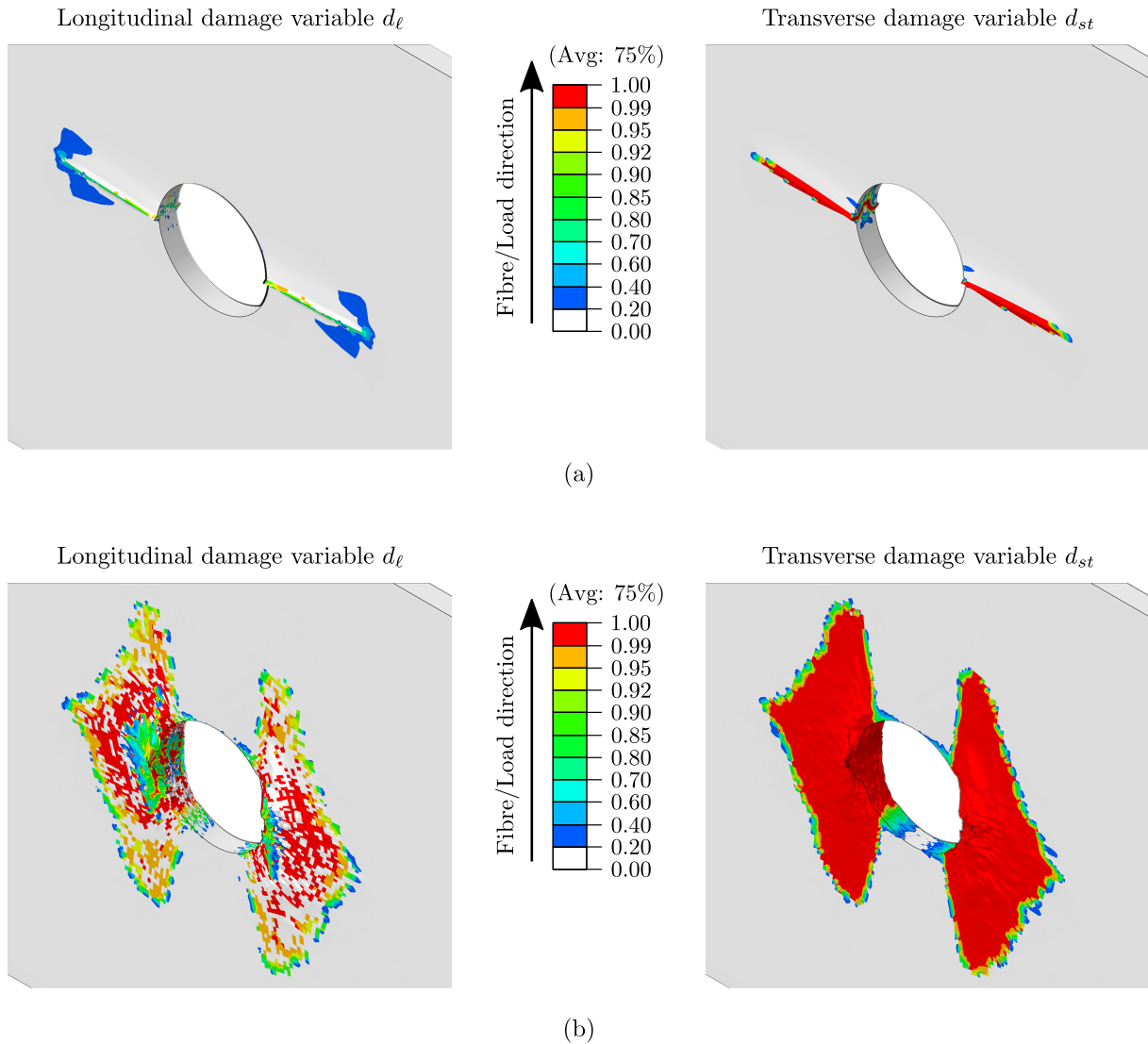


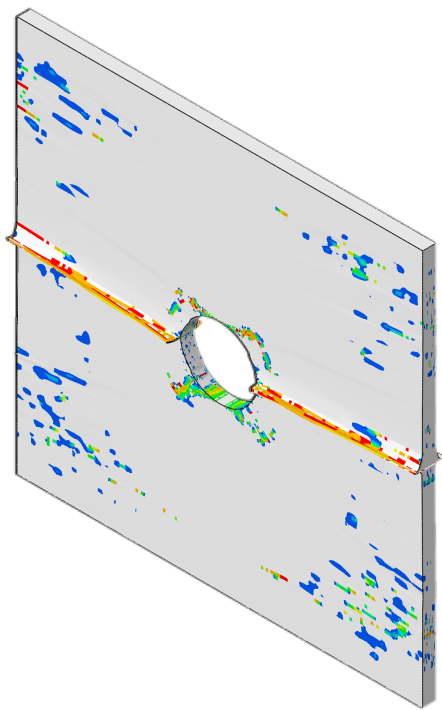
Figure 3.15.: Predicted failure mechanism at the remote failure strength of the $[90]_8$ laminate in an open-hole compressive test using: a) enhanced model; and b) original model.

The constitutive models which use $\tilde{\sigma}$ can generate spurious damage due to damage in the other directions. After the onset of damage in one direction, the effective stresses in other directions increase. Therefore, the activation of the damage functions in the rest of the directions can be achieved. Longitudinal failure promotes artificial transverse cracking, which in turn, also promotes artificial longitudinal failure. That becomes in an unstable damage evolution accentuated after the failure strength. This could explain the fibre damage field in Fig. 3.15b. The enhanced constitutive model does not experience that phenomenon because the evolution of the transverse variables is not affected by d_ℓ . Therefore, no spurious transverse damage can affect to d_ℓ .

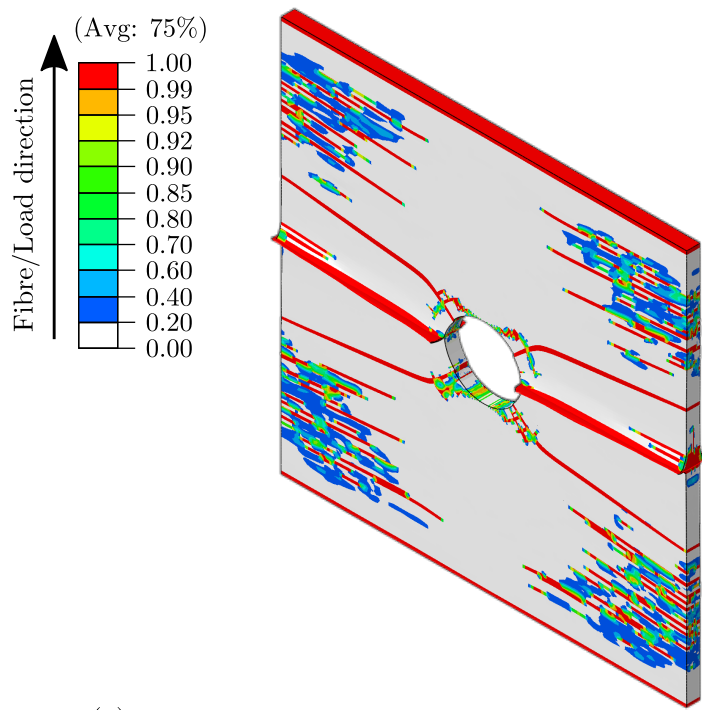
Fig. 3.16 displays the external failure pattern and the deformed shape of the numerical results when 2.25% of the axial strain is applied. The failure pattern and the deformed shape of the specimen from the enhanced model are in agreement with the expected results.

Matrix cracks are localised at the hole edge and propagated to the specimen edge, as well as the out-of-plane displacement of the layers at the midplane. Hence, the matrix cannot contain the fibres and, therefore, the longitudinal compressive damage is activated at the midplane of the specimen. However, all elements are fully-damaged in the transverse direction from the original model, therefore, the elements present a large distortion, see Fig. 3.16b. The large distorted elements in Fig. 3.16b are removed, otherwise, the results cannot be analysed. It is worth mentioning that the enhanced constitutive model prevents Abaqus' error regarding excessive distortion of the elements, as the failure propagation is stable. Therefore, FE simulations can be successfully completed using the enhanced model.

Longitudinal damage variable d_ℓ

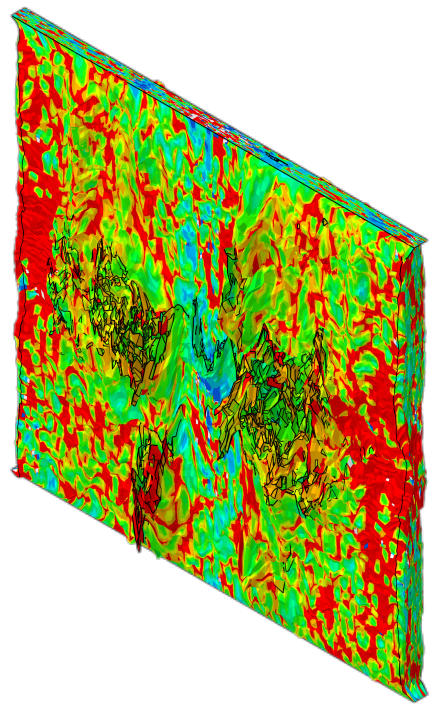


Transverse damage variable d_{st}

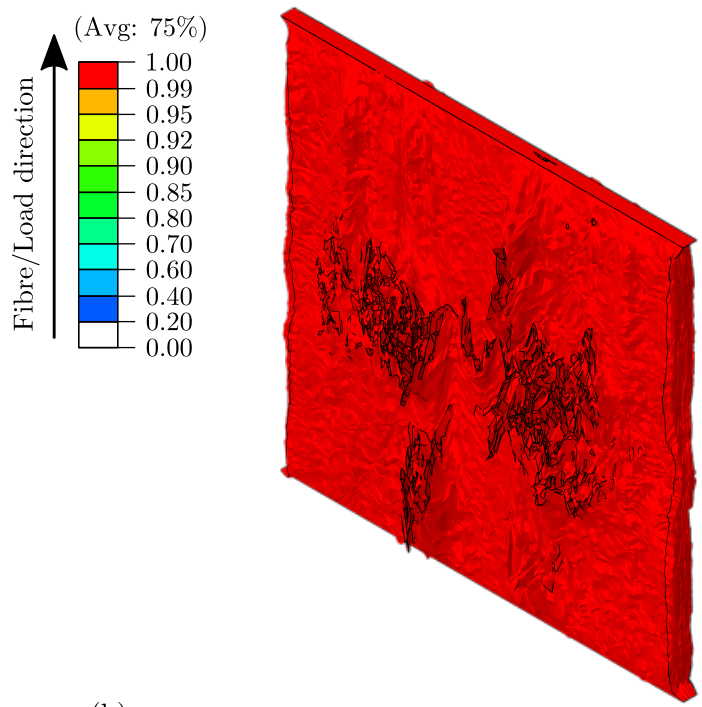


(a)

Longitudinal damage variable d_ℓ



Transverse damage variable d_{st}



(b)

Figure 3.16.: Predicted failure pattern when 2.25% of the axial strain is applied from the $[90]_8$ laminate in the open-hole compressive test: a) enhanced model; and b) original model. The large distorted elements in b) are removed.

Transverse Poisson's ratios

Unidirectional FRP laminates behave as homogenous transversely isotropic materials [150–153] and, thus, have a plane of symmetry with respect to a rotation about the fibre-oriented axis. The material properties of this transverse plane are the same in all directions. Therefore, five elastic material properties are required in the generalised Hooke's law. Several standardised methodologies have been developed to measure them: the longitudinal Young's modulus [98, 99], the transverse Young's modulus [98, 99], the shear Young's modulus [104, 105, 154], and the elastic longitudinal Poisson's ratio (ν_{12}) [98]. However, there is no standardised method for measuring the elastic transverse Poisson's ratio (ν_{23}).

FRP structures exhibit non-linear response under certain loading conditions, such as compressive or shear loading states in the directions governed by the matrix [8–10]. This behaviour is largely due to plastic strains, especially in thermoplastic-based composite materials [155, 156]. The evolution of the plastic strains is governed by the plastic transverse Poisson's ratio (ν_{23}^p). Several constitutive models, developed to predict the inelastic deformation due to plastic strains, use a non-associative plastic flow rule and they can be adjusted using ν_{23}^p [124, 157–160].

In solid mechanics, ν_{23} is defined as the negative quotient of the transverse strain (ε_{33}) to the axial strain applied (ε_{22}) on the transverse plane. Transverse Poisson's ratio is an important material property of FRPs in the elastic and plastic regions. In the literature, few works are addressed to the experimental measurement of ν_{23} . Recently, Khaled et al. [161] carried out a transverse tensile and compressive tests using a unidirectional carbon/epoxy composite material. Specimens with fibres aligned through-the-thickness of the panel were employed, thus limiting the width and length of the specimens to the thickness of the panel. The authors used 96 plies per panel which equals to 18.3 mm specimen length. Curing thick laminates can lead to significant residual stresses which can cause delamination cracking and residual shape distortions [162–164]. Furthermore, special gripping assemblies were manufactured to transfer the load from a hydraulic grip onto the specimen. The strain fields were measured with digital image correlation (DIC) techniques. The elastic Poisson's ratio from tensile tests was reported, and the elastic and plastic Poisson's ratios from compressive tests were also presented.

Frederiksen [165] presented an approach to estimate ν_{23} of unidirectional FRP laminates from the natural frequencies of a plate specimen. The measurement of frequencies was

obtained through non-destructive impact testing and a model analysis, and ν_{23} was estimated based on the higher-order shear deformation theory [166] and an optimisation algorithm. Kohlhauser and Hellmich [167] proposed a methodology to estimate the elastic material constants of isotropic, transversely isotropic and orthotropic materials by combining ultrasonic-mechanical and uniaxial tests. The method is based on the generalised Hooke's law, the authors presented an approach to estimate the components of the stiffness tensor using an ultrasonic-mechanical test. The material properties of a carbon/aluminium composite material were estimated. First, the Young's modules were obtained from uniaxial tests. Subsequently, several ultrasonic pulse transmission tests were performed at different directions and the components of the stiffness tensor were calculated. Finally, the Poisson's ratios were estimated from the stiffness tensor.

The only use of ultrasonic-mechanical testing leads to significant errors in the estimation of ν_{23} . Kohlhauser and Hellmich [167] reported a relative error between the measured ν_{23} from ultrasonic-mechanical tests and the one estimated by the combined method higher than 70% in FRPs. Accordingly, the estimation of ν_{23} based on the modal analyses or ultrasonic-mechanical techniques is a current challenge [168].

Baere et al. [169] carried out tensile tests to measure the longitudinal Poisson's ratio (ν_{12}) from a wave cross-ply laminate using a carbon fibre thermoplastic-based composite material. The experimental data showed a clear tendency for ν_{12} to decrease when the longitudinal strain exceeds 0.6%. The authors analysed the influence of the experimental methodology on this tendency. Different tensile loading levels and cycle tests were employed, with different measuring equipment (strain gauges, optical fibre and extensometer). The authors concluded that the relationship between ν_{12} and longitudinal strain, as observed in the experimental data, reflects the material's behaviour rather than any influence from the experimental setup. Yilmaz et al. [170] also analysed the relationship between ν_{12} and the longitudinal strain of different stacking sequences of a glass fibre thermoset-based composite material (stitched fabric technology). Similar experimental setups to those conducted in [169] were employed. The authors concluded that the ν_{12} decreases as the longitudinal strain increases because the transverse microcracks release the compressive strain in the transverse direction.

Alternatively, micro-mechanics FE models can also be employed to estimate ν_{23} . Generally, several loading states are applied to micro-mechanical FE models using characterised constituent materials (fibre and matrix). Then, the Hooke's law and the averaging techniques [171] are applied to the numerical results and the elastic material properties at the meso-scale level can be determined [34, 172]. In addition, micro-mechanical-based

analytical models are used to estimate ν_{23} [173]. Furthermore, out-of-plane material properties can be estimated using inverse identification methods combining experimental data and FE models. Seon et al. [138] carried out an open-hole compressive test using a carbon/epoxy material and DIC equipment to measure the surface strain field. The authors employed an algorithm to minimise the least square error between the DIC-measured strain field and FE models-predicted strains by tuning the elastic material properties of the FE model.

In many works in the literature, the value of the transverse Poisson's ratios is assumed [79, 124, 127, 159], as well as the transverse shear modulus [174]. There is no standardised test to experimentally measure the elastic and plastic values of transverse Poisson's ratios. In the present chapter, a new methodology is proposed to measure the elastic transverse Poisson's ratio in tension (ν_{23T}) and in compression (ν_{23C}) as well as the plastic transverse Poisson's ratio in compression (ν_{23C}^p) from standardised tests for measuring elastic and strength properties [98, 99]. The methodology and data reduction approach is described in [Section 4.1](#), and measured transverse Poisson's ratios are discussed in [Section 4.2](#).

4.1 Material and methods

The analysed material was a carbon fibre-reinforced poly-ether-ether-ketone (PEEK). The consolidated ply thickness of a unidirectional laminate was equal to 0.182 mm and a fibre volume content of 56%. The hot stamping manufacturing process was employed following the manufacturing procedure from the material supplier. All panels were examined through an ultrasound non-destructive inspection using a C-scan technique to ensure good consolidation of the laminates.

The total strain field of each specimen was measured using both strain gauges and DIC equipment. Then, the total strain was decomposed into two components: elastic strain and plastic strain. At the beginning of each test, the total strain was deemed to be elastic strain until the stress-strain relationship was not linear (see [Fig. 4.6](#)). Subsequently, unloaded-reloaded steps were performed in which the external load vanishing, thus the total strain was considered as plastic strain.

4.1.1 Transverse tensile test

The elastic transverse Poisson's ratio in tension (ν_{23T}) was measured from a transverse tensile test. However, the plastic Poisson's ratio in tension could not be obtained from this test since no plastic strains were found. The test was carried out following the ASTM-D3039M standard [98] and using DIC equipment. Three specimens with 25 mm ×

175 mm in-plane dimensions with a stacking sequence of [90]₁₁ were tested. Glass fibre tabs 25 mm long were used at the ends of the specimens to prevent slippage between the tester clamps and the specimens, ensuring a uniform stress field around the clamping tool. The thickness and dimensions of the specimens were verified and accomplished the ASTM-D3039M standard. Therefore, the dimensions and shape of the specimens ensure a uniform strain field along their gauge length.

An electromechanical testing machine MTS Insight50 with a 50 kN capacity using manual grips was employed for the transverse tensile test, see Fig. 4.1a. In addition, a 50 kN MTS load cell calibrated at 100% was used. The tensile test was conducted under displacement control at 2 mm/min at room temperature.



Figure 4.1.: Experimental setup of the transverse tensile (a) and compressive (b) tests.

The DIC equipment was located on the lateral surface of the specimens to measure the total axial strain ($\bar{\varepsilon}_{22}^{DIC}$) (the in-plane direction perpendicular to the fibre dominant direction) and the total out-of-plane strain ($\bar{\varepsilon}_{33}^{DIC}$), see Fig. 4.2a. In addition, two strain gauges located on the in-plane surfaces of the specimens (one on the top face and the other on the bottom face, see Fig. 4.2a) and aligned with the load direction were used. The measurements from the strain gauges were employed to cross-validate the measurement of ε_{22} from the DIC equipment. The specimens were loaded until their failure was reached (see Fig. 4.2c), and the load, the gauge strains and the DIC displacement fields were stored during the test.

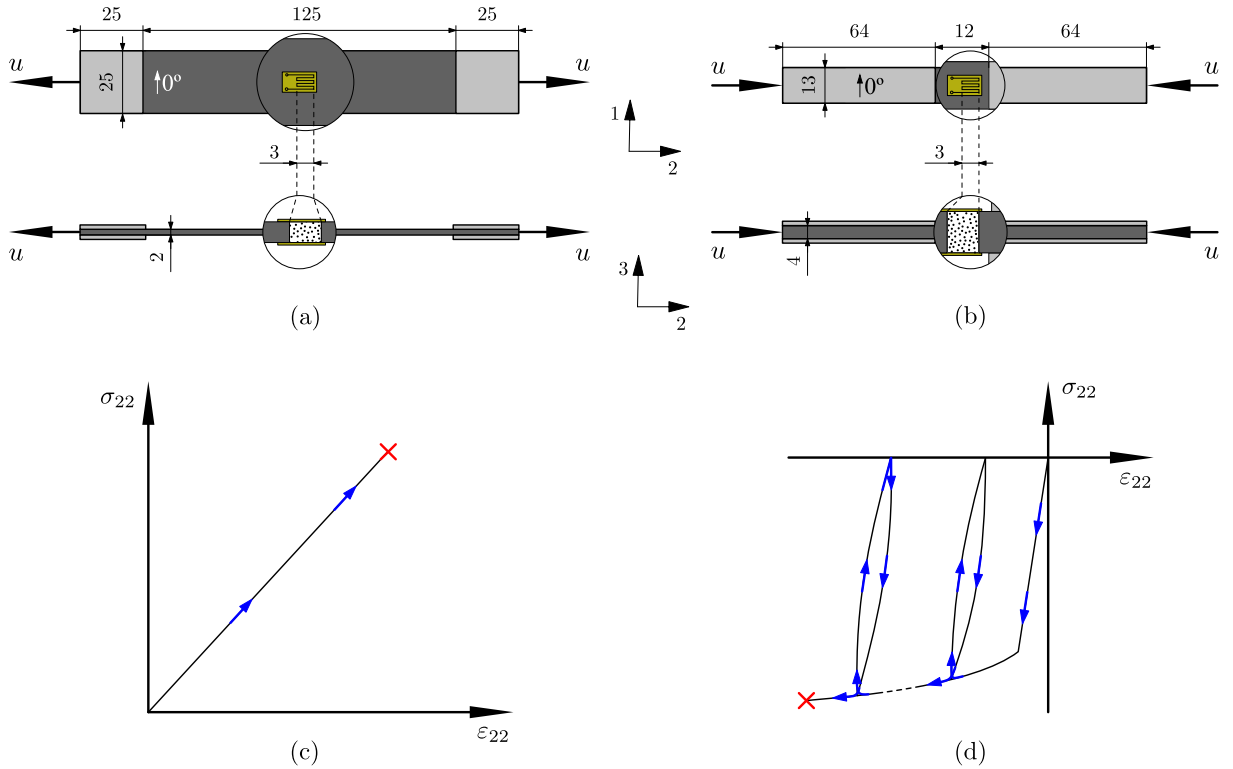


Figure 4.2.: Schematic representation of: a) and c) transverse tensile test, and b) and d) transverse compressive test. 1 refers to the longitudinal direction, and 2 and 3 to the transverse directions. All dimensions are in mm.

4.1.2 Transverse compressive test

The elastic transverse Poisson's ratio in compression (ν_{23C}), as well as in the plastic region (ν_{23C}^p), from a transverse compressive test were measured. The in-plane dimensions of the specimens were 13 mm \times 140 mm, following the ASTM-6641M standard [99]. Three specimens with a stacking sequence of [90]₂₂ were tested. Glass fibre tabs 64 mm long and located on the ends of the specimens to avoid the slippage between the tester clamps and the specimens were added. The dimensions of the specimens meet the requirements of the ASTM-6641M standard. Consequently, the dimensions and shape of the specimens ensure a uniform strain field along their gauge length.

A servo-hydraulic test machine MTS Insight300 with a capacity of 300 kN and an MTS 300 kN load cell calibrated at 100% were used. In addition, the compressive plates and the fixture system from the ASTM-D6641M standard [99] were employed, see Fig. 4.1b. The compressive test was carried out under displacement control at 2 mm/min at room temperature.

As with the tensile test, DIC equipment was located on the lateral surface of the specimens to measure the total axial and out-of-plane strains, see Fig. 4.2b. The axial strain was also measured using two strain gauges (one on the top face and the other on the bottom

face, see Fig. 4.2b) to cross-validate the measurement of ε_{22} from the DIC equipment but also to quantify the percent bending.

In this test, the specimens were loaded under transverse compression until to the onset of the plastic region (when the linearity in the axial stress (σ_{22}) vs. axial strain curve was lost), and the specimens were then unloaded. After that, the specimens were reloaded to increase the plastic strains (ε_{22}^p and ε_{33}^p , axial and out-of-plane plastic strains, respectively), and were then unloaded. This last cycle was repeated until the specimens failed, see Fig. 4.2d. The load in the unloaded steps was not equal to zero. A residual load (approx. 2% of the peak load of the first cycle) was used to prevent readjustment and movements between the specimen clamping tool and the test machine. Otherwise, the DIC measurements can be affected since the relative position between the specimen and the DIC equipment can change. This residual load produces an error relative less than 0.9% in the transverse Poisson's ratios compared with releasing the specimens. Furthermore, the effect of the residual load can be seen in Fig. 4.11a where $\sigma_{22} \approx 0$ at the end of each unloading cycle. In addition, the residual load was held for 15 s, which corresponds to 75 DIC images, to avoid viscous effects due to dynamic loading conditions, see Fig. 4.3. No significant relaxation of the material was observed when the specimens were in the unloaded steps under the residual load, therefore, 15 s a conservative value.

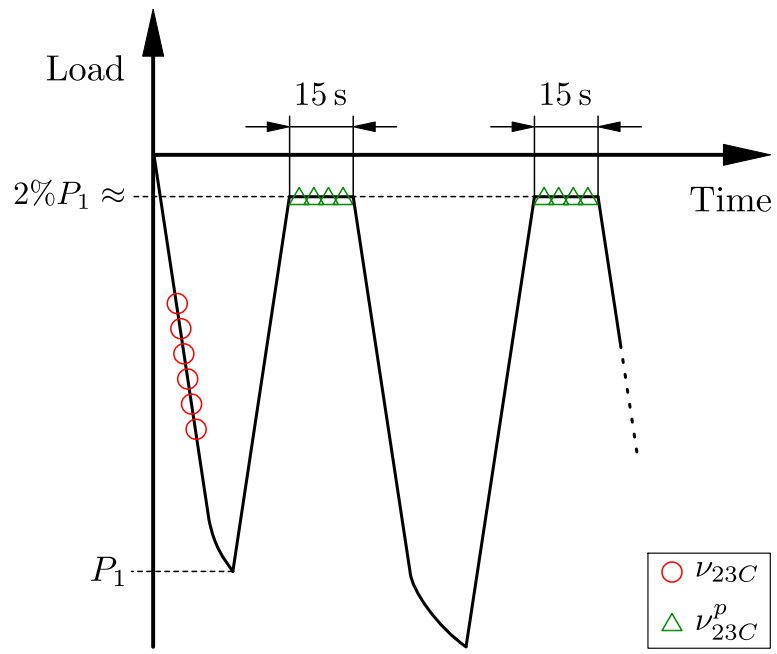


Figure 4.3.: Schematic representation of load vs. time curve of the transverse compressive test. The elastic transverse Poisson's ratio was measured where the red circles are located, and the plastic transverse Poisson's ratio was measured where the green triangles are located.

4.1.3 Instrumentation and data reduction

The data acquisition system used in the proposed method can be divided into two main groups: a QuantumX system to measure the load and the axial strain from strain gauges, and a 2D DIC acquisition system to measure the axial and through-the-thickness strains. The strain gauges used were HBM LY41-3/350. The DIC equipment was composed of a 5 megapixels camera with a 2/3 in. CCD sensor providing 14-bit grayscale images. The lens was selected from the MachVis software for a field of view of 10 mm, resulting in a focal length of 120 mm and two extension tubes of 24 mm and 12 mm. The lens aperture size was set equal to f/11 to avoid lens distortions or diffraction limits [175]. The exposure time was fixed to 8 ms, less than the inverse of the focal length [176]. The solutions2010vic commercial software was used to post-process the data from the DIC equipment with a subset of 77 and a step of 17. Different values of the subset and step were tested and no significant differences were found in the analysed data.

The analysed area of the DIC equipment was similar to the measuring grid of the strain gauges (3 mm × 2.5 mm). The measured strain from a strain gauge is the average value of the strains under its measuring grid [177]. Furthermore, the DIC equipment was centered with respect to the strain gauges, see Fig. 4.2a and b. Therefore, the average values of the DIC axial strain field were compared with the measurements of the strain gauges. The average strain from the DIC equipment was calculated as

$$\bar{\varepsilon}_{ij}^{DIC} = \frac{1}{A_{DIC}} \int_A \varepsilon_{ij}^{DIC} d\Omega_{DIC}, \quad (4.1)$$

where A_{DIC} is the DIC area analysed, Ω_{DIC} refers to the DIC area domain, ε_{ij}^{DIC} is the strain field in the ij direction in the Cartesian coordinate system.

The relative error of the DIC axial strain with respect to the average strain obtained from the two strain gauges was calculated. This relative error in the elastic region was used to test the reliability of the present methodology. In the present work, DIC strain refers to the average value of the strain field obtained from the DIC equipment for the corresponding loading state ($\bar{\varepsilon}_{ij}^{DIC}$).

The elastic transverse Poisson's ratios for both tensile and compressive tests were calculated as

$$\nu_{23} = -\frac{\varepsilon_{33}^e}{\varepsilon_{22}^e}, \quad (4.2)$$

where ε_{22}^e and ε_{33}^e are the axial and out-of-plane elastic strains, respectively. Both strains were obtained from the DIC equipment and the ratio was calculated. The elastic strains

in the compressive test were captured in the first cycle of the σ_{22} vs. ε_{22} curves at the straight part (red circles in Fig. 4.3).

The plastic transverse Poisson's ratio under compression was calculated as

$$\nu_{23C}^p = -\frac{\varepsilon_{33}^p}{\varepsilon_{22}^p}. \quad (4.3)$$

Both plastic strains were obtained from the compressive test in the unloaded steps. DIC strains measured at these unloaded steps were assumed to be plastic strains and used in Eq. (4.3). Therefore, several ν_{23C}^p at each plastic axial strain were measured (green triangles in Fig. 4.3).

The proposed methodology is summarised in Fig. 4.4 for the transverse compressive test. The specimen was loaded under transverse compressive loading stress state before reaching the non-linear relationship in the σ_{22} vs. ε_{22} curve. The strain field of the lateral surface of the specimen was then calculated from the displacement field measured by the DIC equipment. Subsequently, the average of the strain field was calculated with Eq. (4.1) and they were assumed to be elastic strains. Finally, the elastic transverse Poisson's ratio in compression was calculated from Eq. (4.2) and graphical represented as a function of ε_{22}^e , see Fig. 4.4a. Similar procedure was used for ν_{23C}^p when the specimen was unloaded after non-linear σ_{22} - ε_{22} relationship was observed, see Fig. 4.4b. In this case, the DIC strain was assumed to be the plastic strain when no external load was applied. The last cycle was repeated several times.

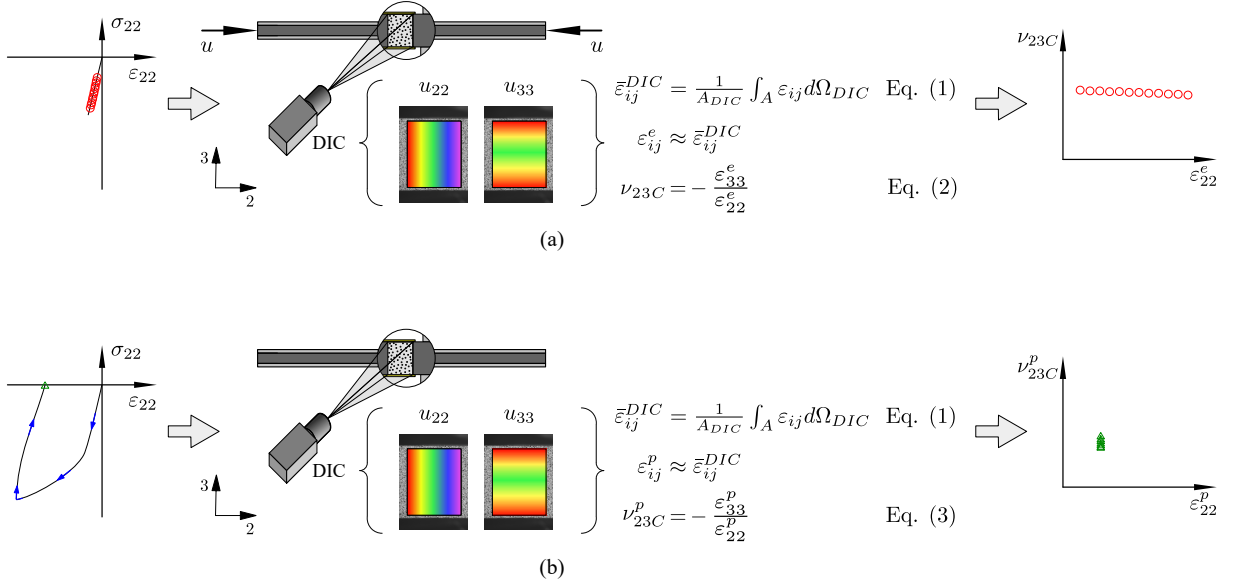


Figure 4.4.: Schematic representation of the procedure to measure the elastic (a) and plastic (b) transverse Poisson's ratios in compression.

Once the tests were finished, the transverse Poisson's ratios were also obtained by performing a linear regression analysis of the corresponding axial strain vs. out-of-plane strain curves. The absolute value of the slopes of the linear regression analyses from each analysis was considered as the corresponding transverse Poisson's ratio. The intercept of the corresponding linear regression was forced equal to zero, since no out-of-plane strain is expected when no axial strain is applied.

The random error of the measured strains from the strain gauges was calculated as

$$\mathbb{E}_{SG} = \pm \Delta \mathbb{E}_{SG}, \quad (4.4)$$

where $\Delta \mathbb{E}_{SG}$ is the accuracy from the data acquisition system plus that of the strain gauges. This accuracy was obtained through a calibration certificate from an external laboratory.

The source of uncertainty for the DIC strain measurements in the elastic region can be divided into two main groups: random error (\mathbb{E}_{rand}) and standard error (\mathbb{E}_{std}). The random error may come from the DIC equipment, the speckle pattern, the lighting, environmental influences, the correlation algorithm [178–180], etc., whereas the standard error is related to the standard deviation of the corresponding strain field ($S_{\bar{\varepsilon}_{ij}^{DIC}}$) in each interval time (DIC image).

The random error from the DIC equipment was quantified as

$$\mathbb{E}_{rand_{ij}} = \pm \Delta \mathbb{E}_{rand_{ij}}, \quad (4.5)$$

where $\Delta \mathbb{E}_{rand}$ is the noise-floor of the DIC measurements. $\Delta \mathbb{E}_{rand_{ij}}$ was estimated for each specimen at the beginning of each test by acquiring the DIC strains over a time period (aprox. 10 seconds, 50 DIC images) when the specimen was unloaded [181, 182]. Therefore, zero strains should be measured in this step since zero displacements were applied. However, all measured DIC strains must result from random error. Consequently, the average value of each DIC strain during this time period was considered to be $2\Delta \mathbb{E}_{rand_{ij}}$ for each direction ($\Delta \mathbb{E}_{rand_{22}}$ for $\bar{\varepsilon}_{22}^{DIC}$ and $\Delta \mathbb{E}_{rand_{33}}$ for $\bar{\varepsilon}_{33}^{DIC}$).

The standard error of the DIC strains in the elastic region was estimated as

$$\mathbb{E}_{std_{ij}} = \pm z_{\alpha/2} \frac{S_{\bar{\varepsilon}_{ij}^{DIC}}}{\sqrt{N_{px}}}, \quad (4.6)$$

where $z_{\alpha/2}$ is the confidence range, and N_{px} refers to the number of pixels of each analysed area with the DIC equipment. A normal distribution of the samples and a level of confidence equal to 95% were assumed ($z_{\alpha/2} = 1.960$). Finally, the Euclidean norm of $\mathbb{E}_{rand_{ij}}$ and $\mathbb{E}_{std_{ij}}$ was proposed to determine the uncertainty of each measured DIC strain in the elastic region,

$$\mathbb{E}_{DIC_{ij}} = \sqrt{\mathbb{E}_{rand_{ij}}^2 + \mathbb{E}_{std_{ij}}^2}. \quad (4.7)$$

The uncertainty of the elastic transverse Poisson's ratios (ν_{23T} and ν_{23C}) from the DIC equipment was estimated as

$$\mathbb{E}_{\nu_{23}} = \left| \frac{\partial \nu_{23}}{\partial \varepsilon_{22}^e} \right| \Delta \mathbb{E}_{rand_{22}} + \left| \frac{\partial \nu_{23}}{\partial \varepsilon_{33}^e} \right| \Delta \mathbb{E}_{rand_{33}}, \quad (4.8)$$

where ε_{22}^e and ε_{33}^e were measured from the tensile test for the uncertainty of ν_{23T} in $\mathbb{E}_{\nu_{23T}}$, or from the compressive test for the uncertainty of ν_{23C} in $\mathbb{E}_{\nu_{23C}}$. The uncertainty of ε_{22}^p was estimated using Eq. (4.7), where the same noise-floors in Eq. (4.5) were used. Moreover, the uncertainty of ν_{23}^p was also quantified using Eq. (4.8) replacing the elastic strains by the plastic strains.

4.2 Results and discussion

The accuracy of the strain gauges and the noise-floor of the DIC equipment from each test are summarised in Table 4.1. The accuracy of the strain gauges is better than that of the DIC equipment. Moreover, there is no clear trend in the DIC accuracy according to the test nor to the strain direction. As will be shown later, the accuracy of the equipments were suitable for the measurements carried out in the present work. Three specimens per each test were used, hence, the rows in the tables and the symbols in the figures represent the results from each specimen tested. The error bars displayed in the figures correspond to the errors explained in Section 4.1.3 and the no significant errors were omitted for the sake of clarity.

Uniform lateral strain fields were observed during the tensile test, see the strain field of ε_{22}^{DIC} and ε_{33}^{DIC} at the same external load ($\bar{\varepsilon}_{22}^{DIC} \approx 0.5\%$) in Fig. 4.5a. However, non-uniform strain fields were measured from the compressive test (see Fig. 4.5b) evidencing that the specimens were undergoing some bending. This misalignment may come from imperfections in the specimens, the test fixture, the testing procedure, etc. Nonetheless, the percent bending for each specimen met the requirements of the ASTM-6641M standard (they were less than $9.3\% < 10\%$). Furthermore, the observed failure modes in the compressive test accomplished the standard.

Table 4.1.: Accuracy of the equipment used in the experimental tests, the different rows represent different specimens.

Measurement instrument			Tensile	Test Compressive
Strain gauges	ΔE_{SG}	($\mu\varepsilon$)		0.28
DIC	$\Delta E_{rand_{22}}$	($\mu\varepsilon$)	13.26	24.07
			5.89	4.05
			6.79	55.90
	$\Delta E_{rand_{33}}$	($\mu\varepsilon$)	33.65	1.94
			19.56	2.78
			7.75	21.53

The elastic axial strain (ε_{22}^e) was captured from 3000 $\mu\text{m}/\text{m}$ to 7500 $\mu\text{m}/\text{m}$ of the total strain, see Fig. 4.6. The values of σ_{22} in Fig. 4.6 have been omitted since the material supplier has proprietary of the data. Within this range, there was enough strain to be properly measured. In the present work, the relative error of the DIC equipment with respect to the strain gauges significantly increases for ε_{22}^e less than 3000 $\mu\text{m}/\text{m}$ (relative error greater than 12.5%). Furthermore, the relative error of the slope from the σ_{22} vs. ε_{22} curve (obtained from the cross-head load cell and the strain gauges, respectively) with respect to the transverse Young's modulus (provided by the material supplier) was less than 6.1% in tension and 0.5% in compression. Therefore, axial strain within 3000 $\mu\text{m}/\text{m}$ and 7500 $\mu\text{m}/\text{m}$ in absolute terms can be assumed to be an elastic strain in both loading states (tension and compression) for the selected material (no plastic strains were considered within this range).

As explained in Section 4.1, the DIC axial strain was compared with the average strain measured from two strain gauges located on the in-plane surfaces of the specimens. The comparison demonstrated the ability of the DIC setup to capture the axial strain in the transverse tensile test, see Fig. 4.7. The DIC axial strain measured from two of the three specimens was greater than that measured from the strain gauges; being greater when ε_{22}^e increases. However, the DIC axial strain from the third specimen was under the gage measurements; being smaller when ε_{22}^e decreases. The relative error of ε_{22}^e for each specimen was calculated, and the highest relative error was less than 12.5%.

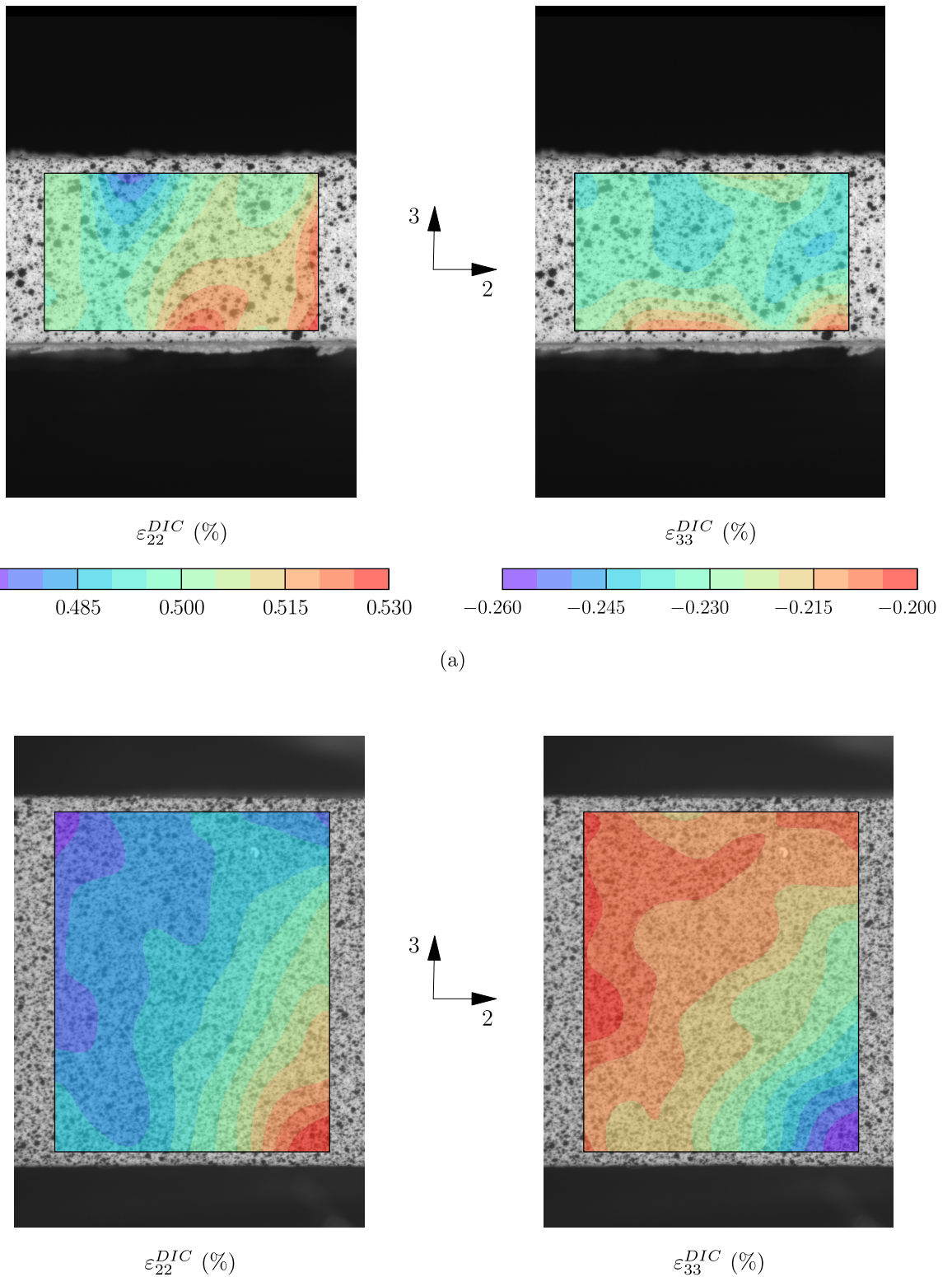


Figure 4.5.: Lateral strain field from the transverse tensile (a) and compressive (b) tests using the DIC equipment at $\text{abs}(\varepsilon_{22}^{DIC}) \approx 0.5\%$. The specimens were loaded in the horizontal direction (2-axis direction).

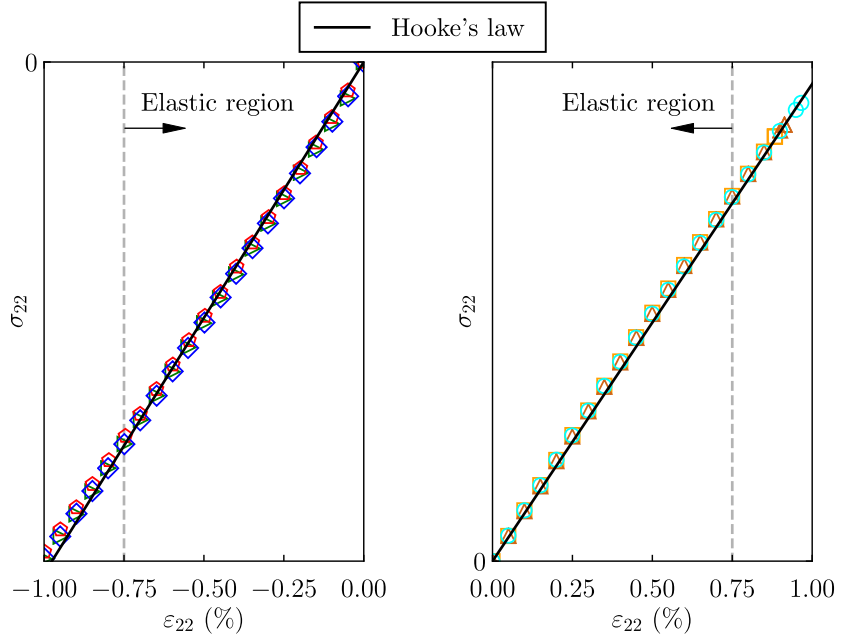


Figure 4.6.: Stress vs. strain curve obtained from the transverse compressive (left) and tensile (right) tests using the average strain from the two strain gauges, the different marks represents different specimens. For the sake of clarity, the error bars are omitted since no significant error was measured.

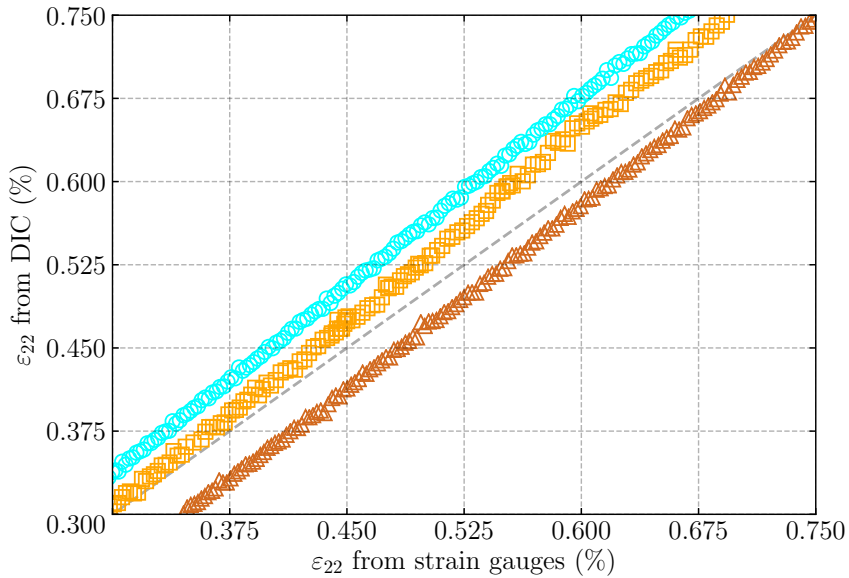


Figure 4.7.: Goodness-of-fit plot of the DIC axial strain vs. average strain measured from the two strain gauges from the transverse tensile test, the different marks represents different specimens. For the sake of clarity, a dashed straight curve with slope equal to 1 is shown and the error bars are omitted since no significant error was measured.

A clear trend of ν_{23T} , obtained from Eq. (4.2), as a function of ε_{22}^e was found in the transverse tensile test, see Fig. 4.8. The transverse Poisson's ratio in tension (ν_{23T}) decreases when elastic axial strain (ε_{22}^e) increases for two of the three specimens tested.

A linear regression analysis using ν_{23T} as a function of ε_{22}^e from all three specimens was performed. The obtained slope (-0.10) of this regression analysis confirms the trend, but it is also noteworthy that a coefficient of variation of ν_{23T} less than 7.9% was observed. This behaviour was also observed in the ν_{12} -longitudinal strain relationship of glass FRP laminates [169, 170]. Yilmaz et al. [170] attributed the reduction of ν_{12} when the longitudinal strain increases due to transverse microcracking. In addition, the coefficient of determination ($R^2 = 1.00$) indicates that ν_{23T} is linearly proportional to ε_{22}^e in the analysed range of ε_{22}^e . The measured errors of ν_{23T} and ε_{22}^e were not significant since the biggest error of ν_{23T} was $\text{IE}_{\nu_{23T}} = 5.06 \times 10^{-3}$ and that of ε_{22}^e was $\text{IE}_{DIC_{22}} = 34.43 \times 10^{-4}\%$.

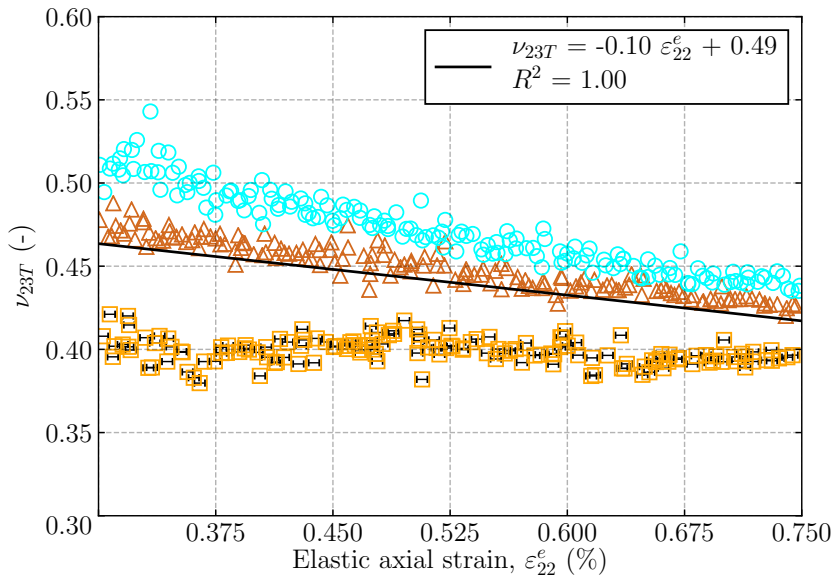


Figure 4.8: Elastic transverse Poisson's ratio in tension vs. DIC elastic axial strain curve, the different marks represents different specimens.

The DIC axial strain measured from the transverse compressive test was also compared with the average strain from the strain gauges in Fig. 4.9. In all the specimens, the DIC axial strain was higher vs. the strain measured using the strain gauges; being smaller when the amount of the compressive ε_{22}^e increases. The highest relative error was less than 6.2%. Therefore, the DIC equipment also properly measured ε_{22} in the transverse compressive test.

As for ν_{23T} , a similar trend is obtained from the measured ν_{23C} using Eq. (4.2) in all three specimens, see Fig. 4.10. The transverse Poisson's ratio measured in compression (ν_{23C}) decreases when the amount of compressive elastic axial strain (ε_{22}^e) increases. In addition, a linear regression analysis was also carried out of ν_{23C} vs. ε_{22}^e using the measured values from all three specimens. The slope (0.11) of this regression analysis confirms this trend,

but it is also noteworthy that a coefficient of variation of ν_{23C} less than 4.3% was observed. Furthermore, the coefficient of determination ($R^2 = 1.00$) also indicates that ν_{23C} is linearly proportional to ε_{22}^e in the analysed range of ε_{22}^e . Again, the measured errors of ν_{23C} and ε_{22}^e were not significant since the biggest error of ν_{23C} was $\mathbb{E}_{\nu_{23C}} = 2.30 \times 10^{-2}$ and that of ε_{22}^e was $\mathbb{E}_{DIC_{22}} = 26.26 \times 10^{-4}\%$. It is worth mentioning that the elastic transverse Poisson's ratio does not follow a linear dependency of the axial strain when $\varepsilon_{22}^e = (-0.3, 0.3)\%$, since the intercepts of Figs. 4.8 and 4.10 are different.

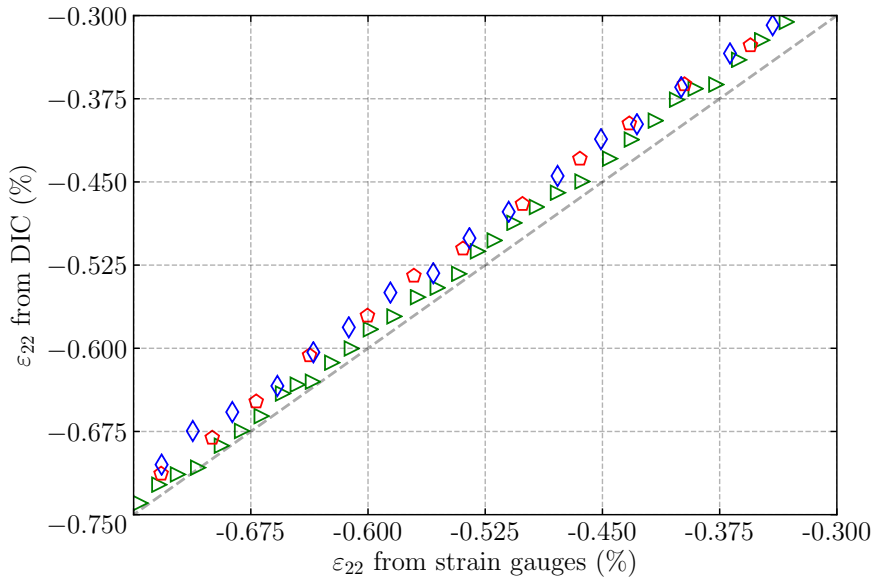


Figure 4.9.: Goodness-of-fit plot of the DIC axial strain vs. average strain measured from the strain gauges from the transverse compressive test, the different marks represents different specimens. For the sake of clarity, a dashed straight curve with slope equal to 1 is shown and the error bars are omitted since no significant error was measured.

The elastic Poisson's ratio in compression (ν_{23C}) was also measured from the rest of the cycles performed in the transverse compressive tests, the results of Figs. 4.9 and 4.10 correspond to the elastic region of the first cycle under loading conditions. The elastic transverse strains (ε_{22}^e and ε_{33}^e) of the remaining cycles were estimated by subtracting the corresponding plastic strains from the total strains measured by the DIC equipment under equal stress level, see Fig. 4.11a where the zoom corresponds to the referenced stress range. No significant differences were observed in ν_{23C} between the different cycles before to plastic strains, see Fig. 4.11b from the first cycle to the third cycle. A relative error less than 5% was obtained of ν_{23C} from the remaining cycles with respect to ν_{23C} from the loading region of the first cycle when no significant plastic strains were observed. Additionally, the value of ν_{23C} obtained from the loading region of each cycle was lower than the that measured from the unloading region of the same cycle. Moreover, the latter being much larger than ν_{23C} obtained in the loading region of the first cycle.

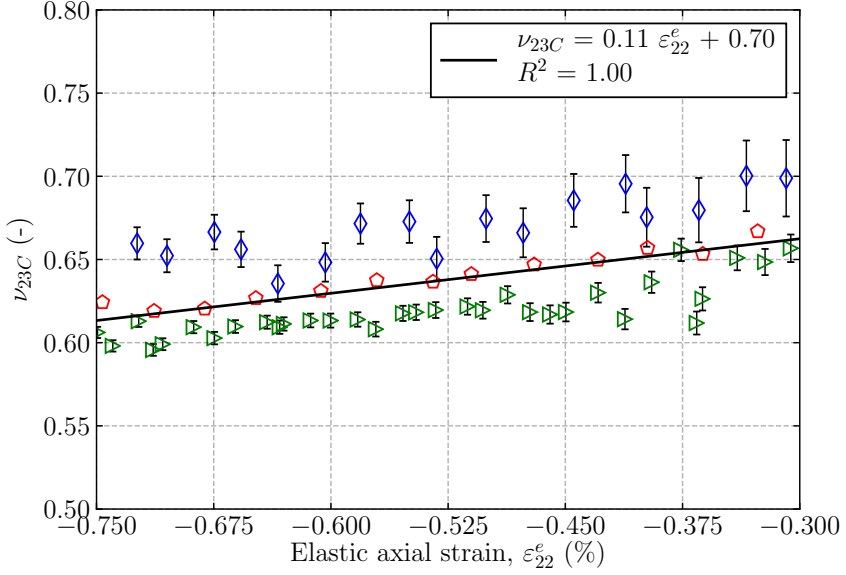


Figure 4.10.: Elastic transverse Poisson's ratio in compression vs. DIC elastic axial strain curve, the different marks represents different specimens.

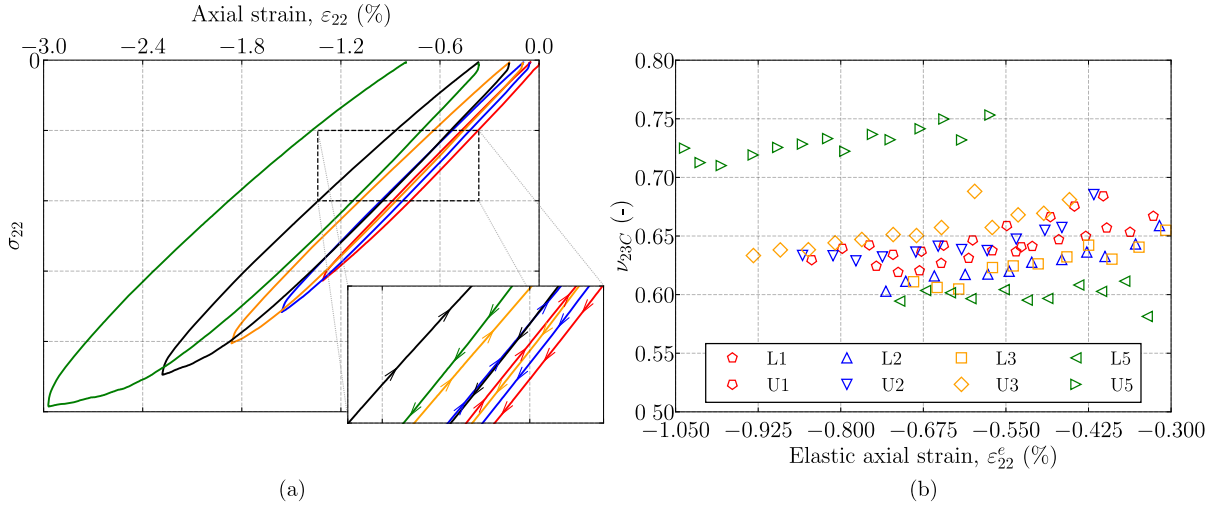


Figure 4.11.: Stress vs. strain curve from the transverse compressive test (a) and elastic transverse Poisson's ratio in compression vs. DIC elastic axial strain from different loading cycles (b). The results presented correspond to values from a single specimen, and L refers to loading region, U refers to unloading region and the number to the cycle.

Regarding ν_{23C}^p , plastic dilatancy was observed when the amount of compressive plastic axial strain was significantly increased ($\nu_{23C}^p > 1$ when $\varepsilon_{22}^p < -1\%$) by assuming no plastic strain in the longitudinal direction ($\varepsilon_{11}^p = 0$) [124, 159, 160], see Fig. 4.12. Therefore, the analysed material behaves as a frictional material since plastic dilatancy is evidenced, i.e., volume increases due to the deviatoric plastic strain. A linear regression analysis of ν_{23C}^p vs. ε_{22}^p was performed. The intercept (1.00) of this regression analysis suggests

that the analysed material presents no volumetric plastic strains ($\nu_{23C}^p \approx 1$) at small axial plastic strain by assuming no plastic strain in the longitudinal direction. In addition, the coefficient of determination ($R^2 = 1.00$) and the slope (-0.05) confirm that the plastic transverse Poisson's ratio (ν_{23C}^p) linearly increases when the amount of the compressive plastic axial strain (ε_{22}^p) increases, see Fig. 4.12.

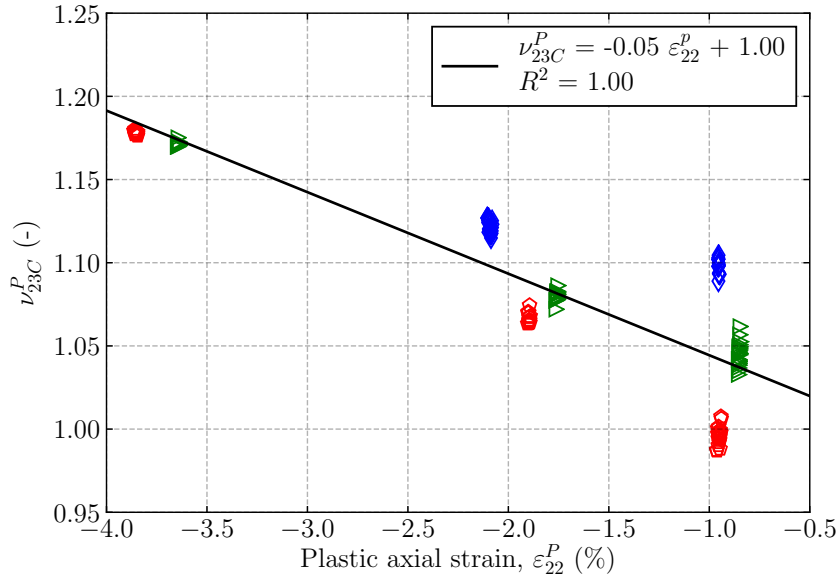


Figure 4.12.: Plastic transverse Poisson's ratio in compression vs. DIC plastic axial strain curve measured from the transverse compressive test, the different marks represents different specimens. The error bars are omitted since no significant error was measured

Table 4.2 summarises the transverse Poisson's ratios obtained from the corresponding linear regression analysis of the corresponding $\bar{\varepsilon}_{33}^{DIC}$ vs. $\bar{\varepsilon}_{22}^{DIC}$ curve. The comparison of ν_{23C} with ν_{23T} shows that $\nu_{23C} > \nu_{23T}$, which indicates different behaviour depending on the loading direction (compression or tension). In the elastic region, a higher expansion was observed in compression than contraction in tension, which is in agreement with the results reported by Khaled et al. [161]. In addition, the values of the elastic transverse Poisson's ratios (ν_{23C} and ν_{23T}) are similar to those reported in literature for CFRPs [161].

All the studied Poisson's ratios (ν_{23T} , ν_{23C} and ν_{23C}^p) in Table 4.2 are greater than the longitudinal Poisson's ratio ($\nu_{12} = 0.34$) in the ranges of the corresponding analysed axial strain. The same observation was found when the transverse Poisson's ratios were obtained using Eq. (4.2) or Eq. (4.3) (Figs. 4.8 and 4.10). As expected, the contraction in tension is lower in the longitudinal direction than that obtained in the transverse direction ($\nu_{12} < \nu_{23T}$), due to the stiffness of the fibres.

Table 4.2.: Transverse Poisson's ratio obtained from the corresponding linear regression analysis of $\bar{\varepsilon}_{33}^{DIC}$ vs. $\bar{\varepsilon}_{22}^{DIC}$, the different rows represent different specimens.

ν_{23T} (-)	ν_{23C} (-)	ν_{23C}^P (-)
0.39	0.61	1.16
0.44	0.63	1.15
0.46	0.66	1.12

Lempriere [183] established the thermodynamically admissible conditions for transversally isotropic materials. The conditions prevent negative energy when the material is loaded. The rules were defined as a function of the elastic material properties. The elastic transverse Poisson's ratios reported in this chapter met these thermodynamic requirements of positive strain energy.

Failure envelope shape definition

The failure criteria developed for FRP laminates can be divided into two main groups: i) polynomial criterion, and ii) failure criteria related to failure mechanisms. The polynomial criterion cannot distinguish the failure mechanism and does not consider fibre-matrix interface phenomena. In addition, the formulation of the polynomial criterion is reduced to a mathematical expression as a function of different material properties such as unidirectional strengths. However, the failure criteria related to failure mechanisms take into account the possible failure mechanisms using a mathematical expression for each of them. Most of them are developed by considering plane stress conditions at the lamina level.

Hill [184] generalised the Von Mises yield for anisotropic metallic materials and Tsai [185] employed it in FRP laminates. This polynomial criterion (Tsai-Hill criterion) does not distinguish between the tensile and compressive strengths. Therefore, Tsai-Hill criterion is not adequate for materials with different tensile and compressive behaviours, such as FRP structures. Tsai et al. [75] extended the Tsai-Hill criterion to account for different strengths in tension and compression (Tsai-Wu criterion). This is the most general criterion and can be particularised to obtain all the polynomial.

The maximum stress failure criteria predicts the failure at certain direction (longitudinal, transverse, shear, etc.) when the stress state reaches the maximum allowable value. No interaction between the stress components are considered and, thus, no accurate predictions are obtained under multiaxial loading conditions. The maximum strain failure criteria is comparable to the maximum stress but at the strain level.

The Hashin failure criteria, developed by Hashin [83], distinguish between different failure mechanisms, including longitudinal tensile and compressive modes, as well as transverse tensile and compressive modes. These failure criteria are quadratic criteria and were developed based on the first four transverse isotropic stress invariants, as they are defined in Eqs. (2.5)–(2.8). The quadratic failure criterion for matrix cracking implies that the plane of fracture is the maximum transverse shear plane, which may not always be the case.

The Puck [82] and LaRc [84, 85] failure criteria address the limitation of the Hashin criteria. They are based on experimental observations and micro-mechanics models, as well as the Mohr-Coulomb failure criteria [186], which combines normal and shear stresses on the fracture plane. Under normal tensile stress conditions, fracture is caused by both the tensile and shear stresses. However, the fracture plane is promoted at a certain

fracture angle under normal compressive stress due to shear stresses. The Puck and LaRC failure criteria distinguish between fibre failure and matrix cracking and require complex experimental tests to fully calibrate their shape parameters.

Recently, Camanho et al. [123] proposed a quadratic failure criteria for unidirectional FRP laminates based on the Puck and LaRC criteria. The criteria distinguish between fibre failure and matrix cracking. The fracture plane under compression is oriented with respect to the angle that maximises the fibre kinking failure index. The proposed criteria are capable of fitting the available experimental data in the literature. Further analysis is needed to demonstrate its capabilities under stress conditions where the criteria have not been tested. For instance, the failure criteria is not tested under longitudinal compressive loads combined with transverse compressive stress states.

Several failure criteria have been proposed for FRP laminates, but none have been identified as optimal in terms of accurate predictions compared with others. All current criteria have limitations that prevent generalisation to all types of composites, applications or loading conditions. Most failure criteria have been formulated for unidirectional FRP laminates (woven and textile laminates being considered as combinations of different unidirectional plies).

Based on the previous literature observations, a numerical study is carried out to analyse the influence of the failure criteria on the strength under complex loading conditions. [Section 5.1](#) presents the calibration guidelines for the failure shape envelope coefficients of the constitutive model proposed in this thesis and their bounds are presented in [Section 5.2](#). Finally, different envelope shape coefficients are proposed and their effect on the remote failure strength of FHC tests is analysed in [Section 5.3](#).

5.1 Calibration of the envelope shape coefficients

The calibration of the envelope shape coefficients of the plasticity and damage model for FRP laminates is described in this section. First, the identification of the failure envelope shape coefficients is presented. Then, the same assumptions and approach can be used to estimate the plastic envelope shape coefficients replacing the strengths by the corresponding yield stresses.

The envelope shape coefficient μ_t controls the failure in the transverse shear direction (S_T), but also in the biaxial tensile (Y_{TB}) and compressive (Y_{CB}) directions, see Fig. 2.3a. This parameter (μ_t) can be calculated using the following expressions:

$$\mu_t(S_T) = \left(\frac{S_T(Y_C + Y_T)}{Y_C Y_T} \right)^2 - 1, \quad (5.1)$$

$$\mu_t(Y_{TB}) = \frac{(Y_C Y_T - Y_{TB}(Y_C - Y_T))^2}{Y_{TB}^2(Y_C + Y_T)^2 - (Y_C Y_T - Y_{TB}(Y_C - Y_T))^2}, \quad (5.2)$$

or

$$\mu_t(Y_{CB}) = \frac{(Y_C Y_T - Y_{CB}(Y_T - Y_C))^2}{Y_{CB}^2(Y_C + Y_T)^2 - (Y_C Y_T - Y_{CB}(Y_T - Y_C))^2}, \quad (5.3)$$

where the expressions are obtained when $F_t = 0$ and applying a pure transverse shear stress state or the corresponding pure biaxial loading state, respectively. Significant difficulties occur when testing composite materials under transverse shear or biaxial loading [69]. Fenner and Daniel [187] proposed a methodology for transverse shear loading using a sandwich-beam under three-point bending test. Otherwise, S_T can be estimated from [136] as

$$S_T = \frac{Y_C}{2 \tan(\alpha_0)}, \quad (5.4)$$

assuming that the damage (or plasticity) occurs in the plane of maximum longitudinal shear stresses, where the value experimentally obtained of the angle of this plane (α_0) is approximately equal to 53° [188].

The failure envelope for the $\tilde{\sigma}_{22} - \tilde{\sigma}_{12}$ effective stress space is defined using $\mu_{s\ell}$, see Fig. 2.3b. This parameter can be calibrated by imposing that the slope at $\tilde{\sigma}_{22} = 0$ must be equal to the longitudinal matrix friction coefficient η_ℓ , as the Coulomb fracture line in the Mohr-Coulomb criterion. Therefore, the coefficient reads

$$\mu_{s\ell} = \frac{2\eta_\ell Y_C Y_T + S_L(Y_C - Y_T)}{4\eta_\ell Y_C Y_T}, \quad (5.5)$$

η_ℓ can be approximated from [188] as

$$\eta_\ell \approx -\frac{S_L \cos(2\alpha_0)}{Y_C \cos(\alpha_0)}. \quad (5.6)$$

Alternatively, $\mu_{s\ell}$ can be estimated from off-axis tests by fitting the failure envelope (or yield surface) shape with the experimental data. Moreover, from the yield surfaces reported by Daniel [80] and failure envelopes from [80, 123, 136], $\mu_{s\ell}$ and $\mu_{s\ell p}$ must be defined close to one.

The envelope shape coefficients η_t and η_t^q are the coefficients of the linear and quadratic terms, respectively, related to the hydrostatic transverse pressure (\tilde{p}_t) in $\phi_{\ell C}$. Therefore, they define the failure envelope for the $\tilde{\sigma}_{11} - \tilde{\sigma}_{22}$ effective stress space, see Fig. 2.3c. The experiments carried out by Soden et al. [97] suggest that these two parameters can be estimated for CFRPs as

$$\begin{aligned}\eta_t &= \frac{X_C(Y_C - Y_T)}{Y_C Y_T} \\ \eta_t^q &= \left(\frac{X_C(Y_C + Y_T)}{Y_C Y_T} \right)^2.\end{aligned}\quad (5.7)$$

Moreover, others envelopes can be defined, such as the slope equals to Y_T/X_C , where

$$\begin{aligned}\eta_t &= \frac{2X_C}{Y_T} \\ \eta_t^q &= 0.\end{aligned}\quad (5.8)$$

The linear and quadratic terms related to the longitudinal shear stresses in $\phi_{\ell C}$ are $\eta_{s\ell}$ and $\eta_{s\ell}^q$, respectively. They define the failure envelope for the $\tilde{\sigma}_{11} - \tilde{\sigma}_{12}$ effective stress space, see Fig. 2.3d. They can be tuned for CFRPs from the experimental data reported by Soden et al. [97] as

$$\begin{aligned}\eta_{s\ell} &= \frac{X_C}{2S_L} \\ \eta_{s\ell}^q &= 0,\end{aligned}\quad (5.9)$$

hence, the slope is defined as $2S_L/X_C$. Furthermore, others envelopes can be defined: with the slope equals to S_L/X_C , where

$$\begin{aligned}\eta_{s\ell} &= \frac{X_C}{S_L} \\ \eta_{s\ell}^q &= 0;\end{aligned}\quad (5.10)$$

or with perfect parabolic curve, where

$$\begin{aligned}\eta_{s\ell} &= 0 \\ \eta_{s\ell}^q &= \left(\frac{X_C}{S_L} \right)^2.\end{aligned}\quad (5.11)$$

Alternatively, the failure envelopes (or yield surfaces) can be estimated from the simulation of a representative cell (modelling polymer and fibres) under multiple multi-axial loading

conditions combined with a data-driven approach [189, 190]. After that, the envelope shape coefficients can be adjusted.

5.2 Bounds of the envelope shape coefficients

The bounds of the shape coefficients of the failure envelope are presented in this section. The bounds of the shape coefficients of the plasticity modelling can be calculated using the same assumptions and approach. The loading functions in Eqs. (2.26)–(2.28) are proposed to be used with null or positive values of the failure envelope shape coefficients. Consequently, the shape coefficients of the $\tilde{\sigma}_{22} - \tilde{\sigma}_{33}$ and $\tilde{\sigma}_{22} - \tilde{\sigma}_{12}$ effective stress spaces (μ_t and $\mu_{s\ell}$, respectively) must be defined equal to or greater than zero. Therefore, the bounds of the plastic envelope shape coefficients μ_{tp} and $\mu_{s\ell p}$ must be also defined non-negative.

The shape coefficients η_t and η_t^q define the failure envelope for the $\tilde{\sigma}_{11} - \tilde{\sigma}_{22}$ effective stress space. Specifically, η_t and η_t^q correspond to the linear and quadratic coefficients, respectively, of the terms of \tilde{p}_t in $\phi_{\ell C}$ defined in Eq. (2.27). The upper bound of η_t is determined by matching $\phi_{\ell C} \leq \phi_t$ and evaluating it with all effective stress components equal to zero except for $\tilde{\sigma}_{22} > 0$. This allows to prevent a discontinuity in the failure envelope in the intersection of these loading functions at $\tilde{\sigma}_{11} = 0$ and $\tilde{\sigma}_{22} > 0$, see Fig. 5.1a. Consequently, the upper bound of η_t yields

$$\eta_t \leq \frac{2X_C}{Y_T} - \sqrt{\eta_t^q}. \quad (5.12)$$

Subsequently, the lower bound of η_t is also defined by matching $\phi_{\ell C} \leq \phi_t$ but evaluating it with all effective stress components equal to zero except for $\tilde{\sigma}_{22} < 0$. In this case, the continuity of the failure envelope at $\tilde{\sigma}_{11} = 0$ and $\tilde{\sigma}_{22} < 0$ is ensured with

$$\eta_t \geq \sqrt{\eta_t^q} - \frac{2X_C}{Y_C}, \quad (5.13)$$

see Fig. 5.1b. Therefore, the bounds of η_t are defined as a function of the strength material properties and η_t^q .

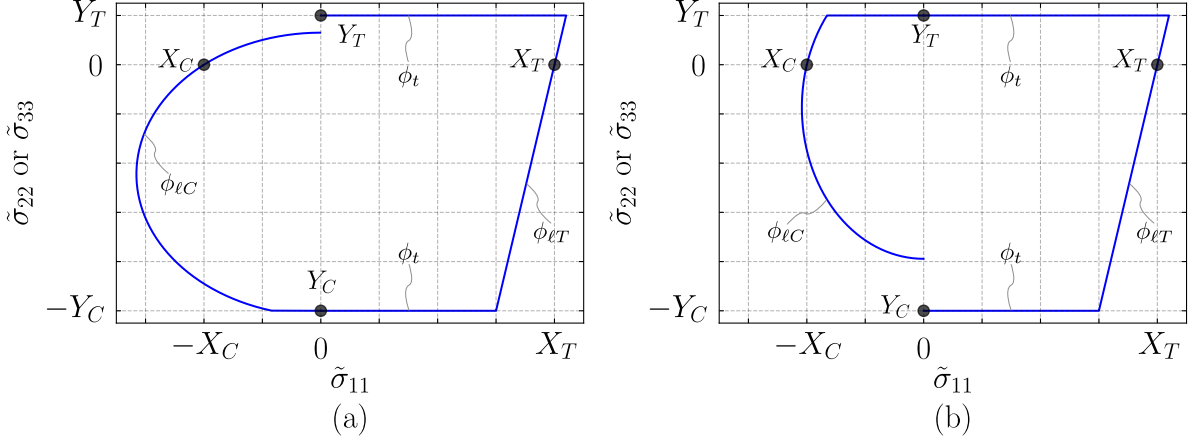


Figure 5.1.: Schematic representation of the failure envelope for the $\tilde{\sigma}_{22} - \tilde{\sigma}_{33}$ effective stress space with discontinuity: a) $\eta_t > \frac{2X_C}{Y_T} - \sqrt{\eta_t^q}$, and b) $\eta_t < \sqrt{\eta_t^q} - \frac{2X_C}{Y_C}$.

The failure envelope for the $\tilde{\sigma}_{11} - \tilde{\sigma}_{12}$ effective stress space is defined by $\eta_{s\ell}$ and $\eta_{s\ell}^q$. These shape coefficients correspond to the linear and quadratic coefficients, respectively, of the terms of $\tilde{\tau}_\ell$ in $\phi_{\ell C}$ defined in Eq. (2.27). The bounds of $\eta_{s\ell}$ are defined by evaluating $\phi_{\ell C} \leq \phi_t$ with all effective stress components equal to zero except for $|\tilde{\sigma}_{12}| > 0$ due to the symmetry of the failure envelope in this effective stress space. This avoids a discontinuity in the failure envelope at the intersection of these loading functions at $\tilde{\sigma}_{11} = 0$ and $|\tilde{\sigma}_{12}| > 0$, see Fig. 5.2. Consequently, the bounds of $\eta_{s\ell}$ are

$$|\eta_{s\ell}| \leq \frac{X_C}{S_L} - \sqrt{\eta_{s\ell}^q}, \quad (5.14)$$

due to the symmetry of $\tilde{\sigma}_{11} - \tilde{\sigma}_{12}$ effective stress space with respect to the $\tilde{\sigma}_{11}$ -axis. Therefore, the bounds of $\eta_{s\ell}$ are defined as a function of the strength material properties and $\eta_{s\ell}^q$.

Finally, the bounds of the plastic envelope shape coefficients are

$$\begin{aligned} \mu_{tp} &\in \mathbf{R}^+ \\ \mu_{s\ell p} &\in \mathbf{R}^+, \end{aligned} \quad (5.15)$$

and the bounds of the plastic potential envelope shape coefficients are

$$\begin{aligned} \hat{\mu}_{tp} &\in \mathbf{R}^+ \\ 0 \leq \hat{\mu}_{s\ell p} &\leq 1. \end{aligned} \quad (5.16)$$

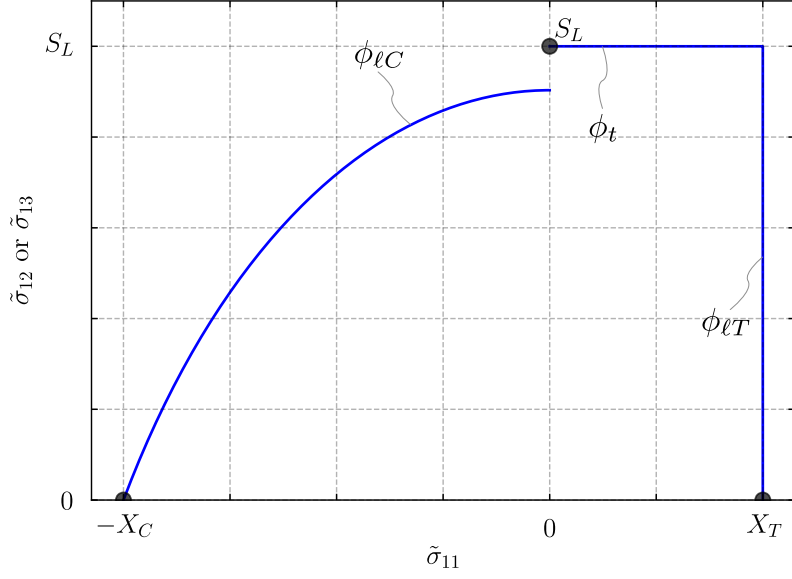


Figure 5.2.: Schematic representation of the failure envelope for the $\tilde{\sigma}_{11} - \tilde{\sigma}_{12}$ effective stress space with discontinuity $|\eta_{s\ell}| > \frac{X_C}{S_L} - \sqrt{\eta_t^q}$.

The condition of $\hat{\mu}_{s\ell p}$ is defined to guarantee the convexity of the plastic potential function. The bounds of the failure envelope shape coefficients are

$$\begin{aligned}
 \mu_t &\in \mathbf{R}^+ \\
 \mu_{s\ell} &\in \mathbf{R}^+ \\
 \sqrt{\eta_t^q} - \frac{2X_C}{Y_C} &\leq \eta_t \leq \frac{2X_C}{Y_T} - \sqrt{\eta_t^q} \\
 \eta_t^q &\in \mathbf{R}^+ \\
 |\eta_{s\ell}| &\leq \frac{X_C}{S_L} - \sqrt{\eta_{s\ell}^q} \\
 \eta_{s\ell}^q &\in \mathbf{R}^+.
 \end{aligned} \tag{5.17}$$

Therefore, the following constraints are also imposed in Eq. (5.17),

$$\begin{aligned}
 \eta_t^q &\leq \left(\frac{X_C(Y_C + Y_T)}{Y_C Y_T} \right)^2 \\
 \eta_{s\ell}^q &\leq \left(\frac{X_C}{S_L} \right)^2.
 \end{aligned} \tag{5.18}$$

5.3 Influence of the failure envelope on the failure strength of filled-hole compressive laminates

As explained before, aeronautical components are usually certified following the building block approach [2, 21, 22]. FHC tests are commonly conducted to characterise the compressive strength with a filled-hole for determining the design allowable values that drive the design at the higher levels [191]. These tests are complex due to the presence of the bolt, which leads to significant out-of-plane stresses and complex failure mechanisms. Therefore, the FHC test is selected in this analysis due to its importance in the design of aeronautical structures and corresponds to a structural detail test.

Firstly, the experimental test campaign is described. Secondly, the FE modelling strategy is presented. Finally, the numerical analysis is carried out by comparing numerical predictions with different failure envelope shape coefficients and experimental data.

5.3.1 Experimental campaign

In this section, numerical predictions are compared to experimental data from Airbus' database. The experimental test campaign consisted in FHC tests of a CFRP system. It is important to note that the experimental test campaign were not carried out in this thesis; only their experimental data are used. The experiments were carried out by Airbus following the AITM 1-0008 internal standard. Firstly, the carbon/epoxy specimens were assembled with the corresponding bolt and nut, and a preload to the bolt and nut was then applied. After that, the assembly was installed in a universal testing machine, by fixing the ends of the specimen. Tabs were used to prevent slippage between the tester clamps and the specimens. Finally, a compressive load at the upper end was applied until the assembly collapses. In all cases analysed in this work, the assembly failed due to carbon/epoxy failure (the bolt and nut did not present any apparent damage at the macro-scale level).

Different stacking sequences were tested to evaluate the robustness of the present analysis and their conclusions. In addition, different laminate thickness, hole diameters, specimen widths, bolt metrics and preloads were explored. The gauge length of the specimens was as short as possible (between 21 mm and 32 mm, similar to the width) to avoid buckling. The stacking sequences cannot be revealed due to confidentiality. Hence, for better understanding, [Table 5.1](#) presents the percentage of plies oriented at each angle (θ). The 0° angle was oriented with the longitudinal axis of the specimen, which also corresponds with the loading direction. Based on their stacking sequences, the specimens

can be grouped as: i) quasi-isotropic laminates (QI), ii) laminates with a high number of $\theta = 0^\circ$ plies (FI), and (iii) laminates with a high number of $\theta = \pm 45^\circ$ plies (SH).

Table 5.1.: Configurations of the filled-hole compressive tests analysed.

Configuration	$0^\circ / \pm 45^\circ / 90^\circ$	Hole diameter (mm)	Width (mm)	Number of plies	Preload (N)
SH-12np	16/68/16	5.02	22	12	3247
SH-10np	20/40/40	5.02	22	10	3247
QI-W19	25/50/25	4.15	19	16	3805
QI-W22	25/50/25	5.02	22	16	3247
QI-W25	25/50/25	5.80	25	16	6498
QI-W22P	25/50/25	4.84	22	16	5338
FI-22np	45/55/0	6.35	32	22	12950
FI-24np	50/40/10	6.35	32	24	12950

All specimen configurations, following the nomenclature explained above, are defined in [Table 5.1](#). The same hole diameter, width and preload was used in the SH laminates, but different stacking sequences and number of plies, with the SH-12np having more plies (12np refers to 12 plies). The same stacking sequence was used in all the QI laminates, but the hole diameter and preload were different. The QI-W19, QI-W22 and QI-W25 laminates have different hole diameters, widths and preloads. The QI-W22 and QI-W22P configurations have the same width (22 mm), but higher preload was applied to the QI-W22P case (here, W refers to the width and P to the higher preload compared with QI-W22). The FI configurations were defined with the same hole diameter, width and preload, but different stacking sequences and number of plies. A minimum of four specimens were tested per configuration.

5.3.2 Finite element modelling strategy

In the present chapter, the failure strength and the failure pattern of the FHC tests are predicted using FE models with the enhanced constitutive model presented in [Chapter 3](#). The FE models are developed following the approach explained in [Section 2.4](#). [Table 5.2](#) summarises the tests carried out to characterise the model input parameters of the selected carbon/epoxy material. Note that the input values cannot be disclosed for confidentiality reasons.

The constitutive model used requires five elastic material properties to reproduce the elastic behaviour of composite materials: three elastic modulus and two elastic Poisson's ratios. They are measured from longitudinal and transverse tensile tests and an in-plane shear tensile test, except for the transverse elastic Poisson's ratio (ν_{23}). No significant effect of ν_{23} on the failure strength of open-hole tests is observed in [Section 2.4](#) and, thus,

this material property for the analysed material is assumed here to be $\nu_{23} = 0.45$, which is a common value for aeronautical CFRPs [161, 192].

Table 5.2.: Tests carried out to determine the model input parameters for the carbon/epoxy unidirectional prepreg system used.

	Description	Symbol	Test
Elastic	Longitudinal Young's modulus	E_{11}	EN 2561B [193]
	Transverse Young's modulus	E_{22}	EN 2597B [194]
	Longitudinal shear's modulus	G_{12}	AITM 1.0002
	Longitudinal Poisson's ratio	ν_{12}	EN 2561B [193]
	Transverse Poisson's ratio	ν_{23}	Assumed
Plastic	Transverse compressive yield stress curve	Y_{CP}	EN 2850B [195]††
	Transverse tensile yield stress curve	Y_{TP}	EN 2597B [194]††
	Longitudinal shear yield stress curve	S_{LP}	AITM 1.0002††
	Plastic Poisson's ratios	ν_{23T}^p, ν_{23C}^p and ν_{122}^p	Assumed
Damage	Longitudinal tensile strength	X_T	EN 2561B [193]
	Shape of the longitudinal tensile softening law	f_{X_T} and $f_{\mathcal{G}_{X_T}}$	DENT [107]*
	Longitudinal tensile fracture toughness	\mathcal{G}_{X_T}	DENT [107]
	Longitudinal compressive strength	X_C	EN 2850B [195]
	Longitudinal compressive fracture toughness	$f_{\mathcal{G}_{X_C}} \mathcal{G}_{X_C}$	DENC [108]
	Shape of the longitudinal compressive softening law	f_{X_C} and $f_{\mathcal{G}_{X_C}}$	DENC [108]*
	Transverse tensile strength	Y_T	EN 2597B [194]
	Transverse tensile fracture toughness	\mathcal{G}_{Y_T}	AITM 1-0005‡
	Transverse compressive strength	Y_C	EN 2850B [195]
	Transverse compressive fracture toughness	\mathcal{G}_{Y_C}	Assumed
	Longitudinal shear strength	S_L	AITM 1.0002
	Longitudinal shear fracture toughness	\mathcal{G}_{S_L}	AITM 1-0006‡

†† Assuming no damage occurs until the specimen fails, the plastic strain can then be calculated by subtracting the elastic strain, as the ratio of stress to Young's modulus, from the total strain.

* Inversely identified using finite element simulations.

‡ Assuming that the intralaminar fracture toughness is equivalent to the interlaminar fracture toughness.

Three hardening curves are needed to predict the plastic strain, obtained from: a transverse compressive test, a transverse tensile test and an in-plane shear tensile test. In addition, the plastic Poisson's ratios are also needed to define the evolution of the plastic strains. No volumetric plastic strains are considered, therefore, the transverse plastic Poisson's ratios are defined equal to 1 and $\nu_{122}^p = 0$ (no plastic strains are considered in the longitudinal direction).

The ply strengths are obtained from: longitudinal compressive and tensile tests, transverse compressive and tensile tests, and an in-plane shear tensile test. The longitudinal compressive and tensile fracture toughnesses are obtained from double edge notched compressive and tensile (DENC and DENT, respectively) tests [107, 108], respectively. The transverse tensile fracture toughness, and the longitudinal shear fracture toughness are measured

from interlaminar mode-I and mode II tests, respectively, both carried out based on Airbus internal procedures. The transverse compressive fracture toughness is assumed equal to IM7/8552 material system ($\mathcal{G}_{Y_C} = 2.8\text{N/mm}$)

The shape of the longitudinal softening laws (the shape of each softening segment in Fig. 2.4) are fitted using the experimental data from the DENC and DENT tests. Different specimen sizes were tested to properly calibrate these shapes. Firstly, FE models to predict the failure strengths of DENC tests are defined. Eight-node 3D solid elements with reduced integration (C3D8R) are employed. The in-plane mesh element size is defined equal to 0.5 mm around the notch, where the damage is expected to grow. This element size prevents the snap-back effect in all softening laws defined [101], its value being more than three times lower than the critical element size for the analysed material, see Appendix F. In addition, three elements through-the-thickness of each ply are used, as in the previous chapters. Then, the axial displacement is applied on the top face at low loading rate to avoid dynamic effects during the simulation, while the opposite face is clamped, see Fig. 5.3a. Finally, the shapes of the longitudinal compressive softening laws are adjusted to match the experimental failure strengths. The same procedure is carried out to calibrate the shapes of the longitudinal tensile softening law from the DENT tests.

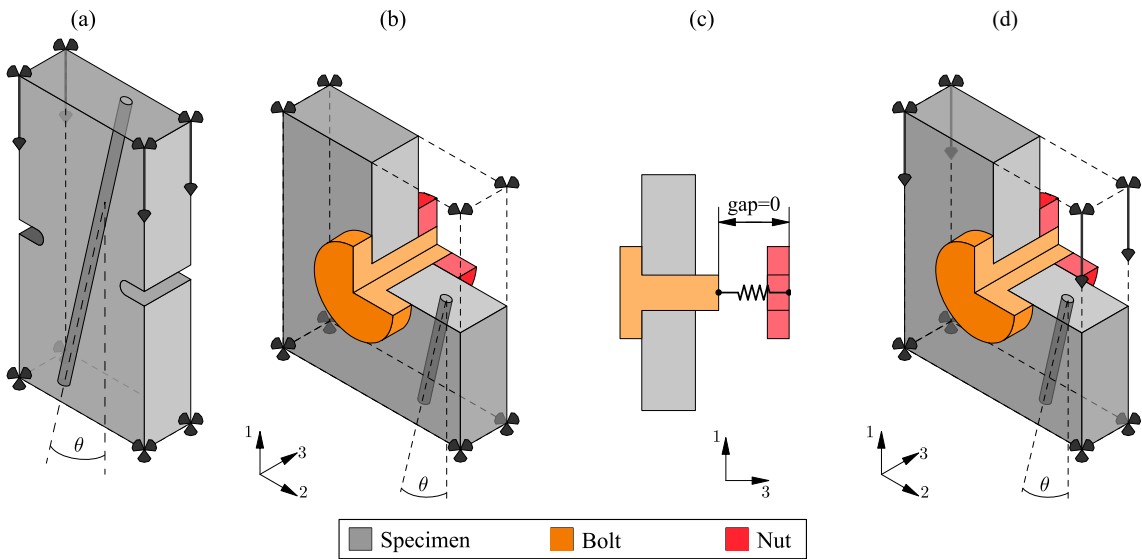


Figure 5.3: Schematic representation of the finite element models. a) Double edge notched compressive test, b) filled-hole compressive preload step with boundary conditions to avoid the rigid body motion, c) connection between the bolt and nut with a virtual connector element to model the preload; a gap between the bolt and nut is presented for the sake of clarity, and d) filled-hole compressive loading step with boundary conditions.

The FE model for the FHC tests is defined using two types of material model: i) the elastoplastic damage model (see Chapter 3) for the laminate and ii) linear elastic isotropic

material for the bolt and nut. The in-plane element size of the specimen is defined equal to 0.5 mm around the hole (more than three times lower than the critical element size to prevent the snap-back effect), and three elements through-the-thickness of each ply again. The bolt and nut are defined with an element size of 0.5 mm around the areas in contact with the specimen and a coincident node mesh between all parts is imposed to improve the contact interactions. C3D8R solid elements are employed in all the parts of the assembly. All FE models use the same mesh element size and discretisation to perform a fair comparison between FHC configurations.

The specimen length of the FE models is defined by the experimental gauge length of the corresponding configuration. The bolt is modelled as two concentric cylinders, one with the hole diameter and the thickness of the specimen plus the nut length, and the other with the diameter and length of its head, see [Fig. 5.3b](#). The nut is defined as a cylinder with a concentric hole equal to the hole diameter. Therefore, there is no clearance between the parts. General contact is defined with hard contact normal behaviour and tangential behaviour given by frictional contact, with a friction coefficient of 0.15.

The simulation consists in two steps: preload and loading. In the first step, the assembly is preloaded. The bolt preload is defined using a virtual connector element (CONN2D2 Abaqus element) to link the bolt with the nut, see [Fig. 5.3c](#). The connector between these two parts is defined as purely elastic, with a low stiffness (100 N/mm) to avoid modifying the stiffness of the FE model in this direction. Then, a compressive axial load (axis 3 in [Fig. 5.3b](#)) equal to the preload is defined in the virtual connector element using a smooth step, while the bottom and top faces of the specimen are restricted to avoid rigid body motion, see [Fig. 5.3b](#). After that, the loading step starts, and the length of the virtual connector element is fixed by setting its axial velocity equal to zero and removing its axial load. This allows to keep the bolt preload, but also allows the parts to deform, altering the contact force between parts as needed to reach equilibrium. In addition, an axial compressive displacement is applied to the specimen top face, while the bottom face is clamped, until catastrophic failure, see [Fig. 5.3d](#). The model is run for each configuration, and with different failure envelopes as explained next in [Section 5.3.3](#).

The proposed FE modelling strategy allows to define the bolt preload with a single step in Abaqus/Explicit solver. Another FE strategy is to define the preload using a thermal step; the bolt/washer is defined with a thermal expansion coefficient in the preload direction and a temperature is applied to contract or expand the bolt or washer, respectively [117, 196–201]. Hence, a calibration step must be carried out to determine the temperature to be applied for the corresponding bolt preload. Thus, three steps have to be performed: i)

calibration step, ii) bolt preload step and iii) loading step. Consequently, the proposed FE strategy is efficient in terms of computational time in the pre-processing and solver FE steps.

5.3.3 Failure envelopes definition

The failure envelope shape coefficient μ_t defines the $\sigma_{22} - \sigma_{33}$ stress space and, thus, controls transverse failure. In the present chapter, the failure envelope in this stress space is adjusted based on the biaxial compressive strength of the material ($Y_{CB} = 2Y_C$ [202]) and Eq. (5.3), see Fig. 5.4a. The failure envelope for the $\sigma_{22} - \sigma_{12}$ stress space is controlled by $\mu_{s\ell}$. This value can be estimated from off-axis tests by fitting the failure envelope with the experimental data. Here, $\mu_{s\ell}$ is assumed equal to 1 as with the IM7/8552 material system, see Fig. 5.4b.

The failure envelope shape coefficients $\eta_{s\ell}$ and $\eta_{s\ell}^q$ control the $\tilde{\sigma}_{11} - \tilde{\sigma}_{12}$ effective stress space. Unfortunately, there is uncertainty in this effective stress space due to the lack of appropriate multiaxial tests. Consequently, $\eta_{s\ell}$ and $\eta_{s\ell}^q$ are defined based on the results from Soden et al. [203], and Eq. (5.9) is used to estimate these two parameters, see Fig. 5.4d.

The largest uncertainty in the failure envelope is the $\tilde{\sigma}_{11} - \tilde{\sigma}_{22}$ effective stress space due to the lack of experimental data. This space governs the onset of damage in the longitudinal compressive direction and its propagation. The failure envelope in this effective stress space can be defined by adjusting the shape coefficients η_t and η_t^q .

In this chapter, the influence of the failure envelope in the $\tilde{\sigma}_{11} - \tilde{\sigma}_{22}$ effective stress space on the FHC strength is explored. Fig. 5.4c presents the different envelopes that will be explored. The Quadratic envelope is adjusted based on the failure criteria presented by Camanho et al. [123], and is less conservative than the rest of the envelopes, note that this is an approximate adjustment. The LaRC03 mod. envelope is defined from the modified LaRC03 failure criterion proposed by Maimí et al. [49] in which the misalignment angle of the kinking failure mechanism is assumed to be constant. Notice that the Quadratic envelope is purely a quadratic function in the effective stress space presented in Fig. 5.4c, while LaRC03 mod. envelope is purely a linear function. Therefore, two new envelopes are defined in this effective stress space by combining linear (η_t) and quadratic (η_t^q) terms of $\phi_{\ell C}$. The 52X_CQ envelope crosses the transverse tensile strength (Y_T) at 52% of the longitudinal compressive strength (X_C) and with a greater weight in the quadratic term compared with 53X_CL envelope, which crosses Y_T at 53% of X_C .

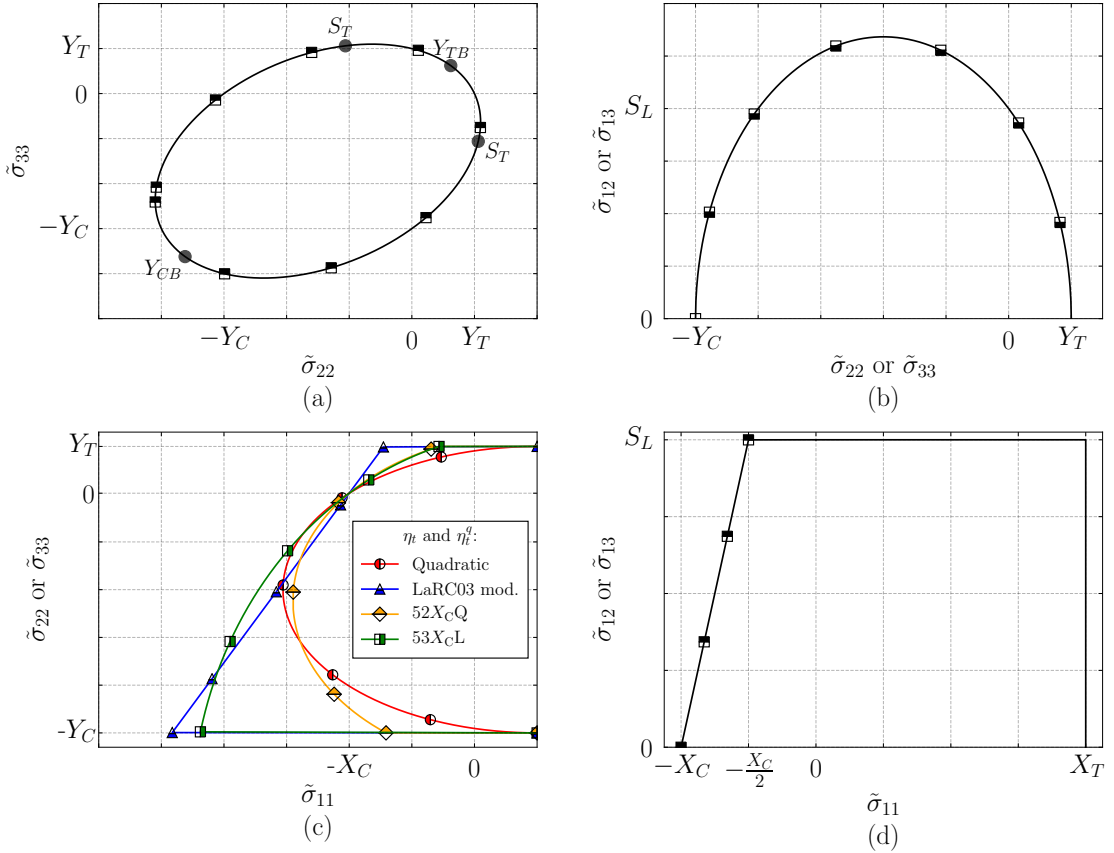


Figure 5.4: Schematic representation of the failure envelopes for the effective stress space at the onset of damage: (a) $\tilde{\sigma}_{22}$ - $\tilde{\sigma}_{33}$, (b) $\tilde{\sigma}_{22}$ - $\tilde{\sigma}_{12}$, (c) $\tilde{\sigma}_{11}$ - $\tilde{\sigma}_{22}$, and (d) $\tilde{\sigma}_{11}$ - $\tilde{\sigma}_{12}$. Note that, b) and d) are symmetric with respect to their X-axis.

5.3.4 Results and discussion

This section analyses the failure strength of the FHC configurations in Table 5.1 obtained with each failure envelope of Fig. 5.4. After that, the influence of the failure envelope on the failure strength and failure mechanisms of the FHC tests is analysed. Please note that all results are normalised for confidentiality reasons.

Fig. 5.5 presents the failure strength predictions for each FHC configuration and for each failure envelope. Overall, changing the failure envelope leads to a massive effect on the failure strength for all tested configurations, and tendencies are also not obvious as will now be analysed.

For the SH-12np case, the $52X_CQ$ and $53X_C$ failure envelopes underpredict the experimental failure strength (with a relative error between 12% and 14%), while the Quadratic case, underestimates the experimental data with an error of 21%. Opposite to this, the LaRC03 mod. envelope overpredicts with an error of 16%. The SH-10np specimen is identical to the previous one, but with a different stacking sequence (see Table 5.1). Completely opposite

to before, in this case the Quadratic envelope is the one closest to the experimental data, while the LaRC03 mod. envelope (which was reasonably close previously) is now heavily overpredicting, with an error of 50%.

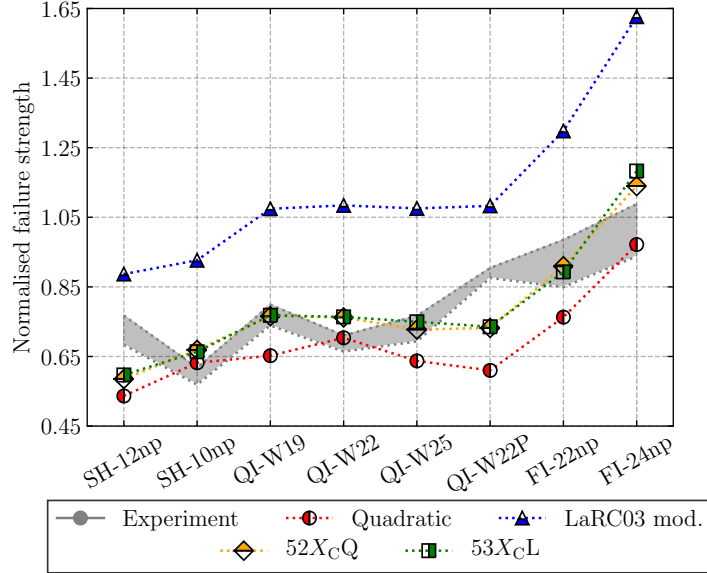


Figure 5.5: Normalised strength for each FHC configuration and for each failure envelope. Results are all normalised by the experimental average strength of FI-24np.

Similar findings are observed with the quasi-isotropic specimens (QI-W19, QI-W22, QI-W25 and QI-W22P). All these cases have the same stacking sequence, but different preload and geometrical dimensions (see Table 5.1). Here, the LaRC03 mod. envelope overpredicts the experimental data (with relative errors between 20% and 52%), while the Quadratic envelope underestimates all cases, with relative errors between 10% and 30%, except for the QI-W22. The intermediate envelopes ($52X_CQ$ and $53X_CL$) are in good agreement with the experimental data, with errors lower than 8% overall, although there is a slight underprediction for the QI-W22P (16% for both envelopes).

Finally, the FI-22np and FI-24np cases both have the same width, bolt and preload, but different stacking sequences. Note that these laminates are much thicker than the laminates analysed before (see Table 5.1). In these cases, the LaRC03 mod. envelope again overestimates the test results by 32% and 50% for the FI-22np and FI-24np cases, respectively. The Quadratic one underestimates the strength by 10% for the FI-22np configuration, but captures well the experimental value for the FI-24np case. The intermediate envelopes are again in good agreement with the experimental data, with a relative error lower than 5%. These findings prove that numerical predictions may be accurate for a specific test case, but they may fail to reproduce the experiments as soon as something is modified (such as the stacking sequence or the bolt diameter).

Taking into account all results, the $53X_C L$ and $52X_C Q$ failure envelopes are the most representative of this material, since these envelopes presented a lower relative error compared to the experimental data. Nonetheless, the shape of these two envelopes is very different, see Fig. 5.4c. This indicates that for the analysed FHC configurations, failure occurred when the longitudinal direction was under compression and the transverse hydrostatic pressure was under tension (with $\tilde{\sigma}_{22}$ or $\tilde{\sigma}_{33} \geq 0$ and $-X_C \leq \tilde{\sigma}_{11} \leq 0$), since these envelopes are quite similar in this area. Depending on the specimen case, the effective stress state can be slightly more to the right or to the left of this quadrant, which causes the Quadratic or the LaRC03 mod. envelopes to have better predictions or not. This can be observed by analysing the trends from Fig. 5.5 and comparing it with the envelopes from Fig. 5.4c. For example, in the SH-12np configuration, the LaRC03 mod. predicted higher strength than the $53X_C L$ and $52X_C Q$ envelopes, while the quadratic prediction was the lowest. Therefore, the stress state that led to failure must be located in a region where the LaRC03 mod. is the least restrictive, the $53X_C L$ and $52X_C Q$ envelopes coincide, and the quadratic surface is the most restrictive.

The large difference in strength, by slightly modifying the envelope, also suggests that the failure mechanisms are different. This will be analysed by comparing the failure mechanisms in the onset of damage (where and how failure started to develop) in the QI-W25 specimen. This configuration is selected, since here both LaRC03 mod. and Quadratic envelopes are quite far from the experiments.

Fig. 5.6 presents the stress vs. strain curve predicted by each failure envelope for the QI-W25 specimen, as well as a picture of the transverse and longitudinal damage initiation with each failure envelope. Note this representation is done by plotting all the elements within the laminate with a damage value equal to or larger than 0.99, and giving all these elements one colour or another accordingly to the failure envelope. The transverse damage initiation is shown at the instant indicated by the cross point in the stress vs. strain curve, while the bullet dot indicates the instant at which the longitudinal damage is shown. Before deeper analysis, note that in all cases there is some damage caused by the bolt pretension, which can be seen around the edges of the hole and bolt head. All experimental and numerical stress vs. strain curves are mostly linear up to catastrophic failure, with no significant loss of stiffness.

With the Quadratic envelope, transverse damage starts to grow perpendicular to the loading direction at plies 3 and 5 (which are 0° plies), just from the bolt head diameter. Notice that damage starts from the bolt head rather than the hole, due to the presence of the pretension. This happened with all models, however the longitudinal damage starts to

grow with a slightly higher strain (see Fig. 5.6a) propagated from the edges parallel to the loading axis at the centre, again in plies 3 and 5, see Fig. 5.6c.

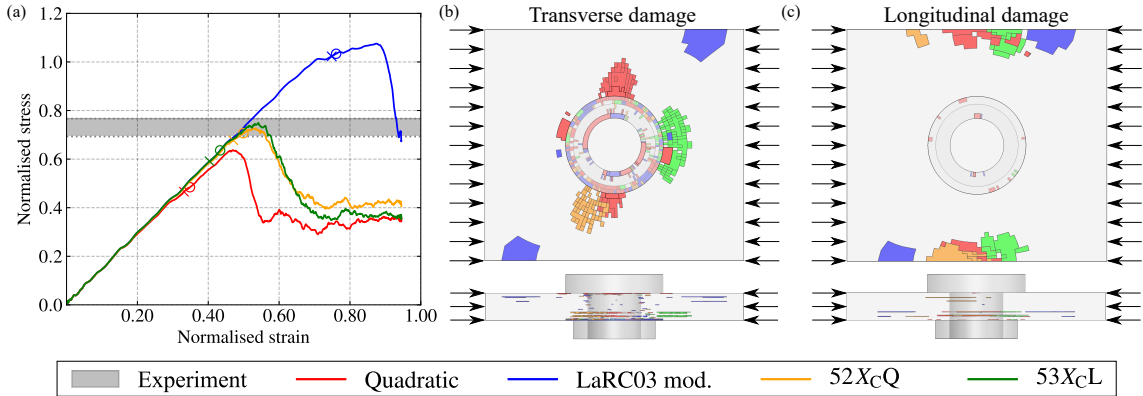


Figure 5.6.: Comparison of the failure mechanisms, at the onset of damage, with each failure envelope for the QI-W25 configuration. a) Normalised stress vs. strain curve, b) transverse damage and c) longitudinal damage. The cross and bullet points indicate the instant when transverse and longitudinal damage, respectively, are shown.

The LaRC03 mod. envelope shows a different mechanism, the stress state caused transverse damage to start at the edges, oriented with a 45° angle, at plies 12 and 14 (0° plies). As with the transverse damage, the longitudinal damage from the LaRC03 mod. envelope begins to propagate slightly later in the same location and orientation, but in layers 3 and 5. Therefore, this complete difference in damage explains why the two models provide different results.

Similar failure mechanisms from the 52X_CQ envelope are observed. Transverse damage starts around the bolt head diameter, perpendicular to the loading direction, in plies 3 and 5, like the Quadratic case. Longitudinal damage again grows from the edges at the centre in all 0° plies. Finally, the model with failure envelope 53X_CL provided completely different failure pattern, and the transverse damage initiated at the right hand side of the bolt head diameter in plies 3 and 5, thus, parallel to the loading axis. Longitudinal damage is more in-line with the Quadratic and the 52X_CQ envelopes, growing from the edges at the centre in plies 3 and 5 again.

While some aspects are common in all models (damage mainly started in the 0° plies and especially in plies 3 and 5, which are 0° plies), matrix cracking evolution is completely different in all cases. Firstly, this may look unreasonable, since the different failure envelopes here considered (see Fig. 5.4c) only alter the onset of damage in the longitudinal direction and its propagation and do not affect the transverse damage. However, this can be explained as follows. The bolt preload promotes localised longitudinal damage around the hole. This damage is different for each defined failure envelope. As a consequence, this

changed the stress redistribution in the matrix, inducing a different transverse damage development. Eventually, this caused catastrophic transverse damage in a different location, despite the fact that only the longitudinal failure criterion is modified.

A further interesting point to highlight is that longitudinal failure developed at the free edges, and not at the hole. This may be because the fibres are confined by the presence of the preloaded bolt, which delays fibre damage from developing around the hole. However, in open-hole tests, damage often initiates from the hole edge, and the shape of the longitudinal softening law has a greater influence on predicting the open-hole failure strength [204]. In line with this, the influence of modifying f_{X_C} and $f_{G_{X_C}}$ on the FHC strength predicted is analysed and no significant effect is found.

The influence the preload on the failure strength is analysed by modifying the bolt preload in the SH-10np configuration. Increasing or decreasing the preload by 20% led to a relative difference less than 0.5% compared with the failure strength obtained with the default preload and, thus, there is no significant influence on the predicted FHC strength. Moreover, the influence of modifying η_{sl} and η_{sl}^q ($\tilde{\sigma}_{11} - \tilde{\sigma}_{12}$ or $\tilde{\sigma}_{11} - \tilde{\sigma}_{13}$ effective stress space) on the FHC predictions is analysed and no significant influence is found for the cases analysed.

These results highlight that the failure envelope not only changes the predicted failure strength, but also the predicted failure mechanisms. While there are multiple failure criteria (or damage onset criteria) in the literature, some of them even physically based (LaRC, Puck, Hashin, etc.), it is well known that these criteria do not work well in many regions of the failure envelopes. Especially, the $\tilde{\sigma}_{11} - \tilde{\sigma}_{22}$ or $\tilde{\sigma}_{11} - \tilde{\sigma}_{33}$ stress spaces have not been greatly studied due to the lack of appropriate multiaxial tests. A big part of the physics of the problem (i.e., what happens under multiaxial loads) is not well understood and, thus, the models are not well adjusted for all the domain. Consequently, to properly understand the physical behaviour of the material, it is key to design new multiaxial tests to obtain the failure envelopes accurately, such as the VERTEX test rig [205].

The failure envelopes that accurately predict the FHC strength ($53X_CL$ and $52X_CQ$) may not be reproducible with some typical failure criterion, e.g. Hashin, LaRC03, etc. Thus, developing models where the envelopes can be adjusted, as in the present model, could be convenient. It is worth mentioning that the authors also verified the failure initiation in the rest of the specimens and found very similar conclusions to the ones reported with the QI-W25 specimen. Despite the differences in failure development between failure envelopes and configurations, the transverse failure pattern in all configurations and envelopes mainly grows parallel to the longitudinal direction, similar to a delamination pattern. Therefore,

this indicates that fibre kinking and delamination are the predominant failure mechanisms of the analysed configurations.

A further interesting point is to verify that the predicted failure pattern resembles the experimental data. The $53X_C L$ failure envelope is selected, since this envelope provided accurate strength prediction for all specimen configurations. Fig. 5.7 compares the predicted failure pattern after failure strength with a photo of one specimen of the QI-W25, QI-W22P and QI-W19 configurations. The comparison in Fig. 5.7 highlights that the model predicts a similar failure pattern to the experiments. In the QI-W25 case, the FE model predicts the experimental crack growing in a -45° angle from the bolt, together with visible damage around all the bolt perimeter. Some delaminations can also be seen in the experiment, comparable to the out-of-plane transverse damage observed in the numerical results. In the QI-W22P virtual case, two cracks can be seen growing again from the bolt to the edges with a -45° orientation, which are in good agreement with the experimental data. In line with this, the QI-W19 specimen again shows two cracks from the bolt to the edges, together with some damage around the bolt; this failure pattern is properly predicted by the FE model. Delaminations can also be observed experimentally, while the model predicts a similar pattern with the transverse damage growing at the vicinity between plies. Therefore, by adjusting the failure envelope properly, the FE model predicts multiple configurations with different conditions (stacking sequence, preload, dimension, etc.) and obtains similar failure patterns compared with the experiments.

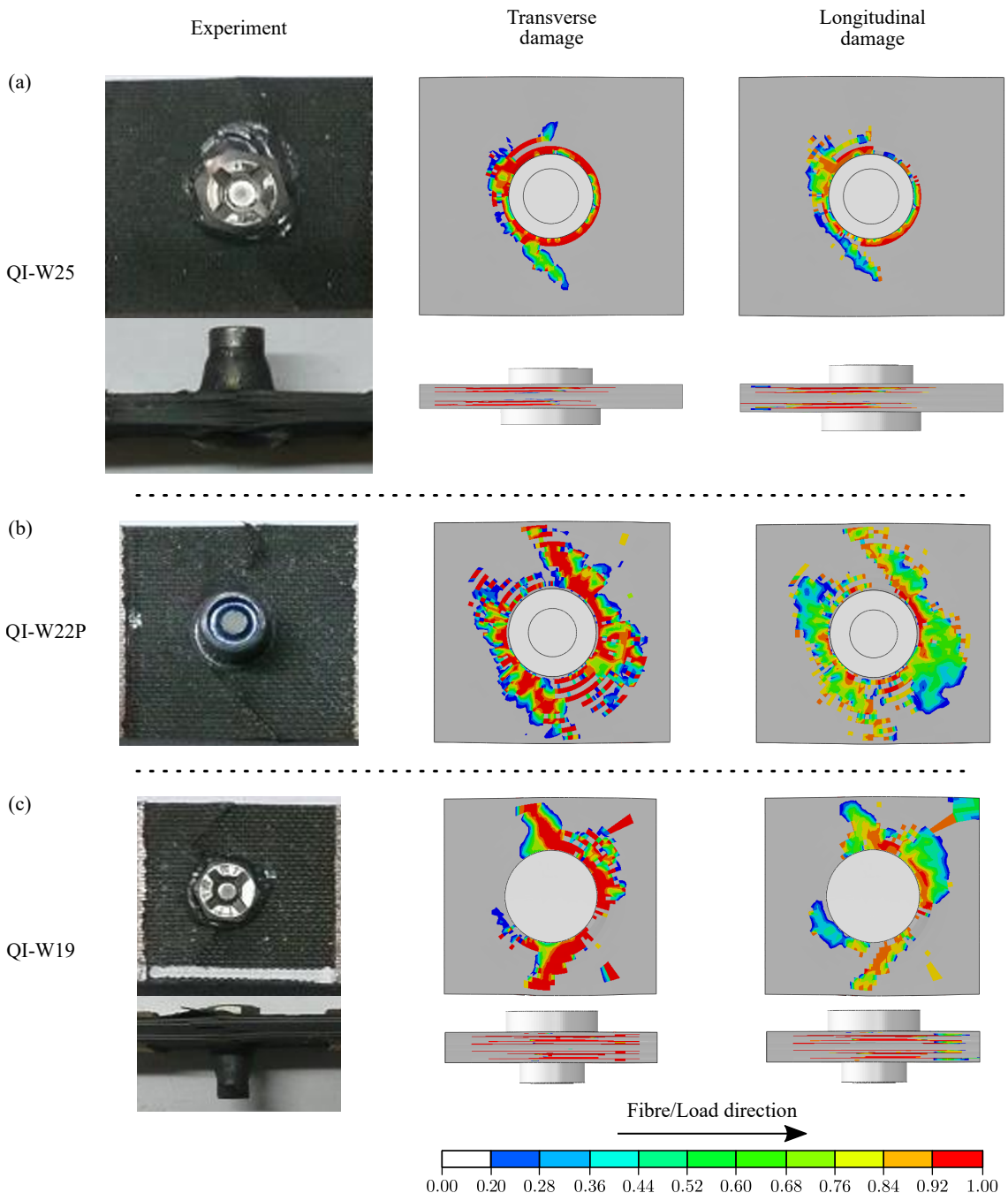


Figure 5.7.: Comparison of the failure pattern between the experiments and FE model for three different configurations: a) QI-W25, b) QI-W22P and c) QI-W19.

Complex simulations under multiaxial loading conditions

Numerical-experimental comparisons of different loading cases are carried out in this chapter. The main objective is to demonstrate the capabilities of the enhanced constitutive model for predicting the failure mechanisms of CFRP laminates under complex loading conditions. An end-notched flexural (ENF) test is conducted to show the ability of the model to predict the failure mechanism of a unidirectional CFRP laminate under pure mode-II loading conditions. Subsequently, two different CFRP configurations under four-point bending test using L-shaped specimens and another two different CFRP configurations under single-lap shear (SLS) composite bolted joints are used. The aim of the latter cases is to demonstrate the capabilities of the enhanced constitutive model under 3D complex loading conditions.

6.1 End-notched flexure test

The ENF test carried out by Jiménez and Miravete [206] is employed to demonstrate the ability of the enhanced constitutive model to properly capture the failure mechanism under mode-II loading conditions. The specimen was manufactured using the IM7/8552 material system; the material properties used in this FE analysis are summarised in [Table 2.3](#). The dimensions of the specimen are 25 mm × 150 mm with 28 plies oriented along the length direction of the specimen.

To generate the initial delamination during the experimental test, a 50 mm film insert was located in the midplane of the specimen, see [Fig. 6.1](#). This initial delamination is modelled by creating two laminates with half the number of plies as of the specimen (14 plies instead of 28 plies). The contact interfaces of these two laminates are then bonded together using tie constraints, except in the region where the film insert would be positioned, see [Fig. 6.2](#). Therefore, the film insert is not explicitly modelled, but the initial delamination is defined.

The fixture tools are modelled with rigid shell elements: two rollers are located on the bottom surface of the specimen with a span length of 110 mm and another roller is positioned on the top surface. Only a quarter of the rollers are defined in the FE model with a 25 mm diameter and a mesh element size of 0.2 mm × 0.2 mm. 3D eight-node C3D8R solid elements are employed to model the laminate using the enhanced constitutive

model. The in-plane mesh element size of the specimen is defined equal to 0.2 mm around the area where the damage is expected to occur in order to prevent snap-back effect, as explained in [Appendix F](#). In this case, the refined mesh is located from the initial delamination to the centre of the specimen. Additionally, three elements through-the-thickness of each ply are used, thus minimising the hourglass effects caused by the use of reduced integration elements.

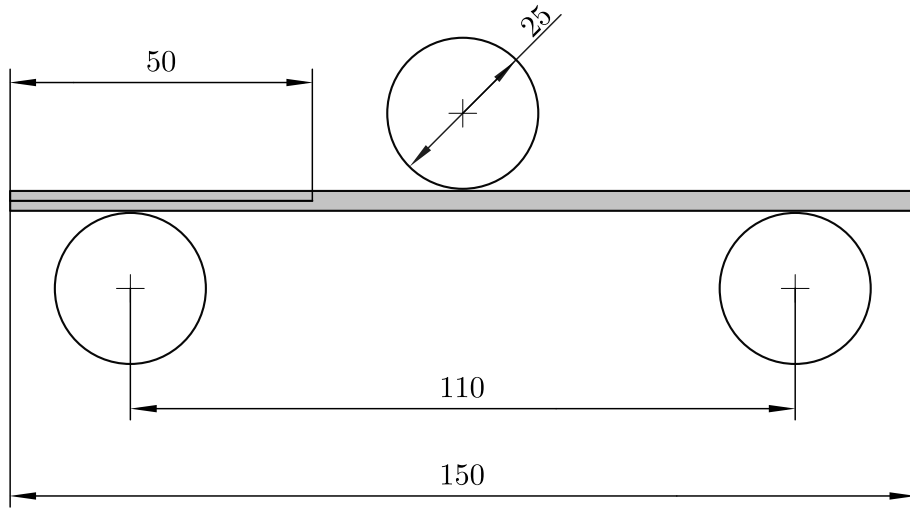


Figure 6.1.: Schematic representation of the assembly of the end-notched flexure finite element model. All dimensions are in mm.

A vertical displacement is applied to the top roller at low velocity to prevent kinetic effects while fixing their remaining degrees of freedom. The two bottom rollers are clamped and additional boundary conditions are defined in the specimen to avoid rigid body motions, see [Fig. 6.2](#). General contact is defined by normal hard contact and friction contact in the tangential direction with a coefficient of friction of 0.30 [\[206\]](#).

The predicted failure load is in good agreement with the experimental data, see [Fig. 6.3](#). In addition, the model is able to capture the rise in load after the peak load has been reached. The oscillations observed in the numerical curve are possibly caused by the applied loading rate. The vertical displacement rate in the simulation is higher than that of the experimental test, but is maintained at a low level to prevent kinetic effects. This enables a satisfactory balance between the loading rate and computational time.

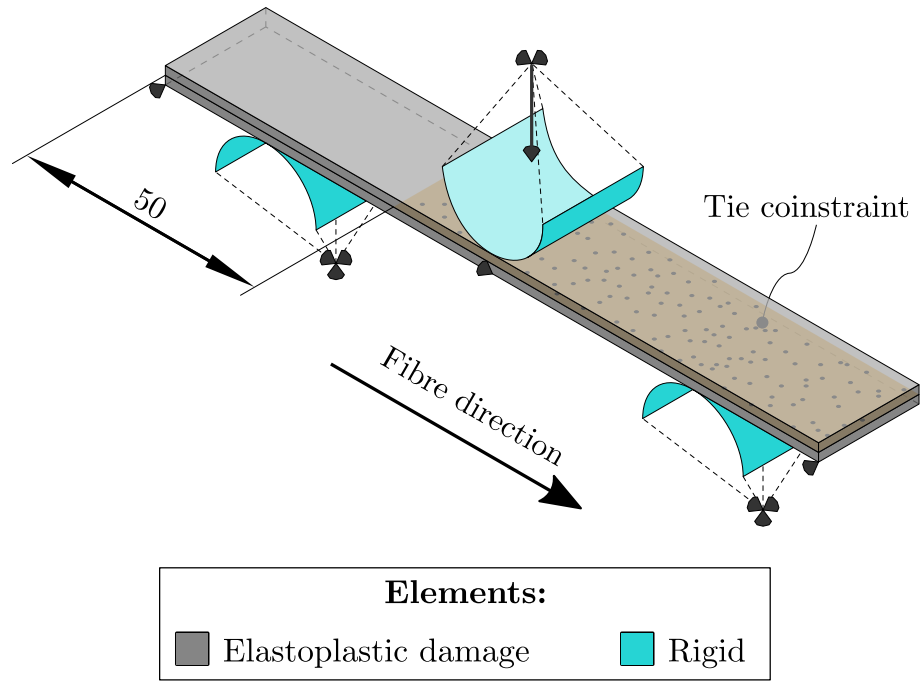


Figure 6.2.: Schematic representation of the applied boundary conditions of the end-notched flexure finite element model. The dimension of the film insert is in mm.

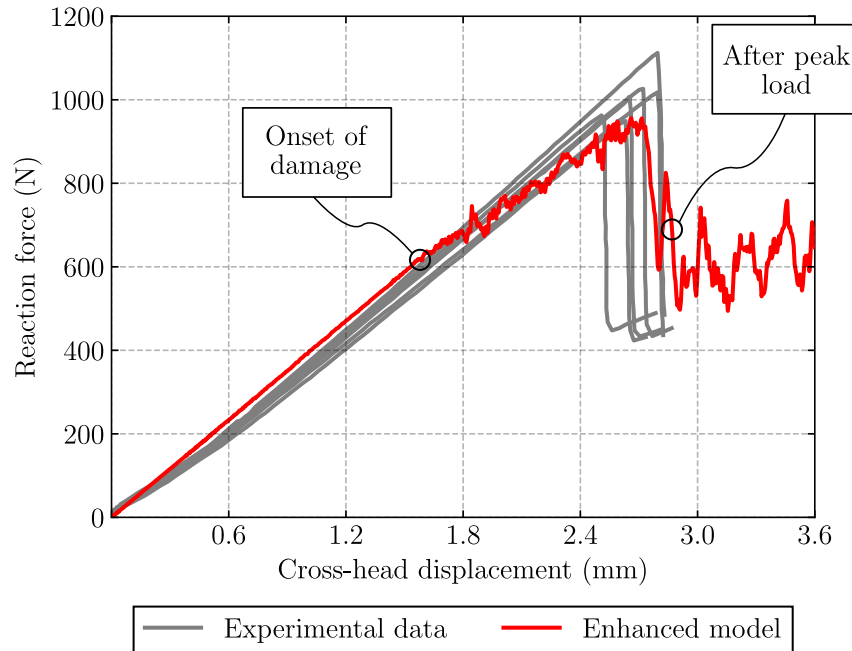


Figure 6.3.: Numerical-experimental comparison of reaction force vs. cross-head displacement of the end-notched flexure test carried out by Jiménez and Miravete [206].

The onset of damage occurs at the film tip in the upper elements of the lower laminate (central interface of the specimen), the same interface where the film insert is positioned in the experimental test, see Fig. 6.4a. The damage propagates then through that row of

elements during the simulation. The failure pattern after the peak load is presented in Fig. 6.4b. Note that the elements located at the interface between the upper and lower laminates show the typical delaminated failure pattern, although no cohesive elements are used at the ply interfaces to model delamination. In addition, the sliding deformation after the peak load between the laminates can be observed at the end of the specimen where the film insert is located.

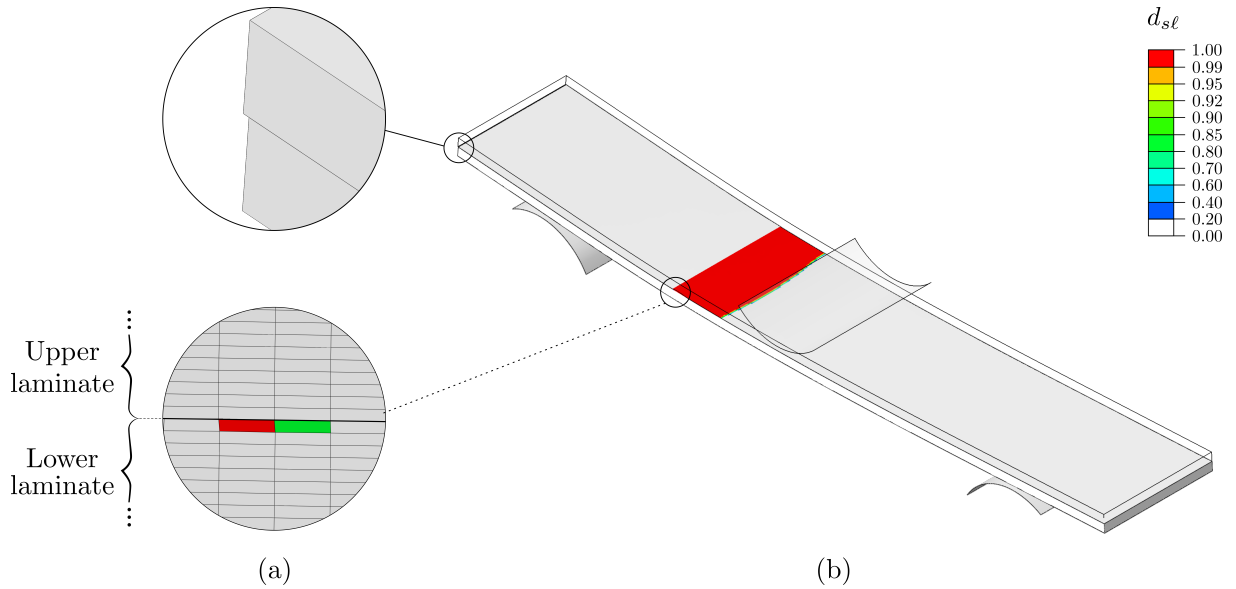


Figure 6.4.: Numerical-experimental comparison of the end-notched flexure test carried out by Jiménez and Miravete [206]: a) failure pattern at the onset of damage and b) failure pattern at after the peak load. $d_{s\ell}$ is damage variable associated to the in-plane mode-II matrix cracking.

6.2 Four-point bending tests using L-shaped specimens

The ability of the enhanced constitutive model to predict failure load and patterns under non-uniform out-of-plane stress states is demonstrated through four-point bending tests using L-shaped specimens. The curved section of these specimens are loaded under a bending moment inducing non-regularised stresses [207, 208]. These tests were carried out by Airbus in accordance with the AITM 1-0069 internal standard.

The L-shaped specimens were manufactured with the CFRP system presented in Chapter 5. The total length of each leg of the specimen in the FE models is defined as 71 mm, see Fig. 6.5. This length is less than the experimental one, allowing the FE models to be reduced and, thus, the computational time. The stiffness of the assembly and the stress state in the corner radius of the L-shaped specimens are not affected by this simplification.

In this case, the critical dimensions are: the corner radius and its angle, the distance between the support rollers (bottom cylinders), the distance between the loading rollers (top cylinders), and the thickness and width of the specimen [209]. These dimensions are correctly modelled, allowing the stress state in the corner radius of the L-shaped specimens to be properly predicted.

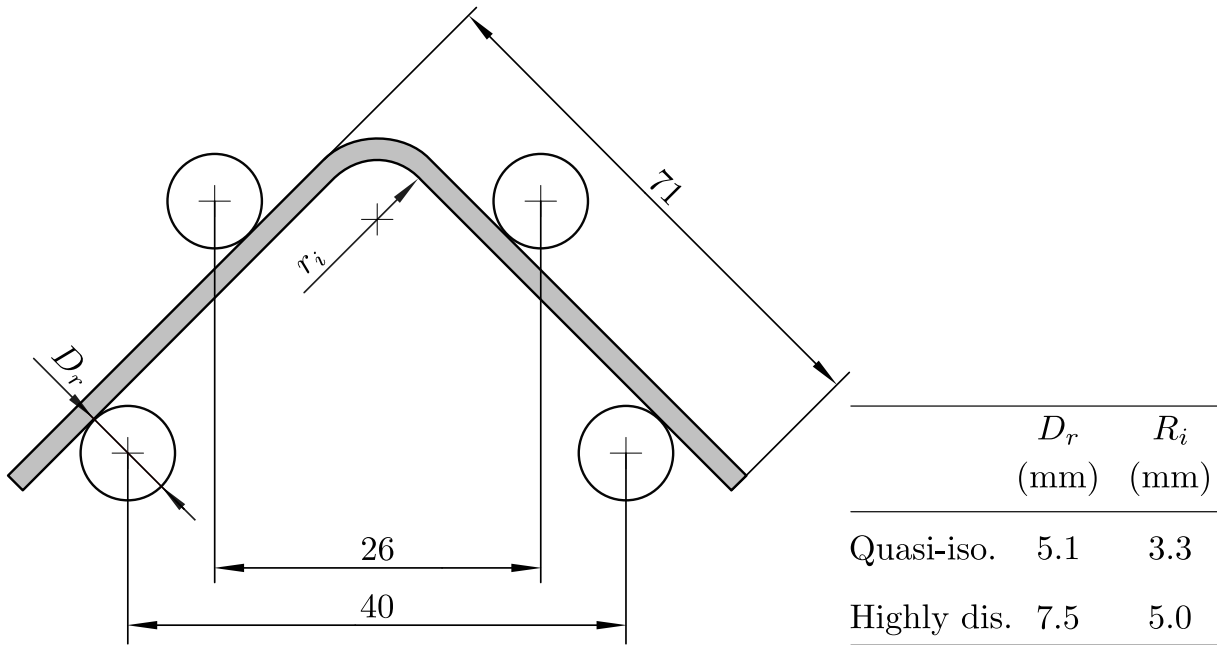


Figure 6.5.: Dimensions of the four-point bending test on L-shaped specimens. All dimension are in mm.

Two different stacking sequences were made with the following ratios of the orientated angle of plies ($0^\circ / \pm 45^\circ / 90^\circ$): a quasi-isotropic laminate (25/50/25) and a highly disoriented laminate (11/67/22). The dimensions of the test assembly are presented in Fig. 6.5. Both configurations have identical dimensions with the exception of the laminate thickness, which is significantly greater in the quasi-isotropic laminate (nearly twice the thickness). The roller diameter and the corner mean radius are also different between the configurations. The failure patterns obtained with these two configurations are different, as presented below, allowing a better demonstration of the capabilities of the enhanced constitutive model.

The four rollers of the assembly are modelled using purely elastic shell elements with an approximate mesh element size of $0.6 \text{ mm} \times 0.6 \text{ mm}$. Their material properties are summarised in Table 6.1 (standard steel with elastic isotropic behaviour). They are defined with a diameter of 7.5 mm with the distances between the two cylindrical loading bars (top rollers) equal to 26 mm and the distances of the support bars (bottom rollers) of 40 mm. The specimens are modelled using 3D eight-node C3D8R solid elements using

the enhanced constitutive model. The in-plane mesh element size of the CFRP laminates is approximately of $0.6 \text{ mm} \times 0.6 \text{ mm}$ in the in-plane directions. These dimensions are approximately three times less of the critical element size for the analysed material to prevent the snap-back effect, see [Appendix F](#). In addition, three elements through-the-thickness of each ply are used, thereby reducing the hourglass effects resulting from the use of reduced integration elements.

Table 6.1.: Material properties for steel and titanium alloy.

Description	Steel	Titanium alloy	Unit
Density	7.80	4.42	kg/m^3
Elastic Young's modulus	210000	110000	MPa
Poisson's ratio	0.3	0.28	-

As with the ENF FE model, a vertical displacement is applied to the top rollers at low velocity to prevent kinetic effects and fix their remaining degrees of freedom. The bottom rollers are clamped and additional boundary conditions are defined in the specimen to avoid rigid body motions, see [Fig. 6.6](#). General contact is defined by normal hard contact and frictionless contact in the tangential direction, as the rollers can rotate on ball bearings minimising the friction.

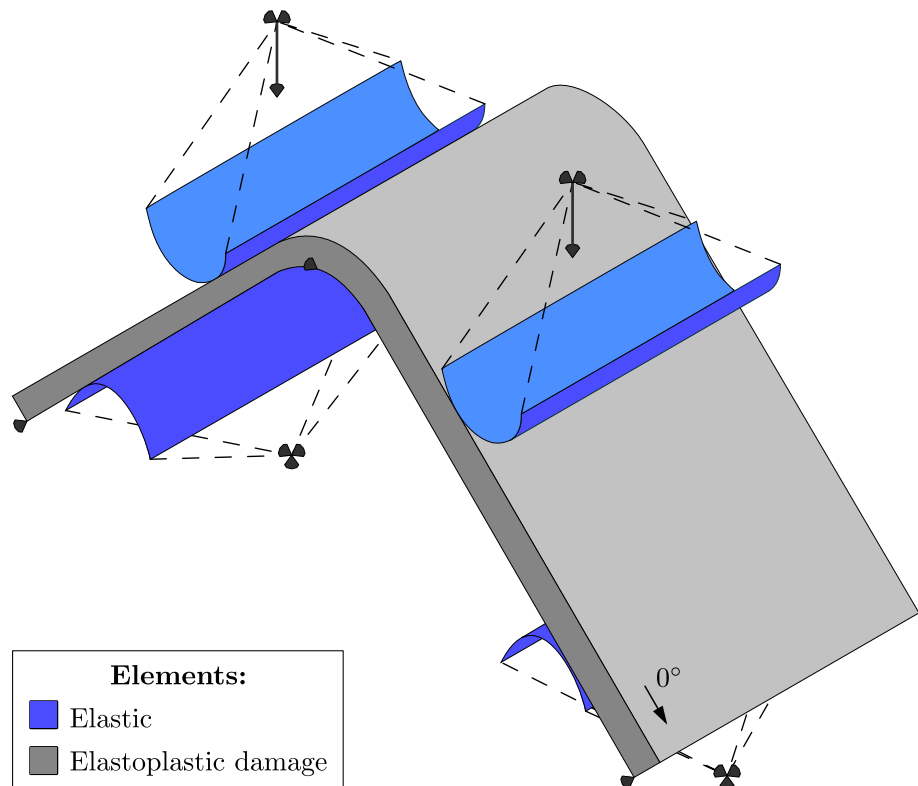


Figure 6.6.: Schematic representation of the applied boundary conditions of the four-point bending finite element model with a L-shaped specimen.

The failure load is properly predicted by the numerical model for both stacking sequences, see Fig. 6.7. Note that these results are normalised with respect to its average value of the failure load. In both cases, the onset of damage appears in the numerical models just as the peak load is reached. As with the ENF FE results, the oscillations in the curves from the numerical models may be attributed to the loading rate applied. The rate of the vertical displacement applied in the simulation is greater than that in the experimental test, but low enough to prevent kinetic effects. This achieves a suitable balance between the loading rate and computational time.

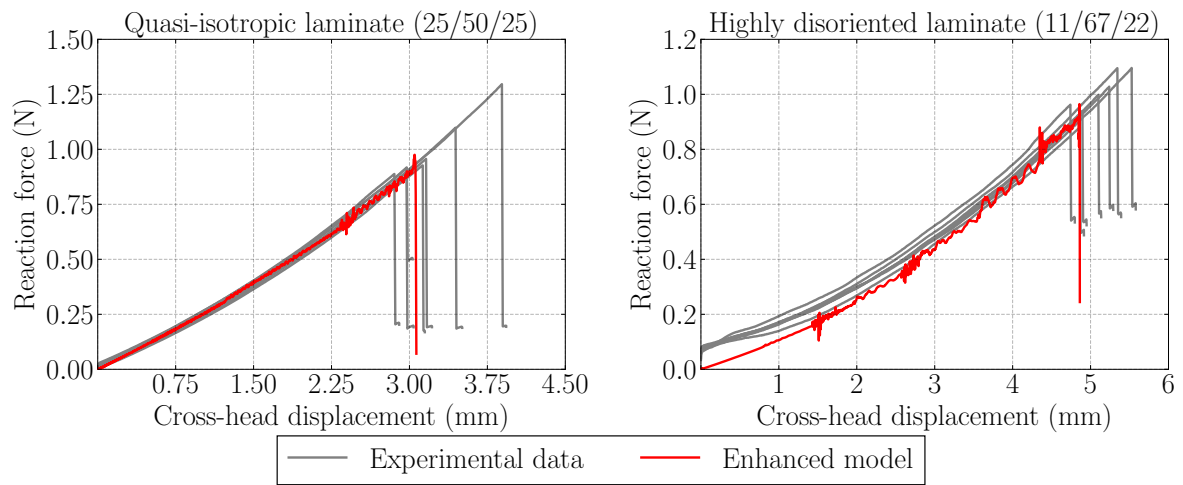


Figure 6.7.: Numerical-experimental comparison of the four-point bending test using L-shaped specimens with the quasi-isotropic laminate (25/50/25) (left) and the highly disoriented laminate (11/67/22) (right) carried out by Airbus. The reaction force is normalised with respect to its experimental average value.

Two main failure mechanisms are observed in the quasi-isotropic specimens from the experimental tests (see Fig. 6.8a.): delaminations and matrix cracking. The delaminations are located near and below to the mean corner radius and the matrix cracking spread through-the-thickness linking certain delaminated planes. The numerical model predicts three main fracture planes, which are in good agreement with the to the experimental delaminated areas, located at the mean corner radius and below it (see Fig. 6.8b): one plane in the elements of a 45° ply in contact with a -45° ply, another in the elements of another 90° ply in contact with a 0° ply and the last in the elements of a -45° ply in contact with a 0° ply. In addition, matrix cracking is predicted; however, no connection between the above-mentioned fracture planes is observed in the FE results. Nevertheless, a link is noted between two fracture planes in the right arm.

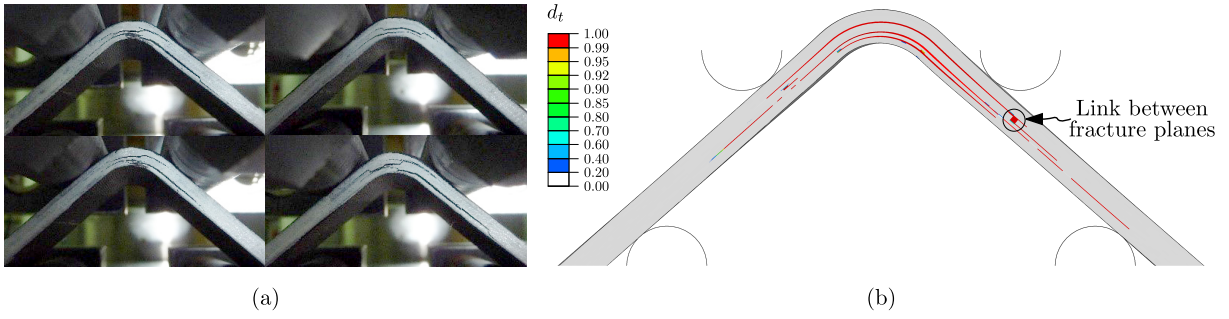


Figure 6.8.: Numerical-experimental comparison of the external failure pattern at the peak load from the quasi-isotropic laminate (25/50/25): a) experimental data, and b) numerical results. d_t is damage variable associated to the mode-I matrix cracking.

A single delamination is observed in the highly disoriented configuration from the experimental tests, Fig. 6.9a. The fracture plane of this delamination is located near to the inner corner radius. The FE model also predicts a single fracture plane situated in a comparable position to the experimental one, see Fig. 6.9b. In the FE model, this plane is located in the elements of a 90° ply in contact with a 45° ply. No matrix cracking is observed in either experimental or numerical tests.

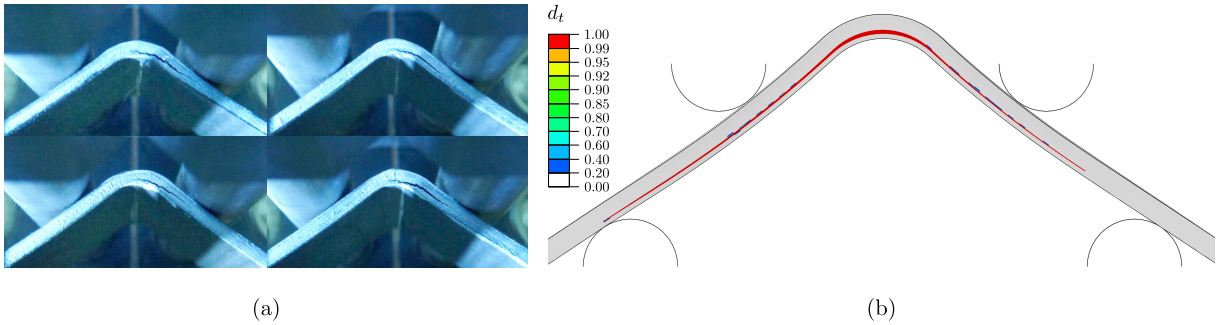


Figure 6.9.: Numerical-experimental comparison of the external failure pattern at the peak load from the highly disoriented laminate (11/67/22): a) experimental data, and b) numerical results. d_t is damage variable associated to the mode-I matrix cracking.

6.3 Single-lap shear composite bolted joint tests

Failure prediction in bolted composite joints is a challenging problem due to the combination of different failure mechanisms, different interactions between parts (composite and/or metallic laminates, bolt, nut, washer, fastener, etc.), the bolt preload, clearance, etc. The failure modes depends on the material, stacking sequence, joint geometry, bolt preload [210–213]. The macroscopic failure mechanisms in bolted composite joints can divided in: net-tension, shear-out, bearing, cleavage-tension, bolt pulling though laminate and bolt failure [211–214]. They can occur individually or as a combination of several of the previously listed failure modes.

The SLS composite bolted joint presented by Zhuang et al. [201] are employed to compare the numerical predictions of the failure strength and failure mechanisms with those observed in the experimental tests. Two configurations are selected to demonstrate the capabilities of the enhanced model to predict the mechanical behaviour of SLS composite bolted joints. The selected configurations exhibited different macroscopic failure modes: SLS-Net specimens failed as a result of net-tension failure mechanism, while SLS-Bearing configuration showed a bearing failure mode. Net-tension failure is a catastrophic mechanism due to the high tensile stress in the net area of the hole, whereas bearing failure is governed by the compressive stress in the inner area of the hole and is a progressive failure mode [211–213].

The assembly is composed by: a CFRP laminate, a steel plate, and a bolt with its corresponding nut and washer. The geometry and dimensions of each configuration are presented in Fig. 6.10 and summarised in Table 6.2. Both configurations were manufactured with the same layup $[(90/0/45/-45)_3]_s$, the significant difference between them is their width (W_s), edge-to-hole distance (e_s) and length of the supplementary metal plate (L_s). The IM7/8852 composite material system was employed in the experimental tests. A supplementary plate was added to the CFRP laminate with the same material and stacking sequence. The nut, washer and steel plate were made in CK45 steel and the bolt with titanium alloy. A "finger-tight" torque (2.2 Nm) was applied to the bolted joint.

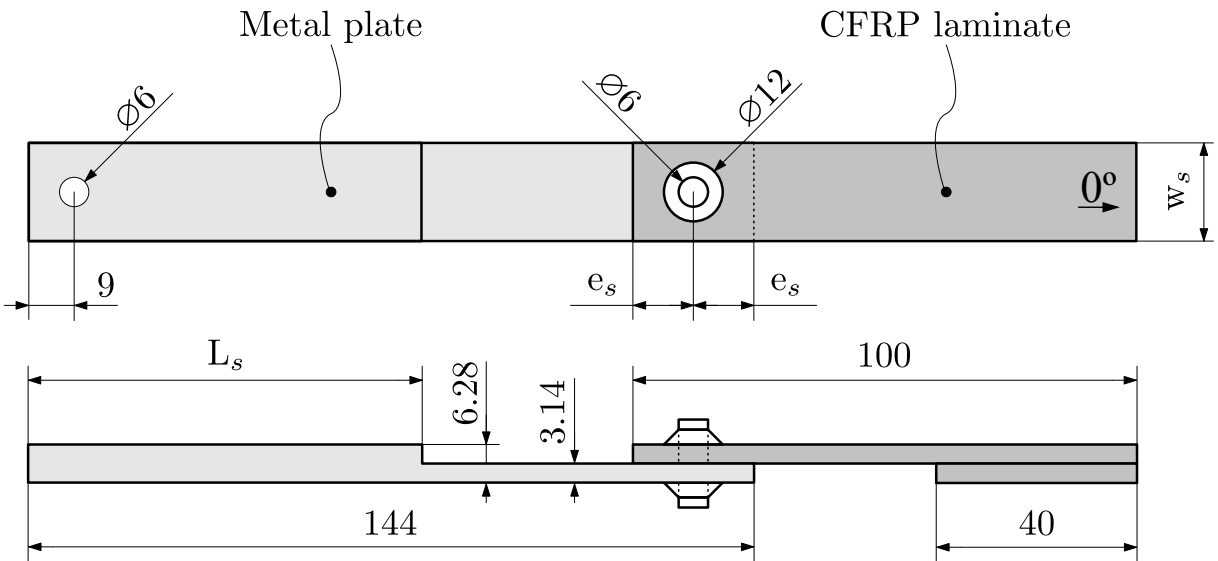


Figure 6.10.: Geometry and dimensions of the single-shear bolted joints. All dimensions are in mm.

Table 6.2.: Dimensions of the single-lap shear tests [201].

Configuration	W_s (mm)	e_s (mm)	L_s (mm)
SLS-Net	12	2	78
SLS-Bearing	36	6	84

The steel plate, nut and bolt are simplified from the experimental test. The bolt is modelled as two concentric cylinders, one with the hole diameter (6 mm) and the thickness of the specimen plus the nut length, and the other with the diameter (12 mm) and length of its head, see [Fig. 6.11](#). The nut is defined as a cylinder with a concentric hole equal to the hole diameter, therefore, there is no clearance between the parts. The left hole of the metal plate in [Fig. 6.10](#) is not modelled. This hole was used in the experimental test to fix the assembly. In the FE model, the metal plate is fixed on the left face of [Fig. 6.10](#) based on the Saint-Venant's principle.

The material behaviour of the CFRP laminates is defined with the enhanced constitutive model in the region where damage is expected (around the hole, see [Fig. 6.11](#)) with an in-plane mesh element size of approximately 0.24 mm × 0.24 mm. This element size prevent snap-back effect, as explained in [Appendix F](#). The rest of the regions of the CFRP laminate are defined purely elastic with an element size of 0.6 mm × 0.6 mm. Three elements through-the-thickness per ply are used to define the CFRP laminate.

The metal parts are defined using purely elastic elements, their material properties are defined in [Table 6.1](#). The mesh element dimensions of the plate are defined equal to those of the CFRP part to obtain coincident mesh between these two components with five elements through-the-thickness per plate. The bolt and nut are modelled with similar mesh strategy of the CFRP laminate and metal plate to also obtain an approximately coincident mesh, see [Fig. 6.11](#). All components are defined using 3D eight-node C3D8R solid elements.

As in the FHC FE model, the simulation is defined with two steps: preload and loading. The bolt preload is applied using a virtual connector with axial load between the bolt and nut, see [Section 5.3.2](#). After that, an axial tensile displacement is applied on the top face of the CFRP laminate, while the bottom face of the metal plate is clamped, until catastrophic failure, see [Fig. 6.11](#). Additionally, general contact is defined in both steps using hard contact normal behaviour and tangential behaviour given by frictional contact, with a friction coefficient of 0.2 [201].

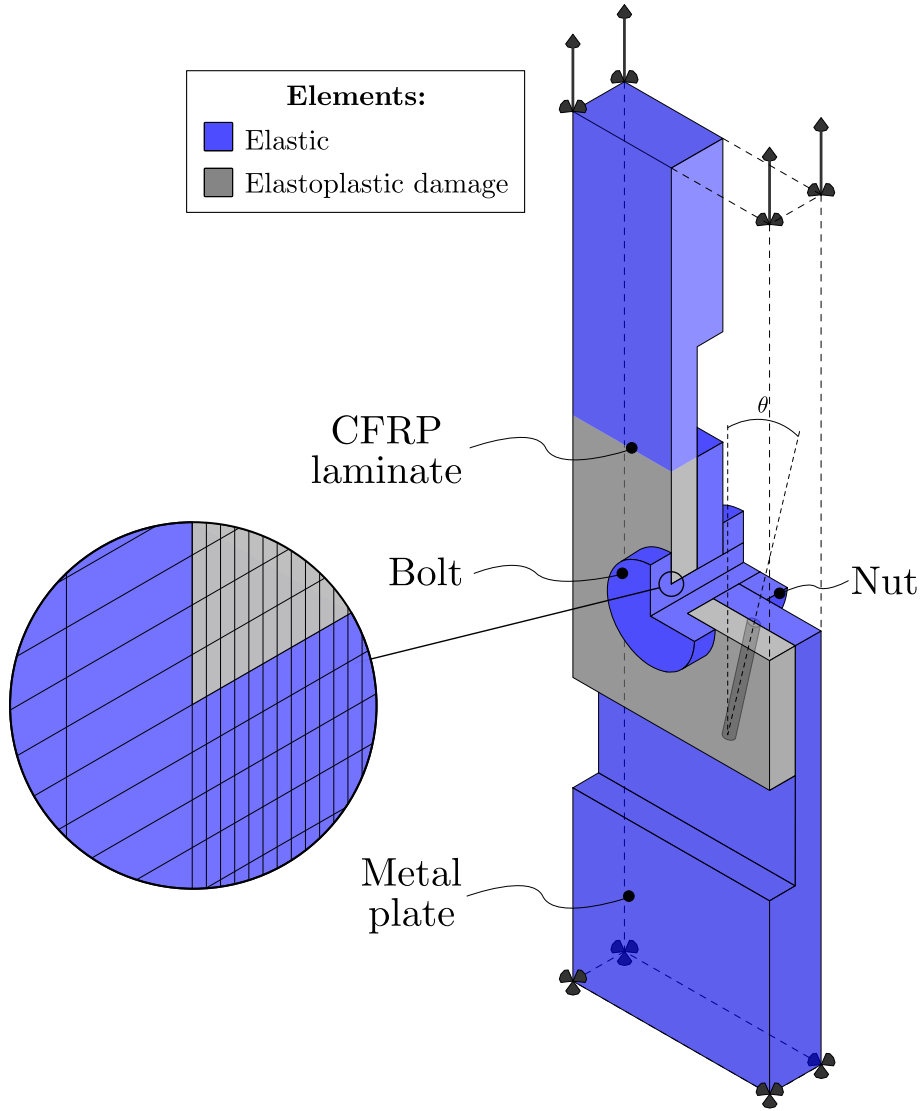


Figure 6.11.: Schematic representation of the mesh and boundary conditions applied on the single-lap shear FE model.

The enhanced model is able to properly predict the failure strength of SLS-Net specimen, as well as its failure pattern, see Fig. 6.12a and b. As is reported by Zhuang et al. [201], the net-tension failure mechanism was observed in the SLS-Net specimens. In the numerical model, fibre damage is first observed in the outer 0 ply located close to the plane between the laminate and the steel plate. Matrix cracking then develops in the 90 plies in combination with fibre damage in the 0 plies until catastrophic failure is reached. This behaviour is in concordance with the numerical observation of Zhuang et al. [201]. Additionally, the deformed shape after the peak load is presented in Fig. 6.12c, the bolt and nut rotate as well as the free end of the composite laminate and steel plate, being larger in the end laminate as its stiffness has been lost.

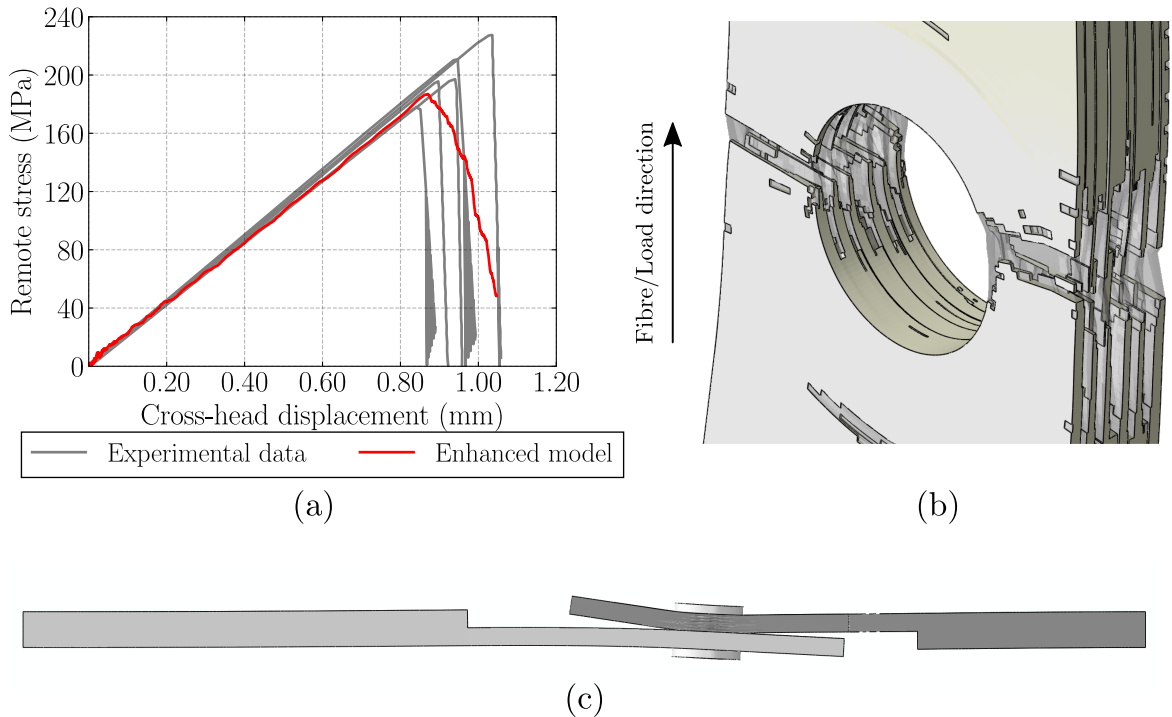


Figure 6.12: Predicted results of the SLS-Net configuration: a) numerical-experimental comparison of the stress vs. cross-head displacement curve, b) failure pattern, and c) deformed shape at 1.05 mm. The fully damaged elements in (b) are represented with dark transparent colour.

In contrast, the constitutive model predicts the onset of damage ("knee point") of the SLS-Bearing specimens but not its propagation, see Fig. 6.13a. In the numerical model, the onset of matrix cracking is reached and the catastrophic failure is observed in the stress vs. cross-head displacement curve. However, the bearing failure mechanism reported in the experiments is properly predicted, see Fig. 6.13b. The friction effects dominates the bearing failure mode since the out-of-plane confinement applied by th preload and the compressive load due to the bolt in the hole area induce fibre kinking, transverse and shear failure mechanisms [201, 212]. Therefore, the numerical prediction can be improved by considering friction effects in the constitutive model, see Section 8.2. The lateral deformed shape shows how the bolted joint rotates after the numerical peak load is reached, see Fig. 6.13c.

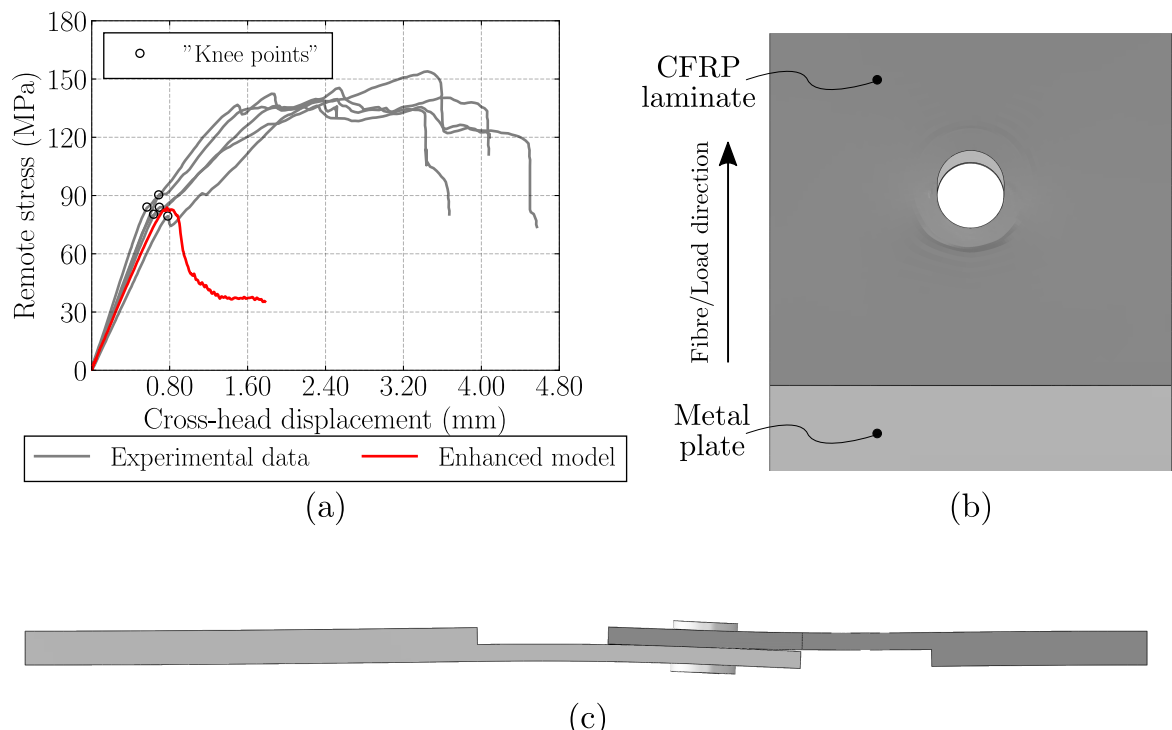


Figure 6.13.: Predicted results of the SLS-Bearing configuration: a) numerical-experimental comparison of the stress vs. cross-head displacement curve, b) front deformed shape, and c) lateral deformed shape at 1.8 mm.

Viscoelastic-viscoplastic viscodamage constitutive model

FRP structures are often subjected to dynamic loadings such as impacts in the aeronautical and automotive sectors [215–218]. Numerous experimental investigations have been carried out to understand the dynamic effects on the material properties and the stress-strain relationships of CFRPs. Hsiao et al. [219] performed off-axis compressive tests under quasi-static and dynamic loading conditions using a CFRP laminate. The authors observed a strain rate dependency on the stress-strain behaviour, along with an increase in off-axis compressive strength and modulus of elasticity at high strain rates. In addition, with increasing the loading rate, the plastic hardening response in compression also increases. However, the ultimate compressive strain decreases for off-axis angles less or equal to 45°. No significant strain rate dependency on the ultimate strain was found in off-axis compressive tests for off-axis angles greater than 60° [8, 220, 221]. Vinson and Woldesenbet [222] observed that the strain rate sensitivity of the failure compressive strength decreases as the off-axis angle increases because the failure mode changes. The off-axis tensile strength and its elastic modulus also increases with increasing loading rates [9, 221]. As with the off-axis behaviour, the longitudinal shear modulus, yielding stress and strength also increase in the in-plane shear test at higher strain rates [223, 224].

Ploeckl et al. [225] carried out compressive tests using a quasi-isotropic laminate with a CFRP under different loading rates. Although the authors reported no significant strain rate effects on the elastic modulus, but the compressive strength and the ultimate strain do increase with higher loading rates. Similar behaviour is observed for unidirectional CFRP laminates under longitudinal compressive loading conditions [225–229]. In contrast, no significant strain rate dependency on the stress-strain response under longitudinal tensile conditions has been found for unidirectional CFRP laminates [230, 231]. Jacob et al. [232] reported no significant difference from quasi-static to dynamic loading conditions for the longitudinal tensile and compressive strengths. Cheng et al. [233] carried out quasi-static and dynamic compact tensile tests in a cross-ply CFRP laminate, finding no clear trend of the longitudinal tensile fracture toughness as a function of the strain rate. However, other authors have reported a significant effect of the strain rate on the longitudinal tensile fracture toughness (this material property decreased with increasing strain rate) [234, 235]. Depending on the data reduction method and testing techniques, the fracture toughness increased or decreased as a function of the loading rate conditions.

Kuhn et al. [236] performed DENC tests using different loading rates and specimen sizes on cross-ply CFRP laminates. The authors reported a strong dependency of the strain rate on the longitudinal compressive fracture toughness, with its value being greater at higher strain rates. In addition, the cross-ply CFRP laminates exhibited a strain rate effect on the elastic stiffness, where its value increases with strain rate increases, but the ultimate strain decreases with increasing the loading rate [237, 238]. Perry and Walley [229] observed an increase in the cross-ply elastic modulus in compression with increasing loading rates, but no significant strain rate effect was found in tension [237].

Consequently, the dynamic effects must be considered in constitutive models for CFRPs to predict the inelastic deformation and fracture under dynamic loading conditions. Koerber et al. [9] developed a 3D constitutive model for CFRPs which considers plastic deformations with a failure criterion for the onset of damage (no damage propagation was considered). A non-associative plastic flow rule was defined using the overstress function proposed by Perzyna [239]. The strain rate effects in the elastic and strength properties were considered by introducing experimentally-obtained scaling functions. Kang et al. [240] presented a 3D constitutive model to predict the inelastic deformation in a dynamic tensile biaxial test using a CFRP laminate. An isotropic yield function was defined by combining the Tsai-Hill equivalent stress criterion and the Voce-type strain-hardening law. The strain rate dependency was introduced by scaling the isotropic term of the yield criterion as a function of the strain rate. In numerous studies of constitutive models for CRPF materials, scaling functions are applied to the material properties to account for the strain rate dependency on the elastic region [241–244], as well as on the plastic and damage regions [80, 245–247].

Chang et al. [248] developed a viscoelastic constitutive model based on the generalised Maxwell model. The non-linear stress-strain relationships of CFRPs in the elastic region due to different loading rate and temperature conditions were predicted. Gerbaud et al. [249] proposed a 3D viscoelastic-viscoplastic model for CFRPs, and the model was extended to Finite Strain theory [250]. The generalised Maxwell model was employed to consider the viscous effects in the elastic region due to strain rates. The loading strain rate dependency on the plastic region was introduced by a non-associative plastic flow rule using the Overstress model [239]. Hegde and Mulay [251] developed a 1D viscoelastic damage model for viscoelastic matrix materials. The generalised Maxwell model was also used and coupled to a damage model. A single damage variables were employed to degrade: i) the quasi-static stiffness and ii) the stiffness of the Maxwell element.

From observations in the literature, no 3D constitutive model addresses modelling of CFRPs by considering the viscoelastic-viscoplastic behaviour to account for viscodamage evolution and fracture toughness. [Table 7.1](#) summarises the features of the published constitutive models addressed to the strain rate dependency. Currently, there are only two constitutive models which account for the viscoelastic, viscoplastic and viscodamage effects of CFRPs [9, 241], but the scale functions being used in the viscoelastic region can induce thermodynamic inconsistencies as strain rates change. Furthermore, Koerber et al. [9] only modelled the initiation, not the propagation of the failure.

Table 7.1.: Modelling strategies used in the literature to address the dynamic effects in CFRP laminates, where V refers to a strain-rate dependent (viscous) procedure and I refers to a strain-rate independent approach.

Authors	Elasticity	Plasticity	Damage	
			Initiation	Propagation
Koerber et al. [9]	V ¹	V ²	V ¹	-
Kang et al. [240]	I	V ¹	-	
Eskandari et al. [241]	V ¹	V ²	-	V ¹
Tan and Liu [242]	V ¹	V ¹	-	
Shi et al. [243]	V ¹	-	-	V ¹
Jin et al. [244]	V ¹	-	-	V ¹
Raimondo et al. [245]	I	V ¹	-	V ¹
Daniel [246]	I	-	-	V ¹
Daniel [80]	I	V ¹	-	V ¹
Ma et al. [247]	I	-	-	V ¹
Chang et al. [248]	V ³	-	-	
Gerbaud et al. [249]	V ³	V ²	-	
Lopes et al. [250]	V ³	V ²	-	
Hegde and Mulay [251]	V ³	-	-	I

¹ Using scale functions.

² Using the overstress model [239].

³ Using the Generalised Maxwell model.

In the present chapter, a 3D viscoelastic-viscoplastic and viscodamage model is proposed to predict the constitutive behaviour of CFRPs under dynamic loading conditions. The proposed constitutive model is based on the generalised Maxwell viscoelastic model and the Overstress viscoplastic model [239]. The onset of damage is developed using experimental scale functions. Failure propagation is defined by softening laws which take into account the energy dissipated by the corresponding viscodamage process. The constitutive model is described in [Section 7.1](#) and its thermodynamic consistency is demonstrated in [Section 7.2](#). A simple longitudinal shear virtual test at different loading rates and a relaxation test are carried out in [Section 7.3](#) to verify the stress-strain response of the presented constitutive

model at the Gauss-point level. In addition, a numerical-experimental comparison of the off-axis compressive tests at different loading rates is performed to show the predictive capabilities of the model.

7.1 Constitutive model

The 3D elastoplastic damage model developed in [Chapter 3](#) is extended to include the viscous effects due to the dynamic loading conditions. Different hypothesis have been considered to develop the constitutive model from the experimental observations available in the literature: i) the longitudinal direction (fibre dominated direction) is strain rate-independent except its strength; ii) a viscoelastic and viscoplastic behaviour is considered in the directions governed by the matrix; iii) damage related properties, strengths and fracture toughnesses can be defined as strain rate-dependent; iv) bilinear softening laws are considered in the longitudinal compressive and tensile directions and linear for the rest of the directions (as in the original model).

The additive decomposition of the infinitesimal strain tensor is considered as

$$\boldsymbol{\varepsilon} = \boldsymbol{\varepsilon}^{ve} + \boldsymbol{\varepsilon}^{vp}, \quad (7.1)$$

where $\boldsymbol{\varepsilon}^{ve}$ is the viscoelastic strain tensor which contains the cracking strains and $\boldsymbol{\varepsilon}^{vp}$ is the viscoplastic strain tensor. The model assumes purely elastic response before the onset of damage in the longitudinal direction. No significant dependence of the strain rates in neither the longitudinal Young's modulus, or in the inelastic deformation was observed in the literature for CFRP laminates for both tensile and compressive loading directions [225–231] (see [Fig. 7.1.a](#)). However, in the transverse directions, strong strain rate dependency on the elastic modulus and during the hardening process in CFRPs was observed [8, 9, 219, 221, 223, 224]. Then, a viscoelastic response followed to a viscoplastic behaviour in the directions governed to the matrix is considered. After that, the onset of damage can be reached in any direction and develops without increasing the viscoplastic strains at the Gauss-point level, see [Fig. 7.1](#).

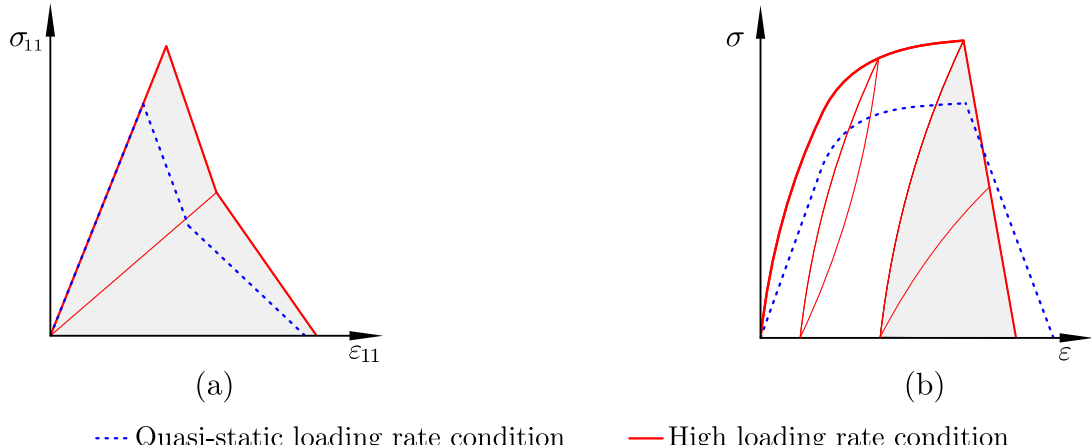


Figure 7.1.: Schematic representation of uniaxial stress vs. strain curve response at the Gauss-point level: a) in the longitudinal direction, and b) in the directions governed by the matrix.

7.1.1 Modelling Viscoelasticity

The viscoelastic effects of CFRPs under different loading rate conditions is modelled using the generalised Maxwell model. The 1D rheological scheme of the viscoelastic part can be divided into two main elements connected in parallel (see Fig. 7.2): i) a Hookean element and ii) a Maxwell element, which consists of a Hookean element and a Newtonian dashpot connected in series. The Hookean element (top left branch in Fig. 7.2) provides the quasi-static stiffness that remains after the dynamic effects have relaxed as the dashpot releases the Maxwell element (bottom left branch in Fig. 7.2).

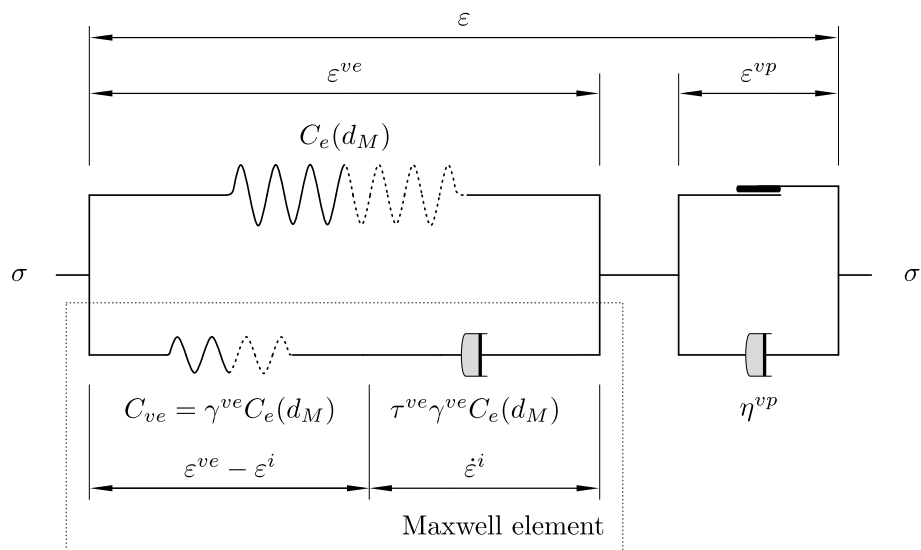


Figure 7.2: Schematic representation of the 1D rheological scheme of the proposed constitutive model.

The Helmholtz free-energy density function proposed in Voigt notation reads

$$\Psi := \frac{1}{2}(\boldsymbol{\varepsilon} - \boldsymbol{\varepsilon}^{vp})^T \mathbb{C}_e (\boldsymbol{\varepsilon} - \boldsymbol{\varepsilon}^{vp}) + \frac{1}{2}(\boldsymbol{\varepsilon} - \boldsymbol{\varepsilon}^{vp} - \boldsymbol{\varepsilon}^i)^T \mathbb{C}_{ve} (\boldsymbol{\varepsilon} - \boldsymbol{\varepsilon}^{vp} - \boldsymbol{\varepsilon}^i), \quad (7.2)$$

where $\boldsymbol{\varepsilon}^i$ is the inelastic strain tensor due to viscoelastic effects, and \mathbb{C}_e and \mathbb{C}_{ve} are the quasi-static and Maxwell elasticity tensors, respectively, see Fig. 7.2. The quasi-static elasticity tensor is defined using the compliance tensor ($\mathbb{H} = \mathbb{C}_e^{-1}$) presented in Eq. (2.10).

The viscoelastic effects in CFRP laminates are only observed in the directions governed by the matrix (in the transverse isotropic plane with respect to the longitudinal direction). Therefore, \mathbb{C}_{ve} is defined proportional to \mathbb{C}_e in the direction governed by the matrix as

$$\mathbb{C}_{ve} := \boldsymbol{\Gamma} \mathbb{C}_e \boldsymbol{\Gamma} \quad (7.3)$$

with

$$\boldsymbol{\Gamma} = \bar{\gamma}^{ve} \mathbb{I}^{ve}, \quad (7.4)$$

where $\bar{\gamma}^{ve}$ is a viscoelastic parameter and \mathbb{I}^{ve} is the identity matrix with the first component equal to zero (longitudinal direction). Based on this hypothesis, a single relaxation time of the Newtonian dashpot of the Maxwell element (τ^{ve}) is defined for the directions governed by the matrix [249]. Consequently, the stress equilibrium in the Maxwell element (bottom left branch in Fig. 7.2) reads

$$\boldsymbol{\Gamma} \mathbb{C}_e \boldsymbol{\Gamma} (\boldsymbol{\varepsilon} - \boldsymbol{\varepsilon}^{vp} - \boldsymbol{\varepsilon}^i) = \boldsymbol{\Gamma} \mathbb{C}_e \boldsymbol{\Gamma} \mathbb{T}^{ve} \dot{\boldsymbol{\varepsilon}}^i, \quad (7.5)$$

where $\mathbb{T}^{ve} = \tau^{ve} \mathbf{I}$ (\mathbf{I} is the identity matrix). These two assumptions allow the implementation of the constitutive model to be simplified. The use of a single τ^{ve} allows the differential equation for the stress (or strain) on the Maxwell element in one-dimensional (1D) to be solved and extending it to 3D directly [249]. Furthermore, the viscoelastic strain rate dependence of CFRP plies can be characterised by two viscoelastic parameters.

The mechanical energy dissipated is defined from the Clausius-Duhem inequality to ensure the thermodynamically consistency of the model and the irreversibility of the dissipated processes [88]. Considering an isothermal state, an energy dissipation carried out in an adiabatic manner, and a constant density, the Clausius-Duhem inequality reads

$$\Xi = \boldsymbol{\sigma} \dot{\boldsymbol{\varepsilon}} - \dot{\Psi} \geq 0, \quad (7.6)$$

where Ξ is the mechanical energy dissipated per unit volume. Applying the corresponding chain rules in Eq. (7.2), the inequality of Eq. (7.6) yields

$$\left(\boldsymbol{\sigma} - \frac{\partial\Psi}{\partial\boldsymbol{\varepsilon}}\right)\dot{\boldsymbol{\varepsilon}} - \frac{\partial\Psi}{\partial\boldsymbol{\varepsilon}^i}\dot{\varepsilon}^i - \frac{\partial\Psi}{\partial\boldsymbol{\varepsilon}^{vp}}\dot{\boldsymbol{\varepsilon}}^{vp} - \sum_M \frac{\partial\Psi}{\partial d_M}\dot{d}_M \geq 0. \quad (7.7)$$

The expression in parenthesis of the first term in Eq. (7.7) must be equal to zero to guarantee this inequality since the strains can freely vary, yielding the constitutive equation:

$$\boldsymbol{\sigma} := \frac{\partial\Psi}{\partial\boldsymbol{\varepsilon}}, \quad (7.8)$$

where $\boldsymbol{\sigma}$ is the stress tensor that can be rewritten from the generalised Maxwell model as

$$\boldsymbol{\sigma} = \mathbb{C}_e(\boldsymbol{\varepsilon} - \boldsymbol{\varepsilon}^{vp}) + \mathbf{G}\mathbb{C}_e\mathbf{G}(\boldsymbol{\varepsilon} - \boldsymbol{\varepsilon}^{vp} - \boldsymbol{\varepsilon}^i). \quad (7.9)$$

The demonstration of the non-negativity of the rest of the terms of Eq. (7.7) is presented in Section 7.2.

The relaxation time of the Newtonian dashpot of the Maxwell element (τ^{ve}) can be measure through a relaxation test from the tangent line where the material starts to relax (σ_{22}) and the stress relaxed ($E_{22}\varepsilon_{22}^{ve}$) [252], see Fig. 7.3. Additionally, for a given τ^{ve} , the viscoelastic parameter ($\bar{\gamma}^{ve}$) can be fitted from an experimental transverse tensile test at constant loading rate. The transverse stress Cartesian component applying uniaxial transverse stress state conditions in Eq. (7.9) at constant strain rate yields

$$\sigma_{22} = E_{22} \left(1 + \gamma^{ve} \tau^{ve} \dot{\varepsilon}_{22}^{ve} \left(1 - \exp \left(\frac{-\varepsilon_{22}^{ve}}{\tau^{ve} \dot{\varepsilon}_{22}^{ve}} \right) \right) \right) \varepsilon_{22}^{ve}, \quad (7.10)$$

where γ^{ve} is the uniaxial viscoelastic parameter. Therefore, γ^{ve} can be fitted from a pure transverse test using Eq. (7.10) and, thus, $\bar{\gamma}^{ve}$ in Eq. (7.4) can be rewritten as a function of the uniaxial viscoelastic parameter as

$$\bar{\gamma}^{ve} = \sqrt{\gamma^{ve} \left(1 - \frac{E_{22}}{E_{11}} \nu_{12}^2 \right)}. \quad (7.11)$$

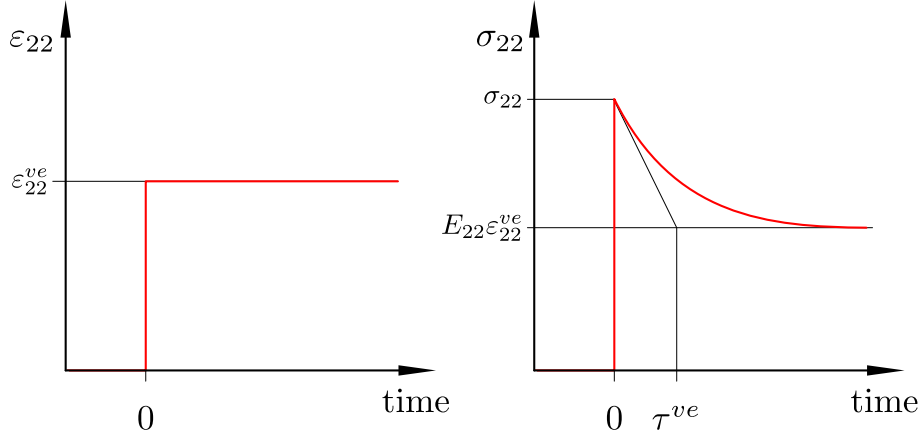


Figure 7.3.: Schematic representation of a transverse tensile test to measure the relaxation time of the Newtonian dashpot of the Maxwell element (τ^{ve}).

7.1.2 Modelling Viscoplasticity

A non-associative viscoplastic flow rule is employed allowing the volumetric viscoplastic strains and the plastic Poisson's ratios to be imposed,

$$\dot{\varepsilon}^{vp} := \lambda^{vp} \frac{\partial \varphi^p}{\partial \sigma}, \quad (7.12)$$

where λ^{vp} is the viscoplastic multiplier parameter and φ^p is the viscoplastic potential function defined in Eq. (2.21). The main difference in modelling plasticity between the model developed in the previous chapters (the original and enhanced elastoplastic damage models) and the one proposed in the present chapter is the definition of λ^{vp} .

The explicit function for λ^{vp} proposed by Perzyna [239], and used in many previously-developed constitutive models [241, 249, 250], is adopted. The Overstress model [239] allows the yield function to become larger than zero for describing the viscoplastic strain. In addition, the loading-unloading hysteresis observed in the stress-strain relationships in CFRP laminates, which can be attributed to a viscoplastic behaviour of matrix rich zones [253], can be predicted from the Overstress model [254]. The viscoplastic multiplier parameter is defined as

$$\lambda^{vp} := \frac{\langle (\phi^p)^{1/\beta^{vp}} \rangle}{\eta^{vp}}, \quad (7.13)$$

where ϕ^p is the yield function defined in Eq. (2.12), $\eta^{vp} \in (0, \infty)$ is the viscoplasticity-related parameter, and β^{vp} is the rate sensitivity parameter. Then, the proposed model matches the previous elastoplastic damage models with vanishing viscosity ($\eta^{vp} \rightarrow 0$) in Eq. (7.13) since $\dot{\varepsilon}^{vp} \rightarrow \infty$. However, the Overstress model does not reproduce the quasi-static plastic response with vanishing $\beta^{vp} \rightarrow 0$. For example, under uniaxial transverse compressive loading conditions using a quasi-static strain rate and $\beta^{vp} \rightarrow 0$,

the viscoplasticity modelling produces two times the transverse compressive yield stress ($\sigma_{22} = -2Y_{CP}$) [255]. This behaviour can be avoided by modifying Eq. (7.13) as in [255–257].

The yield function is defined as a function of the yield stresses in Eq. (2.12), and they are defined as a function of the equivalent viscoplastic strain ($\bar{\varepsilon}^{vp}$) (viscoplastic internal variable). In the proposed model, the yield stress-equivalent viscoplastic strain relationships are defined using an experimental curve for each of them, as in the previous models, and the rate of the viscoplastic internal variable is then defined as

$$\dot{\varepsilon}^{vp} := \sqrt{\frac{1}{2} \|\dot{\varepsilon}^{vp}\|}. \quad (7.14)$$

7.1.3 Modelling Viscodamage

An undamaged domain, in which the material response is viscoelastic and viscoplastic under loading states, is defined to account for the longitudinal failure and matrix cracking. Three loading functions are defined to enclose the undamaged domain. The viscodamage activation functions associated to the longitudinal and transverse failure mechanisms are defined using Eqs. (2.29) and (3.2), respectively, and the longitudinal viscoelastic domains by using Eq. (2.30) and the transverse viscodamage domain as Eq. (3.10).

The loading functions proposed by Quintanas-Corominas et al. [86], which were used in the previous proposed constitutive models, are also used in the present model. However, the quasi-static strengths are replaced with the viscous strengths. Therefore, the non-interacting maximum allowable strain criteria is employed in the longitudinal tensile as

$$\phi_{\ell T} := \frac{\varepsilon_{11}^{ve} E_{11}}{X_T^v}, \quad (7.15)$$

where X_T^v is the viscous longitudinal tensile strength. The longitudinal compressive loading function reads

$$\phi_{\ell C} := \frac{1}{X_C^v} \left(\sqrt{\tilde{\sigma}_{11}^2 + \eta_t^q \tilde{p}_t^2 + \eta_{s\ell}^q \tilde{\tau}_\ell^2} + \eta_t \tilde{p}_t + \eta_{s\ell} \tilde{\tau}_\ell \right), \quad (7.16)$$

where X_C^v is the viscous longitudinal compressive strength. The transverse loading function reads

$$\phi_t := \sqrt{\left(\frac{Y_C^v + Y_T^v}{Y_T^v Y_C^v} \right)^2 \frac{\tau_t^2 + \mu_t p_t^2}{1 + \mu_t} + \left(\frac{\mu_{s\ell}}{S_L^v} \tau_\ell \right)^2} + \frac{Y_C^v - Y_T^v}{Y_T^v Y_C^v} p_t + \frac{1 - \mu_{s\ell}}{S_L^v} \tau_\ell, \quad (7.17)$$

where Y_C^v and Y_T^v are the viscous transverse compressive and tensile strengths, respectively, S_L^v is the viscous longitudinal shear strength. The viscous strengths in Eqs. (7.15)–(7.17) can be defined by considering the dynamic effects using experimental expressions as a function of the: strain rate [9, 80, 241–247], viscoplastic strains as in metallic material models [258, 259], strain rate, and ultimate strain as in concrete constitutive models [260], etc.

The softening law of each transverse viscodamage variable is defined in the equivalent viscoelastic domain to simplify the implementation. The stress tensor in Eq. (7.9) can be rewritten as

$$\boldsymbol{\sigma} = \mathbf{C}_e \bar{\boldsymbol{\varepsilon}}^{ve}, \quad (7.18)$$

where the equivalent viscoelastic strain tensor yields

$$\bar{\boldsymbol{\varepsilon}}^{ve} = \boldsymbol{\varepsilon}^{ve} + \mathbb{H}\boldsymbol{\Gamma}\mathbf{C}_e\boldsymbol{\Gamma}(\boldsymbol{\varepsilon}^{ve} - \boldsymbol{\varepsilon}^i). \quad (7.19)$$

Therefore, the definition of the viscodamage evolution functions match those of the original constitutive model since Eq. (7.18) has the same form to the quasi-static model ($\boldsymbol{\sigma} = \mathbf{C}_e \boldsymbol{\varepsilon}^e$) replacing $\bar{\boldsymbol{\varepsilon}}^{ve}$ by $\boldsymbol{\varepsilon}^e$. Additionally, the softening laws follow the same shape in the proposed domain ($\bar{\boldsymbol{\varepsilon}}^{ve}$) as opposed to the $\boldsymbol{\varepsilon}^{ve}$ domain in the previous models. However, the correct amount of energy dissipated by viscodamage is guaranteed in the $\boldsymbol{\varepsilon}^{ve}$ domain.

The outcome of this simplification on the softening response is analysed in Fig. 7.4, and no significant effect is observed. The transverse viscodamage variables can be explicitly obtained following the approach presented in Chapter 3. The relationship of the longitudinal viscodamage variables with the corresponding viscoelastic threshold domain is described in Chapter 2. The fracture toughnesses can be also defined as a function of the strain rate using experimental expressions. Finally, a bilinear softening law is defined for the longitudinal direction and a linear softening law in the directions governed by the matrix.

7.2 Thermodynamic consistency of the viscoelastic-viscoplastic viscodamage model

The demonstration of the thermodynamic consistency of the viscoelastic-viscoplastic viscodamage model is presented in this section. To ensure the thermodynamically irreversibility of dissipation processes, the energy dissipated must be positive or at least null. The

mechanical energy dissipated of the present constitutive model can be rewritten from Eq. (7.6) as

$$\Xi = -\frac{\partial \Psi}{\partial \dot{\boldsymbol{\varepsilon}}^i} \dot{\boldsymbol{\varepsilon}}^i - \frac{\partial \Psi}{\partial \boldsymbol{\varepsilon}^{vp}} \dot{\boldsymbol{\varepsilon}}^{vp} - \sum_M \frac{\partial \Psi}{\partial d_M} \dot{d}_M \geq 0. \quad (7.20)$$

Then, if each term in Eq. (7.20) is equal to or greater than zero, the thermodynamic irreversibility of dissipation processes will be ensured. The following subsections describe the demonstration that the present constitutive model fulfils the inequality of Eq. (7.20).

7.2.1 Thermodynamic consistency of the viscoelastic energy dissipated

The mechanical energy dissipated due to a viscoelastic process from Eq. (7.20) reads

$$-\frac{\partial \Psi}{\partial \dot{\boldsymbol{\varepsilon}}^i} \dot{\boldsymbol{\varepsilon}}^i = (\mathbf{C}_{ve}(\boldsymbol{\varepsilon} - \boldsymbol{\varepsilon}^{vp} - \dot{\boldsymbol{\varepsilon}}^i))^T \dot{\boldsymbol{\varepsilon}}^i, \quad (7.21)$$

where $\partial_{\dot{\boldsymbol{\varepsilon}}^i}(\Psi)$ is the stress tensor of the Hookean element of the Maxwell component (bottom left branch in Fig. 7.2, left hand side of Eq. (7.5)). Therefore, by introducing the right hand side of Eq. (7.5) into Eq. (7.21), the viscoelastic mechanical energy dissipated yields

$$-\frac{\partial \Psi}{\partial \dot{\boldsymbol{\varepsilon}}^i} \dot{\boldsymbol{\varepsilon}}^i = (\mathbf{\Gamma C}_e \mathbf{\Gamma T}^{ve} \dot{\boldsymbol{\varepsilon}}^i)^T \dot{\boldsymbol{\varepsilon}}^i. \quad (7.22)$$

The non-negativity of \mathbf{C}_e can be demonstrate by the definition of \mathbb{H} , since the inverse of a positive semi-definite matrix is also a positive semi-definite matrix, Condition v) in Appendix H. Therefore, the non-negativity of \mathbb{H} can be demonstrate by the product of an arbitrary vector $(\boldsymbol{\sigma})$ with \mathbb{H} , Condition ii) in Appendix H, as

$$\boldsymbol{\sigma}^T \mathbb{H} \boldsymbol{\sigma} = \frac{\sigma_\ell^2}{(1-d_\ell)E_{11}} - \frac{4\nu_{12}\sigma_\ell p_t}{E_{11}} + \frac{p_t^2}{(1-d_t)E_t} + \frac{\tau_t^2}{(1-d_{st})G_t} + \frac{\tau_\ell^2}{(1-d_{s\ell})G_{12}}. \quad (7.23)$$

Applying the thermodynamic restrictions of the elastic material properties of transversely isotropic materials [90],

$$\begin{aligned} E_{11}, E_{22}, G_{12} &> 0 \\ |\nu_{23}| &< 1 \\ |\nu_{12}| &< \sqrt{\frac{E_{11}}{E_{22}}} \\ -1 &< \nu_{23} < 1 - 2\nu_{12}^2 \frac{E_{11}}{E_{22}}, \end{aligned} \quad (7.24)$$

and by setting the range of the damage variables to $d_M \in [0, 1]$, the expression in Eq. (7.23) is always non-negative,

$$\boldsymbol{\sigma}^T \mathbb{H} \boldsymbol{\sigma} \geq 0. \quad (7.25)$$

Therefore, \mathbb{H} is a positive semi-definite matrix and its inverse matrix (\mathbb{C}_e) is also a positive semi-definite matrix.

The non-negativity of $\mathbf{\Gamma} \mathbb{C}_e \mathbf{\Gamma} \mathbf{T}^{ve}$ can be demonstrated because the product of positive semi-definite matrices is equal to its transpose, Condition iv) in Appendix H, thereby resulting also in a positive semi-definite matrix,

$$\tau^{ve} \bar{\gamma}^{ve2} \mathbb{I}^{ve} \mathbb{C}_e \mathbb{I}^{ve} = \tau^{ve} \bar{\gamma}^{ve2} (\mathbb{I}^{ve} \mathbb{C}_e \mathbb{I}^{ve})^T. \quad (7.26)$$

Therefore, $\mathbf{\Gamma} \mathbb{C}_e \mathbf{\Gamma} \mathbf{T}^{ve}$ is a positive semi-definite matrix for all $\tau^{ve} \geq 0$. Finally, Eq. (7.22) can be rewritten as

$$-\frac{\partial \Psi}{\partial \dot{\boldsymbol{\varepsilon}}^i} \dot{\boldsymbol{\varepsilon}}^i = \dot{\boldsymbol{\varepsilon}}^{iT} (\mathbf{\Gamma} \mathbb{C}_e \mathbf{\Gamma} \mathbf{T}^{ve})^T \dot{\boldsymbol{\varepsilon}}^i, \quad (7.27)$$

where the right hand side of Eq. (7.27) yields the condition of the product of a positive semi-definite matrix by a non-negative vector ($\dot{\boldsymbol{\varepsilon}}^i$), Condition ii) in Appendix H. Hence, the mechanical energy dissipated due to a viscoelastic process is always positive or at least null.

7.2.2 Thermodynamic consistency of the viscoplastic energy dissipated

The mechanical energy dissipated due to a viscoplastic process from Eq. (7.20) yields

$$-\frac{\partial \Psi}{\partial \dot{\boldsymbol{\varepsilon}}^{vp}} \dot{\boldsymbol{\varepsilon}}^{vp} = (\mathbb{C}_e(\boldsymbol{\varepsilon} - \boldsymbol{\varepsilon}^{vp}) + \mathbb{C}_{ve}(\boldsymbol{\varepsilon} - \boldsymbol{\varepsilon}^{vp} - \boldsymbol{\varepsilon}^i))^T \dot{\boldsymbol{\varepsilon}}^{vp}. \quad (7.28)$$

Then, Eq. (7.28) can be rewritten by inserting Eq. (7.9) and Eq. (7.12) as

$$-\frac{\partial \Psi}{\partial \dot{\boldsymbol{\varepsilon}}^{vp}} \dot{\boldsymbol{\varepsilon}}^{vp} = \lambda \boldsymbol{\sigma}^T \frac{\partial \varphi^p}{\partial \boldsymbol{\sigma}}. \quad (7.29)$$

Therefore, the mechanical energy dissipated of Eq. (7.28) yields

$$\begin{aligned} -\frac{\partial \Psi}{\partial \dot{\boldsymbol{\varepsilon}}^{vp}} \dot{\boldsymbol{\varepsilon}}^{vp} &= \lambda \sqrt{\left(\frac{\hat{Y}_{CP} + \hat{Y}_{TP}}{\hat{Y}_{TP} \hat{Y}_{CP}} \right)^2 \frac{\tau_t^2 + \hat{\mu}_{tp} p_t^2}{1 + \hat{\mu}_{tp}} + \left(\frac{\hat{\mu}_{s\ell p}}{\hat{S}_{LP}} \tau_\ell \right)^2} \\ &\quad + \lambda \left(\frac{\hat{Y}_{CP} - \hat{Y}_{TP}}{\hat{Y}_{TP} \hat{Y}_{CP}} p_t + \frac{1 - \hat{\mu}_{s\ell p}}{\hat{S}_{LP}} \tau_\ell \right). \end{aligned} \quad (7.30)$$

Hence, the first and third terms in parenthesis of Eq. (7.30) will always be non-negative for all $\hat{\mu}_{s\ell p} \leq 1$. Then, the right hand side of Eq. (7.30) only will be negative if $p_t < 0$, since $\lambda \geq 0$ from the Kuhn-Tucker conditions and all viscoplastic potential parameter must be defined positive. The worst case scenario to meet the negativity of the mechanical energy dissipated due to a viscoplastic process is

$$\begin{aligned}\sigma_{23} &= \sigma_{13} = \sigma_{12} = 0 \\ \sigma_{22} &= \sigma_{33} < 0.\end{aligned}\quad (7.31)$$

Hence, by introducing the conditions of Eq. (7.31) in Eq. (7.30), the viscoplastic mechanical energy dissipated yields

$$\left. \left(-\frac{\partial \Psi}{\partial \boldsymbol{\varepsilon}^{vp}} \dot{\boldsymbol{\varepsilon}}^{vp} \right) \right|_{Eq. (7.31)} = \frac{\lambda}{\hat{Y}_{TP} \hat{Y}_{CP}} \left((\hat{Y}_{CP} + \hat{Y}_{TP}) \sqrt{\frac{\hat{\mu}_{tp}}{1 + \hat{\mu}_{tp}}} - (\hat{Y}_{CP} - \hat{Y}_{TP}) \right) |p_t|. \quad (7.32)$$

Therefore, the following conditions are imposed to ensure the non-negativity of the mechanical energy dissipated by a viscoplastic process:

$$\begin{aligned}\hat{\mu}_{s\ell p} &\leq 1 \\ \hat{Y}_{TP} &\leq \hat{Y}_{CP} \\ \frac{1 + \frac{\hat{\mu}_{tp}}{1 + \hat{\mu}_{tp}}}{1 - \frac{\hat{\mu}_{tp}}{1 + \hat{\mu}_{tp}}} &\leq \frac{\hat{Y}_{CP}}{\hat{Y}_{TP}}.\end{aligned}\quad (7.33)$$

7.2.3 Thermodynamic consistency of the viscodamage energy dissipated

The mechanical energy dissipated due to a viscodamage process defined in Eq. (7.20) can be rewritten knowing that $\mathbb{C}_e(d_M)$ (its inverse is defined in Eq. (2.10)) and applying the corresponding chain rule as

$$\begin{aligned}- \sum_M \frac{\partial \Psi}{\partial d_M} \dot{d}_M &= - \frac{1}{2} \left((\boldsymbol{\varepsilon} - \boldsymbol{\varepsilon}^{vp})^T \sum_M \left(\frac{\partial \mathbb{C}_e}{\partial d_M} \dot{d}_M \right) (\boldsymbol{\varepsilon} - \boldsymbol{\varepsilon}^{vp}) \right) \\ &\quad - \frac{1}{2} \left((\boldsymbol{\varepsilon} - \boldsymbol{\varepsilon}^{vp} - \boldsymbol{\varepsilon}^i)^T \boldsymbol{\Gamma} \sum_M \left(\frac{\partial \mathbb{C}_e}{\partial d_M} \dot{d}_M \right) \boldsymbol{\Gamma} (\boldsymbol{\varepsilon} - \boldsymbol{\varepsilon}^{vp} - \boldsymbol{\varepsilon}^i) \right).\end{aligned}\quad (7.34)$$

The derivative of \mathbb{C}_e with respect to d_M can be rewritten as

$$\frac{\partial \mathbb{C}_e}{\partial d_M} = -\mathbb{C}_e \frac{\partial \mathbb{H}}{\partial d_M} \mathbb{C}_e, \quad (7.35)$$

therefore, Eq. (7.34) yields

$$\begin{aligned} -\sum_M \frac{\partial \Psi}{\partial d_M} \dot{d}_M &= \frac{1}{2} \left((\boldsymbol{\varepsilon} - \boldsymbol{\varepsilon}^{vp})^T \sum_M \left(\mathbb{C}_e \frac{\partial \mathbb{H}}{\partial d_M} \mathbb{C}_e \dot{d}_M \right) (\boldsymbol{\varepsilon} - \boldsymbol{\varepsilon}^{vp}) \right) \\ &\quad + \frac{1}{2} \left((\boldsymbol{\varepsilon} - \boldsymbol{\varepsilon}^{vp} - \boldsymbol{\varepsilon}^i)^T \boldsymbol{\Gamma} \sum_M \left(\mathbb{C}_e \frac{\partial \mathbb{H}}{\partial d_M} \mathbb{C}_e \dot{d}_M \right) \boldsymbol{\Gamma} (\boldsymbol{\varepsilon} - \boldsymbol{\varepsilon}^{vp} - \boldsymbol{\varepsilon}^i) \right), \end{aligned} \quad (7.36)$$

where \mathbb{C}_e is a positive semi-definite matrix as proved in Section 7.2.1. The non-negativity of $\partial_{d_M}(\mathbb{H})$ can be demonstrated by the non-negativity of their eigenvalues, Condition i) in Appendix H. The eigenvalues of $\partial_{d_\ell}(\mathbb{H})$ are

$$\begin{aligned} \lambda_{\partial_{d_\ell}(\mathbb{H})_1} &= \frac{1}{E_{11}(1-d_\ell)^2} > 0 \\ \lambda_{\partial_{d_\ell}(\mathbb{H})_{2-6}} &= 0, \end{aligned} \quad (7.37)$$

the eigenvalues of $\partial_{d_t}(\mathbb{H})$ are

$$\begin{aligned} \lambda_{\partial_{d_t}(\mathbb{H})_1} &= \frac{1}{E_t(1-d_t)^2} > 0 \\ \lambda_{\partial_{d_t}(\mathbb{H})_{2-6}} &= 0, \end{aligned} \quad (7.38)$$

the eigenvalues of $\partial_{d_{st}}(\mathbb{H})$ are

$$\begin{aligned} \lambda_{\partial_{d_{st}}(\mathbb{H})_1} &= \frac{1}{G_t(1-d_{st})^2} > 0 \\ \lambda_{\partial_{d_{st}}(\mathbb{H})_2} &= \frac{1}{2} \lambda_{\partial_{d_{st}}(\mathbb{H})_1} > 0 \\ \lambda_{\partial_{d_{st}}(\mathbb{H})_{3-6}} &= 0, \end{aligned} \quad (7.39)$$

and the eigenvalues of $\partial_{d_{s\ell}}(\mathbb{H})$ are

$$\begin{aligned} \lambda_{\partial_{d_{s\ell}}(\mathbb{H})_{1-2}} &= \frac{1}{G_{12}(1-d_{s\ell})^2} > 0 \\ \lambda_{\partial_{d_{s\ell}}(\mathbb{H})_{3-6}} &= 0. \end{aligned} \quad (7.40)$$

Therefore, $\partial_{d_M}(\mathbb{H})$ is a positive semi-definite matrix:

$$\frac{\partial \mathbb{H}}{\partial d_M} \geq 0. \quad (7.41)$$

The non-negativity of the first summand term in Eq. (7.36) can be demonstrate since the transpose matrix of a symmetric matrix is equal to the matrix itself, [Condition iv\)](#) in [Appendix H](#),

$$\mathbb{C}_e \frac{\partial \mathbb{H}}{\partial d_M} \mathbb{C}_e = \left(\mathbb{C}_e \frac{\partial \mathbb{H}}{\partial d_M} \mathbb{C}_e \right)^T, \quad (7.42)$$

then,

$$\mathbb{C}_e \frac{\partial \mathbb{H}}{\partial d_M} \mathbb{C}_e \dot{d}_M \geq 0, \quad (7.43)$$

since $\dot{d}_M \geq 0$ because the damage is irreversible. Using the same procedure, the non-negativity of the second summand term in Eq. (7.36) yields

$$\boldsymbol{\Gamma} \mathbb{C}_e \frac{\partial \mathbb{H}}{\partial d_M} \mathbb{C}_e \boldsymbol{\Gamma} = \left(\boldsymbol{\Gamma} \mathbb{C}_e \frac{\partial \mathbb{H}}{\partial d_M} \mathbb{C}_e \boldsymbol{\Gamma} \right)^T, \quad (7.44)$$

and, therefore,

$$\boldsymbol{\Gamma} \mathbb{C}_e \frac{\partial \mathbb{H}}{\partial d_M} \mathbb{C}_e \boldsymbol{\Gamma} \dot{d}_M \geq 0. \quad (7.45)$$

Finally, the mechanical energy dissipated by a viscodamage process is a product of a positive semi-definite matrices and an arbitrary vector, [Condition ii\)](#) in [Appendix H](#). For example, the left hand side terms in Eq. (7.42) is positive semi-definite matrix multiplied by $(\boldsymbol{\varepsilon} - \boldsymbol{\varepsilon}^{vp})$, then,

$$(\boldsymbol{\varepsilon} - \boldsymbol{\varepsilon}^{vp})^T \sum_M \left(\mathbb{C}_e \frac{\partial \mathbb{H}}{\partial d_M} \mathbb{C}_e \dot{d}_M \right) (\boldsymbol{\varepsilon} - \boldsymbol{\varepsilon}^{vp}) \geq 0. \quad (7.46)$$

Similar, the left hand side terms in Eq. (7.44) is positive semi-definite matrix multiplied by $(\boldsymbol{\varepsilon} - \boldsymbol{\varepsilon}^{vp} - \boldsymbol{\varepsilon}^i)$, hence,

$$(\boldsymbol{\varepsilon} - \boldsymbol{\varepsilon}^{vp} - \boldsymbol{\varepsilon}^i)^T \boldsymbol{\Gamma} \sum_M \left(\mathbb{C}_e \frac{\partial \mathbb{H}}{\partial d_M} \mathbb{C}_e \dot{d}_M \right) \boldsymbol{\Gamma} (\boldsymbol{\varepsilon} - \boldsymbol{\varepsilon}^{vp} - \boldsymbol{\varepsilon}^i) \geq 0. \quad (7.47)$$

Therefore, the mechanical energy dissipated due to a viscodamage process is equal to or greater than zero.

7.2.4 Thermodynamic restrictions of the material properties

The thermodynamic restrictions to ensure the non-negativity of the mechanical energy dissipated presented in Eq. (7.20) can be divided in three main groups: viscoelastic restrictions, viscoplastic restrictions and viscodamage restrictions. They are presented in the previous subsections. Then, the restrictions are summarised, the one from the viscoelastic mechanical energy dissipated reads

$$\begin{aligned} \tau^{ve} &\geq 0 \\ E_{11}, E_{22}, G_{12} &> 0 \\ |\nu_{23}| &< 1 \\ |\nu_{12}| &< \sqrt{\frac{E_{11}}{E_{22}}} \\ -1 < \nu_{23} &< 1 - 2\nu_{12}^2 \frac{E_{11}}{E_{22}}. \end{aligned} \tag{7.48}$$

The restrictions from the viscoplastic mechanical energy dissipated are

$$\begin{aligned} \hat{Y}_{CP}, \hat{Y}_{TP}, \hat{S}_{LP}, \hat{\mu}_{tp} &\geq 0 \\ 0 \leq \hat{\mu}_{s\ell p} &\leq 1 \\ \hat{Y}_{TP} &\leq \hat{Y}_{CP} \\ \frac{1 + \frac{\hat{\mu}_{tp}}{1 + \hat{\mu}_{tp}}}{1 - \frac{\hat{\mu}_{tp}}{1 + \hat{\mu}_{tp}}} &\leq \frac{\hat{Y}_{CP}}{\hat{Y}_{TP}}. \end{aligned} \tag{7.49}$$

Finally, the restrictions imposed from a viscodamage process are those defined in Eq. (7.48), except the first conditions, and

$$0 \leq d_M \leq 1. \tag{7.50}$$

7.3 Numerical predictions

Several tests are performed to demonstrate the capabilities of the proposed constitutive model at the Gauss-point level. In addition, the off-axis compressive experimental tests carried out by Koerber et al. [8] are used to demonstrate the ability of the present model to predict the inelastic deformation and fracture of CFRPs under different loading rates. In both cases, the IM7/8552 unidirectional prepreg system is employed with the quasi-static model input parameters listed in Table 2.3. The dynamic model input parameters are listed in Table 7.2 and their calibration is explained in detail in Section 7.3.3. Note that,

only four dynamic parameters are required in the viscoelastic and viscoplastic regions due to the isotropy of the CFRP laminates in the directions governed by the matrix.

Table 7.2.: Dynamic model input parameters for a unidirectional IM7/8552 prepreg system.

	Symbol	Value	Unit
Density	-	1570 [261]	kg/m ³
Viscoelastic	γ^{ve}	0.35	-
	τ^{ve}	10^{-4}	s
Viscoplastic	β^{vp}	1.00	-
	η^{vp}	2.25×10^{-5}	s
Viscodamage	η^{vd}	4.00×10^{-5}	s

7.3.1 Calibration of the strengths under dynamic conditions

Based on the experimental observations reported in the literature, the transverse strengths and the longitudinal compressive strength for the selected material (IM7/8552) can be defined as

$$\sigma_u^{dyn} := \sigma_u \left(1 + (1.13 \times 10^{-4} \dot{\varepsilon}_{ij}^{ve})^{\frac{1}{4}} \right), \quad (7.51)$$

where σ_u is the strength under quasi-static loading conditions (e.g. the longitudinal compressive strength is $\sigma_u^{dyn}(\sigma_u = X_C) = X_C^{dyn}$). Eq. (7.51) is proposed by Wiegand [262] and calibrated for the selected material in [9, 220] for a 1D strain rate state, thus Eq. (7.51) must be extended to a 3D state to be employed in the present constitutive model. The following norm is defined to evaluate Eq. (7.51) under a 3D state for the longitudinal compressive strength,

$$\dot{\phi}_{\ell C}^{qs} := \frac{d\phi_{\ell C}^{qs}}{d\varepsilon^{ve}} \dot{\varepsilon}^{ve}, \quad (7.52)$$

where $\phi_{\ell C}^{qs}$ is the longitudinal compressive loading function defined in Eq. (7.16), and evaluated by replacing X_C^v with X_C and $d_M = 0$. Therefore, σ_u^{dyn} can be rewritten using $\dot{\phi}_{\ell C}^{qs}$ under a pure uniaxial loading state (as with Eq. (7.51) was obtained) and yields

$$X_C^{dyn} = X_C \left(1 + \left(1.13 \times 10^{-4} \frac{\dot{\phi}_{\ell C}^{qs} X_C}{E_{11}} \right)^{\frac{1}{4}} \right). \quad (7.53)$$

The norm to obtain the transverse strengths ($\dot{\phi}_t^{qs}$) is defined as Eq. (7.52) by replacing $\dot{\phi}_{\ell C}^{qs}$ by $\dot{\phi}_t^{qs}$ in Eq. (7.17) and using the quasi-static strengths. Therefore, Eq. (7.52) can be rewritten for Y_C^{dyn} as

$$Y_C^{dyn} = Y_C \left(1 + \left(1.13 \times 10^{-4} \frac{\dot{\phi}_t^{qs} Y_C}{E_{22}} \right)^{\frac{1}{4}} \right). \quad (7.54)$$

The rest of the transverse strengths (Y_T^{dyn} and S_L^{dyn}) have the same form of Eq. (7.54) by replacing Y_C and E_{22} with the corresponding quasi-static strength and Young's modulus, respectively. Explicit FE solver is used to obtain the numerical predictions, and both norms ($\dot{\phi}_{\ell C}^{qs}$ and $\dot{\phi}_t^{qs}$) are numerically integrated using the backward Euler method. No significant error is found in the numerical integration process of $\dot{\phi}_{\ell C}^{qs}$ and $\dot{\phi}_t^{qs}$ since the increment of the time in the explicit FE solver is less than 10^{-8} s.

In the present model, the longitudinal tensile strength is defined strain rate-independent since no experimental data on the strength-strain rate relationship are available for the selected material. As with the longitudinal tensile strength, the fracture toughnesses are defined constants since no clear trend or experimental data were found.

A viscosity regularisation of the strengths is considered to prevent high strength rates with high strain rate. The viscous strength rate is defined as

$$\dot{\sigma}_u^v := \frac{\sigma_u^{dyn} - \sigma_u^v}{\eta^{vd}}, \quad (7.55)$$

where η^{vd} is a viscodamage-related parameter. This viscous regularisation is applied at all strengths defined in Eqs. (7.16) and (7.17). For example, the viscous longitudinal compressive strength (X_C^v) is obtained using Eq. (7.53) and then its viscous regularisation ($(\dot{\sigma}_u^v(\sigma_u^{dyn} = X_C^{dyn}) = \dot{X}_C^v)$) is applied based on Eq. (7.55).

7.3.2 Gauss-point level tests

Virtual tests at the Gauss-point level are carried out to verify that the present constitutive model complies with the assumptions made in its development (see Section 7.1). A single Gauss-point is loaded under simple longitudinal shear conditions (see Fig. 7.4a) at a high loading rate ($\dot{\varepsilon}_{12} = 200 \text{ s}^{-1}$), as well as at a quasi-static loading rate ($\dot{\varepsilon}_{12} = 10^{-4} \text{ s}^{-1}$). The Gauss-point is defined as a cube of $0.24 \text{ mm} \times 0.24 \text{ mm} \times 0.24 \text{ mm}$ (the same in-plane mesh element size is used in the off-axis compressive FE models of Section 7.3.3).

The schematic representation of the deformed shape of the simple longitudinal shear test is presented in Fig. 7.4b. The stress-strain response obtained from the high strain rate in the viscoelastic region is stiffer than that obtained from the quasi-static loading rate conditions, see Fig. 7.4c. The stress component from the Maxwell element in that region is linear since τ^{ve} of the selected material is large enough compared with the time when the viscoplastic process starts ($\tau^{ve} \gg 2.10 \times 10^{-5}$ s). The viscoplastic hardening from the dynamic case starts with a smaller ε_{12} compared with the quasi-static simulation, but at similar σ_{12} (see cross markers in Fig. 7.4c). Furthermore, the hardening process is also stiffer at the high strain rate, which can be observed by comparing the two responses with no damage ($d_{st} = 0$) in Fig. 7.4c. This indicates a high strain rate dependency of the analysed material on both the viscoelastic and viscoplastic hardening processes under simple longitudinal shear loading conditions.

The increase in the strength with the high strain rate obtained from Eq. (7.51) using $\sigma_u = S_L$ at $\dot{\varepsilon}_{12} = 200 \text{ s}^{-1}$ ($S_L^v = S_L^{dyn} = 128.09 \text{ MPa}$) is properly predicted from the dynamic simulation in Fig. 7.4c. Equivalent energy dissipated by the viscodamage process is obtained from both loading rate conditions (0.8 N/mmm, grey area in Fig. 7.4c) since the fracture toughness is defined as strain rate-independent for the selected material which match \mathcal{G}_{S_L} . Therefore, the absolute value of the slope of the softening law increases with a high strain rate.

The effect of implementing the equivalent viscoelastic domain (see Eq. (7.18)) on the viscodamage softening response is analysed using a linear regression analysis in the softening region. Although the softening is not a straight line due to the non-linearities contributed by the Maxwell element, but this is not significant. The coefficient of determination from the linear regression analysis conducted in the viscodamage softening region is equal to one ($R^2 = 1.00$, linear stress-strain relationship in the viscodamage softening).

A relaxation test is also carried out applying simple longitudinal shear loading conditions. A Gauss-point is loaded to a prescribed strain ($\varepsilon_{12} = 4\%$) at $\dot{\varepsilon}_{12} = 200 \text{ s}^{-1}$ and, then, maintained it loaded at $\dot{\varepsilon}_{12} = 0$ over a long period of time, see Fig. 7.5a. In this case, a time-dependent response is observed. Firstly, the nominal longitudinal shear stress (σ_{12}) increases with the increasing of ε_{12} . Then, ε_{12} remains constant and σ_{12} slowly decreases since the stress component of the Maxwell element decreases and the viscoplastic process relaxes until they vanish, see Fig. 7.5b. Finally, the material is damaged without increasing ε_{12} but due to how S_L^v is relaxed. The viscodamage variable d_{se} is activated after ε_{12} is fixed since S_L^v relaxes faster than σ_{12} . Therefore, σ_{12} decreases at the end of the test not only because the material relaxes, but also because a failure mechanism is initiated

$(d_{s\ell} > 0)$. Note that, less than 30% of \mathcal{G}_{S_L} is dissipated during the relaxation test. In addition, the longitudinal shear strength is also strain rate-dependent and its viscous regularisation is observed in Fig. 7.5b; S_L^v tends to S_L at the end of the test.

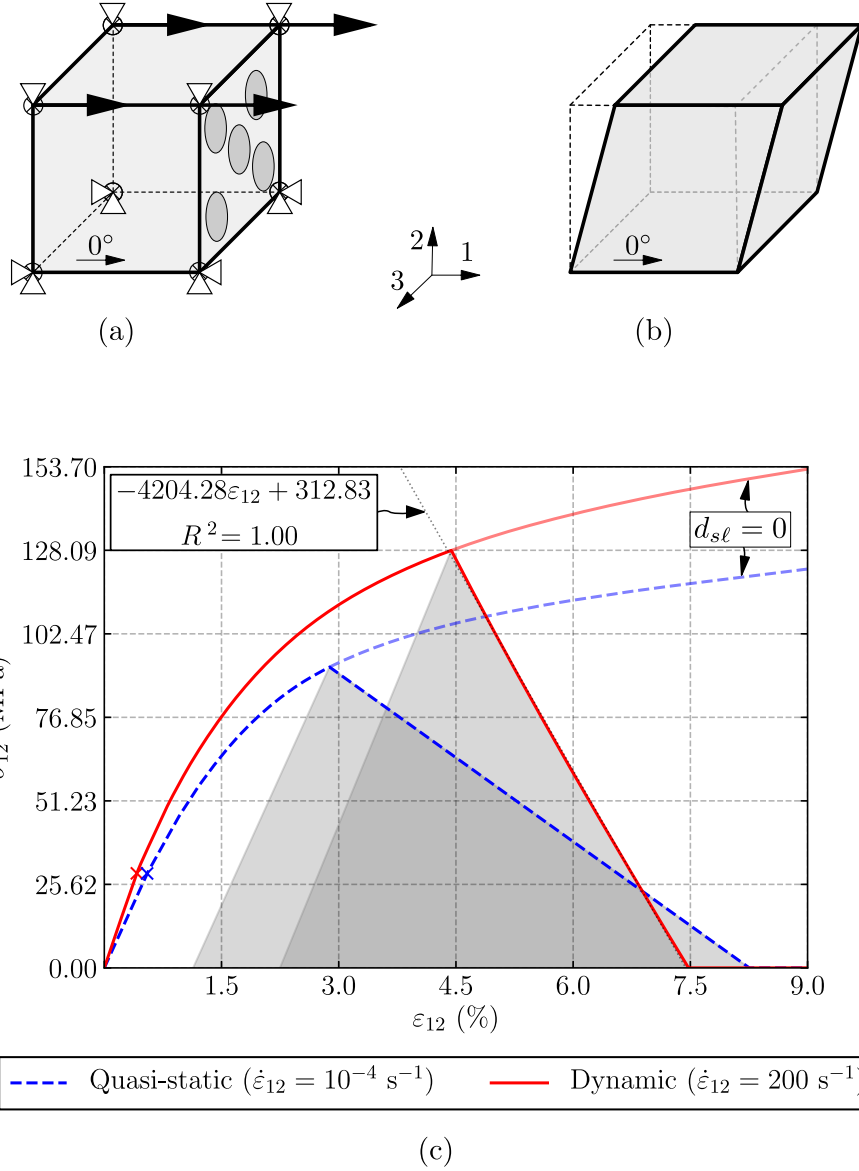


Figure 7.4: Simple longitudinal shear virtual test at the Gauss-point level at two different strain rate conditions: a) boundary conditions, b) deformed shape, and c) stress vs. strain curve. The cross markers in the stress vs. strain curve represent when the viscoplastic process starts. The dotted black straight line in the stress vs. strain curve represents the linear regression analysis curve applied to the viscodamage softening behaviour of the dynamic response, and the grey areas refer to the energy dissipated by viscodamage.

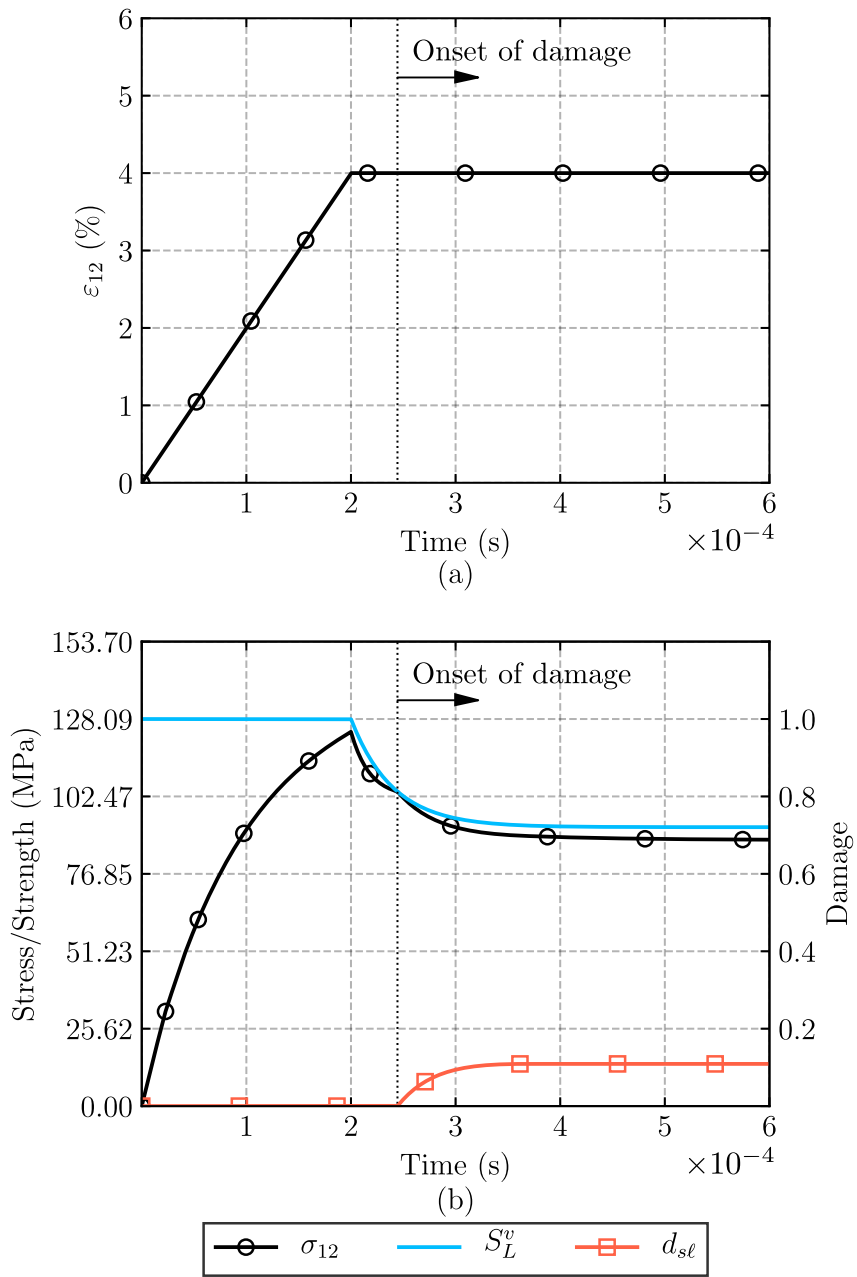


Figure 7.5.: Relaxation virtual test under simple longitudinal shear loading conditions at the Gauss-point level: a) strain applied and b) nominal longitudinal shear stress, evolution of the longitudinal shear strength and viscodamage variable.

The stress-strain relationship obtained from the relaxation case until to fix $\varepsilon_{12} = 4\%$ matches the one obtained from the monotonic virtual test under simple longitudinal shear conditions at high strain rate, see Fig. 7.6. However, the stress vertically drops during the relaxation step but does not reach the stress from the quasi-static test at $\varepsilon_{12} = 4\%$. In both cases (quasi-static and relaxation tests), the stress remains constant at $\sigma_{12} = (1 - d_{s\ell})E_{12}\varepsilon_{22}^{ve}$ but with different viscoplastic and viscodamage states due to how the material has been loaded over time.

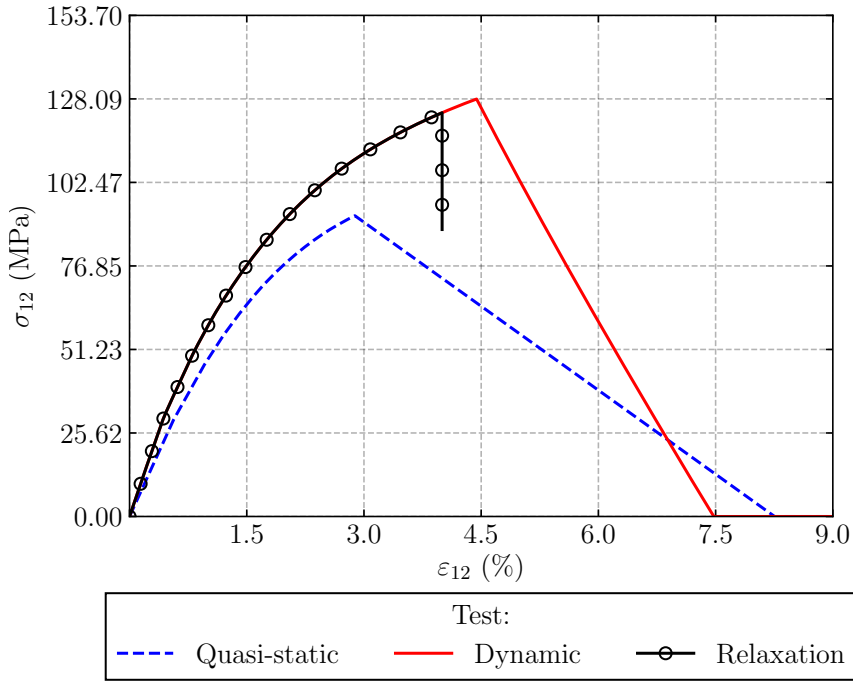


Figure 7.6.: Comparison between the relaxation test and the monotonically increasing tests at different strain rates applying simple longitudinal shear loading conditions.

7.3.3 Off-axis compressive tests

The mechanical response of the off-axis compressive tests carried out by Koerber et al. [8] under different loading rates with the fibre angle orientation $\theta = 15^\circ, 30^\circ, 45^\circ, 60^\circ, 75^\circ$ and 90° is predicted using FE models. The present constitutive model is implemented in a user material subroutine (VUMAT) and the Abaqus/Explicit solver [137] is used to obtain the FE results, employing 3D eight-node C3D8R solid elements with reduced integration. The in-plane element size is defined equal to 0.24 mm to prevent the snap-back of the constitutive softening laws for each failure mechanism [101]. In addition, three elements through-the-thickness of each ply are used.

The in-plane dimensions of the specimens are 10 mm \times 20 mm with 32 plies. Vertical displacement is applied on the top face of the FE models and the bottom face is fixed

in this direction, see Fig. 7.7a. The quasi-static FE simulations are performed applying the vertical displacement at constant low velocity to prevent kinetic effects. However, the loading rates applied during the dynamic experimental tests are employed in the dynamic simulations, see Fig. 7.7b. In addition, the remaining boundary conditions shown in Fig. 7.7a are defined to prevent rigid body motions.

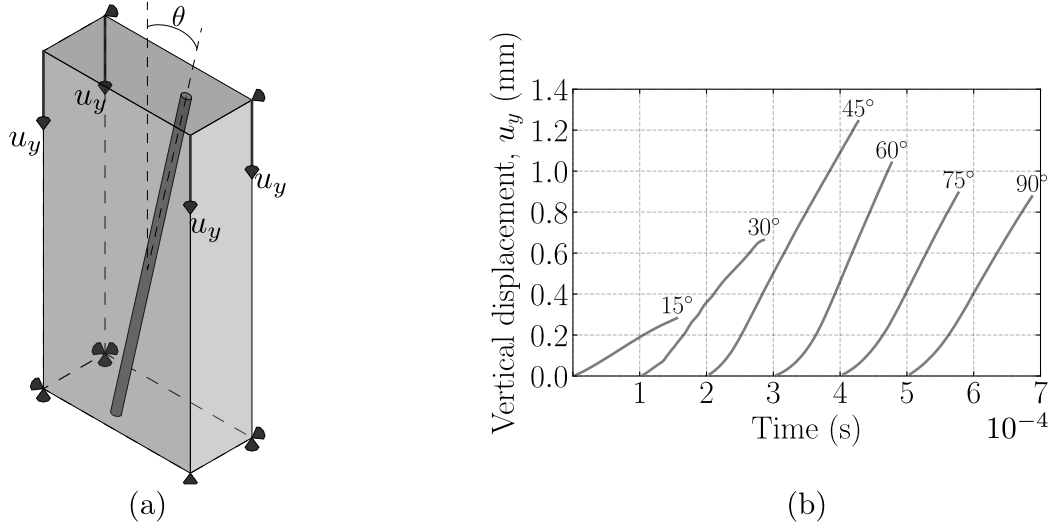


Figure 7.7.: Schematic representation of the boundary conditions (a), and the displacement vs. time curves applied to the dynamic tests in the off-axis compressive tests [8] (b).

Because no experimental data were found in the literature, the dynamic model input parameters summarised in Table 7.2 are fitted by tuning these parameters. Eq. (7.10) cannot be employed with the experimental data measured from [8] since the loading rate in the elastic region is not constant, see the first sections of the curves in Fig. 7.7b. The 45° dynamic test is used to compare the numerical stress vs. strain curve with those experimentally obtained since the highest experimental ultimate strain was obtained from this test. Firstly, the viscoelastic input parameters (τ^{ve} , γ^{ve}) are varied with pure viscoelastic FE response (the viscoplastic and viscodamage model are disabled in this step) to properly capture the initial slope of the experimental data. Then, the viscoplastic parameters (β^{vp} , η^{vp}) are fitted using the fully constitutive model to reproduce the hardening response. Finally, the viscodamage-related parameter (η^{vd}) is set equal to 4.00×10^{-5} . The effect of η^{vd} on the failure strength is not significant since the loading rate is almost constant when the specimen fails and this stabilisation time is large enough compared with η^{vd} , see Fig. 7.7b.

The stress vs. strain curves from the present constitutive model and the strain rate-independent constitutive model presented in Chapter 2 are compared to the experimental data reported by Koerber et al. [8] in Fig. 7.8. The initial slope of the dynamic tests are properly predicted from the present constitutive model for $\theta = 15^\circ, 30^\circ, 45^\circ$ and 60° and a

slightly stiffer elastic response is observed for $\theta = 75^\circ$ and 90° . The hardening response of the dynamic simulations is in good agreement with the experimental data. Furthermore, the failure strength of the specimens from the high strain rate numerical models is also in good agreement with the experimental data, with its highest relative error being less than 7.81% for $\theta = 60^\circ$. Good agreement is also found in the ultimate strain between the numerical and experimental dynamic results except for $\theta = 30^\circ$ and 45° in which a small change in stress produces a significant increase in axial strain.

The quasi-static numerical results from the compressive off-axis tests are also compared to the corresponding experimental data. The elastic and hardening response are properly predicted from the present constitutive model. In addition, the numerical failure strength is also in good agreement with the experimental data, except for $\theta = 45^\circ$ and 60° . Similar predictions are obtained from the strain rate-independent constitutive model proposed in [Chapter 2](#). The failure strength predictions in the quasi-static results can be improved by experimentally measuring S_L as explained in [Section 2.4.1](#). This material property has a significant influence on the $\sigma_{22} - \sigma_{12}$ stress space of the failure envelope and is not experimentally obtained in the present work. S_L is assumed from an in-plane shear test following the ASTM D 3518/3518M-94 test standard [104] and, thus, S_L is estimated when 5% of the axial strain is reached. Note that, the present constitutive model overpredicts the failure strength from the quasi-static tests compared with those obtained from the original model (refers to [Chapter 2](#)). This is due to using the definition of the material strengths as a function of the strain rate as described by [Eq. \(7.51\)](#).

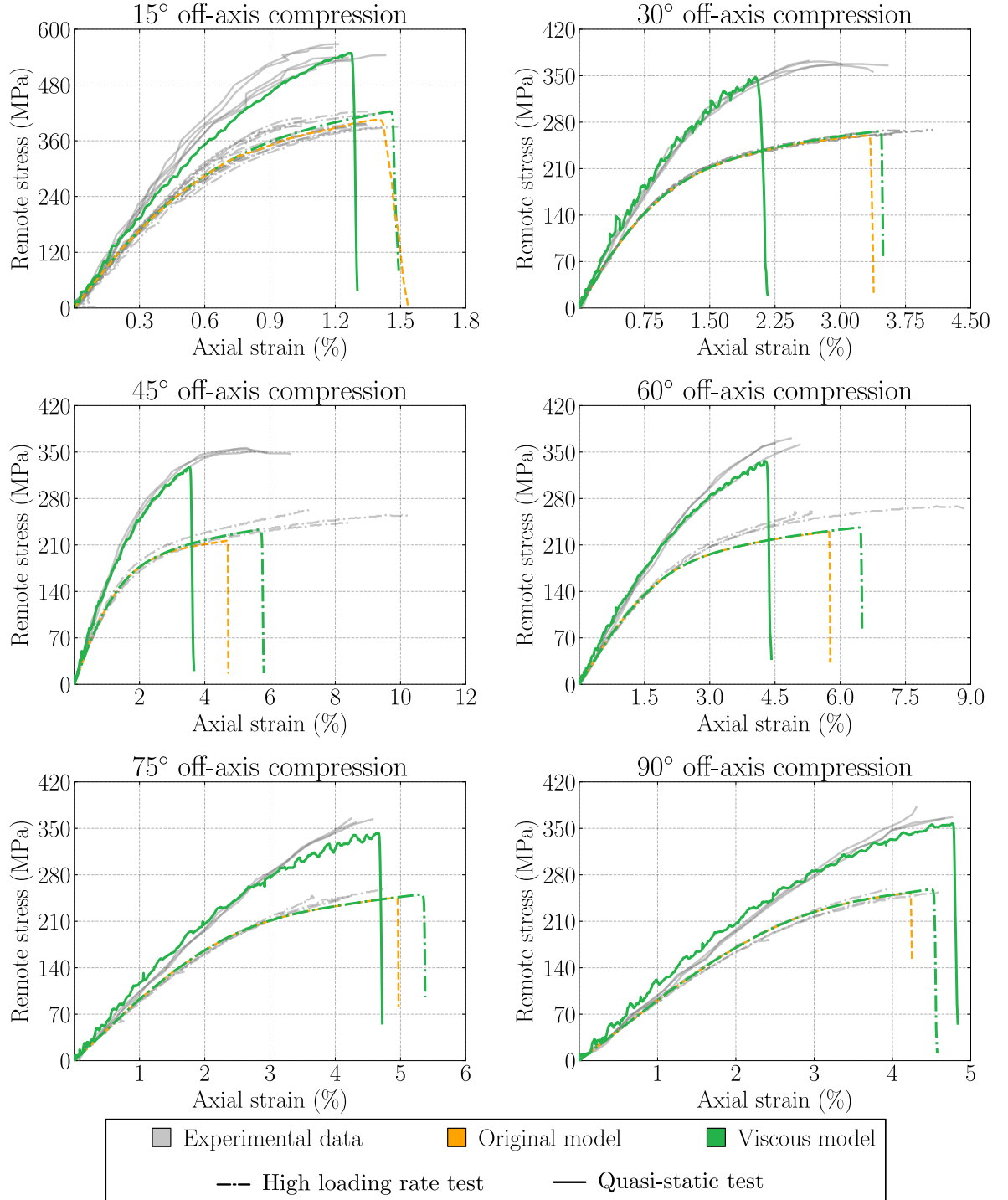


Figure 7.8.: Numerical-experimental comparison of the remote stress vs. axial strain curves of the off-axis compressive tests performed by Koerber et al. [8].

Numerical limitations of the constitutive model

The proposed constitutive model is based on the Infinitesimal Strain theory (see [Eqs. \(2.1\) and \(7.1\)](#)). The model assumes that the material and spatial descriptions are equivalent and that the displacement gradients are very small [263]. For instance, rigid body rotations (and motions) at the Gauss-point level affect the strain tensor, as demonstrated in [Section 8.1.1](#). Another important aspect is that the model cannot differentiate between the simple longitudinal shear loading conditions applied parallel to the fibres and one applied perpendicular to the fibres, as reported in [Section 8.1.2](#).

As discussed in [Section 6.3](#), the constitutive model does not fully predict the mechanical behaviour of FRPs that are dominated by the bearing failure mechanism. The friction effects significantly influence on the bearing failure mode and, therefore, considering friction effects in the constitutive model may improve the numerical prediction of the SLS-Bearing configuration, see [Fig. 6.13](#). [Section 8.2](#) explores the potential numerical results when the friction effects are considered in the softening laws.

8.1 Infinitesimal Strain theory

8.1.1 Rigid body rotation virtual test

In the Infinitesimal Strain theory, the rigid body rotations and motions can generate fictitious strain values. As a result, the numerical predictions may diverge from experimental observations when significant rotations and/or displacements are applied. To demonstrate this limitation, a FE analysis is carried out.

A FE model is defined at the Gauss-point level using two steps: i) a rigid body rotation of an angle of $\psi = 2.5^\circ$ is applied, and ii) a small displacement is applied in the longitudinal direction to be in the elastic region, see [Fig. 8.1a](#). The longitudinal direction is oriented with respect to the horizontal axis (1-axis in the global coordinate system). The displacement-to-element size ratio is defined equal to 0.1%, which represents the expected longitudinal strain value. The loading conditions are applied at constant low velocity to prevent kinetic effects.

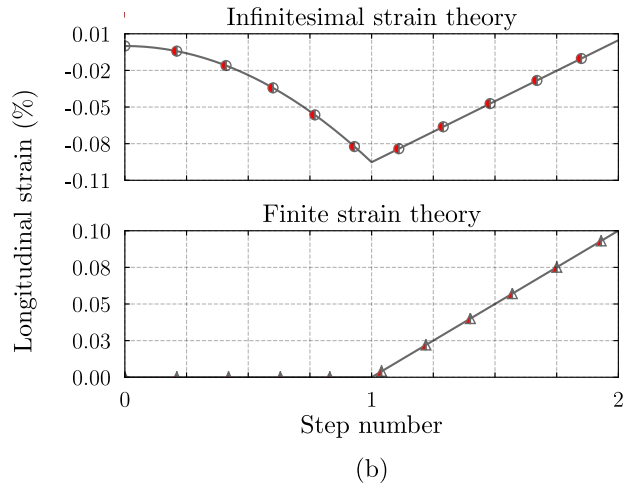
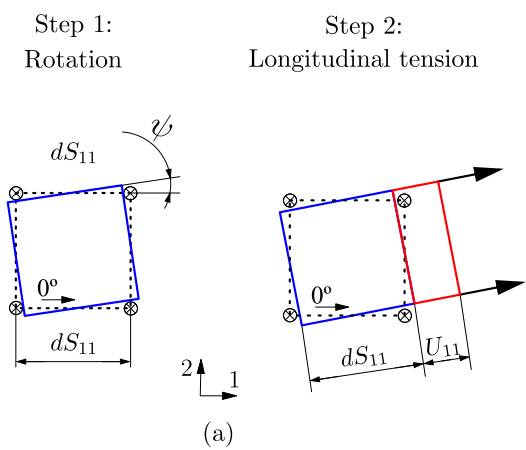


Figure 8.1.: Comparison of the longitudinal strain from the Infinitesimal Strain theory with that obtained from Green-Lagrange strain tensor (Finite Strain theory) when a rotation and a small longitudinal displacement is applied: a) schematic representation of the loading case, and b) longitudinal strain vs. step number curves. Note that the rotation and displacement in (a) are exaggerated for the sake of its understanding.

The longitudinal strain component obtained from the Infinitesimal Strain theory is affected by the rigid body rotation in the first step, see Fig. 8.1b. The infinitesimal strain tensor reads

$$\boldsymbol{\varepsilon} = \frac{1}{2} (\mathbf{F} + \mathbf{F}^T) - \mathbf{I}. \quad (8.1)$$

In the rotation step, the longitudinal strain component yields

$$\varepsilon_{11} = \cos(\psi) - 1, \quad (8.2)$$

and at the end of the virtual test reads

$$\varepsilon_{11} = \frac{-dS_{11} + (U_{11} + dS_{11}) \cos(\psi)}{dS_{11}}, \quad (8.3)$$

where dS_{11} and U_{11} are the initial length and total displacement applied, respectively, see Fig. 8.1a. Consequently, the longitudinal strain calculated in the rotation step is not null, which affects the total longitudinal strain applied at the end of the virtual test, see Fig. 8.1b. The obtained longitudinal strain at the end of the virtual test differs from the expected value ($U_{11}/dS_{11} = 0.1\%$).

The fictitious strain values due to the rigid body rotation and motion can be prevent using the Finite Strain theory. The same FE analysis is conducted using the Green-Lagrange strain tensor and its results are also presented in Fig. 8.1b. In this case, the final

longitudinal strain is approximately equal to 0.1%, which is the expected value (U_{11}/dS_{11}). The Green-Lagrange strain tensor reads

$$\mathbf{E} = \frac{1}{2} (\mathbf{F}^T \mathbf{F} - \mathbf{I}). \quad (8.4)$$

Therefore, the longitudinal strain component in the rotation step yields

$$E_{11} = 0, \quad (8.5)$$

and at the end of the virtual test reads

$$E_{11} = \frac{1}{2} \frac{ds_{11}^2 - dS_{11}^2}{dS_{11}^2}, \quad (8.6)$$

where ds_{11} is equal to the final longitudinal length, in this case $ds_{11} = dS_{11} + U_{11}$. For the small displacement-to-element size ratio applied in the virtual test, Eq. (8.6) is approximately equal to U_{11}/dS_{11} .

8.1.2 Simple longitudinal shear virtual test

The mechanical behaviour of FRPs under simple longitudinal shear loading conditions is expected to differ depending on the loading direction. Under shear conditions parallel to the fibres, failure propagates only through the matrix, while the fibre length remains constant and unloaded, see Fig. 8.2a. In contrast, in the shear conditions perpendicular to the fibres, failure initiates in the matrix and the fibres rotate supporting the load and preventing instantaneous failure propagation until the fibre pull-out and fibre failure occur [264, 265], see Fig. 8.2b.

Two numerical FE models are defined at the Gauss-point level. A material point is loaded applying a simple shear loading condition in the 12-axis (parallel to the fibres) and other in the 21-axis (perpendicular to the fibres) to compare its numerical response, see Fig. 8.3a. The longitudinal directions of each Gauss-point is oriented to the horizontal axis (1-axis in the global coordinate system). The displacement is applied at constant low velocity to prevent kinetic effects. The FE analysis is carried out by only considering damage modelling, the plasticity model is disable.

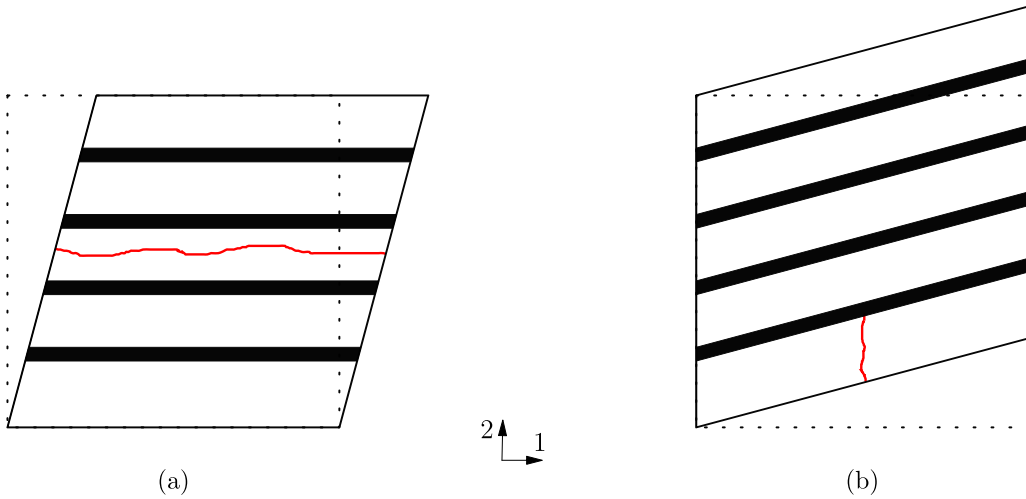


Figure 8.2.: Schematic representation of the deformed shape of unidirectional FRP laminates under longitudinal shear conditions applying in: a) parallel to the fibres, and b) perpendicular to the fibres.

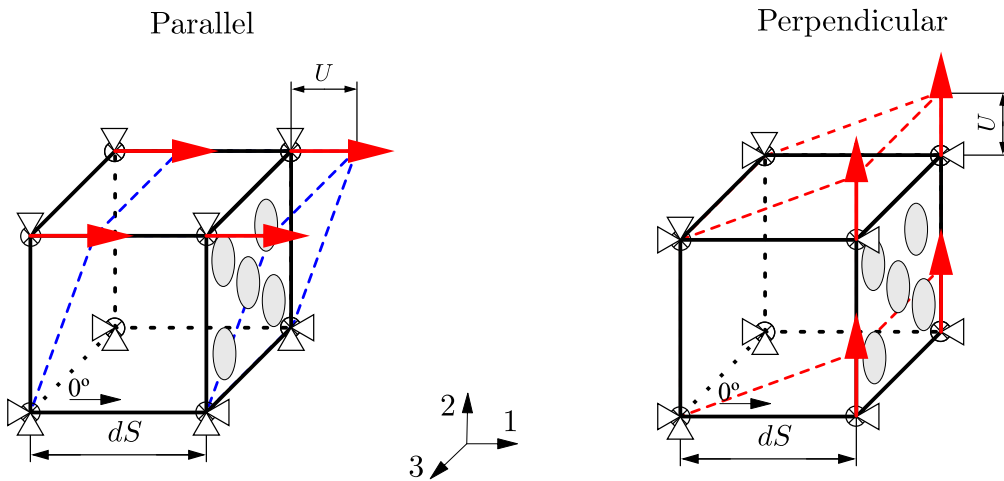
Same numerical predictions are obtained from both the longitudinal shear tests (parallel and perpendicular to the fibres) using the proposed constitutive model based on the Infinitesimal Strain theory, see Fig. 8.3b. The longitudinal shear component in the 12-axis is

$$\varepsilon_{12} = F_{12} + F_{21}, \quad (8.7)$$

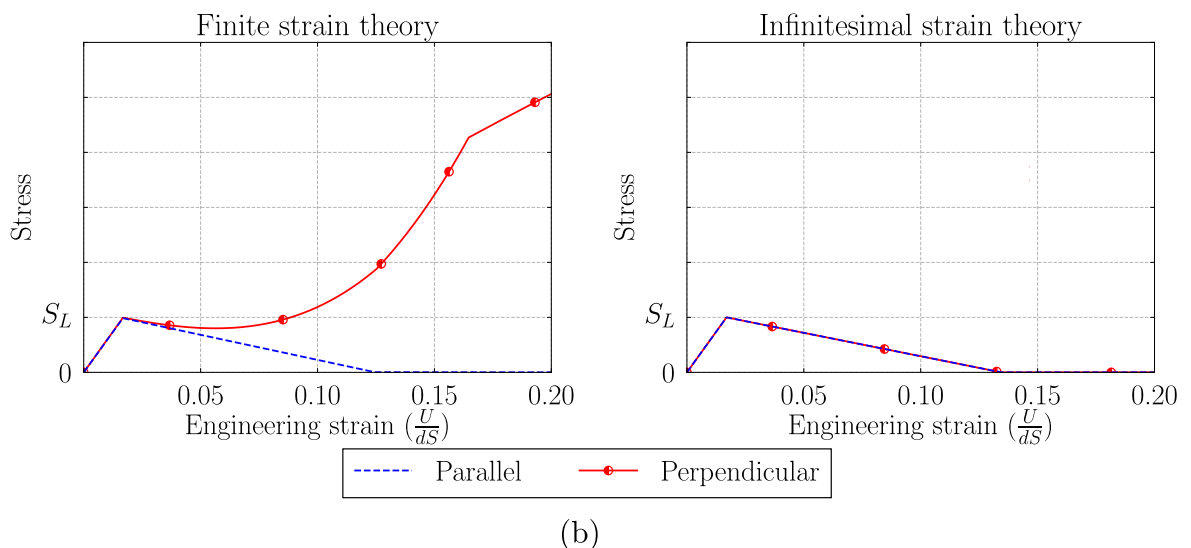
and is independent to the principal components of \mathbf{F} . Therefore, in this case, the fibre rotation cannot be captured since ε_{12} is independent of F_{11} . However, the shear components of the Green-Lagrange strain tensor are calculated as a function of the shear components of \mathbf{F} , as well as but also with their principal components,

$$E_{12} = \frac{1}{2} (F_{11}F_{12} + F_{22}F_{21} + F_{32}F_{31}). \quad (8.8)$$

Therefore, E_{12} take into account the fibre rotation. The damage modelling is implemented using \mathbf{E} and the implementation algorithm is summarised in Algorithm 3. The predicted response from the constitutive model based on the Finite Strain theory is presented in Fig. 8.3c. The results are consistent with the expected behaviour. The model with the fibres parallel to the onset of damage is reached and the load decreases. However, under longitudinal shear conditions perpendicular to the fibres, the model can support load after the onset of damage. Further analysis is required to determine whether the numerical response from the finite strain formulation agrees with experimental observations in FRP laminates.



(a)



(b)

Figure 8.3.: Simple longitudinal shear virtual test: a) schematic representation of the boundary conditions, and b) stress vs. engineering strain curves.

Algorithm 3: Algorithm of the damage modelling based on the finite strain theory at time $t_{(n+1)}$

Input:

deformation gradient tensor at $t_{(n+1)}$: \mathbf{F}

internal variables at $t_{(n+1)}$: $r_{\ell T_{(n)}}, r_{\ell C_{(n)}}, r_{t_{(n)}}$

Initialisation:

Green-Lagrange strain tensor Eq. (8.4)

Second-Piola effective stress tensor: $\tilde{\mathbf{S}} = \tilde{\mathbb{C}}_e \mathbf{E}$

Effective stress invariants as a function of $\tilde{\mathbf{S}}$ Eqs. (2.5)–(2.8)

Loading functions Eqs. (2.26)–(2.28)

Elastic domain threshold Eq. (2.30)

Damage variables Eqs. (2.31)–(2.33)

Second-Piola stress tensor: $\mathbf{S} = \mathbb{C}_e \mathbf{E}$

Cauchy stress tensor: $\boldsymbol{\sigma} = \frac{1}{|\mathbf{F}|} \mathbf{F} \cdot \mathbf{S} \cdot \mathbf{F}^T$

Corotational Cauchy stress tensor [266][†]: $\boldsymbol{\sigma}^{cor} = \mathbf{R}^T \boldsymbol{\sigma} \mathbf{R}$

[†] Step required for the Abaqus/Explicit solver [111].

8.2 Friction effects

The purpose of this section is to analyse a potential solution for improving the prediction of the SLS-Bearing test by introducing friction effects on the damage modelling. Alfano and Sacco [267] developed a cohesive zone model by combining progressive elastic interface damage with a unilateral friction law for the debonding process and complete decohesion. Based on this model, Catalanotti et al. [268] extended the interface damage model developed by Turon et al. [53, 55] with a simple Coulomb friction law. Under compressive out-of-plane loading conditions, the stress-crack opening displacement relationship of the proposed interface damage model can be divided into four main regions. Firstly, there is a linear behaviour until the material strength with no compressive loads is reached (e.g. S_L under longitudinal shear loading conditions). Secondly, the stress non-linearly increases until the strength is reached. Thirdly, stress decreases, and finally the Gauss-point is fully damaged and a plateau stress is reached, in which the load-carrying capacity is due to the friction effect, see Fig. 8.4.

According to the literature observations, the transverse strengths related to compressive shear loadings (S_L and Y_C) have increased by 5% as well as their corresponding fracture toughnesses (\mathcal{G}_{S_L} and \mathcal{G}_{Y_C}). Additionally, the upper bound of the transverse damage variables associated to compressive shear loadings (d_{se} and d_{st}) has been set equal to 0.85. The main objective of these modifications is to define the softening laws similar to the one presented in Fig. 8.4. These modifications are made with the aim of keeping the model

simple and to analyse a possible improvement. It is important to remark that a correct formulation is necessary to account for friction effects in the damage modelling.

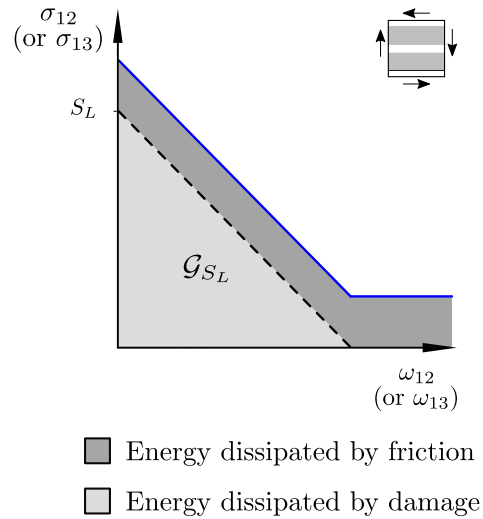


Figure 8.4.: A schematic representation of the stress vs. crack opening displacement curve under longitudinal shear loading conditions for different compressive loads.

The SLS-Bearing FE model presented in [Section 6.3](#) is now carried out with the described modifications in the softening laws. The predicted stress vs. cross-head displacement curve obtained from the modified constitutive model to account for friction effects shows two main regions, see [Fig. 8.5](#). Firstly, the stress monotonically increases and the "knee point" is reached. Secondly, the initial stiffness decreases but the load-carrying capacity continues to increase. This mechanical response is comparable to the experimental data. Again, note that the modifications in the constitutive model are simplifications and further analysis is required to introduce the friction effect into the damage modelling.

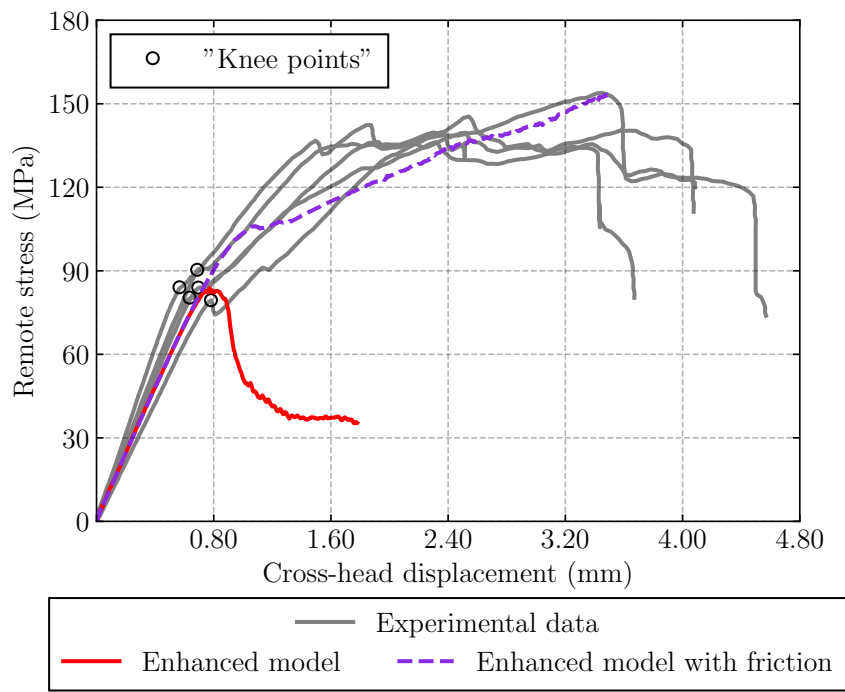


Figure 8.5.: Comparison of the predicted stress vs. cross-head displacement curve of the SLS-Bearing configuration obtained using both the enhanced model and the enhanced model with friction effects.

Conclusions

9.1 Concluding remarks

A new 3D constitutive model to predict the plastic deformation and the progressive failure of unidirectional laminated composite materials was developed in the [Chapter 2](#). The model is thermodynamically consistent to ensure irreversibility of the dissipative material processes. The Infinitesimal Strain theory has been followed and new yield and plastic potential functions were proposed in conjunction with existing loading functions. The shape of the yield envelope can be modified by setting the plastic envelope shape coefficients. The new non-associative flow rule used in the plasticity modelling enables the plastic Poisson's ratios and the volumetric plastic strains to be imposed. In addition, the failure criteria can be modified by setting the failure envelope shape coefficients. The model is based on the framework of 3D continuum damage mechanics, and the objectivity of the damage model is ensured by regularising the dissipated energy by damage with the characteristic element size (Crack Band model [89]).

The constitutive model was implemented in a commercial finite element code using a user-defined material subroutine. A VUMAT Fortran subroutine was developed to be used with the Abaqus/Explicit solver. The implementation was verified by applying different loading cases at the Gauss-point level. The numerical results of this verification analysis were compared to the known data, and good agreement was found between them. Therefore, the implementation of the constitutive model in a user material subroutine was satisfactorily validated.

A methodology to prevent spurious damage generated in continuum damage mechanics constitutive models which use the effective stress tensor was presented in [Chapter 3](#). The proposed model (enhanced model) can be straightforwardly implemented in previously developed constitutive models. An explicit implementation of the damage modelling to be used with a finite element explicit solver was also presented. The numerical results obtained from the enhanced constitutive model and those obtained from a model which use the effective stress tensor were compared with the experimental data obtained from an open-hole compressive test using a quasi-isotropic laminate. The comparison demonstrated the improvements that the enhanced model provides to predict failure mechanisms. Good agreement on the failure patterns between the enhanced model and the experimental data,

as well as on the failure strength, were found. However, the model which use the effective stress tensor does not properly capture the failure pattern after the failure strength.

Moreover, two unidirectional virtual tests were carried out to explain the improvements of the enhanced model seen on the open-hole compressive test with a quasi-isotropic laminate. Discrepancies on the failure strength on 90° laminate was found between the models. The enhanced constitutive model predicted the expected deformed shape and failure propagation. However, the model which use the effective stress tensor becomes unstable in terms of failure propagation after the failure remote load, and its deformed shape was inconsistent with the expected shape.

Guidelines were provided to calibrate the numerical parameters of the model. The remaining input model parameters can be experimentally obtained from standard tests. In this sense, a new methodology to measure the transverse Poisson's ratios for characterising a unidirectional fibre-reinforced polymer composite material at room temperature under quasi-static loading conditions was proposed in [Chapter 4](#). A thermoplastic-based composite material (carbon fibre/poly-ether-ether-ketone) was used to illustrate how the proposed procedure was employed to measure the elastic transverse Poisson's ratios in tension and compression, as well as the plastic transverse Poisson's ratio in compression.

Transverse tensile and transverse compressive tests were carried out using digital image correlation (DIC) equipment to measure the strain field on the lateral surface of the specimens. The average axial strain obtained from the DIC was compared with the one measured from two strain gauges and good agreement was found. Accordingly, the corresponding transverse Poisson's ratio was then calculated from the DIC measurements.

There is a clear trend of the elastic transverse Poisson's ratio in tension to decrease when the elastic axial strain increases in two of the three specimens tested. In the same way, the elastic transverse Poisson's ratio in compression decreases when the amount of the compressive elastic axial strain increases. The comparison of the elastic transverse Poisson's ratios suggested more contraction in compression than expansion in tension. Assuming no plastic strain in the longitudinal direction, the plastic transverse Poisson's ratio in compression indicates no volumetric plastic strains for small axial plastic strains, whereas plastic dilatancy was observed as the amount of compressive plastic axial strain increased.

The novelty of the proposed methodology of [Chapter 4](#), compared to those proposed in the literature, lies in the use of standard tests with additional measuring equipment and a novel data reduction method to obtain the transverse Poisson's ratio. The proposed method

does not increase the overall number of experimental tests required for characterising a fibre-reinforced polymer composite material. Furthermore, there is no requirement for additional specimens or fixture tools.

Guidelines were provided to calibrate the plastic and failure envelope shape coefficients in [Chapter 5](#), and their bounds were presented. Additionally, the influence of the failure envelope shape coefficients on the failure strength of filled-hole compressive tests was analysed. Different stacking sequences, bolt metric, specimen width, thickness and preloads of filled-hole compressive experimental tests of carbon fibre-reinforced polymer (CFRP) laminates were employed in this analysis. The enhanced constitutive model was used and different shapes of the failure envelope in the 11-22 effective stress space were analysed. This effective stress space is the one whose definition has higher uncertainty due to the lack of appropriate multiaxial tests. In total, four envelopes were explored: one based on LaRC failure criteria [84, 85] modified by Maimí et al. [49], a Quadratic envelope based on the failure criteria proposed by Camanho et al. [123], and two envelopes adjusted in-between the previous two envelopes.

The results obtained showed that the failure envelope definition has a significant effect on the prediction of the filled-hole failure strength and their failure mechanisms. By varying the failure criteria, damage started to develop and propagate differently, eventually altering significantly the predicted failure strength. In addition, the same failure criteria led to a good prediction of some filled-hole configurations, but led to overpredictions/underpredictions with other tests. This highlights the importance of validating models against different of experimental configurations. By adjusting properly the failure envelope shape, it was possible to reproduce all the tests consistently.

The findings of [Chapter 5](#) indicate that determining the failure envelope shape experimentally is important; it is necessary to develop further multiaxial test methods, or other suitable approaches, for obtaining the failure envelopes. The results also prove that even some well established failure theories may not be able to be adjusted to the envelopes here found, indicating that they may not be appropriate for predicting some loading states. These results also emphasise the importance of accurately establishing failure envelope, rather than overemphasising the development of complex models.

The predictive capabilities of the constitutive model proposed in [Chapters 2](#) and [3](#) were demonstrated by comparing the numerical predictions with experimental data from different tests. In most of the numerical-experimental comparisons, the same material system was used to demonstrate that good predictions can be obtained with the correct characterisation of the model input parameters. The numerical-experimental comparison

from off-axis tests showed a satisfactory agreement of the plastic deformation and the failure strength in [Chapter 2](#). In addition, the model properly predicted the fracture plane from off-axis compressive tests. The model also was employed to predict the failure strength of open-hole tensile and compressive tests in [Chapters 2 and 3](#), good agreement between the numerical-experimental data was found. Furthermore, the model was employed to predict the mechanical response of CFRP laminates under out-of-plane loading conditions in [Chapter 6](#).

A numerical-experimental comparison of an end-notched flexure test was conducted to demonstrate the capabilities of the model to predict a failure pattern similar to delamination under mode-II loading conditions. The model accurately predicted the load vs. cross-head displacement curve and the failure pattern. Additionally, four-point bending tests using L-shaped specimens were performed to show the ability of the model to predict failure load and patterns under non-uniform out-of-plane stress states. Good predictions were found in the load vs. cross-head displacement curve and fracture plane localisation. Finally, single-lap shear composite bolted joint tests were used in the numerical-experimental comparisons. The model was able to accurately predict the mechanical response in case of net-tension failure mechanism and the "knee points" when bearing failure occurs.

The enhanced constitutive model was extended in [Chapter 7](#) to account for the strain rate dependence of CFRP laminates. The generalised Maxwell model was employed to predict the viscoelastic response under dynamic loading conditions. An overstress model was used to account for the viscoplastic strains of CFRPs. In addition, a new viscodamage model was proposed to account for the onset of damage as well as its propagation under different loading rates. The viscodamage modelling was based on enhanced model and was extended to dynamic conditions using experimental strength-strain rate relationships. In addition, the Crack Band model was used to ensure the proper dissipation of energy due to damage.

The viscous constitutive model was implemented to be used with the Abaqus/Explicit solver to demonstrate its predictive capabilities. The constitutive model successfully replicated the stiffer stress-strain response of CFRPs at high strain rates. Furthermore, the response of a relaxation test illustrated how the material relaxes and how the onset and propagation of viscodamage occurs without increasing the strains, since the strength relaxes faster than the stresses.

A numerical-experimental comparison of off-axis compressive tests at different loading rates was also carried out to demonstrate the ability of the viscous constitutive model to predict the mechanical response of CFRP laminates. The comparison of the dynamic

tests showed good agreement in the viscoelastic, viscoplastic and viscodamage regions. In addition, quasi-static tests were properly predicted by the viscous constitutive model and showed good agreement with the previously strain rate-independent model (enhanced model).

Three limitations of the proposed constitutive model were presented in [Chapter 8](#). The first limitation is the use of Infinitesimal Strain theory when rigid body rotations occur. The second limitation is the inability to distinguish between simple longitudinal shear loading conditions applied parallel to the fibres and those applied perpendicular to the fibres. The third limitation is the inability to fully predict the mechanical response of CFRP laminates when bearing failure occurs. Additionally, possible solutions were proposed to these limitations. The model can be extended to Finite Strain theory and consider the friction effects in the softening laws.

The material model can be used to predict the mechanical response of thermoset-based composite materials under quasi-static and dynamic loading conditions, as well as for thermoplastic-based composites at which the plastic behaviour could be more significant. The presented constitutive model can also be applied for the prediction of cases where the out-of-plane stress state governs the mechanical response of the structure, such as filled-hole specimens with a preloaded bolt, interlaminar shear strength tests, etc. These capabilities have been widely demonstrated.

This thesis has focused on CFRP laminates, but the proposed constitutive model can predict the mechanical response of other homogeneous transversally isotropic materials by applying the corresponding material characterisation. The yield function, the non-associative flow rule and the loading functions make the model more flexible to predict the plastic deformation and fracture of a large range of materials. Furthermore, the softening laws can be modified according to the selected material response. Additionally, the strain rate dependency of the viscodamage parameters can be also modified to align with corresponding experimental evidence for the selected material.

In conclusion, the main objective of this thesis, as well as the partial objectives, have been achieved. Five scientific articles have already been published on the subject of this thesis. The present work has contributed to the improvement of computational and experimental methods for predicting the plastic deformation and fracture of CFRP laminates under quasi-static and dynamic loading conditions. Further work is required to enhance the reliability of computational tools. Furthermore, new experimental tests are necessary to gain a better understanding of the mechanical response of CFRP laminates.

9.2 Perspectives and future work

The present thesis represents progress in predicting the plastic deformation and fracture of fibre-reinforced polymer structures under quasi-static and dynamic loading conditions. However, there are limitations detected from both experimental and numerical perspectives which can be suggested as future works.

The main limitation encountered during the development of this thesis concerns to obtain experimental evidence regarding the mechanical behaviour of FRP laminates. The literature lacks information on the shape of the failure envelope under specific loading conditions, particularly with regards to FRPs under longitudinal compressive loads. Further multiaxial test methods or other suitable approaches are needed to obtain the failure envelope of FRPs. From the numerical point of view, an inverse method can be proposed using optimisation algorithms to fit the shapes of the plastic and failure envelopes. The objective function of the optimisation approach can be defined as a function of the experimental data under different loading conditions and the envelope shape coefficients as the independent variables.

Another significant limitation detected is about to experimental evidence on the mechanical behaviour of FRPs under dynamic loading conditions. The literature does not provide a clear consensus on the strain rate effects on the failure response of FRPs. For instance, there is no clear relationship between fracture toughness and strain rate. Some experimental investigations suggest that fracture toughness increases with higher strain rates. However, other experimental observations conclude that fracture toughness is independent of the strain rate. Robust test methods including data reduction procedures are needed to better understand the mechanical response of FRPs under dynamic loading conditions.

The capabilities of the viscoelastic-viscoplastic and viscodamage model presented in [Chapter 7](#) are demonstrated by a numerical-experimental comparison of off-axis compressive tests at different strain rates. An interesting future consideration is to extend the comparison/validation of the proposed constitutive model to better determine its full capabilities and limitations. This validation could also be performed at different levels, such as the structural or sub-component level of the building block approach.

The proposed constitutive model is based on the Infinitesimal Strain theory (see [Eqs. \(2.1\) and \(7.1\)](#)). The model assumes that the material and spatial descriptions are equivalent and that the displacement gradients are very small [263]. For instance, rigid body rotations (and motions) at the Gauss-point level affect the strain tensor. Another important aspect to consider is that the proposed model cannot distinguish between a simple longitudinal shear

loading condition applied parallel to the fibres and one applied perpendicular to the fibres. These two limitations are discussed in [Section 8.1](#). The proposed constitutive model could be extended to Finite Strain theory based on the model proposed by Eidel and Gruttmann [269]. The authors developed an elastoplastic constitutive model for orthotropic metallic materials at the finite plastic strains [269, 270]. The model was modified to account for FRPs laminates [271] and extended to account for viscoelastic-viscoplastic finite strains [250].

The proposed constitutive model could be extended to incorporate friction effects during transverse failure mechanisms, as discussed in [Section 8.2](#). This could be achieved by adopting the model proposed by Alfano and Sacco [267], which is commonly used in interface damage models for FRPs [268, 272]. A simple Coulomb friction law could be introduced in the softening laws governed by the matrix under compressive normal and sliding loading conditions.

Appendices

Determination of the parameters of the plastic flow potential function

The evolution of the plastic strains is defined as a function of the derivative of the plastic potential function with respect to the stress tensor $\partial_{\sigma}(\varphi^p)$, as a non-associative flow rule is used, see Eq. (2.14). The parameters of the plastic potential function of the plasticity model are defined in this appendix. These parameters do not have a physical sense, they are used to control the plastic dilatancy or contractility in the plastic zone. In addition, they define the direction of the plastic flow. For this reason, the ratios between them are relevant and not their absolute values.

The volumetric plastic strain rate is defined as

$$\dot{\varepsilon}_{vol}^p := \frac{1}{2} \text{tr} \dot{\varepsilon}^p, \quad (\text{A.1})$$

and combining it with Eq. (2.14), $\dot{\varepsilon}_{vol}^p$ in Voigt notation reads

$$\dot{\varepsilon}_{vol}^p = \frac{1}{2} \lambda \left[\left(\frac{\hat{Y}_{CP} - \hat{Y}_{TP}}{\hat{Y}_{CP} \hat{Y}_{TP}} \right) + \left(\frac{\hat{Y}_{CP} + \hat{Y}_{TP}}{2 \hat{Y}_{CP} \hat{Y}_{TP}} \right)^2 \left(\frac{\sigma_{22} + \sigma_{33}}{\sqrt{\sigma \hat{\mathbb{K}} \sigma}} \right) \left(\frac{2\hat{\mu}_{tp}}{\hat{\mu}_{tp} + 1} \right) \right], \quad (\text{A.2})$$

where \hat{Y}_{CP} , \hat{Y}_{TP} and \hat{S}_{LP} are the plastic potential stresses and $\hat{\mu}_{tp}$ and $\hat{\mu}_{slp}$ are the plastic potential curvature parameters, all of them are defined as constant parameters. In addition, λ is the plastic multiplier and $\hat{\mathbb{K}}$ is the second order tensor that contains the coefficients of the non-linear terms of the plastic potential function Eq. (2.21); $\hat{\mathbb{K}}$ is defined in Eq. (C.2) replacing the yield stresses by the corresponding plastic potential parameters (e.g. Y_{CP} by \hat{Y}_{CP}).

The volumetric plastic strain rate can be

$$\dot{\varepsilon}_{vol}^p \begin{cases} < 0, & \rightarrow \text{plastic compressibility}, \\ = 0, & \rightarrow \text{no volumetric plastic strains}, \\ > 0, & \rightarrow \text{plastic dilatancy}. \end{cases} \quad (\text{A.3})$$

The plastic potential parameters can be adjusted by three tests to impose the plastic dilatancy or compressibility: pure transverse tensile test, pure transverse compressive test and pure longitudinal shear test. Note that these tests are used to adjust the yield

function, hence, the total number of tests required to calibrate the plasticity model is not increased. The plastic Poisson's ratio from the transverse tensile test must be defined as

$$\nu_{23T}^p := -\frac{\varepsilon_{33}^p}{\varepsilon_{22}^p}, \quad (\text{A.4})$$

where ε_{ij}^p is obtained from the transverse tensile test. Similarly, the plastic Poisson's ratio from the transverse compressive test ν_{23C}^p must be defined as Eq. (A.4) replacing ε_{ij}^p with those obtained from the transverse compressive test. Therefore, ν_{23T}^p and ν_{23C}^p can be rewritten as a function of $\boldsymbol{\varepsilon}^p$. Firstly, the Backward Euler integration method is applied in Eq. (A.1),

$$\boldsymbol{\varepsilon}^p := \gamma \frac{\partial \varphi^p}{\partial \boldsymbol{\sigma}}, \quad (\text{A.5})$$

where γ is the consistency parameter. Finally, each plastic strain component of ν_{23T}^p and ν_{23C}^p can be calculated from Eq. (A.5) by applying the corresponding loading conditions. They yield

$$\nu_{23T}^p = \frac{\hat{Y}_{TP} - \hat{\mu}_{tp} \hat{Y}_{CP}}{\hat{Y}_{CP}(\hat{\mu}_{tp} + 1)}, \quad (\text{A.6})$$

and

$$\nu_{23C}^p = \frac{\hat{Y}_{CP} - \hat{\mu}_{tp} \hat{Y}_{TP}}{\hat{Y}_{TP}(\hat{\mu}_{tp} + 1)}. \quad (\text{A.7})$$

In addition, the following ratio is defined as

$$\nu_{122}^p := -\frac{\varepsilon_{22}^p}{\varepsilon_{12}^p}, \quad (\text{A.8})$$

using ε_{ij}^p from the longitudinal shear test, and applying the corresponding loading conditions in Eq. (A.5), ν_{122}^p yields

$$\nu_{122}^p = -\frac{(\hat{Y}_{TP} - \hat{Y}_{CP}) \hat{S}_{LP}}{2 \hat{Y}_{CP} \hat{Y}_{TP}}. \quad (\text{A.9})$$

Finally, the relationships between the plastic potential parameters can be found by combining Eqs. (A.6), (A.7) and (A.9) as

$$\frac{\hat{Y}_{CP}}{\hat{Y}_{TP}} = \frac{\nu_{23C}^p + 1}{\nu_{23T}^p + 1}, \quad (\text{A.10})$$

$$\frac{\hat{S}_{LP}}{\hat{Y}_{TP}} = \frac{2\nu_{122}^p(\nu_{23C}^p + 1)}{\nu_{23T}^p - \nu_{23C}^p}, \quad (\text{A.11})$$

and

$$\hat{\mu}_{tp} = \frac{1 - \nu_{23C}^p \nu_{23T}^p}{(\nu_{23C}^p + 1)(\nu_{23T}^p + 1)}. \quad (\text{A.12})$$

Therefore, the no volumetric plastic strains ($\nu_{23T}^p = \nu_{23C}^p = 1$ and $\nu_{122}^p = 0$) are imposed by the following relationships

$$\frac{\hat{Y}_{CP}}{\hat{Y}_{TP}} = 1, \quad (\text{A.13})$$

and

$$\hat{\mu}_{tp} = 0. \quad (\text{A.14})$$

Damage variables

The evolution of the damage variables d_M as a function of the corresponding elastic domain threshold r_N are described in this appendix. The damage constitutive model used in this study is based on the model developed by Quintanas-Corominas et al. [86]. The model uses four damage variables to define the degradation of the elastic properties:

- i) $d_\ell(r_{\ell T}, r_{\ell C})$: fibre breakage ($\sigma_\ell > 0$) or fibre kinking ($\sigma_\ell < 0$) associated to the first stress invariant σ_ℓ Eq. (2.5).
- ii) $d_t(r_t)$: mode-I matrix cracking associated to the second stress invariant p_t Eq. (2.6).
- iii) $d_{st}(r_t)$: mode-II matrix cracking associated to the third stress invariant τ_t Eq. (2.7).
- iv) $d_{s\ell}(r_{\ell T}, r_t)$: longitudinal tensile and matrix failure mechanisms associated to the fourth stress invariant τ_ℓ Eq. (2.8).

B.1 Longitudinal damage variable d_ℓ

The longitudinal damage variables d_ℓ is defined as

$$d_\ell := d_{\ell T} \frac{\langle \sigma_\ell \rangle}{|\sigma_\ell|} + d_{\ell C} \frac{\langle -\sigma_\ell \rangle}{|\sigma_\ell|}, \quad (\text{B.1})$$

where $\langle x \rangle := (x + |x|)/2$ is the McCauley operator. Therefore, if the first stress invariant is positive ($\sigma_\ell > 0$), then, $d_\ell = d_{\ell T}$, otherwise $d_\ell = d_{\ell C}$. This allows a different longitudinal damage evolution in tension ($d_{\ell T}$) than in compression ($d_{\ell C}$).

B.1.1 Longitudinal tensile damage variable $d_{\ell T}$

The longitudinal tensile damage variable ($d_{\ell T}$) as a function of the elastic domain threshold in the longitudinal tensile direction ($r_{\ell T}$) is obtained using a uniaxial longitudinal tensile test. Therefore, the Cartesian components of the stress tensor ($\boldsymbol{\sigma}$) read

$$\begin{aligned} \sigma_{11} &> 0 \\ \sigma_{22} = \sigma_{33} = \sigma_{23} = \sigma_{13} = \sigma_{12} &= 0. \end{aligned} \quad (\text{B.2})$$

Furthermore, the elastic strain tensor yields

$$\boldsymbol{\varepsilon}^e = \mathbb{H} \begin{bmatrix} \sigma_{11} \\ 0 \\ 0 \\ 0 \\ 0 \\ 0 \end{bmatrix}, \quad (\text{B.3})$$

where \mathbb{H} is the compliance tensor defined in Eq. (2.10). The effective stress tensor can be calculated as

$$\tilde{\boldsymbol{\sigma}} = \mathbb{C}_{e0} \boldsymbol{\varepsilon}^e, \quad (\text{B.4})$$

where \mathbb{C}_{e0} is the elasticity tensor without damage ($\mathbb{C}_{e0} = \mathbb{H}^{-1}(d_M = 0)$). Consequently, by combining Eqs. (B.3) and (B.4), the shear effective stresses are equal to zero and the principal effective stresses yield

$$\begin{aligned} \tilde{\sigma}_{11} &= \frac{E_{11} - 4E_t \nu_{12}^2 (1 - d_\ell)}{(E_{11} - 4E_t \nu_{12}^2)(1 - d_\ell)} \sigma_{11} \\ \tilde{\sigma}_{22} &= \frac{2E_t \nu_{12} d_\ell}{(E_{11} - 4E_t \nu_{12}^2)(1 - d_\ell)} \sigma_{11} \\ \tilde{\sigma}_{33} &= \tilde{\sigma}_{22}, \end{aligned} \quad (\text{B.5})$$

where E_{11} is the longitudinal Young's modulus, E_t is the bulk elastic stiffness in the transverse isotropic plane (see Eq. (2.3)), and ν_{12} is the longitudinal Poisson's ratio. Hence, the loading function in the longitudinal tensile direction in Eq. (2.26) reads

$$\phi_{\ell T} = \frac{1}{(1 - d_\ell) X_T} \sigma_{11}, \quad (\text{B.6})$$

where X_T is the longitudinal tensile strength.

The softening law in the longitudinal tensile direction is defined using a bilinear law [101, 102]. The first segment is defined with a large drop stress due to the fibre breakage followed by a large tail related to the fibre pull-out, see Fig. B.1. Hence, the Cartesian component of $\boldsymbol{\sigma}$ referring to the longitudinal direction is defined for each segment as

$$\sigma_{11} := a_{i_s M} \omega_{11} + b_{i_s M}, \quad (\text{B.7})$$

where ω_{11} is the longitudinal crack opening displacement, $a_{i_s M}$ and $b_{i_s M}$ are the slope and intercept, respectively, of the corresponding segment i_s in the stress-crack opening displacement relationship. According to the Crack Band model [89], the average elastic strain of a mesh finite element (ε_{ij}^e) can be related with the crack opening displacement (ω_{ij}) through

$$\omega_{ij} = d_M l_M^* \varepsilon_{ij}^e, \quad (\text{B.8})$$

where l_M^* is the characteristic element length, see [Appendix I](#) for more details on the elastic strain-crack opening displacement relationship.

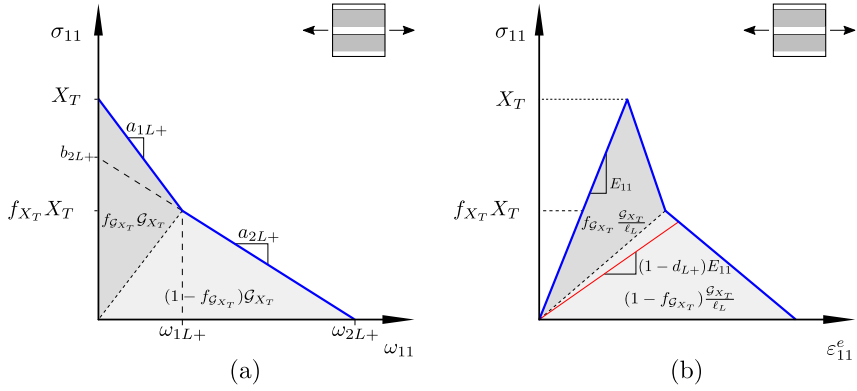


Figure B.1: Softening law in the longitudinal tensile direction: a) stress vs. crack opening displacement curve and b) stress vs. elastic strain curve.

Finally, the damage variables $d_{\ell T}$ as a function of $r_{\ell T}$ is obtained by introducing [Eq. \(B.8\)](#) into [Eq. \(B.7\)](#) and, then, combining it with [Eqs. \(B.3\) and \(B.6\)](#), and assuming that $r_{\ell T} = \phi_{\ell T}$ and $d_{\ell} = d_{\ell T}$. Hence, the longitudinal tensile damage variable for each segment yields

$$d_{i_s \ell T} = \frac{E_{11}(X_T r_{\ell T} - b_{i_s \ell T})}{(E_{11} + a_{i_s \ell T} l_{\ell}^*) X_T r_{\ell T}}, \quad (\text{B.9})$$

where the intercept of the first segment ($b_{1\ell T}$) is equal to X_T and its corresponding slope reads

$$a_{1\ell T} = \frac{f_{\mathcal{G}_{X_T}} X_T - X_T}{\omega_{1\ell T}}, \quad (\text{B.10})$$

where $\omega_{1\ell T}$ is the longitudinal crack opening displacement when the area under the softening law match the first portion of the longitudinal tensile fracture toughness ($f_{\mathcal{G}_{X_T}} \mathcal{G}_{X_T}$). Therefore, $\omega_{1\ell T}$ is obtained by solving the following equation

$$f_{\mathcal{G}_{X_T}} \mathcal{G}_{X_T} = \frac{1}{2} \omega_{1\ell T} X_T, \quad (\text{B.11})$$

where \mathcal{G}_{X_T} is the longitudinal tensile fracture toughness. Hence, $\omega_{1\ell T}$ reads

$$\omega_{1\ell T} = \frac{2f_{\mathcal{G}_{X_T}}\mathcal{G}_{X_T}}{X_T}, \quad (\text{B.12})$$

and the first slope yields

$$a_{1\ell T} = \frac{X_T^2(f_{X_T} - 1)}{2f_{\mathcal{G}_{X_T}}\mathcal{G}_{X_T}}. \quad (\text{B.13})$$

The slope of the second segment is calculated as

$$a_{2\ell T} = \frac{-f_{X_T}X_T}{\omega_{2\ell T} - \omega_{1\ell T}}, \quad (\text{B.14})$$

where $\omega_{2\ell T}$ is the longitudinal crack opening displacement when the area under the softening law match the second portion of the longitudinal tensile fracture toughness $((1 - f_{\mathcal{G}_{X_T}})\mathcal{G}_{X_T})$, therefore, $\omega_{2\ell T}$ is obtained by solving the following equation

$$(1 - f_{\mathcal{G}_{X_T}})\mathcal{G}_{X_T} = \frac{1}{2}\omega_{2\ell T}f_{X_T}X_T, \quad (\text{B.15})$$

hence, the second slope yields

$$a_{2\ell T} = -\frac{f_{X_T}^2X_T^2}{2\mathcal{G}_{X_T}(1 - f_{\mathcal{G}_{X_T}} - f_{\mathcal{G}_{X_T}}f_{X_T})}. \quad (\text{B.16})$$

The intercept of the second segment reads

$$b_{2\ell T} = \frac{f_{X_T}X_T(1 - f_{\mathcal{G}_{X_T}})}{(1 - f_{\mathcal{G}_{X_T}} - f_{\mathcal{G}_{X_T}}f_{X_T})}. \quad (\text{B.17})$$

The active segment in Eq. (B.9) depends on $r_{\ell T}$ in the inflection point ($r_{1\ell T}$) and is calculated matching both segments as

$$r_{1\ell T} = \frac{2f_{\mathcal{G}_{X_T}}\mathcal{G}_{X_T}E_{11} + f_{X_T}X_T^2l_{\ell}^{*}}{X_T^2l_{\ell}^{*}}. \quad (\text{B.18})$$

Finally, the longitudinal tensile damage variable in Eq. (B.9) yields

$$d_{\ell T} = \begin{cases} \frac{2f_{\mathcal{G}_{X_T}}\mathcal{G}_{X_T}E_{11}(r_{\ell T} - 1)}{\left(2f_{\mathcal{G}_{X_T}}\mathcal{G}_{X_T}E_{11} + X_T^2l_{\ell}^*(f_{X_T} - 1)\right)r_{\ell T}}, & \text{if } r_{\ell T} \leq r_{1\ell T} \\ \frac{2\mathcal{G}_{X_T}E_{11}\left((1-f_{\mathcal{G}_{X_T}} - f_{\mathcal{G}_{X_T}}f_{X_T})r_{\ell T} - f_{X_T}(1-f_{\mathcal{G}_{X_T}})\right)}{\left(2\mathcal{G}_{X_T}E_{11}(1-f_{\mathcal{G}_{X_T}} - f_{\mathcal{G}_{X_T}}f_{X_T}) - f_{X_T}^2X_T^2l_{\ell}^*\right)r_{\ell T}}, & \text{otherwise.} \end{cases} \quad (\text{B.19})$$

B.1.2 Longitudinal compressive damage variable $d_{\ell C}$

The longitudinal compressive damage variable ($d_{\ell C}$) as a function of the elastic domain threshold in the longitudinal compressive direction ($r_{\ell C}$) is obtained using a uniaxial longitudinal compressive test. The Cartesian components of σ under this loading state read

$$\begin{aligned} \sigma_{11} &< 0 \\ \sigma_{22} = \sigma_{33} = \sigma_{23} = \sigma_{13} = \sigma_{12} &= 0. \end{aligned} \quad (\text{B.20})$$

The effective stress tensor is obtained by combining Eqs. (B.3) and (B.4), therefore, the effective stresses in Eq. (B.5) are obtained where σ_{11} is replaced by $-\sigma_{11}$. Then, the damage softening law in longitudinal compressive direction is defined as a bilinear function [101, 102]. The first segment defines the onset of kink-band using a large drop followed the horizontal asymptote related to kink-band broadening and contact frictional, see Fig. B.2. Therefore, Eq. (B.7) is used to define each segment.

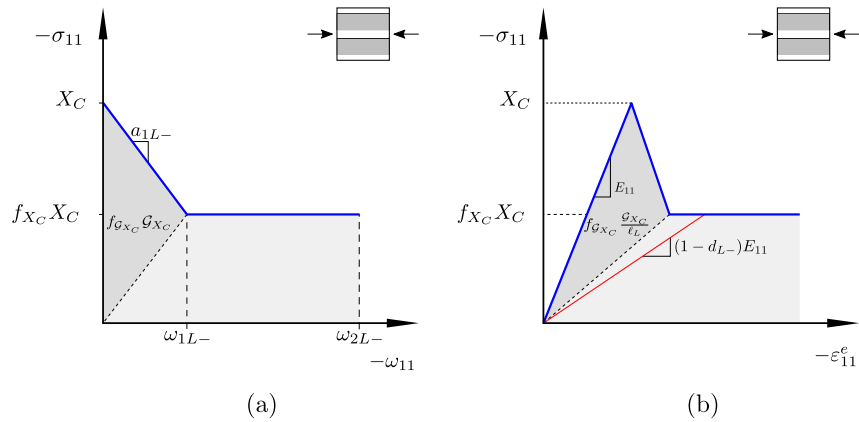


Figure B.2.: Softening law in the longitudinal compressive direction: a) stress vs. crack opening displacement curve and b) stress vs. elastic strain curve.

Subsequently, the loading function in the longitudinal compressive direction ($\phi_{\ell C}$) in Eq. (2.27) is evaluated assuming that $r_{\ell C} = \phi_{\ell C}$ and $d_{\ell} = d_{\ell C}$. Hence, the longitudinal

compressive damage variable for each segment ($d_{i_s \ell C}$) is obtained as a function of the elastic domain threshold $r_{\ell C}$ as

$$d_{i_s \ell C} = \frac{\kappa_{1_{i_s \ell C}}}{2\kappa_{0_{i_s \ell C}}} - \sqrt{\left(\frac{\kappa_{1_{i_s \ell C}}}{2\kappa_{0_{i_s \ell C}}}\right)^2 - \frac{\kappa_{2_{i_s \ell C}}}{\kappa_{0_{i_s \ell C}}}} \quad (\text{B.21})$$

with:

$$\begin{aligned} \kappa_{0_{i_s \ell C}} &= \kappa_{4_{i_s \ell C}}^2 - (\mathbb{H}_{0_{11}} \mathbb{H}_{0_{12}} b_{i_s \ell C})^2 \eta_t^q - \mathbb{H}_{0_{12}}^2 \kappa_{5_{i_s \ell C}} \\ \kappa_{1_{i_s \ell C}} &= (2X_C \kappa_{4_{i_s \ell C}} r_{\ell C} + \kappa_{5_{i_s \ell C}}) \kappa_{3_{i_s \ell C}} \\ \kappa_{2_{i_s \ell C}} &= (X_C^2 r_{\ell C}^2 - b_{\ell C}^2) \kappa_{3_{i_s \ell C}}^2 \\ \kappa_{3_{i_s \ell C}} &= \mathbb{H}_{0_{11}} (\mathbb{H}_{0_{22}} + \mathbb{H}_{0_{23}}) - 2\mathbb{H}_{0_{12}}^2 \\ \kappa_{4_{i_s \ell C}} &= \mathbb{H}_{0_{11}} \mathbb{H}_{0_{12}} b_{i_s \ell C} \eta_t - X_C r_{\ell C} (\mathbb{H}_{0_{11}} a_{i_s \ell C} l_{\ell}^* - 1) \kappa_{3_{i_s \ell C}} \\ \kappa_{5_{i_s \ell C}} &= (2\mathbb{H}_{0_{12}} b_{i_s \ell C})^2, \end{aligned} \quad (\text{B.22})$$

where i_s refers to the corresponding segment of the softening law, $a_{i_s \ell C}$ and $b_{i_s \ell C}$ are the slope and intercept, respectively, of the corresponding segment and $\mathbb{H}_{0_{ij}}$ are the components of the compliance tensor without damage ($\mathbb{H}_0 = \mathbb{H}(d_M = 0)$). The intercept of the first segment ($b_{1\ell C}$) is equal to longitudinal compressive strength (X_C) and its corresponding slope is obtained from Eq. (B.13) where the slope has positive sign and yields

$$a_{1\ell C} = \frac{X_C^2 (1 - f_{X_C})}{2f_{\mathcal{G}_{X_C}} \mathcal{G}_{X_C}}, \quad (\text{B.23})$$

where $f_{\mathcal{G}_{X_C}} \mathcal{G}_{X_C}$ is the longitudinal compressive fracture toughness of the first segment, see Fig. B.2. The slope of the second segment $a_{2\ell C}$ is equal to zero and its intercept is $b_{2\ell C} = f_{X_C} X_C$.

Finally, the longitudinal compressive damage variable in Eq. (B.21) yields

$$d_{\ell C} = \begin{cases} d_{1\ell C} (a_{1\ell C}, b_{1\ell C} = X_C), & \text{if } r_{\ell C} \leq r_{1\ell C} \\ d_{2\ell C} (a_{2\ell C} = f_{X_C} X_C, b_{2\ell C} = 0), & \text{otherwise.} \end{cases} \quad (\text{B.24})$$

The active segment in Eq. (B.24) depends on $r_{\ell C}$ in the inflection point ($r_{1\ell C}$) and is calculated matching both segments.

B.2 Transverse damage variable d_t

The transverse damage variable (d_t) is defined equal to the transverse shear damage variable (d_{st}) when the second invariant p_t is positive and equal to zero when the second invariant is negative, therefore,

$$d_t := d_{st} \frac{\langle p_t \rangle}{|p_t|}. \quad (\text{B.25})$$

The model assumes that the degradation of the matrix stiffness due to mode-I matrix cracking is the same that generated by mode-II matrix cracking when the crack opens ($p_t > 0 \rightarrow d_t = d_{st}$). However, degradation of the matrix stiffness in mode-I is not considered when the crack closes ($p_t < 0 \rightarrow d_t = 0$).

B.3 Transverse shear damage variable d_{st}

The same stiffness degradation due to a mode-II matrix cracking is considered as that due to mode-I matrix cracking. Therefore, the damage softening law in the transverse shear direction (d_{st}) as a function of the elastic domain threshold in the transverse direction (r_t) can be obtained using a uniaxial transverse tensile test. Under these loading conditions, the Cartesian components of σ yield

$$\begin{aligned} \sigma_{22} &> 0 \\ \sigma_{11} = \sigma_{33} = \sigma_{23} = \sigma_{13} = \sigma_{12} &= 0, \end{aligned} \quad (\text{B.26})$$

and the elastic strain tensor reads

$$\boldsymbol{\varepsilon}^e = \mathbb{H} \begin{bmatrix} 0 \\ \sigma_{22} \\ 0 \\ 0 \\ 0 \\ 0 \end{bmatrix}. \quad (\text{B.27})$$

Therefore, the shear effective stresses are equal to zero and the principal effective stresses are obtained by combining Eqs. (B.4) and (B.27) as

$$\begin{aligned}\tilde{\sigma}_{11} &= \frac{E_{11}\nu_{12}d_t}{(E_{11} - 4E_t\nu_{12}^2)(1 - d_t)}\sigma_{22} \\ \tilde{\sigma}_{22} &= \frac{E_{11}(2 - d_t - d_{st}) - 4E_t\nu_{12}^2(2 + d_{st}d_t - 2d_t - d_{st})}{(2E_{11} - 8E_t\nu_{12}^2)(1 + d_{st}d_t - d_t - d_{st})}\sigma_{22} \\ \tilde{\sigma}_{33} &= \frac{E_{11}(d_t - d_{st}) - 4E_t\nu_{12}^2(d_{st}d_t - d_{st})}{(2E_{11} - 8E_t\nu_{12}^2)(1 + d_{st}d_t - d_t - d_{st})}\sigma_{22}.\end{aligned}\quad (\text{B.28})$$

The softening law is defined using a linear law as

$$\sigma_{22} := a_{Y_T}\omega_{22} + b_{Y_T}, \quad (\text{B.29})$$

where a_{Y_T} and b_{Y_T} are the slope and intercept, respectively, of the transverse tensile stress-crack opening displacement softening law, see Fig. B.3a.

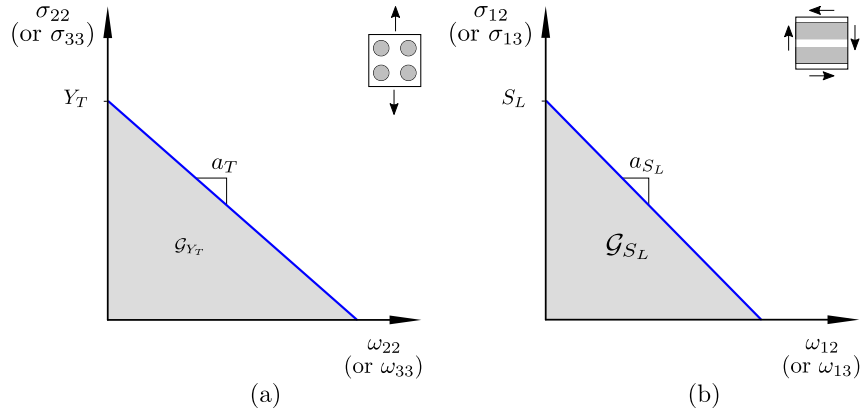


Figure B.3.: Stress vs. crack opening displacement curve of the softening law in: a) transverse tensile direction and b) longitudinal shear direction.

After that, the transverse loading function (ϕ_t) in Eq. (2.28) is evaluated assuming that $r_t = \phi_t$ and $d_t = d_{st}$. Hence, the damage variable reads

$$d_{st} = -\sqrt{-\frac{\kappa_{2_{st}}}{\kappa_{0_{st}}} + \frac{\kappa_{1_{st}}^2}{4\kappa_{0_{st}}^2}} - \frac{\kappa_{1_{st}}}{2\kappa_{0_{st}}} \quad (\text{B.30})$$

with:

$$\begin{aligned}
\kappa_{0_{st}} &= \mathbb{H}_{0_{12}}^2 \kappa_{5_{st}} (\mathbb{H}_{0_{22}} - \mathbb{H}_{0_{23}}) + 4S_T^2 \kappa_{4_{st}}^2 \\
\kappa_{1_{st}} &= \kappa_{5_{st}} \kappa_{6_{st}} - 4S_T^2 \kappa_{4_{st}} \kappa_{3_{st}} \\
\kappa_{2_{st}} &= (S_T \kappa_{3_{st}})^2 - (\mu_t + 1) (Y_C Y_T b_{Y_T} \kappa_{6_{st}})^2 \\
\kappa_{3_{st}} &= 2Y_C Y_T \kappa_{6_{st}} r_t + b_{Y_T} \kappa_{7_{st}} (Y_C - Y_T) \\
\kappa_{4_{st}} &= \mathbb{H}_{0_{12}}^2 b_{Y_T} (\mathbb{H}_{0_{22}} - \mathbb{H}_{0_{23}}) (Y_C - Y_T) + Y_C Y_T \kappa_{6_{st}} r_t (\mathbb{H}_{0_{22}} a_{Y_T} l_t^* + 1) \\
\kappa_{5_{st}} &= \mu_t (\mathbb{H}_{0_{23}} - \mathbb{H}_{0_{22}}) (2\mathbb{H}_{0_{12}} Y_C Y_T b_{Y_T})^2 \\
\kappa_{6_{st}} &= \mathbb{H}_{0_{11}} (\mathbb{H}_{0_{22}}^2 - \mathbb{H}_{0_{23}}^2) + 2\mathbb{H}_{0_{12}}^2 (\mathbb{H}_{0_{23}} - \mathbb{H}_{0_{22}}) \\
\kappa_{7_{st}} &= 2\mathbb{H}_{0_{12}}^2 (\mathbb{H}_{0_{22}} - \mathbb{H}_{0_{23}}) + (\mathbb{H}_{0_{22}} + \mathbb{H}_{0_{23}}) (\mathbb{H}_{0_{11}} \mathbb{H}_{0_{23}} - \mathbb{H}_{0_{11}} \mathbb{H}_{0_{22}}),
\end{aligned} \tag{B.31}$$

where \mathcal{G}_{Y_T} is the mode-I intralaminar fracture toughness and l_t^* is the transverse characteristic element length. The transverse shear strength (S_T) can be obtained from Eq. (5.1) for a given μ_t . The intercept of the softening law (b_{Y_T}) is equal to Y_T and its corresponding slope reads

$$a_{Y_T} = \frac{-Y_T}{\omega_{22}}, \tag{B.32}$$

and the crack opening displacement (ω_{22}) when the area under the softening law match (\mathcal{G}_{Y_T}) is obtained by solving the following equation

$$\mathcal{G}_{Y_T} = \frac{1}{2} \omega_{22} Y_T, \tag{B.33}$$

therefore,

$$a_{Y_T} = -\frac{Y_T^2}{2\mathcal{G}_{Y_T}}. \tag{B.34}$$

B.4 Longitudinal shear damage variable $d_{s\ell}$

The longitudinal shear damage variable is defined as

$$d_{s\ell} := 1 - (1 - d_{s\ell^*})(1 - d_{\ell T}), \tag{B.35}$$

which allows to introduce a degradation of the stiffness in the longitudinal shear direction due to longitudinal shear effective stresses ($\tilde{\sigma}_{12}$ and $\tilde{\sigma}_{13}$), but also due to longitudinal tensile effective stress ($\tilde{\sigma}_{11}$). The damage variable $d_{s\ell^*}$ related to the longitudinal shear

stresses is defined as a function of r_t using a uniaxial longitudinal shear test. Therefore, the Cartesian components of σ yield

$$\begin{aligned}\sigma_{12} &\neq 0 \\ \sigma_{11} = \sigma_{22} = \sigma_{33} = \sigma_{23} = \sigma_{13} &= 0,\end{aligned}\tag{B.36}$$

and all the Cartesian components of the elastic strain tensor are equal to zero except

$$\varepsilon_{12}^e = \frac{1}{(1 - d_{s\ell})G_{12}}\sigma_{12}.\tag{B.37}$$

Then, the effective stresses in Eq. (B.4) are equal to zero except

$$\tilde{\sigma}_{12} = \frac{1}{(1 - d_{s\ell})}\sigma_{12},\tag{B.38}$$

and the transverse loading function in Eq. (2.28) reads

$$\phi_t = \frac{1}{(1 - d_{s\ell})S_L}\sigma_{12}.\tag{B.39}$$

The softening law of $d_{s\ell^*}$ is defined using a linear function as

$$\sigma_{12} := a_{s\ell}\omega_{12} + b_{s\ell},\tag{B.40}$$

where $a_{s\ell}$ and $b_{s\ell}$ are the slope and intercept, respectively, of the longitudinal shear stress-crack opening softening law, see Fig. B.3b.

The damage variable $d_{s\ell^*}$ is obtained by introducing Eq. (B.8) into Eq. (B.40) and, then, combining it with Eqs. (B.37) and (B.39) and assuming only matrix cracking ($d_{\ell T} = 0$) and $r_t = \phi_t$. Therefore, the damage variables yields

$$d_{s\ell^*} = \frac{G_{12}(S_L r_t - b_{s\ell})}{(G_{12} + a_{s\ell} l_{s\ell}^*)S_L r_t},\tag{B.41}$$

where the intercept in the stress vs. crack opening displacement curve ($b_{s\ell}$) is equal to S_L and the slope reads

$$a_{s\ell} = \frac{-S_L}{\omega_{12}},\tag{B.42}$$

see Fig. B.3b. The crack opening displacement (ω_{12}) when the area under the softening law match the total mode-II intralaminar fracture toughness (\mathcal{G}_{S_L}) is obtained by solving the following equation

$$\mathcal{G}_{S_L} = \frac{1}{2}\omega_{12}S_L, \quad (\text{B.43})$$

therefore,

$$a_{s_\ell} = -\frac{S_L^2}{2\mathcal{G}_{S_L}}, \quad (\text{B.44})$$

and the damage variable related to the longitudinal shear stresses yields

$$d_{s\ell^*} = \frac{2\mathcal{G}_{S_L}G_{12}(r_t - 1)}{(2\mathcal{G}_{S_L}G_{12} - S_L^2 l_{s_\ell}^*)r_t}. \quad (\text{B.45})$$

Calculus of the increment of the consistency parameter of the plasticity model ($\Delta\gamma_{(n+1)}^{(k)}$)

The calculus of the increment of the consistency parameter of the plasticity model ($\Delta\gamma_{(n+1)}^{(k)}$) (see Eq. (2.36)) is presented in this appendix. This parameter is used to update the plastic strain tensor in the return mapping of plasticity modelling which is solved using the Newton-Raphson method. The procedure to obtain $\Delta\gamma_{(n+1)}^{(k)}$ is presented at time $t_{(n+1)}$ and in the Newton-Raphson iteration of k . Subscripts and superscripts referring to time and the Newton-Raphson method are avoided in this appendix, only those different from the current time step and Newton-Raphson iteration $((\cdot)_{(n+1)}^{(k)})$ are shown.

The procedure is presented in general form to simplify the notation. Then, the yield function defined in Eq. (2.21) can be rewritten in Voigt notation as

$$\phi^p = \sqrt{\boldsymbol{\sigma}^T \mathbb{K} \boldsymbol{\sigma}} + \mathbb{L}^T \boldsymbol{\sigma} + m \sqrt{\boldsymbol{\sigma}^T \mathbb{M} \boldsymbol{\sigma}} - 1 \leq 0, \quad (\text{C.1})$$

where $\boldsymbol{\sigma}$ is the stress tensor, \mathbb{K} , \mathbb{M} and m are second order tensors and a scalar value, respectively, that contain the coefficients of the non-linear terms in Eq. (2.21), and \mathbb{L} is a first order tensor that contains the coefficients of the linear terms of Eq. (2.21). They read

$$\mathbb{K} = \begin{bmatrix} 0 & 0 & 0 & 0 & 0 & 0 \\ 0 & K_{22} & K_{23} & 0 & 0 & 0 \\ 0 & K_{23} & K_{22} & 0 & 0 & 0 \\ 0 & 0 & 0 & K_{44} & 0 & 0 \\ 0 & 0 & 0 & 0 & K_{55} & 0 \\ 0 & 0 & 0 & 0 & 0 & K_{55} \end{bmatrix} \quad (\text{C.2})$$

with:

$$K_{22} = \left(\frac{Y_{TP} + Y_{CP}}{2Y_{TP}Y_{CP}} \right)^2 \quad (\text{C.3})$$

$$K_{23} = K_{22} \frac{\mu_{tp} - 1}{\mu_{tp} + 1} \quad (\text{C.4})$$

$$K_{44} = K_{22} \frac{4}{\mu_{tp} + 1} \quad (\text{C.5})$$

$$K_{55} = \left(\frac{\mu_{s\ell p}}{S_{LP}} \right)^2, \quad (\text{C.6})$$

where Y_{TP} and Y_{CP} are the transverse tensile and compressive yield stresses, respectively, and S_{LP} is the longitudinal shear yield stress. They are defined as a function of the plastic equivalent strain $\bar{\varepsilon}^p$. The parameters $\mu_{s\ell p}$ and μ_{tp} are the plastic envelope shape coefficients. The rest of tensors and the scalar value of ϕ^p in Eq. (C.1) read

$$\mathbb{L} = \begin{bmatrix} 0 \\ L_{22} \\ L_{22} \\ 0 \\ 0 \\ 0 \end{bmatrix} \quad (\text{C.7})$$

with:

$$L_{22} = \frac{Y_{CP} - Y_{TP}}{2Y_{TP}Y_{CP}}, \quad (\text{C.8})$$

$$m = 1 - \mu_{s\ell p}, \quad (\text{C.9})$$

and

$$\mathbb{M} = \begin{bmatrix} 0 & 0 & 0 & 0 & 0 & 0 \\ 0 & 0 & 0 & 0 & 0 & 0 \\ 0 & 0 & 0 & 0 & 0 & 0 \\ 0 & 0 & 0 & 0 & 0 & 0 \\ 0 & 0 & 0 & 0 & M_{55} & 0 \\ 0 & 0 & 0 & 0 & 0 & M_{55} \end{bmatrix} \quad (\text{C.10})$$

with:

$$M_{55} = \frac{1}{S_{LP}^2}. \quad (\text{C.11})$$

The increment of the consistency parameter reads

$$\Delta\gamma = -\frac{\phi^p}{\frac{d\phi^p}{d\gamma}}, \quad (\text{C.12})$$

see Eq. (2.36). Hence, the calculus of the derivative of the yield function (ϕ^p) with respect to the consistency parameter (γ) is required to update $\Delta\gamma$ in each iteration of the Newton-Raphson algorithm. The yield function defined in Eq. (C.1) reads

$$\phi^p = f(\boldsymbol{\sigma}, \mathbb{K}, \mathbb{L}, m, \mathbb{M}), \quad (\text{C.13})$$

where each variable of the right hand side of Eq. (C.13) are defined as

$$\begin{aligned}\boldsymbol{\sigma} &= f(\gamma) \\ \mathbb{K} &= f(\bar{\varepsilon}^p(\gamma, \boldsymbol{\sigma})) \\ \mathbb{L} &= f(\bar{\varepsilon}^p(\gamma, \boldsymbol{\sigma})) \\ m &= f(\mu_{s\ell p}) \\ \mathbb{M} &= f(\bar{\varepsilon}^p(\gamma, \boldsymbol{\sigma})),\end{aligned}\tag{C.14}$$

where $\bar{\varepsilon}^p$ is the equivalent plastic strain defined in Eq. (2.13). Therefore, applying the corresponding chain rules, $d_\gamma(\phi^p)$ yields

$$\frac{d\phi^p}{d\gamma} = \frac{\partial\phi^p}{\partial\boldsymbol{\sigma}} \frac{d\boldsymbol{\sigma}}{d\gamma} + \left(\frac{\partial\phi^p}{\partial\mathbb{K}} \frac{d\mathbb{K}}{d\bar{\varepsilon}^p} + \frac{\partial\phi^p}{\partial\mathbb{L}} \frac{d\mathbb{L}}{d\bar{\varepsilon}^p} + \frac{\partial\phi^p}{\partial\mathbb{M}} \frac{d\mathbb{M}}{d\bar{\varepsilon}^p} \right) \frac{d\bar{\varepsilon}^p}{d\gamma}.\tag{C.15}$$

The terms of Eq. (C.15) are developed in the following sections. Finally, a comparison between the numerical approximation of Eq. (C.15) with its analytical solution is presented.

C.1 Derivatives as a function of $\boldsymbol{\sigma}$

The partial derivative of the yield function with respect to the stress tensor in Eq. (C.15) reads

$$\frac{\partial\phi^p}{\partial\boldsymbol{\sigma}} = \frac{\mathbb{K}\boldsymbol{\sigma}}{\sqrt{\boldsymbol{\sigma}^T\mathbb{K}\boldsymbol{\sigma}}} + \mathbb{L} + m \frac{\mathbb{M}\boldsymbol{\sigma}}{\sqrt{\boldsymbol{\sigma}^T\mathbb{M}\boldsymbol{\sigma}}},\tag{C.16}$$

and the derivative of the stress tensor with respect to the consistency parameter from Eq. (2.34) yields

$$\frac{d\boldsymbol{\sigma}}{d\gamma} = -\mathbb{C}_e \frac{\partial\varphi^p}{\partial\boldsymbol{\sigma}},\tag{C.17}$$

where \mathbb{C}_e is the elasticity tensor (its inverse matrix ($\mathbb{C}_e = \mathbb{H}^{-1}$) is defined in Eq. (2.10)) and φ^p is the plastic potential function from Eq. (2.21) and is defined in general form as

$$\varphi^p = \sqrt{\boldsymbol{\sigma}^T\hat{\mathbb{K}}\boldsymbol{\sigma}} + \hat{\mathbb{L}}^T\boldsymbol{\sigma} + \hat{m}\sqrt{\boldsymbol{\sigma}^T\hat{\mathbb{M}}\boldsymbol{\sigma}} - 1 \leq 0,\tag{C.18}$$

where $\hat{\mathbb{K}}$, $\hat{\mathbb{M}}$ and \hat{m} are second order tensors and a scalar value, respectively, that contain the coefficients of the non-linear terms in Eq. (2.21), and $\hat{\mathbb{L}}$ is a first order tensor that contains the coefficients of the linear terms in Eq. (2.21). They are defined from Eq. (C.2)

to Eq. (C.11) by replacing the yield parameters with the plastic potential parameters (e.g. Y_{CP} by \hat{Y}_{CP}). Therefore, $\partial_{\sigma}(\varphi^p)$ yields

$$\frac{\partial \varphi^p}{\partial \sigma} = \frac{\hat{\mathbb{K}}\sigma}{\sqrt{\sigma^T \hat{\mathbb{K}}\sigma}} + \hat{\mathbb{L}} + \hat{m} \frac{\hat{\mathbb{M}}\sigma}{\sqrt{\sigma^T \hat{\mathbb{M}}\sigma}}. \quad (\text{C.19})$$

C.2 Derivatives as a function of \mathbb{K}

The partial derivative of the yield function with respect to \mathbb{K} from Eq. (C.15) reads

$$\frac{\partial \phi^p}{\partial \mathbb{K}} = \frac{\sigma^T \sigma}{2\sqrt{\sigma^T \mathbb{K} \sigma}}. \quad (\text{C.20})$$

The derivative of \mathbb{K} with respect to the equivalent plastic strain is obtained by applying the chain rule as

$$\frac{d\mathbb{K}}{d\bar{\varepsilon}^p} = \frac{\partial \mathbb{K}}{\partial Y_{CP}} \frac{dY_{CP}}{d\bar{\varepsilon}^p} + \frac{\partial \mathbb{K}}{\partial Y_{TP}} \frac{dY_{TP}}{d\bar{\varepsilon}^p} + \frac{\partial \mathbb{K}}{\partial S_{LP}} \frac{dS_{LP}}{d\bar{\varepsilon}^p}. \quad (\text{C.21})$$

The yield stresses (Y_{CP} , Y_{TP} and S_{LP}) are defined as a function of $\bar{\varepsilon}^p$ by introducing the corresponding yield stress vs. $\bar{\varepsilon}^p$ curve. Hence, the derivatives of the yield stress with respect to $\bar{\varepsilon}^p$ ($d_{\bar{\varepsilon}^p}(Y_{CP})$, $d_{\bar{\varepsilon}^p}(Y_{TP})$ and $d_{\bar{\varepsilon}^p}(S_{LP})$) are directly obtained from the material card by applying numerical differentiation.

The partial derivative $\partial_{Y_{CP}}(\mathbb{K})$ reads

$$\frac{\partial \mathbb{K}}{\partial Y_{CP}} = \begin{bmatrix} 0 & 0 & 0 & 0 & 0 & 0 \\ 0 & \frac{\partial K_{22}}{\partial Y_{CP}} & \frac{\partial K_{23}}{\partial Y_{CP}} & 0 & 0 & 0 \\ 0 & \frac{\partial K_{23}}{\partial Y_{CP}} & \frac{\partial K_{22}}{\partial Y_{CP}} & 0 & 0 & 0 \\ 0 & 0 & 0 & \frac{\partial K_{44}}{\partial Y_{CP}} & 0 & 0 \\ 0 & 0 & 0 & 0 & 0 & 0 \\ 0 & 0 & 0 & 0 & 0 & 0 \end{bmatrix} \quad (\text{C.22})$$

with:

$$\frac{\partial K_{22}}{\partial Y_{CP}} = -\frac{Y_{CP} + Y_{TP}}{2Y_{TP}Y_{CP}^3}, \quad (\text{C.23})$$

$$\frac{\partial K_{23}}{\partial Y_{CP}} = \frac{\mu_{tp} - 1}{\mu_{tp} + 1} \frac{\partial K_{22}}{\partial Y_{CP}}, \quad (\text{C.24})$$

$$\frac{\partial K_{44}}{\partial Y_{CP}} = \frac{4}{\mu_{tp} + 1} \frac{\partial K_{22}}{\partial Y_{CP}}, \quad (\text{C.25})$$

the partial derivative $\partial_{Y_{TP}}(\mathbb{K})$ yields

$$\frac{\partial \mathbb{K}}{\partial Y_{TP}} = \begin{bmatrix} 0 & 0 & 0 & 0 & 0 & 0 \\ 0 & \frac{\partial K_{22}}{\partial Y_{TP}} & \frac{\partial K_{23}}{\partial Y_{TP}} & 0 & 0 & 0 \\ 0 & \frac{\partial K_{23}}{\partial Y_{TP}} & \frac{\partial K_{22}}{\partial Y_{TP}} & 0 & 0 & 0 \\ 0 & 0 & 0 & \frac{\partial K_{44}}{\partial Y_{TP}} & 0 & 0 \\ 0 & 0 & 0 & 0 & 0 & 0 \\ 0 & 0 & 0 & 0 & 0 & 0 \end{bmatrix} \quad (\text{C.26})$$

with:

$$\frac{\partial K_{22}}{\partial Y_{TP}} = -\frac{Y_{CP} + Y_{TP}}{2Y_{CP}Y_{TP}^3}, \quad (\text{C.27})$$

$$\frac{\partial K_{23}}{\partial Y_{TP}} = \frac{\mu_{tp} - 1}{\mu_{tp} + 1} \frac{\partial K_{22}}{\partial Y_{TP}}, \quad (\text{C.28})$$

$$\frac{\partial K_{44}}{\partial Y_{TP}} = \frac{4}{\mu_{tp} + 1} \frac{\partial K_{22}}{\partial Y_{TP}}, \quad (\text{C.29})$$

and the partial derivative $\partial_{S_{LP}}(\mathbb{K})$ reads

$$\frac{\partial \mathbb{K}}{\partial S_{LP}} = \begin{bmatrix} 0 & 0 & 0 & 0 & 0 & 0 \\ 0 & 0 & 0 & 0 & 0 & 0 \\ 0 & 0 & 0 & 0 & 0 & 0 \\ 0 & 0 & 0 & 0 & 0 & 0 \\ 0 & 0 & 0 & 0 & \frac{\partial K_{55}}{\partial S_{LP}} & 0 \\ 0 & 0 & 0 & 0 & 0 & \frac{\partial K_{55}}{\partial S_{LP}} \end{bmatrix} \quad (\text{C.30})$$

with:

$$\frac{\partial K_{55}}{\partial S_{LP}} = -\frac{2\mu_{s\ell p}^2}{S_{LP}^3}. \quad (\text{C.31})$$

The derivative of the equivalent plastic strain with respect to the consistency parameter from Eq. (2.34) reads

$$\frac{d\bar{\varepsilon}^p}{d\gamma} = \sqrt{\frac{1}{2}} \left\| \frac{\partial \varphi^p}{\partial \sigma} \right\|, \quad (\text{C.32})$$

where $\partial_\sigma(\varphi^p)$ is defined in Eq. (C.19).

C.3 Derivatives as a function of \mathbb{L}

The partial derivative of the yield function with respect to \mathbb{L} from Eq. (C.1) reads

$$\frac{\partial \phi^p}{\partial \mathbb{L}} = \boldsymbol{\sigma}^T. \quad (\text{C.33})$$

The derivative of \mathbb{L} with respect to the equivalent plastic strain is obtained applying the chain rule as

$$\frac{d\mathbb{L}}{d\bar{\varepsilon}^p} = \frac{\partial \mathbb{L}}{\partial Y_{CP}} \frac{dY_{CP}}{d\bar{\varepsilon}^p} + \frac{\partial \mathbb{L}}{\partial Y_{TP}} \frac{dY_{TP}}{d\bar{\varepsilon}^p}, \quad (\text{C.34})$$

where the partial derivative $\partial_{Y_{CP}}(\mathbb{L})$ reads

$$\frac{\partial \mathbb{L}}{\partial Y_{CP}} = \begin{bmatrix} 0 \\ \frac{\partial L_{22}}{\partial Y_{CP}} \\ \frac{\partial L_{22}}{\partial Y_{CP}} \\ 0 \\ 0 \\ 0 \end{bmatrix} \quad (\text{C.35})$$

with:

$$\frac{\partial L_{22}}{\partial Y_{CP}} = \frac{1}{2Y_{CP}^2}, \quad (\text{C.36})$$

and the partial derivative $\partial_{Y_{TP}}(\mathbb{L})$ yields

$$\frac{\partial \mathbb{L}}{\partial Y_{TP}} = \begin{bmatrix} 0 \\ \frac{\partial L_{22}}{\partial Y_{TP}} \\ \frac{\partial L_{22}}{\partial Y_{TP}} \\ 0 \\ 0 \\ 0 \end{bmatrix} \quad (\text{C.37})$$

with:

$$\frac{\partial L_{22}}{\partial Y_{TP}} = -\frac{1}{2Y_{TP}^2}. \quad (\text{C.38})$$

C.4 Derivatives as a function of \mathbb{M}

The partial derivative of the yield function with respect to \mathbb{M} from Eq. (C.1) reads

$$\frac{\partial \phi^p}{\partial \mathbb{M}} = m \frac{\boldsymbol{\sigma}^T \boldsymbol{\sigma}}{2\sqrt{\boldsymbol{\sigma}^T \mathbb{M} \boldsymbol{\sigma}}}. \quad (\text{C.39})$$

The derivative of \mathbb{M} with respect to the equivalent plastic strain is obtained applying the chain rule as

$$\frac{d\mathbb{M}}{d\bar{\varepsilon}^p} = \frac{\partial \mathbb{M}}{\partial S_{LP}} \frac{dS_{LP}}{d\bar{\varepsilon}^p}, \quad (\text{C.40})$$

where the partial derivative $\partial_{S_{LP}}(\mathbb{M})$ reads

$$\frac{\partial \mathbb{M}}{\partial S_{LP}} = \begin{bmatrix} 0 & 0 & 0 & 0 & 0 & 0 \\ 0 & 0 & 0 & 0 & 0 & 0 \\ 0 & 0 & 0 & 0 & 0 & 0 \\ 0 & 0 & 0 & 0 & 0 & 0 \\ 0 & 0 & 0 & 0 & \frac{\partial M_{55}}{\partial S_{LP}} & 0 \\ 0 & 0 & 0 & 0 & 0 & \frac{\partial M_{55}}{\partial S_{LP}} \end{bmatrix} \quad (\text{C.41})$$

with:

$$\frac{\partial M_{55}}{\partial S_{LP}} = -\frac{2}{S_{LP}^3}. \quad (\text{C.42})$$

C.5 Numerical-analytical comparison of $\Delta\gamma$

The analytical expression of $\Delta\gamma$ is a complex algebraic expression, see Eq. (C.15). This section presents a comparison between the numerical approximation of $\Delta\gamma$ and its analytical solution. The main objective of this comparison is to analyse the accuracy and the efficiency in terms of the computational time of the numerical solution of $\Delta\gamma$.

The Newton's difference quotient is employed in the numerical approximation of $\Delta\gamma$ to estimate $d_\gamma(\phi^p)$ in Eq. (C.12) as

$$\frac{d\phi^p}{d\gamma} \approx \frac{\phi^p(\gamma + \Delta\gamma) - \phi^p(\gamma)}{\Delta\gamma}, \quad (\text{C.43})$$

where $\Delta\gamma$ represents a perturbation of γ . The perturbation value should be small to ensure that the variation of the yield function is close to the calculated value ($\phi^p(\gamma + \Delta\gamma) \approx \phi^p(\gamma)$).

Under certain loading conditions, such as at the onset of plasticity, the perturbation value should be close to zero, thus the indeterminate form of Eq. (C.43) can be found [273].

Different values of $\Delta\gamma$ under different loading cases are analysed to determine the order of magnitude of $\Delta\gamma$. The Abaqus/Explicit solver is used for the analysis. Therefore, the finite element solution is then obtained by discretising the time and, hence, by strain increments. Consequently, the analysis of $\Delta\gamma$ is also performed with different values of the strain increment. The analysis is carried out at the Gauss-point level using a single C3D8R element of $0.1 \text{ mm} \times 0.1 \text{ mm} \times 0.1 \text{ mm}$ with the IM7/8552 material system, see Section 2.4.

The relative error between the analytical solution of $\Delta\gamma$ and its numerical solution is calculated along the virtual tests and the maximum value of each test, and the error is then presented in Fig. C.1. A high relative error is found at smaller perturbation values ($\Delta\gamma < 10^{-14}$). In this range, $\Delta\gamma$ is close to the zero and perhaps leads to the indetermination of Eq. (C.43) but also the perturbation is close to the decimal points considered in the calculation (double precision is used in the simulations). The highest maximum relative error is obtained at $\Delta\gamma = 10^{-15}$ and a strain increment of 7×10^{-7} mm in the transverse compressive case. In most cases, perturbation values close to the strain increments also lead to high relative errors.

There is no significant difference in computational time between the numerical and analytical approaches. This may be because the analytical solution is implemented using multiple matrix products. The computational time could potentially be reduced by improving the implementation algorithm. One improvement could be to replace the matrix product with its solution, since there are several matrices with null components and the time-consuming matrix product is used in null operations.

The numerical solution is employed in this thesis with $\Delta\gamma = 10^{-10}$ since accurate approximations of $\Delta\gamma$ are obtained and there is no additional time computational cost. Additionally, the implementation algorithm for the numerical solution is easier and more generic than the analytical approach. The numerical method is independent of the yield function, the algorithm does not change regardless of any changes made to the yield function. In plasticity modelling design, one advantage of using the numerical approach is the ability to modify the yield function without affecting the implementation algorithm.

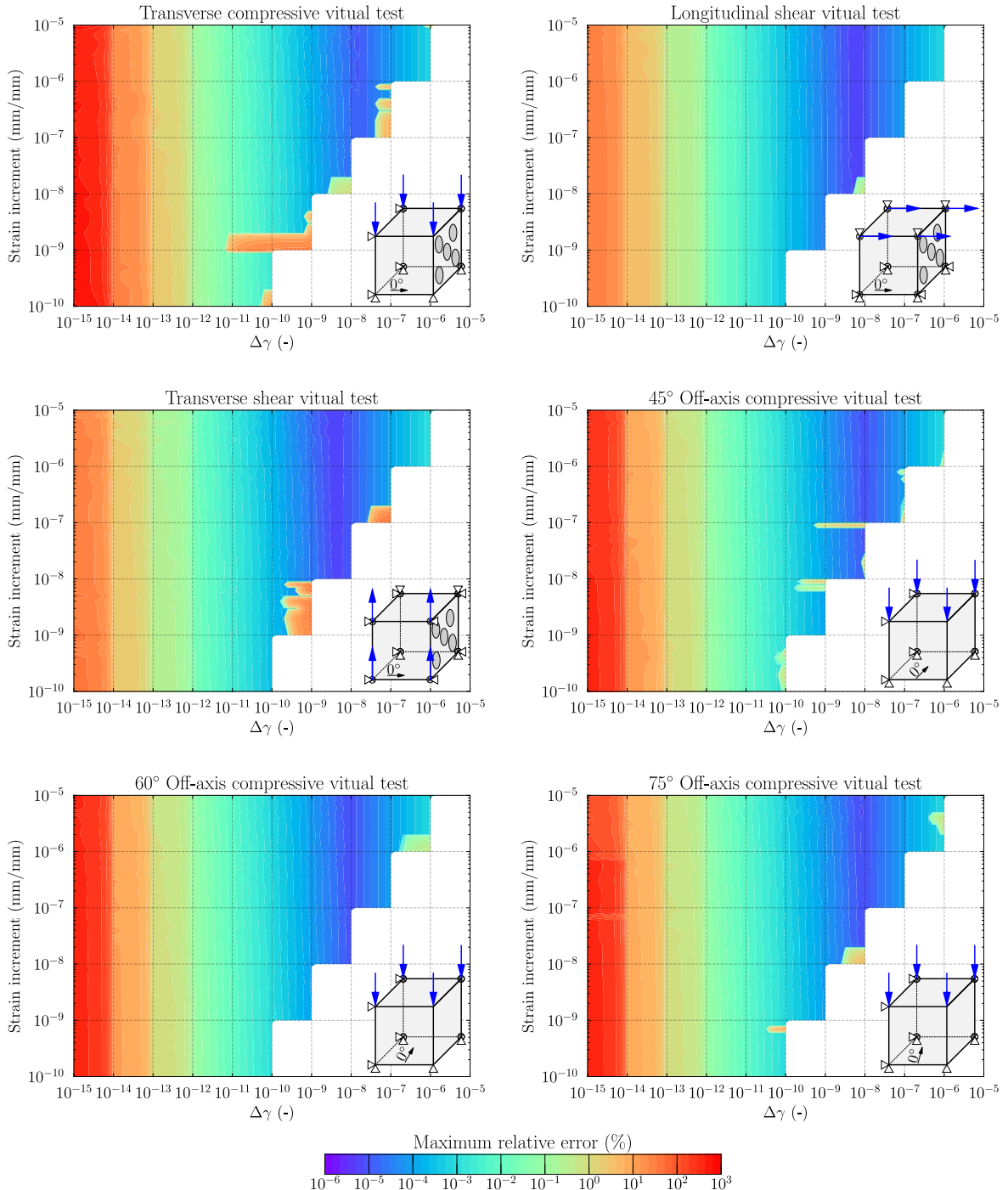


Figure C.1.: Maximum relative error between the analytical solution of $\Delta\gamma$ and its numerical approximation.

Vector product in Fortran

This appendix presents a comparison between the traditional method for calculating the product between a matrix and a vector ($\mathbf{c} = \mathbf{Ab}$) with the efficient approach. The traditional method to calculate the product is using two loops matrix. For example, the Fortran code of the product of a column vector of 6 components with a 6×6 matrix is presented in [Code D.1](#).

```

1  program main
2    implicit none
3    integer, parameter          :: dim=6, rp=8
4    integer                      :: i=1, j=1
5    real(rp), dimension(dim, dim) :: A=1._rp
6    real(rp), dimension(dim)      :: b=2._rp, c=0._rp
7    ! Vector product
8    do j=1, dim
9      do i=1, dim
10        c(i) = c(i) + A(i,j) * b(j)
11    end do
12  end do
13 end program main

```

Code D.1: Fortran code of the traditional algorithm of the product between a matrix and a vector ($\mathbf{c} = \mathbf{Ab}$).

The algorithm in each statement of the traditional approach is presented in [Code D.1](#). Firstly, the matrix **A** and the vectors **b** and **c** are loaded and stored in internal variables. Subsequently, the product of the corresponding component of **A** and **b** is calculated. Finally, the resultant value is added to the corresponding component of **c**.

Algorithm 4: Algorithm in each statement of the above Fortran code (Algorithm D.1).

Load each variable:

- 1 $V_0 = c(1 : n)$
- 2 $V_1 = A(1 : n, j)$
- 3 $S_0 = b(j)$

Calculus:

- 4 $V_1 = V_1 * S_0$
- 5 $V_0 = V_0 + V_1$

Store the calculus:

- 6 $c(1 : n) = V_0$
-

Cowell and Christopher [113] proposed an approach for reducing the computational time of a vector product. The algorithm consist into reduce the number of iterations in the outer loop in [Code D.1](#). The same previous Fortran example is now presented with the proposed methodology in [113]:

```
1 program main
2 implicit none
3 integer, parameter :: dim=6, rp=8
4 integer :: i=1, j=1
5 real(rp), dimension(dim,dim) :: A=1._rp
6 real(rp), dimension(dim) :: b=2._rp, c=0._rp
7 ! Vector product
8 do j=1,dim-1,2
9   do i=1,dim
10     c(i) = (c(i) + A(i,j) * b(j)) + A(i,j+1) * b(j+1)
11   end do
12 end do
13 end program main
```

Code D.2: Fortran code of the suggested algorithm by Cowell and Christopher [113] of the product between a matrix and a vector ($\mathbf{c} = \mathbf{Ab}$). The code is available at: <https://github.com/IR-Cozar/Vector-product-in-Fortran>.

The differences between the algorithms solely impact the transfer of data; the calculations and intermediate values remain constant. The suggested algorithm is outlined in [Code D.2](#). Firstly, the matrix **A** and the vectors **b** and **c** are loaded and stored in internal variables. Subsequently, the product of the corresponding component of **A** and **b** is calculated. Then, **A** and **b** of the next component are loaded and stored in new internal variables. Following this, the corresponding product and sum are calculated before adding the resultant value to the corresponding component of **c**.

Algorithm 5: Algorithm in each statement of the improved Fortran code (Algorithm D.2).

Load each vector:

- 1 $V_0 = c(1 : n)$
- 2 $V_1 = A(1 : n, j)$
- 3 $S_0 = b(j)$

Calculus:

- 4 $V_1 = V_1 * S_0$
- 5 $V_0 = V_0 + V_1$

Load each vector:

- 6 $V_2 = A(1 : n, j + 1)$
- 7 $S_1 = b(j + 1)$

Calculus:

- 8 $V_2 = V_2 * S_1$
- 9 $V_0 = V_0 + V_2$

Store the calculus:

- 10 $c(1 : n) = V_0$
-

The algorithm suggested by Cowell and Christopher [113] is executed only $n/2$ times, in contrast to the traditional one which is executed n times. As a result, the total number of loaded and stored vector \mathbf{c} is decreased. These two actions (load and store) are of great significance in this program. Memory access is frequently the limiting factor in computational processes [113]. These two algorithms have undergone a million evaluations. The computational time difference between them exceeds 30%, being lower in the algorithm proposed in [113].

Prevent division by zero in Fortran

This appendix presents a function to prevent division by zero in Fortran. The function provides a solution to a common programming problem. The algorithm involves obtaining the absolute value of the denominator in a division. Then, comparing it with a tolerance value (a value close to zero) and saving the larger one. Finally, evaluating the division with the larger absolute value, maintaining the sign of the original denominator. A Fortran example is presented in [Code E.1](#).

```

1  program main
2    implicit none
3    integer, parameter          :: rp=8
4    real(rp),parameter         :: tolerance=1e-15
5    real(rp)                   :: a=2._rp, b=0._rp, c=0._rp
6    ! Division by zero
7    c = a/Denominator(b,tolerance)
8  end program main
9
10
10 function Denominator(           &
11   ! Value of the denominator of the division
12   value,                      &
13   ! Tolerance to avoid the division by 0
14   tolerance)                  &
15   ! Maximum value between the value or the division tolerance
16   result(value_out)
17   implicit none
18   integer, parameter          :: rp=8
19   ! Inputs
20   real(rp),intent(in)        :: value,tolerance
21   !
22   ! Output
23   real(rp)                   :: value_out
24   !
25   ! Calculus of the function
26   !
27   value_out = sign(max(abs(value),division_tolerance), value)
28   !
29   return
30 end function Denominator

```

Code E.1: Fortran code to prevent a division by zero. The code is available at: <https://github.com/IR-Cozar/Prevent-a-division-by-zero>.

Critical characteristic element length

This appendix describes the calculus of the critical characteristic length ($l_{M_c}^*$) to be used in the Crack Band model [89] to prevent the snap-back effect. Firstly, the critical length for a linear softening law is presented, and that for a bilinear softening law. Finally, the critical characteristic length value of a material used in this work (IM7/8552 unidirectional prepreg system) is presented.

The characteristic length of a finite element (l_M^*) is employed in the Crack Band model to regularise the fracture toughness. Therefore, the energy dissipated due to damage in a finite element is dependent on both the fracture toughness and size of the finite element. For a constant fracture toughness, the higher the characteristic length is, the smaller the amount of energy dissipated by the finite element due to damage is, see Fig. F.1a. Consequently, at a specific l_M^* , the snap-back effect may occur in the stress vs. strain curve, see Fig. F.1b. To prevent this effect, l_M^* must be defined equal to or less than the critical characteristic length.

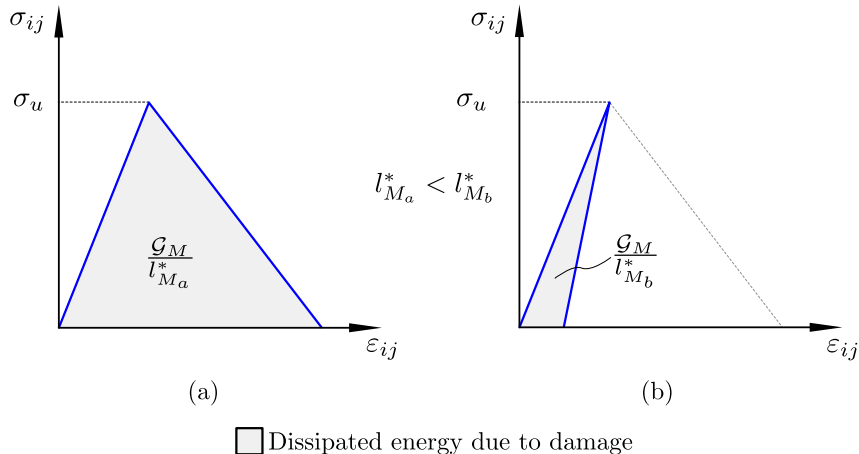


Figure F.1.: Schematic representation of a stress vs. strain curve behaviour using a linear softening law with two different characteristic element lengths: a shorter length (a), and a longer length (b) than the critical length.

F.1 Critical characteristic length for a linear softening law

The critical characteristic length that prevents the snap-back effect of a linear softening law at the corresponding loading direction ($l_{M_{c-1}}^*$) is obtained by equalling the regularised fracture toughness with the elastic energy [101], then

$$l_{M_{c-1}}^* = \frac{2E_M \mathcal{G}_M}{\sigma_u^2}, \quad (\text{F.1})$$

where E_M , \mathcal{G}_M and σ_u are the Young's modulus, the fracture toughness and strength, respectively, of the analysed material in the corresponding direction. For example, in the transverse tensile direction, the critical characteristic length yields

$$l_{t_c-1}^* = \frac{2E_{22} \mathcal{G}_{Y_T}}{Y_T^2}, \quad (\text{F.2})$$

where E_{22} is the transverse Young's modulus, Y_T and \mathcal{G}_{Y_T} are the transverse tensile strength and fracture toughness, respectively.

The schematic representation of the stress-strain relationship with different values of l_M^* in a linear softening law is presented in Fig. F.2. For $l_M^* < l_{M_{c-1}}^*$, stress gradually decreases once the σ_u is reached (see Fig. F.2a). The stress suddenly drops after the onset of damage ($\sigma_{ij} = \sigma_u$) for $l_M^* = l_{M_{c-1}}^*$, see Fig. F.2b. Finally, the snap-back effect is observed in the stress vs. strain curve with $l_M^* > l_{M_{c-1}}^*$, see Fig. F.2c.

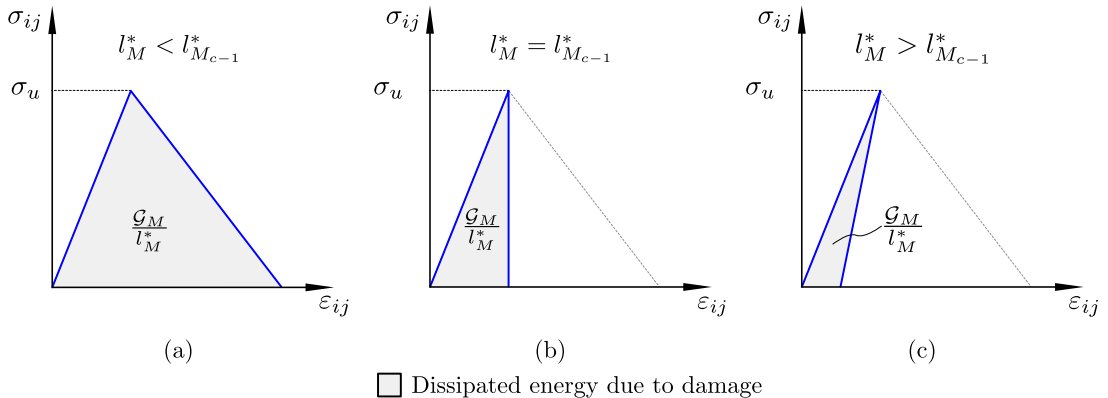


Figure F.2: Schematic representation of a stress vs. strain curve behaviour using a linear softening law with three different characteristic element lengths: a) a shorter length than the critical length, b) with the critical length, and c) a longer length than the critical length.

F.2 Critical characteristic length for a bilinear softening law

The determination of the critical characteristic length to prevent the partial snap-back effect for the bilinear softening law is also necessary to analyse. In this case, the critical length must be calculated for each segment of the softening law, and the minimum value between them is to be taken as the critical characteristic length.

The critical characteristic length for the first segment ($l_{M_{c-2.1}}^*$) is determined by matching the regularised fracture toughness of the first segment ($f_{\mathcal{G}_M} \mathcal{G}_M / l_M^*$) with the grey area in Fig. F.3a. This area corresponds to a sudden drop of the stress from $\sigma_{ij} = \sigma_u$ to $\sigma_{ij} = f_{\sigma_u} \sigma_u$ at the same strain level. Then, $l_{M_{c-2.1}}^*$ yields

$$l_{M_{c-2.1}}^* = \frac{2E_M f_{\mathcal{G}_M} \mathcal{G}_M}{\sigma_u^2 (1 - f_{\sigma_u})}. \quad (\text{F.3})$$

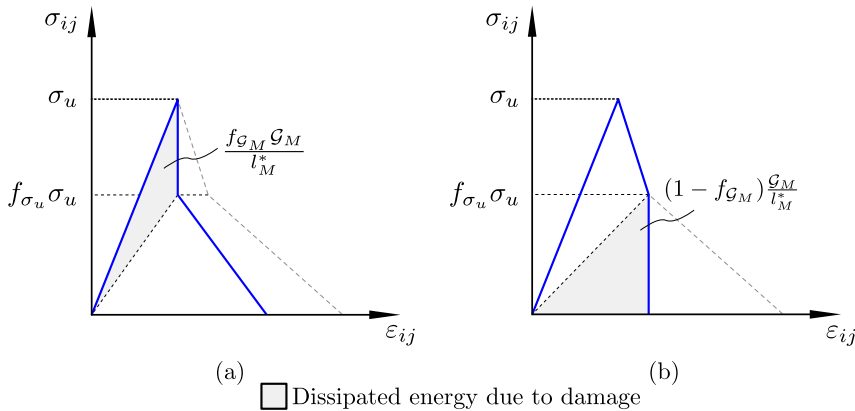


Figure F.3.: Schematic representation of a stress vs. strain curve behaviour using a bilinear softening law with the critical length of: a) first segment and b) second segment.

The critical characteristic length of the second segment ($l_{M_{c-2.2}}^*$) is obtained by matching the rest of the regularised fracture toughness $((1 - f_{\mathcal{G}_M})(\mathcal{G}_M / l_M^*))$ with the grey area in Fig. F.3b. This area corresponds to a sudden drop of the stress from $\sigma_{ij} = f_{\sigma_u} \sigma_u$ to $\sigma_{ij} = 0$ at the same strain level. Then, $l_{M_{c-2.2}}^*$ yields

$$l_{M_{c-2.2}}^* = \frac{2(1 - f_{\mathcal{G}_M} f_{\sigma_u} - f_{\mathcal{G}_M}) E_M \mathcal{G}_M}{\sigma_u^2 f_{\sigma_u}^2}. \quad (\text{F.4})$$

Finally, the critical characteristic length to prevent the snap-back effect in a bilinear softening law yields

$$l_{M_{c-2}}^* = \min(l_{M_{c-2.1}}^*, l_{M_{c-2.2}}^*). \quad (\text{F.5})$$

For example, the critical characteristic element in the longitudinal tensile direction reads

$$l_{M_{c-2}}^* = \min \left(\frac{2E_{11}f_{\mathcal{G}_{X_T}}\mathcal{G}_{X_T}}{X_T^2(1-f_{X_T})}, \frac{2(1-f_{\mathcal{G}_{X_T}}f_{X_T}-f_{\mathcal{G}_{X_T}})E_{11}\mathcal{G}_{X_T}}{X_T^2{f_{X_T}}^2} \right), \quad (\text{F.6})$$

where E_{11} is the longitudinal Young's modulus, X_T and \mathcal{G}_{X_T} are the longitudinal tensile strength and fracture toughness, respectively, and f_{X_T} and $f_{\mathcal{G}_{X_T}}$ are the portions of X_T and \mathcal{G}_{X_T} , respectively, see Fig. B.1.

F.3 Critical characteristic length IM7/8522 unidirectional prepreg system

This section explains the procedure to determine the critical length for a specific material system. The selected material system in this appendix is the IM7/8552 unidirectional prepreg system, which is used in the main chapters of this document. Firstly, Eq. (F.1) is employed to calculate the critical length of l_t^* (for the transverse direction) used in Eq. (B.31) and the one of $l_{s_\ell}^*$ (for the longitudinal shear direction) used in Eq. (B.41). Then, the critical characteristic length of l_ℓ^* for the longitudinal tensile and compressive damage variables in Eq. (B.24) and Eq. (B.22), respectively, is calculated using Eq. (F.6). Table F.1 summarises $l_{M_c}^*$ for each direction with the material properties listed in Table 2.3. Finally, the critical characteristic element length for the selected material is defined as the minimum value listed in Table F.1. For the IM7/8522 material system, the critical characteristic element length is determined as 0.99 mm from the transverse direction.

Table F.1: Critical characteristic element length to prevent the snap-back effect in each direction.

Description		Symbol	Value	Unit
Longitudinal tensile direction	First segment	l_ℓ^*	3.88	mm
	Second segment		62.11	mm
Longitudinal compressive direction	First segment	l_ℓ^*	11.00	mm
	Second segment		—	mm
Longitudinal shear direction		l_t^*	1.31	mm
Transverse direction		$l_{s_\ell}^*$	0.99	mm

Verification of the implementation of the constitutive model

The verification of the implementation of the constitutive model under quasi-static loading rates in a user material subroutine is presented in this appendix. The model is implemented in a VUMAT Fortran subroutine to be used in Abaqus/Explicit solver. The implementation is verified using loading conditions with known solutions following ASME [112]. The numerical results are obtained from a Finite Element (FE) model, which is defined with a Gauss-point loaded under the corresponding loading states depending of the virtual test. In some cases, the known data are the inputs of the constitutive model (e.g. the compressive tensile yield stress (Y_{CP}) vs. equivalent plastic strain ($\bar{\varepsilon}^p$) curve is the known data used to compare to the transverse compressive virtual test in the plasticity verification, see Fig. G.3).

The material properties used in this verification analysis are summarised in Table 2.3 and the curves of the transverse tensile and compressive yield stresses and the longitudinal shear yield stress are presented in Fig. 2.7. A 3D eight-node C3D8R solid element with reduced integration and a size of $0.1 \text{ mm} \times 0.1 \text{ mm} \times 0.1 \text{ mm}$ is employed. The virtual tests are carried out with non-geometric linearities disabled. The verification of the plasticity modelling is presented in the first section of this appendix, see Appendix G.1. The verification of the damage modelling using the original constitutive model presented in Chapter 2 is then reported in Appendix G.2. Finally, the results of the verification analysis using the enhanced constitutive model presented in Chapter 3 are presented in Appendix G.3.

G.1 Plasticity modelling

The virtual tests performed to verify the implementation of the plasticity model are listed in Table G.1. In this case, the damage variables are set equal to 0 ($d_M = 0$) to avoid the degradation of the elastic material properties. Therefore, elastic behaviour is obtained for the longitudinal virtual test, see Figs. G.1 and G.2. However, the loading states governed by the matrix show a non-linear response due to the plasticity, see Figs. G.1–G.8. After conducting the virtual tests, it can be concluded that the plasticity model is properly implemented since the numerical results match the known data in all the analysed cases.

Table G.1.: Virtual tests performed to verify the implementation of the plasticity model in a user material subroutine.

Loading state	Figure
Longitudinal compression	Fig. G.1
Longitudinal tension	Fig. G.2
Transverse compression	Fig. G.3
Transverse tension	Fig. G.4
Biaxial transverse compression	Fig. G.5
Biaxial transverse tension	Fig. G.6
Longitudinal shear	Fig. G.7
Transverse shear	Fig. G.8

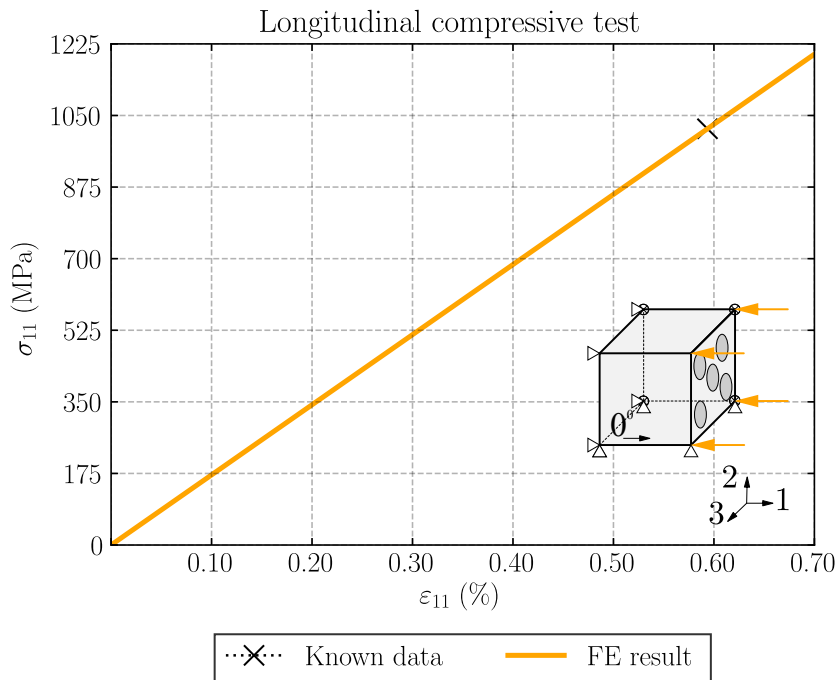


Figure G.1.: The stress vs. strain curve obtained from a longitudinal compressive virtual test. The cross indicates the longitudinal compressive strength X_C .

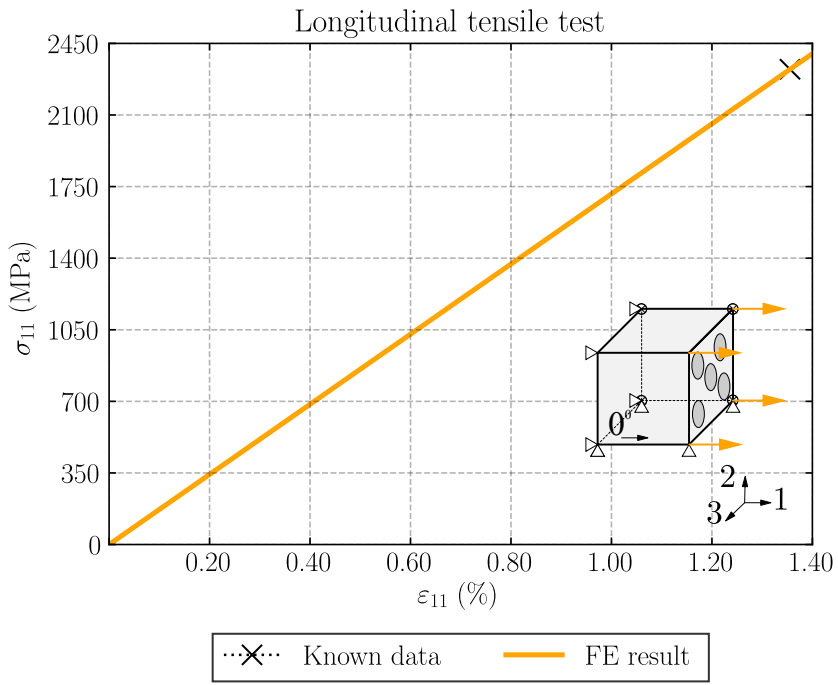


Figure G.2.: The stress vs. strain curve obtained from a longitudinal tensile virtual test. The cross indicates the longitudinal tensile strength X_T .

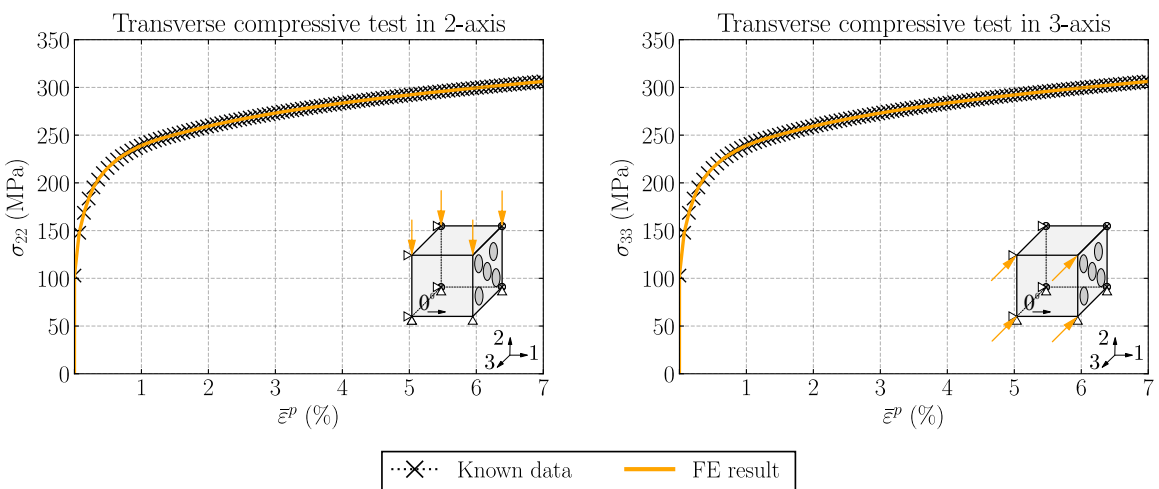


Figure G.3.: The stress vs. equivalent strain curve ($\bar{\varepsilon}^p$) obtained from transverse compressive virtual tests.

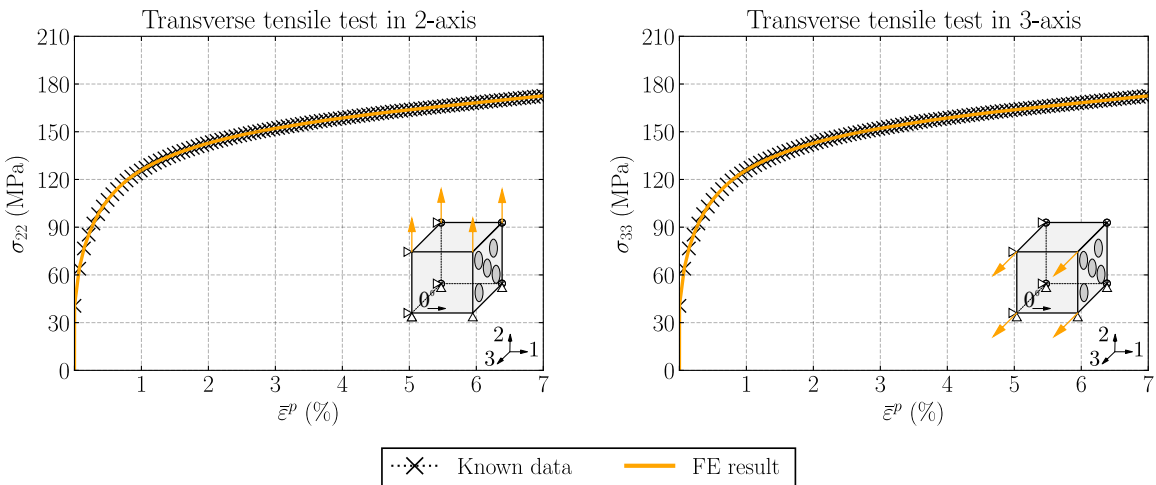


Figure G.4.: The stress vs. equivalent strain curve ($\bar{\varepsilon}^p$) obtained from transverse tensile virtual tests.

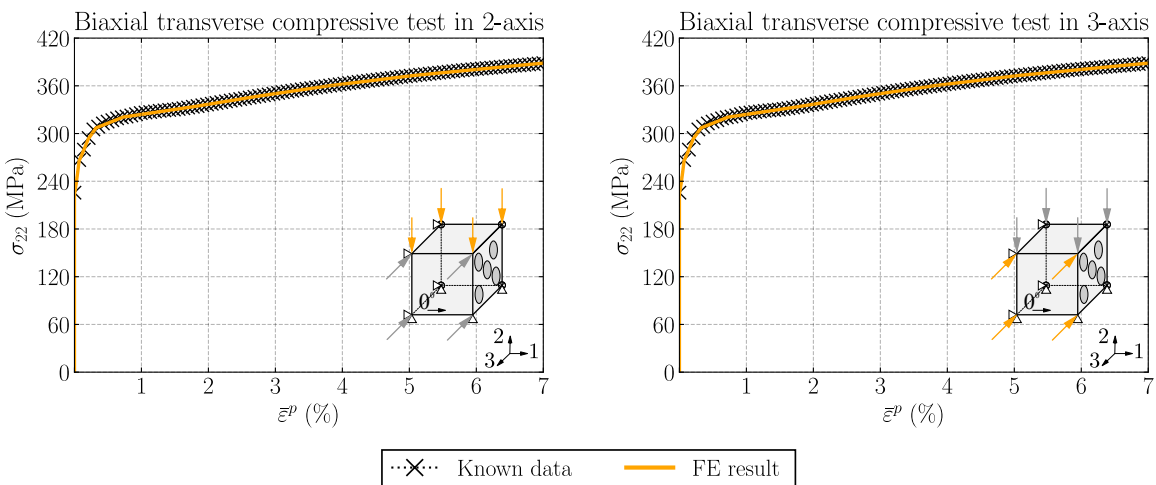


Figure G.5.: The stress vs. equivalent strain curve ($\bar{\varepsilon}^p$) obtained from biaxial transverse compressive virtual tests.

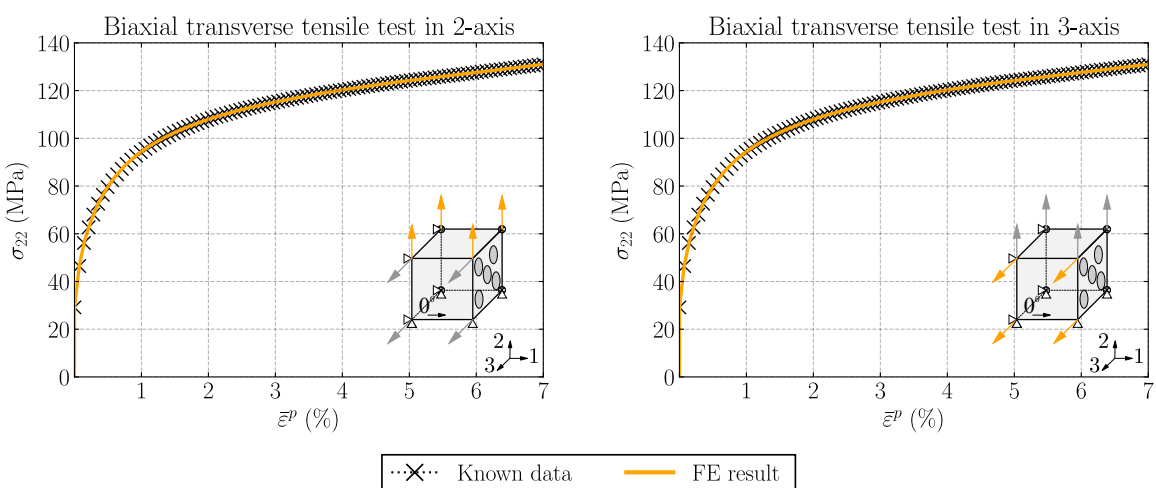


Figure G.6.: The stress vs. equivalent strain curve ($\bar{\varepsilon}^p$) obtained from biaxial transverse tensile virtual tests.

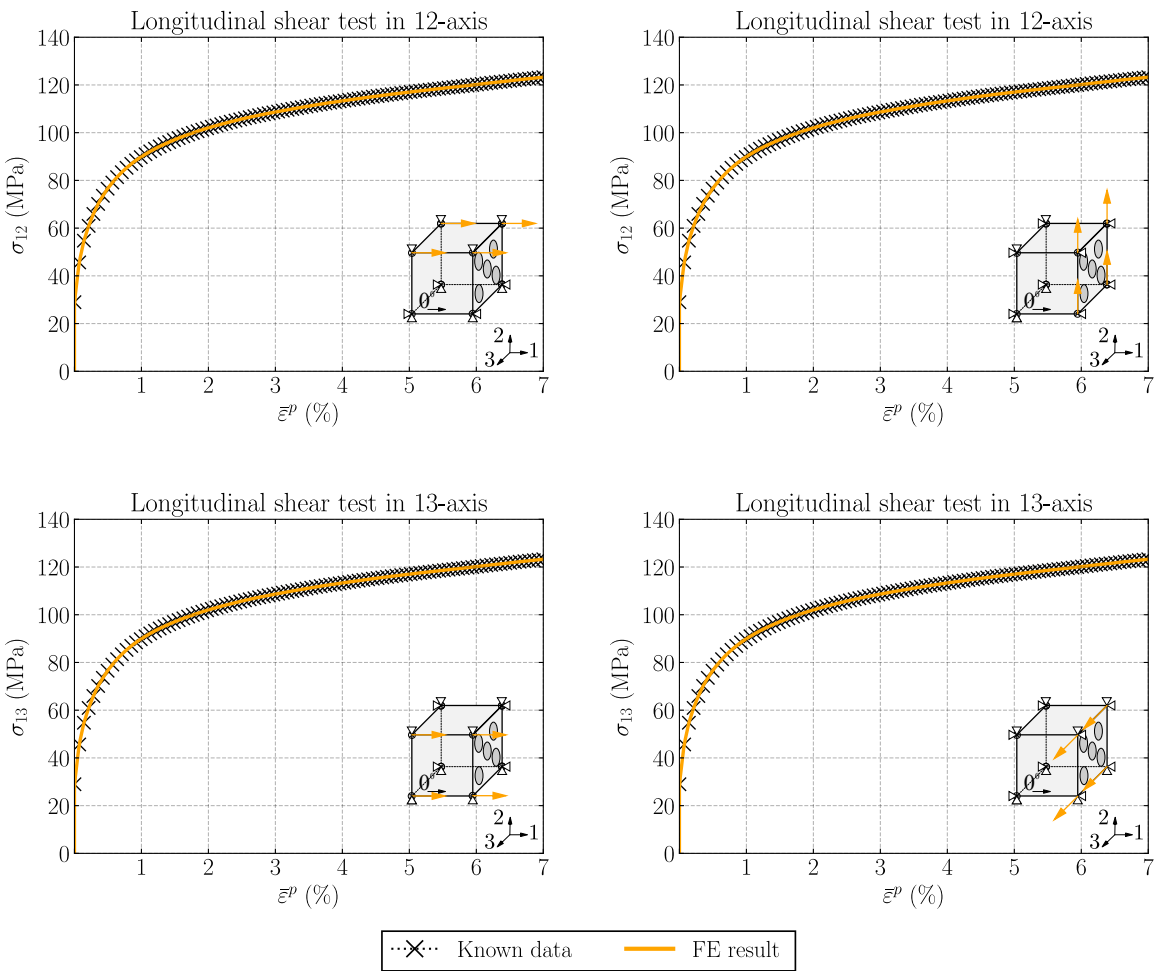


Figure G.7.: The stress vs. equivalent strain curve ($\bar{\varepsilon}^p$) obtained from longitudinal shear virtual tests.

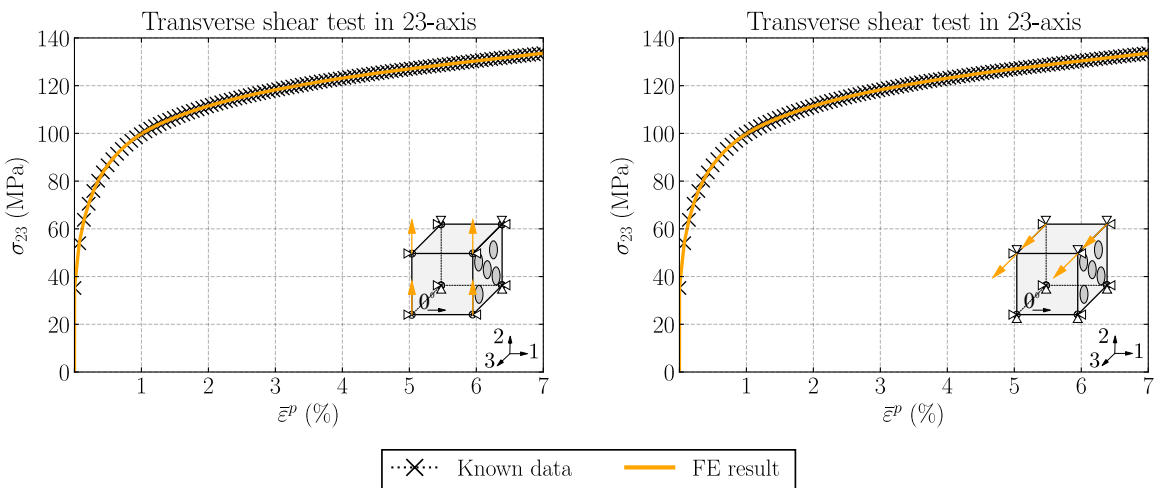


Figure G.8.: The stress vs. equivalent strain curve ($\bar{\varepsilon}^p$) obtained from transverse shear virtual tests.

G.2 Damage modelling using the original model

The verification analysis of the damage model is carried out by disabling the plasticity model, in this case the yield function is set equal to -1 ($\phi^p = -1$). [Table G.2](#) summarises the virtual tests carried out to verify the implementation of the damage model presented in [Chapter 2](#). The first cross marker of the known data of the analysed virtual tests is defined at $(0, 0)$. Then, the second cross marker is obtained at $(\sigma_u/E_{ij}, \sigma_u)$, where σ_u and E_{ij} are the corresponding strength and Young's modulus, respectively. Finally, the rest of the cross markers are defined using the corresponding softening law and fracture toughness.

Table G.2.: Virtual tests performed to verify the implementation of the damage model in a user material subroutine using the original constitutive model proposed in [Chapter 2](#).

Loading state	Figure
Longitudinal compression	Fig. G.9
Longitudinal tension	Fig. G.10
Transverse compression	Fig. G.11
Transverse tension	Fig. G.12
Biaxial transverse compression	Fig. G.13
Biaxial transverse tension	Fig. G.14
Longitudinal shear	Fig. G.15
Transverse shear	Fig. G.16

The softening law for the transverse shear and biaxial tests are not explicitly defined, hence no known data are presented in this region for these tests. The transverse shear strength is obtained from [Eq. \(5.1\)](#) for a given failure envelope shape coefficient μ_t as

$$S_T = \frac{Y_C Y_T}{Y_C + Y_T} \sqrt{1 + \mu_t}, \quad (\text{G.1})$$

where Y_T and Y_C are the transverse tensile and compressive strengths, respectively. The biaxial transverse tensile strength is calculated from [Eq. \(5.2\)](#) for a given μ_t as

$$Y_{TB} = \frac{Y_C Y_T}{(Y_C + Y_T) \sqrt{\frac{\mu_t}{1 + \mu_t}} + Y_C - Y_T}, \quad (\text{G.2})$$

and the biaxial transverse compressive strength is calculated from [Eq. \(5.3\)](#) for a given μ_t as

$$Y_{CB} = \frac{Y_C Y_T}{(Y_C + Y_T) \sqrt{\frac{\mu_t}{1 + \mu_t}} - Y_C + Y_T}. \quad (\text{G.3})$$

The numerical results obtained from loading cases analysed are in agreement with the corresponding known data, see Figs. G.12 and G.14–G.16.

The longitudinal damage variable (d_ℓ) is activated in the longitudinal compressive test (see Fig. G.9), but also the transverse damage variables (d_t , $d_{s\ell}$ and d_{st}) since large values of the transverse principal components of the effective stress tensor ($\tilde{\sigma}_{22}$ and $\tilde{\sigma}_{33}$) are obtained. Under longitudinal compressive loading conditions, only d_ℓ should be non-null at the Gauss-point level. This limitation is present in constitutive models that use the effective stress tensor, and is solved in Chapter 3. In the longitudinal tensile test, the longitudinal tensile damage variable is activated as well as the longitudinal shear damage variable ($d_{s\ell}$) due to the definition of $d_{s\ell}$ in Eq. (2.33), see Fig. G.10. Additionally, the remaining damage variables are also non-null due to the limitation explained previously, as in the longitudinal compressive test. This issue is also solved with the constitutive model proposed in Chapter 3.

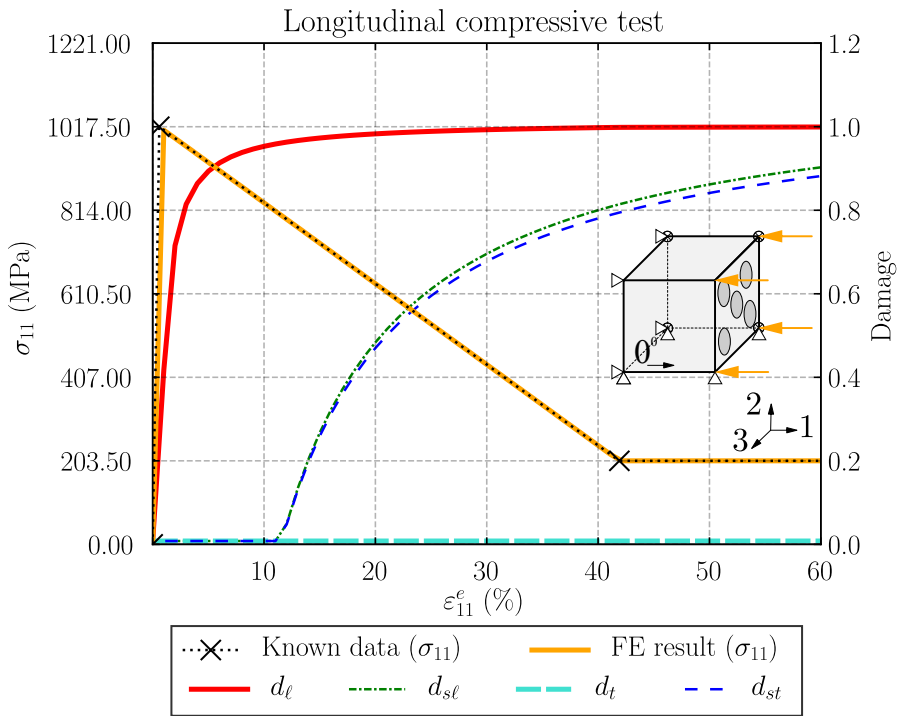


Figure G.9: The stress vs. strain curve obtained from a longitudinal compressive virtual test using the original constitutive model proposed in Chapter 2. The damage variables curves are obtained from the finite element (FE) model.

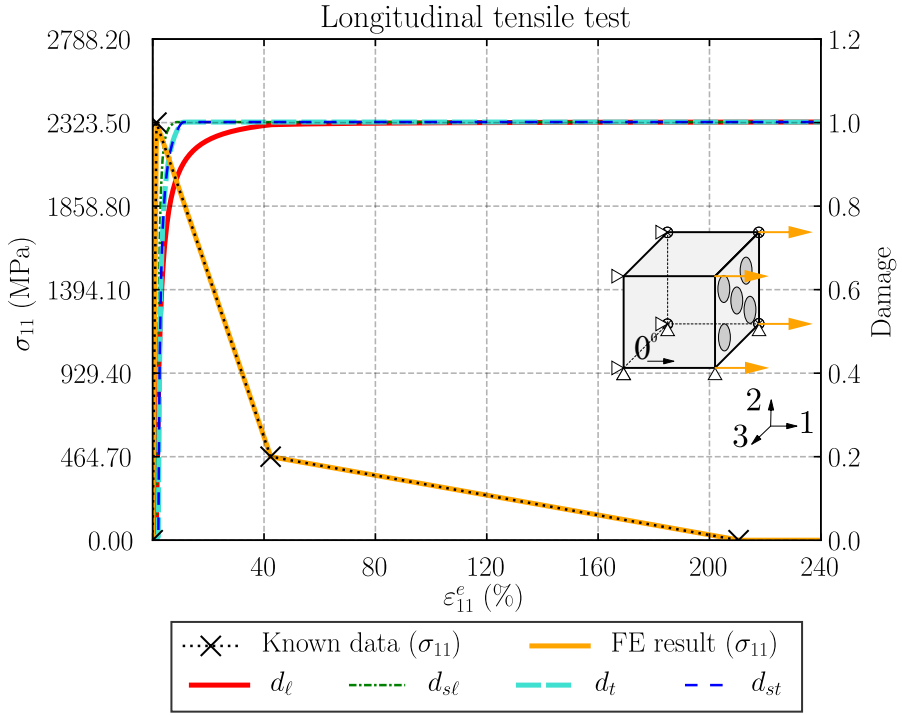


Figure G.10.: The stress vs. strain curve obtained from a longitudinal tensile virtual test using the original constitutive model proposed in [Chapter 2](#). The damage variables curves are obtained from the finite element (FE) model.

The original constitutive model does not explicitly impose the transverse compressive softening law as no damage variable is calibrated with this test, see [Chapter 2](#). Therefore, the softening shape is instead determined by the definition of $d_{s\ell^*}$ from a longitudinal shear tensile test and d_t from a transverse tensile test, see [Fig. G.11](#). In addition, the transverse damage variable (d_t) is not activated in the transverse compressive test since the transverse hydrostatic (p_t) is less than zero, therefore $d_t = 0$, see [Eq. \(2.32\)](#). However, all transverse damage variables (d_t, d_{st} and $d_{s\ell}$) are activated in the transverse tensile tests since they are defined as a function of the transverse threshold elastic domain (r_t) and $p_t > 0$, see [Fig. G.12](#).

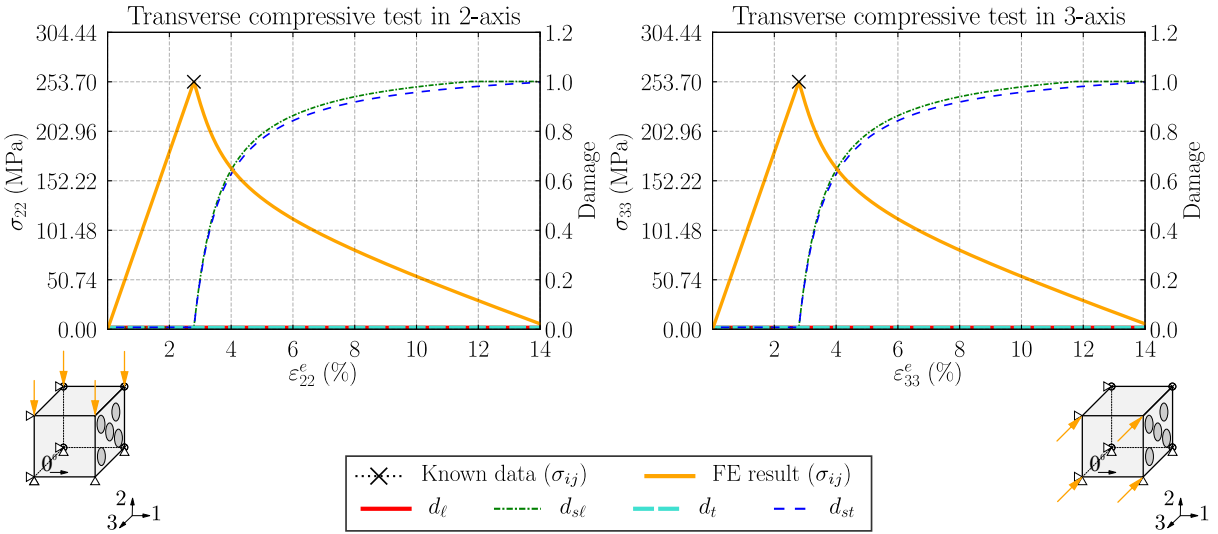


Figure G.11.: The stress vs. strain curve obtained from transverse compressive virtual tests using the original constitutive model proposed in Chapter 2. The damage variables curves are obtained from the finite element (FE) model.

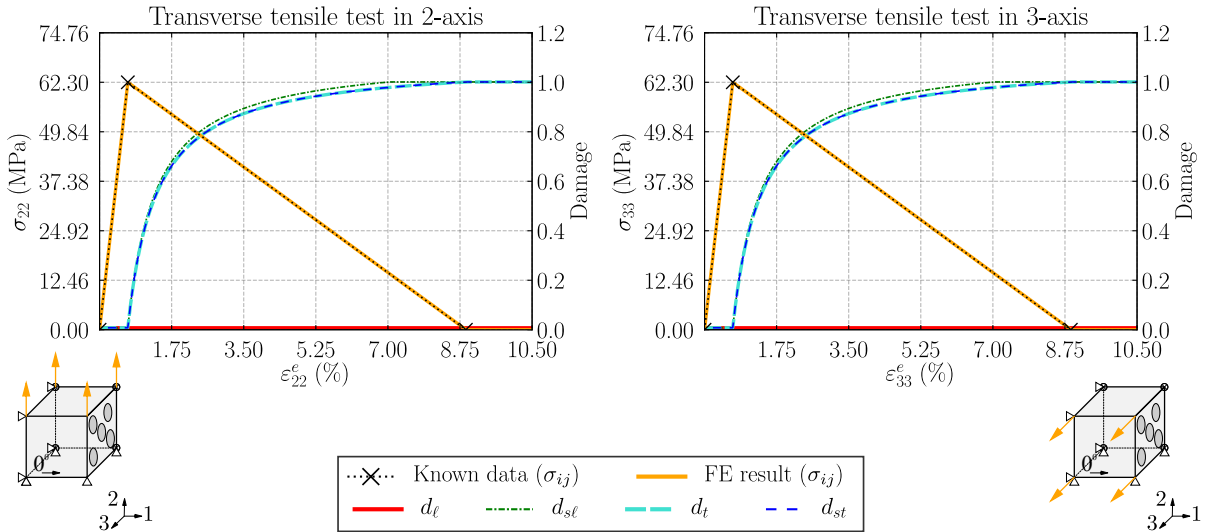


Figure G.12.: The stress vs. strain curve obtained from transverse tensile virtual tests using the original constitutive model proposed in Chapter 2. The damage variables curves are obtained from the finite element (FE) model.

Under biaxial transverse compressive loading conditions, $p_t < 0$ and, thus, $d_t = 0$. At certain strain of the biaxial compressive test, $d_{st} = 1$ resulting in the components of the elasticity tensor being $\mathbb{C}_{e_{23}} = \mathbb{C}_{e_{22}} \neq 0$, see Fig. G.13. Consequently, the load-carrying capacity at the Gauss-point level under biaxial transverse compressive conditions is always non-zero. However, in the biaxial transverse tensile, $\mathbb{C}_{e_{23}}$ and $\mathbb{C}_{e_{22}}$ tend to zero since $p_t > 0$ and, hence, $d_t > 0$, see Fig. G.14.

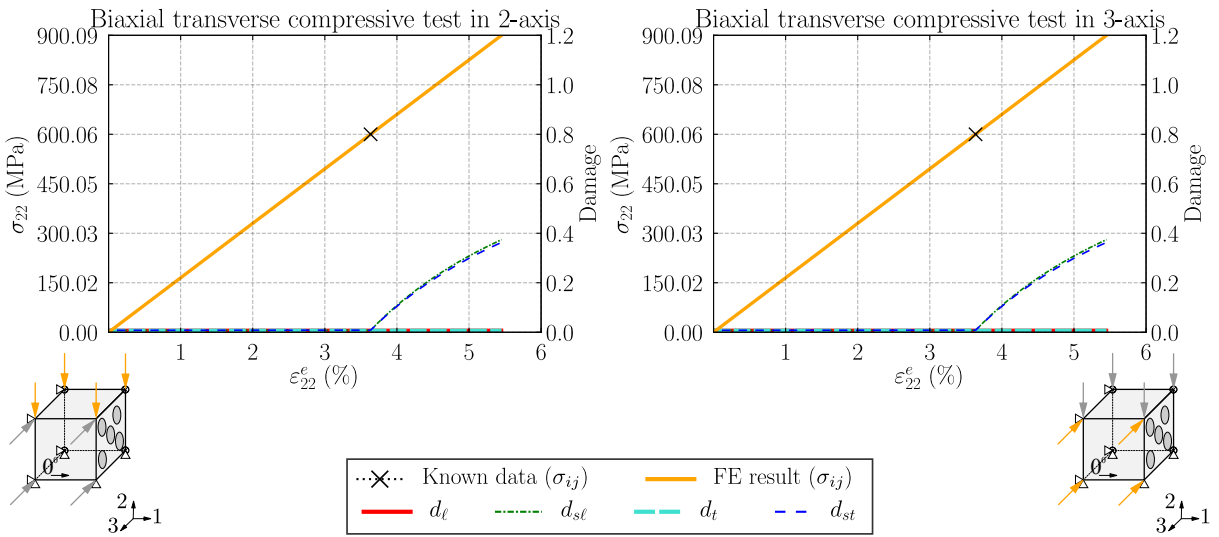


Figure G.13.: The stress vs. strain curve obtained from biaxial transverse compressive virtual tests using the original constitutive model proposed in Chapter 2. The damage variables curves are obtained from the finite element (FE) model.

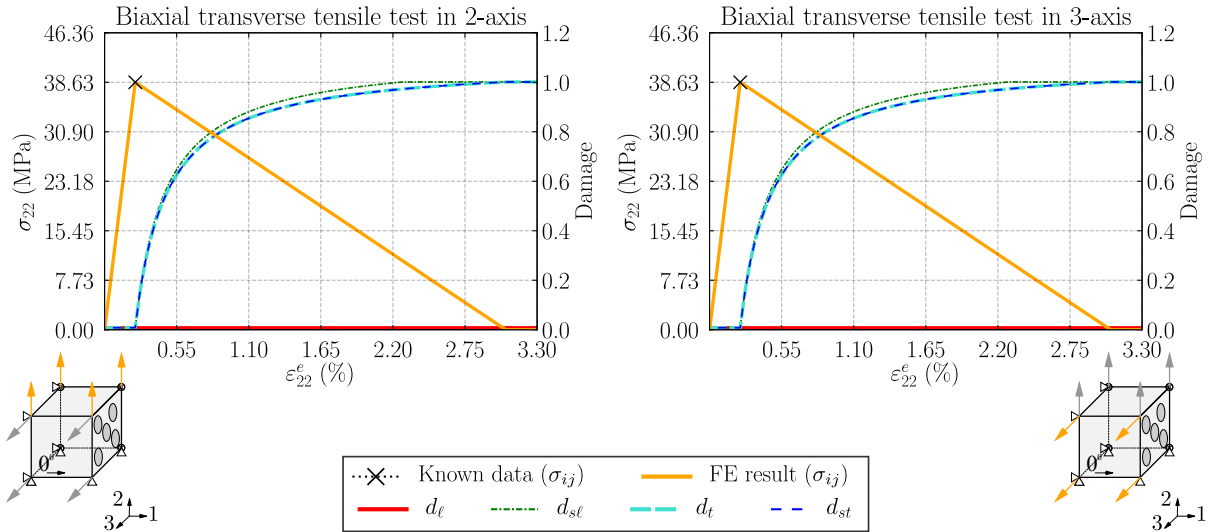


Figure G.14.: The stress vs. strain curve obtained from biaxial transverse tensile virtual tests using the original constitutive model proposed in Chapter 2. The damage variables curves are obtained from the finite element (FE) model.

Linear softening response is observed in the longitudinal shear test and in the transverse shear test, see Figs. G.15 and G.16. In both tests, d_t is not activated since $p_t = 0$. After conducting the virtual tests, it can be concluded that the damage model using the original model is properly implemented since the numerical results also match the known data in all the analysed cases.

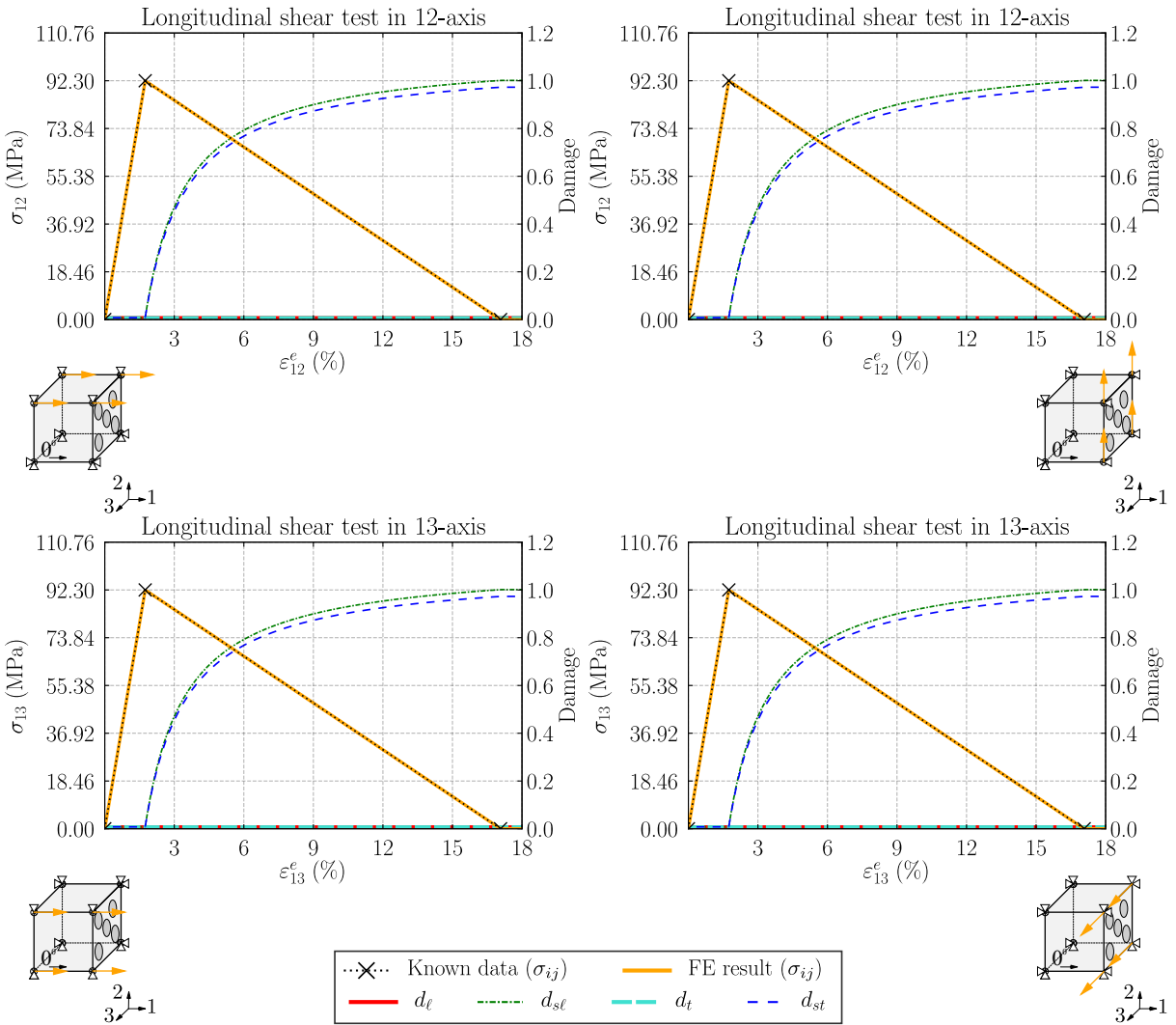


Figure G.15.: The stress vs. strain curve obtained from longitudinal shear virtual tests using the original constitutive model proposed in Chapter 2. The damage variables curves are obtained from the finite element (FE) model.

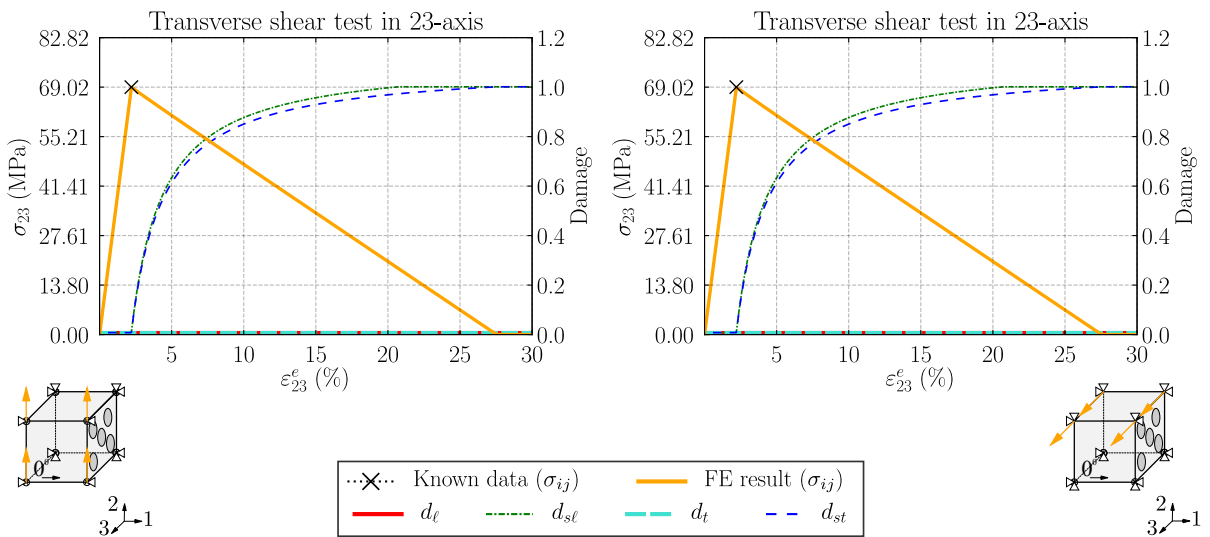


Figure G.16.: The stress vs. strain curve obtained from transverse shear virtual tests using the original constitutive model proposed in Chapter 2. The damage variables curves are obtained from the finite element (FE) model.

G.3 Damage modelling using the enhanced model

This section presents the verification analysis of the damage modelling from the enhanced constitutive model proposed in [Chapter 3](#). The main difference between the original and enhanced models is the evaluation of the transverse loading function with respect to the effective stress tensor or the nominal stress tensor, respectively. Therefore, the predicted mechanical response obtained from each constitutive model under certain loading conditions differs. This section analyses the cases with different behaviour as presented in [Appendix G.2](#). [Table G.3](#) summarises the virtual tests carried out.

Table G.3: Virtual tests performed to verify the implementation of the damage model in a user material subroutine using the enhanced constitutive model proposed in [Chapter 3](#).

Loading state	Figure
Longitudinal compression	Fig. G.17
Longitudinal tension	Fig. G.18
Transverse compression	Fig. G.19

In the longitudinal compressive test, the longitudinal damage variable (d_ℓ) is activated, see [Fig. G.17](#). Unlike the results in [Fig. G.9](#), the transverse damage variables (d_t , $d_{s\ell}$ and d_{st}) remain null under longitudinal compressive loading conditions. Similar to compression, d_ℓ is non-null in the longitudinal tensile test, and the rest of the damage variables are equal to zero except to $d_{s\ell}$ due to its definition in [Eq. \(2.33\)](#), see [Fig. G.18](#).

In the enhanced model, the softening response of the transverse compressive test (see [Fig. G.11](#)) is not purely linear as assumed in [Eq. \(3.4\)](#) since no damage variables are calibrated with this test, see [Fig. G.19](#). Therefore, this softening is not explicitly imposed. No significant discrepancies between the damage energy dissipated and the transverse compressive fracture toughness defined are found with this assumption. In this case, the relative error of the damage energy dissipated with respect to the fracture toughness defined is equal to 2.51%.

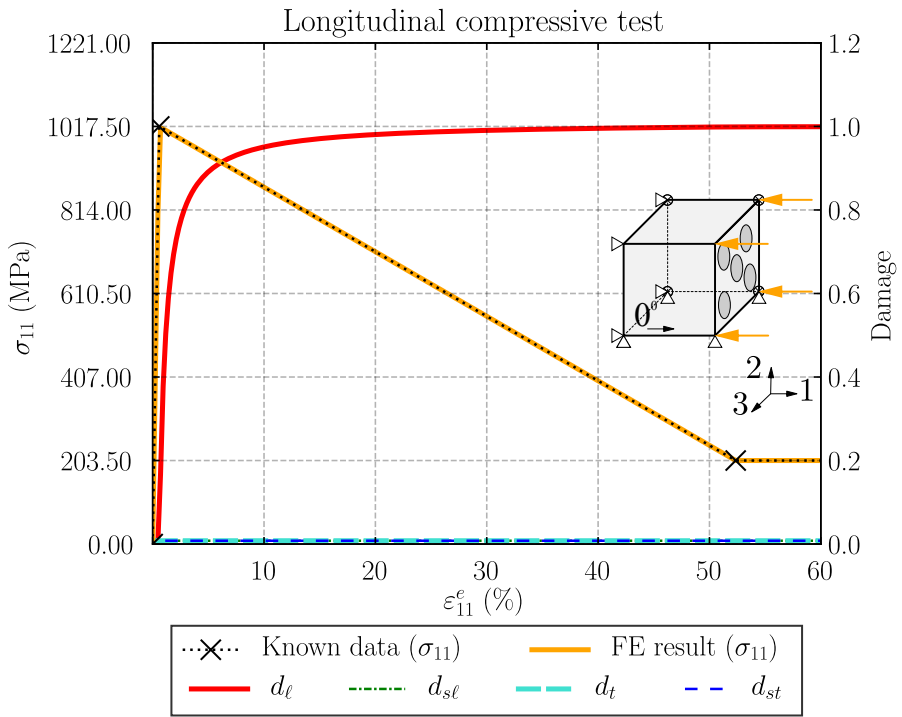


Figure G.17.: The stress vs. strain curve obtained from a longitudinal compressive virtual test using the enhanced constitutive model proposed in Chapter 3. The damage variables curves are obtained from the finite element (FE) model.

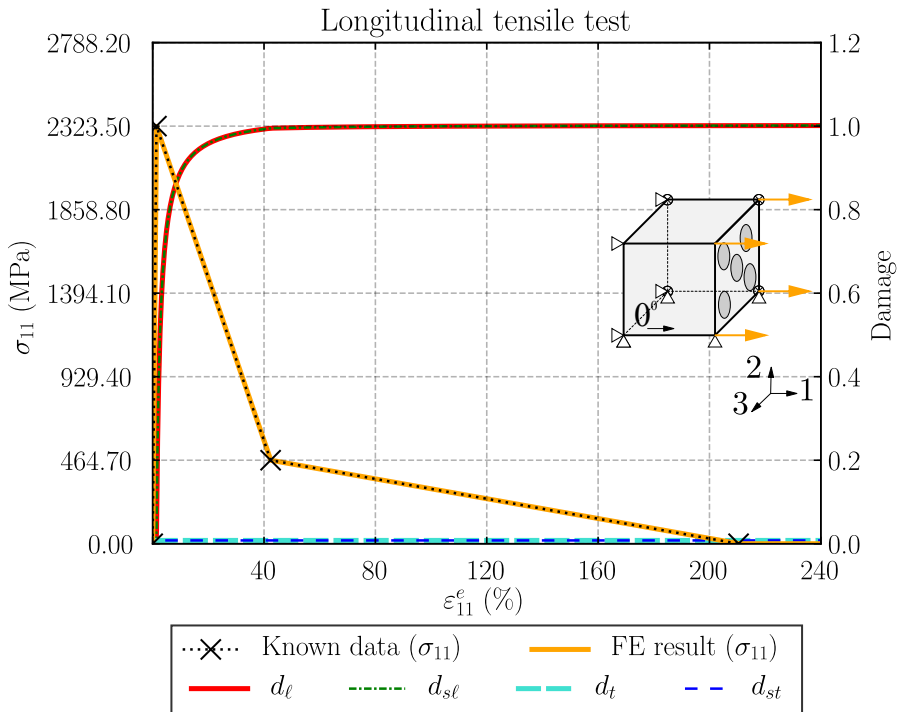


Figure G.18.: The stress vs. strain curve obtained from a longitudinal tensile virtual test using the enhanced constitutive model proposed in Chapter 3. The damage variables curves are obtained from the finite element (FE) model.

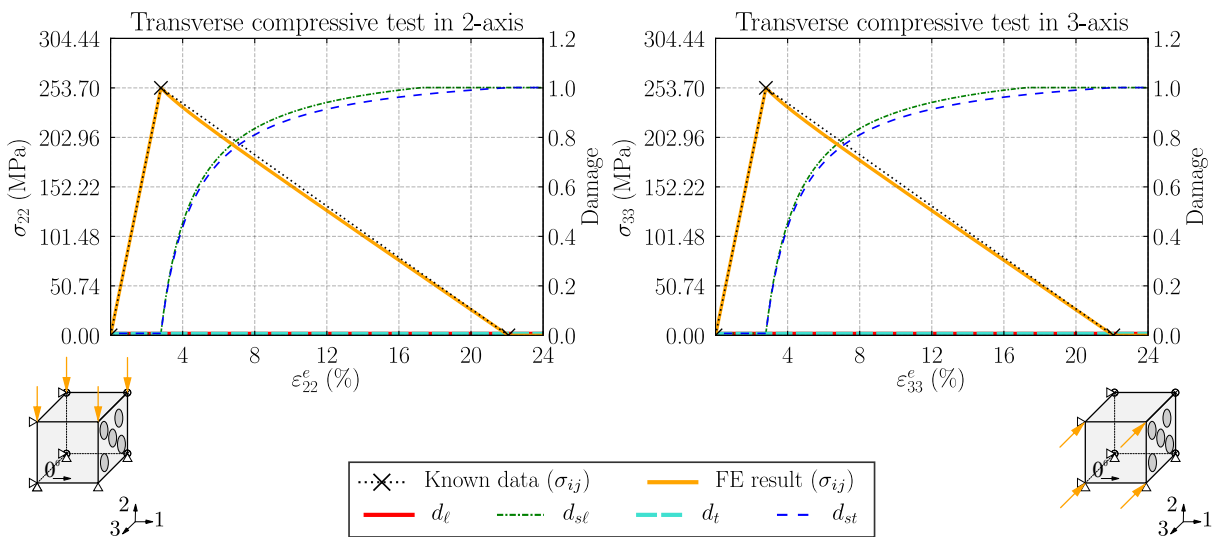


Figure G.19.: The stress vs. strain curve obtained from transverse compressive virtual tests using the enhanced constitutive model proposed in Chapter 3. The damage variables curves are obtained from the finite element (FE) model.

Positive semi-definite matrix

A positive semi-definite or non-negative definite matrix is a real symmetric matrix whose all eigenvalues are equal to or greater than zero. The properties of this type of matrices are [274]:

- i) All eigenvalues are equal to or greater than zero.
- ii) For all non-null vectors $\vec{v} \in \mathbb{R}^n$, the following inequality is meet:

$$\vec{v}^T \mathbf{A} \vec{v} \geq 0, \quad (\text{H.1})$$

where \mathbf{A} is a positive semi-definite matrix.

- iii) The sum of positive semi-definite matrices is a positive semi-definite matrix.
- iv) If \mathbf{A} and \mathbf{B} are positive semi-definitive matrices and

$$\mathbf{A}\mathbf{B} = (\mathbf{A}\mathbf{B})^T, \quad (\text{H.2})$$

then,

$$\mathbf{A}\mathbf{B} \geq 0. \quad (\text{H.3})$$

- v) If a positive semi-definite matrix is invertible, its inverse is also positive semi-definite matrix.

Strain-crack opening displacement relationship

The relationship between the crack opening displacement (ω) and strain in a continuum damage model is presented in this appendix. The Crack Band model [89] is based on the growth of a localisation band or crack within each mesh finite element. This method allows a cohesive zone model to be solved without introducing an interface element; when the stress reaches the strength, the elastic properties of the material are degraded. The total displacement of a mesh finite element without plasticity is

$$u := \omega + u^e, \quad (\text{I.1})$$

where ω is the crack opening displacement and u^e is the elastic displacement, see Fig. I.1. Therefore, the total strain due to damage can be calculated by dividing Eq. (I.1) by the characteristic element length (l^*)

$$\varepsilon := \frac{\omega}{l^*} + \varepsilon^e, \quad (\text{I.2})$$

where ε^e is the elastic strain which can be calculated from the Hooke's law as

$$\varepsilon^e = \frac{\sigma}{E}, \quad (\text{I.3})$$

where σ is the stress component and E is the Young's modulus. In addition, the stress can be written from the continuum damage model as

$$\sigma = (1 - d_M)E\varepsilon, \quad (\text{I.4})$$

where d_M is the damage variable to degrade the elastic material properties. Therefore, the crack opening displacement can be written as a function of the strain by introducing Eq. (I.4) into Eq. (I.3) and, then, combining it with Eq. (I.5),

$$\omega = d_M l^* \varepsilon. \quad (\text{I.5})$$

Note that, ε in Eq. (I.5) is the strain including elastic and cracking strains. In the rest of document, this ε matches elastic strain (ε^e), since ε^e contains both the elastic and cracking strain (in the rest of the document $\varepsilon = \varepsilon^e$).

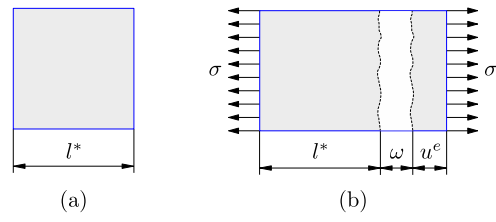


Figure I.1.: Schematic representation of a crack band in a continuum damage model: a) undamaged and unloaded mesh finite element, and b) damaged and loaded mesh finite element.

Bibliography

- [1] M. A. Karataş and H. Gökkaya. “A review on machinability of carbon fiber reinforced polymer (CFRP) and glass fiber reinforced polymer (GFRP) composite materials”. In: *Defence Technology* 14 (4 Aug. 2018), pp. 318–326. ISSN: 22149147. DOI: [10.1016/j.dt.2018.02.001](https://doi.org/10.1016/j.dt.2018.02.001).
- [2] C.- W. State. *Composite materials handbook. Volume 3. Polymer matrix composites. Materials usage, design, and analysis.* Vol. 3. 2012. ISBN: 978-0-7680-7813-8.
- [3] A. Öchsner, M. S. Go, and A. C. Karaoglanli. “Carbon fiber reinforced polymer (CFRP) composite materials, their characteristic properties, industrial application areas and their machinability”. In: ed. by A. Ochsner and H. Altenbach. Springer International Publishing, 2020, pp. 235–253. ISBN: 978-3-030-39062-4. DOI: [10.1007/978-3-030-39062-4_20](https://doi.org/10.1007/978-3-030-39062-4_20). URL: https://doi.org/10.1007/978-3-030-39062-4_20.
- [4] B. K. Cheung and J. P. Carey. “Macromechanics of composite materials”. In: Elsevier Inc., 2017, pp. 307–319. ISBN: 9780081003770. DOI: [10.1016/B978-0-08-100369-5.00008-8](https://doi.org/10.1016/B978-0-08-100369-5.00008-8).
- [5] A. C. Orifici, I. Herszberg, and R. S. Thomson. “Review of methodologies for composite material modelling incorporating failure”. In: *Composite Structures* 86 (1-3 Nov. 2008), pp. 194–210. ISSN: 02638223. DOI: [10.1016/j.compstruct.2008.03.007](https://doi.org/10.1016/j.compstruct.2008.03.007).
- [6] C. R. Schultheisz and A. M. Waas. “Compressive failure of composites, Part I: Testing and micromechanical theories”. In: *Progress in Aerospace Sciences* 32 (1996), pp. 1–42. ISSN: 0376-0421. DOI: [https://doi.org/10.1016/0376-0421\(94\)00002-3](https://doi.org/10.1016/0376-0421(94)00002-3).
- [7] N. A. Fleck and D. Liu. “Microbuckle initiation from a patch of large amplitude fibre waviness in a composite under compression and bending”. In: *European Journal of Mechanics - A/Solids* 20 (1 2001), pp. 23–37. ISSN: 0997-7538. DOI: [10.1016/S0997-7538\(00\)01124-4](https://doi.org/10.1016/S0997-7538(00)01124-4).
- [8] H. Koerber, J. Xavier, and P. P. Camanho. “High strain rate characterisation of unidirectional carbon-epoxy IM7-8552 in transverse compression and in-plane shear using digital image correlation”. In: *Mechanics of Materials* 42 (11 Nov. 2010), pp. 1004–1019. ISSN: 01676636. DOI: [10.1016/j.mechmat.2010.09.003](https://doi.org/10.1016/j.mechmat.2010.09.003).

- [9] H. Koerber, P. Kuhn, M. Ploeckl, F. Otero, P. W. Gerbaud, R. Rolfes, and P. P. Camanho. “Experimental characterization and constitutive modeling of the non-linear stress–strain behavior of unidirectional carbon–epoxy under high strain rate loading”. In: *Advanced Modeling and Simulation in Engineering Sciences* 5 (1 Dec. 2018). ISSN: 22137467. DOI: [10.1186/s40323-018-0111-x](https://doi.org/10.1186/s40323-018-0111-x).
- [10] Y. Chen, Y. Zhao, S. Ai, C. He, Y. Tao, Y. Yang, and D. Fang. “A constitutive model for elastoplastic-damage coupling effect of unidirectional fiber-reinforced polymer matrix composites”. In: *Composites Part A: Applied Science and Manufacturing* 130 (Mar. 2020). ISSN: 1359835X. DOI: [10.1016/j.compositesa.2019.105736](https://doi.org/10.1016/j.compositesa.2019.105736).
- [11] E. S. Shin and K. D. Pae. “Effects of hydrostatic pressure on in-plane shear properties of graphite/epoxy composites”. In: *Journal of Composite Materials* 26 (1992), pp. 828–868. DOI: [10.1177/002199839202600604](https://doi.org/10.1177/002199839202600604).
- [12] J Lankford. “The compressive failure of polymeric composites under hydrostatic confinement”. In: *Composites Part A: Applied Science and Manufacturing* 28 (1997), pp. 409–418. ISSN: 1359-835X. DOI: [https://doi.org/10.1016/S1359-835X\(96\)00140-6](https://doi.org/10.1016/S1359-835X(96)00140-6).
- [13] M. H. Hamidon, M. T. Sultan, A. H. Ariffin, and A. U. Shah. “Effects of fibre treatment on mechanical properties of kenaf fibre reinforced composites: A review”. In: *Journal of Materials Research and Technology* 8 (3 May 2019), pp. 3327–3337. ISSN: 22387854. DOI: [10.1016/j.jmrt.2019.04.012](https://doi.org/10.1016/j.jmrt.2019.04.012).
- [14] K. Friedrich and A. A. Almajid. “Manufacturing aspects of advanced polymer composites for automotive applications”. In: *Applied Composite Materials* 20 (2 Apr. 2013), pp. 107–128. ISSN: 0929189X. DOI: [10.1007/s10443-012-9258-7](https://doi.org/10.1007/s10443-012-9258-7).
- [15] D. H. Kim, D. H. Choi, and H. S. Kim. “Design optimization of a carbon fiber reinforced composite automotive lower arm”. In: *Composites Part B: Engineering* 58 (2014), pp. 400–407. ISSN: 13598368. DOI: [10.1016/j.compositesb.2013.10.067](https://doi.org/10.1016/j.compositesb.2013.10.067).
- [16] D. H. Kim, H. G. Kim, and H. S. Kim. “Design optimization and manufacture of hybrid glass/carbon fiber reinforced composite bumper beam for automobile vehicle”. In: *Composite Structures* 131 (Nov. 2015), pp. 742–752. ISSN: 02638223. DOI: [10.1016/j.compstruct.2015.06.028](https://doi.org/10.1016/j.compstruct.2015.06.028).
- [17] C. Fragassa, A. Pavlovic, and G. Minak. “On the structural behaviour of a CFRP safety cage in a solar powered electric vehicle”. In: *Composite Structures* 252 (Nov. 2020). ISSN: 02638223. DOI: [10.1016/j.compstruct.2020.112698](https://doi.org/10.1016/j.compstruct.2020.112698).

- [18] E. Amasawa, M. Hasegawa, N. Yokokawa, H. Sugiyama, and M. Hirao. “Environmental performance of an electric vehicle composed of 47% polymers and polymer composites”. In: *Sustainable Materials and Technologies* 25 (Sept. 2020). ISSN: 22149937. DOI: [10.1016/j.susmat.2020.e00189](https://doi.org/10.1016/j.susmat.2020.e00189).
- [19] N. Fantuzzi, M. Bacciochi, D. Benedetti, and J. Agnelli. “The use of sustainable composites for the manufacturing of electric cars”. In: *Composites Part C: Open Access* 4 (Mar. 2021). ISSN: 26666820. DOI: [10.1016/j.jcomc.2020.100096](https://doi.org/10.1016/j.jcomc.2020.100096).
- [20] A. K. Mohanty, S. Vivekanandhan, N. Tripathi, P. Roy, M. R. Snowdon, L. T. Drzal, and M. Misra. “Sustainable composites for lightweight and flame retardant parts for electric vehicles to boost climate benefits: A perspective”. In: *Composites Part C: Open Access* 12 (Oct. 2023). ISSN: 26666820. DOI: [10.1016/j.jcomc.2023.100380](https://doi.org/10.1016/j.jcomc.2023.100380).
- [21] E. U. A. S. A. (EASA). *Easy access rules for Acceptable Means of Compliance (AMC) for airworthiness of products, parts and appliances*. 2021. URL: <http://eur-lex.europa.eu/>,
- [22] “Chapter 8 - Building Block Approach (BBA)”. In: ed. by B. Backman. Elsevier, 2005, pp. 99–110. ISBN: 978-0-08-044545-8. DOI: [10.1016/B978-008044545-8/50008-5](https://doi.org/10.1016/B978-008044545-8/50008-5).
- [23] S. D. Müzel, E. P. Bonhin, N. M. Guimarães, and E. S. Guidi. “Application of the finite element method in the analysis of composite materials: A review”. In: *Polymers* 12 (4 Apr. 2020). ISSN: 20734360. DOI: [10.3390/POLYM12040818](https://doi.org/10.3390/POLYM12040818).
- [24] S. Boria, J. Obradovic, and G. Belingardi. “Experimental and numerical investigations of the impact behaviour of composite frontal crash structures”. In: *Composites Part B: Engineering* 79 (Sept. 2015), pp. 20–27. ISSN: 13598368. DOI: [10.1016/j.compositesb.2015.04.016](https://doi.org/10.1016/j.compositesb.2015.04.016).
- [25] J. Obradovic, S. Boria, and G. Belingardi. “Lightweight design and crash analysis of composite frontal impact energy absorbing structures”. In: *Composite Structures* 94 (2 Jan. 2012), pp. 423–430. ISSN: 02638223. DOI: [10.1016/j.compstruct.2011.08.005](https://doi.org/10.1016/j.compstruct.2011.08.005).
- [26] J. M. Guerrero, A. Sasikumar, J. Llobet, and J. Costa. “Testing and simulation of a composite-aluminium wingbox subcomponent subjected to thermal loading”. In: *Composite Structures* 296 (Sept. 2022). ISSN: 02638223. DOI: [10.1016/j.compstruct.2022.115887](https://doi.org/10.1016/j.compstruct.2022.115887).
- [27] J. Llorca, C. Gonzalez, J. M. Molina-Aldareguia, and C. S. Lopes. “Multiscale Modeling of Composites: Toward Virtual Testing ... and Beyond”. In: *The Journal of The Minerals, Metals & Materials Society* 65 (2013), pp. 215–225. DOI: [10.1007/s11837-012-0509-8](https://doi.org/10.1007/s11837-012-0509-8).

- [28] S. N. steffenniemann, dlrde B Kolesnikov boriskolesnikov, dlrde H Lohse-Busch heikelohse busch, dlrde C Hühne christiahuehne, O. M. Q. omquerin, leedsacuk V V Toropov vvtoropov, and leedsacuk D Liu. “The use of topology optimisation in the conceptual design of next generation lattice composite aircraft fuselage structures”. In: *The Aeronautical Journal* 117 (2013), pp. 1197–1154. DOI: [10.1017/S0001924000008745](https://doi.org/10.1017/S0001924000008745).
- [29] W. Vankan, R Maas, and S Grihon. “Efficient optimisation of large aircraft fuselage structures”. In: *The Aeronautical Journal* 118 (2014), pp. 31–52. DOI: [10.1017/S0001924000008915](https://doi.org/10.1017/S0001924000008915).
- [30] D. Liu, H. Lohse-Busch, V. Toropov, C. Hühne, and U. Armani. “Detailed design of a lattice composite fuselage structure by a mixed optimization method”. In: *Engineering Optimization* 48 (10 Oct. 2016), pp. 1707–1720. ISSN: 10290273. DOI: [10.1080/0305215X.2015.1125262](https://doi.org/10.1080/0305215X.2015.1125262).
- [31] S. A. Ardila-Parra, C. M. Pappalardo, O. A. G. Estrada, and D. Guida. “Finite element based redesign and optimization of aircraft structural components using composite materials”. In: *International Journal of Applied Mathematics* 50 (4 2020). URL: <https://hal.science/hal-03020637>.
- [32] F. Savine, F. X. Irisarri, C. Julien, A. Vincenti, and Y. Guerin. “A component-based method for the optimization of stiffener layout on large cylindrical rib-stiffened shell structures”. In: *Structural and Multidisciplinary Optimization* 64 (4 Oct. 2021), pp. 1843–1861. ISSN: 16151488. DOI: [10.1007/s00158-021-02945-9](https://doi.org/10.1007/s00158-021-02945-9).
- [33] A. R. Melro, P. P. Camanho, F. M. A. Pires, and S. T. Pinho. “Micromechanical analysis of polymer composites reinforced by unidirectional fibres: Part I - Constitutive modelling”. In: *International Journal of Solids and Structures* 50 (11-12 June 2013), pp. 1897–1905. ISSN: 00207683. DOI: [10.1016/j.ijsolstr.2013.02.009](https://doi.org/10.1016/j.ijsolstr.2013.02.009).
- [34] A. R. Melro, P. P. Camanho, and S. T. Pinho. “Generation of random distribution of fibres in long-fibre reinforced composites”. In: *Composites Science and Technology* 68 (9 July 2008), pp. 2092–2102. ISSN: 02663538. DOI: [10.1016/j.compscitech.2008.03.013](https://doi.org/10.1016/j.compscitech.2008.03.013).
- [35] A. R. Melro, P. P. Camanho, F. M. A. Pires, and S. T. Pinho. “Micromechanical analysis of polymer composites reinforced by unidirectional fibres: Part II - Micromechanical analyses”. In: *International Journal of Solids and Structures* 50 (11-12 June 2013), pp. 1906–1915. ISSN: 00207683. DOI: [10.1016/j.ijsolstr.2013.02.007](https://doi.org/10.1016/j.ijsolstr.2013.02.007).

- [36] A. Arteiro, G. Catalanotti, A. R. Melro, P. Linde, and P. P. Camanho. “Micro-mechanical analysis of the *in situ* effect in polymer composite laminates”. In: *Composite Structures* 116 (1 2014), pp. 827–840. ISSN: 02638223. DOI: [10.1016/j.compstruct.2014.06.014](https://doi.org/10.1016/j.compstruct.2014.06.014).
- [37] R. P. Tavares, A. R. Melro, M. A. Bessa, A. Turon, W. K. Liu, and P. P. Camanho. “Mechanics of hybrid polymer composites: analytical and computational study”. In: *Computational Mechanics* 57 (3 Mar. 2016), pp. 405–421. ISSN: 01787675. DOI: [10.1007/s00466-015-1252-0](https://doi.org/10.1007/s00466-015-1252-0).
- [38] D. A. Vajari, C. González, J. Llorca, and B. N. Legarth. “A numerical study of the influence of microvoids in the transverse mechanical response of unidirectional composites”. In: *Composites Science and Technology* 97 (June 2014), pp. 46–54. ISSN: 02663538. DOI: [10.1016/j.compscitech.2014.04.004](https://doi.org/10.1016/j.compscitech.2014.04.004).
- [39] C. Dong. “Effects of process-induced voids on the properties of fibre reinforced composites”. In: *Journal of Materials Science and Technology* 32 (7 July 2016), pp. 597–604. ISSN: 10050302. DOI: [10.1016/j.jmst.2016.04.011](https://doi.org/10.1016/j.jmst.2016.04.011).
- [40] M. Mehdikhani, N. A. Petrov, I. Straumit, A. R. Melro, S. V. Lomov, and L. Gorbatikh. “The effect of voids on matrix cracking in composite laminates as revealed by combined computations at the micro- and meso-scales”. In: *Composites Part A: Applied Science and Manufacturing* 117 (Feb. 2019), pp. 180–192. ISSN: 1359835X. DOI: [10.1016/j.compositesa.2018.11.009](https://doi.org/10.1016/j.compositesa.2018.11.009).
- [41] A. Hyde, J. He, X. Cui, J. Lua, and L. Liu. “Effects of microvoids on strength of unidirectional fiber-reinforced composite materials”. In: *Composites Part B: Engineering* 187 (Apr. 2020). ISSN: 13598368. DOI: [10.1016/j.compositesb.2020.107844](https://doi.org/10.1016/j.compositesb.2020.107844).
- [42] F. Sharifpour, J. Montesano, and R. Talreja. “Assessing the effects of ply constraints on local stress states in cross-ply laminates containing manufacturing induced defects”. In: *Composites Part B: Engineering* 199 (Oct. 2020). ISSN: 13598368. DOI: [10.1016/j.compositesb.2020.108227](https://doi.org/10.1016/j.compositesb.2020.108227).
- [43] Y. Chu, L. Sun, X. Yang, J. Wang, and W. Huang. “Multiscale simulation and theoretical prediction for the elastic properties of unidirectional fiber-reinforced polymer containing random void defects”. In: *Polymer Composites* 42 (6 June 2021), pp. 2958–2972. ISSN: 15480569. DOI: [10.1002/pc.26028](https://doi.org/10.1002/pc.26028).
- [44] M. Vinot, C. Liebold, T. Usta, M. Holzapfel, N. Toso, and H. Voggenreiter. “Stochastic modelling of continuous glass-fibre reinforced plastics—considering material un-

- certainty in microscale simulations". In: *Journal of Composite Materials* 57 (1 Jan. 2023), pp. 133–145. ISSN: 1530793X. DOI: [10.1177/00219983221139790](https://doi.org/10.1177/00219983221139790).
- [45] S. Daggumati, A. Sharma, and W. V. Paeppegem. "Synergistic effects of microscale variabilities on the thermo-mechanical behavior of a UD CFRP ply". In: *International Journal of Mechanical Sciences* 242 (Mar. 2023). ISSN: 00207403. DOI: [10.1016/j.ijmecsci.2022.108004](https://doi.org/10.1016/j.ijmecsci.2022.108004).
- [46] O. Vallmajó, A. Arteiro, J. M. Guerrero, A. R. Melro, A. Pupurs, and A. Turon. "Micromechanical analysis of composite materials considering material variability and microvoids". In: *International Journal of Mechanical Sciences* 263 (Feb. 2024). ISSN: 00207403. DOI: [10.1016/j.ijmecsci.2023.108781](https://doi.org/10.1016/j.ijmecsci.2023.108781).
- [47] J. C. Simo and J. W. Ju. "Strain- and stress-based continuum damage models-I. Formulation". In: *International Journal of Solids and Structures* 23 (7 1987), pp. 821–840. ISSN: 0020-7683. DOI: [10.1016/0020-7683\(87\)90083-7](https://doi.org/10.1016/0020-7683(87)90083-7).
- [48] J. C. Simo and J. W. Ju. "Strain- and stress-based continuum damage models-II. Computational aspects". In: *International Journal of Solids and Structures* 23 (7 1987), pp. 847–869. ISSN: 0020-7683. DOI: [10.1016/0020-7683\(87\)90084-9](https://doi.org/10.1016/0020-7683(87)90084-9).
- [49] P. Maimí, P. P. Camanho, J. A. Mayugo, and C. G. Dávila. "A continuum damage model for composite laminates: Part I - Constitutive model". In: *Mechanics of Materials* 39 (10 Oct. 2007), pp. 897–908. ISSN: 01676636. DOI: [10.1016/j.mechmat.2007.03.005](https://doi.org/10.1016/j.mechmat.2007.03.005).
- [50] P. Maimí, P. P. Camanho, J. A. Mayugo, and C. G. Dávila. "A continuum damage model for composite laminates: Part II - Computational implementation and validation". In: *Mechanics of Materials* 39 (10 Oct. 2007), pp. 909–919. ISSN: 01676636. DOI: [10.1016/j.mechmat.2007.03.006](https://doi.org/10.1016/j.mechmat.2007.03.006).
- [51] P. F. Liu and J. Y. Zheng. "Recent developments on damage modeling and finite element analysis for composite laminates: A review". In: *Materials and Design* 31 (8 Sept. 2010), pp. 3825–3834. ISSN: 02641275. DOI: [10.1016/j.matdes.2010.03.031](https://doi.org/10.1016/j.matdes.2010.03.031).
- [52] Q. Guo, W. Yao, W. Li, and N. Gupta. "Constitutive models for the structural analysis of composite materials for the finite element analysis: A review of recent practices". In: *Composite Structures* 260 (Mar. 2021). ISSN: 02638223. DOI: [10.1016/j.compstruct.2020.113267](https://doi.org/10.1016/j.compstruct.2020.113267).
- [53] A. Turon, P. P. Camanho, J. Costa, and C. G. Dávila. "A damage model for the simulation of delamination in advanced composites under variable-mode loading". In: *Mechanics of Materials* 38 (11 Nov. 2006), pp. 1072–1089. ISSN: 01676636. DOI: [10.1016/j.mechmat.2005.10.003](https://doi.org/10.1016/j.mechmat.2005.10.003).

- [54] E. V. González, P Maimí, A Turon, P. P. Camanho, and J Renart. “Simulation of delamination by means of cohesive elements using an explicit finite element code”. In: *Computers, Materials & Continua* 9 (1 2009), pp. 51–92. ISSN: 1546-2226. DOI: [10.3970/cmc.2009.009.051](https://doi.org/10.3970/cmc.2009.009.051).
- [55] A. Turon, E. V. González, C. Sarrado, G. Guillamet, and P. Maimí. “Accurate simulation of delamination under mixed-mode loading using a cohesive model with a mode-dependent penalty stiffness”. In: *Composite Structures* 184 (Jan. 2018), pp. 506–511. ISSN: 02638223. DOI: [10.1016/j.compstruct.2017.10.017](https://doi.org/10.1016/j.compstruct.2017.10.017).
- [56] D. Ranz, J. Cuartero, L. Castejon, R. Miralbes, and H. Malon. “A cohesive zone model approach to interlaminar behaviour of carbon/epoxy laminated curved beams”. In: *Composite Structures* 238 (Apr. 2020). ISSN: 02638223. DOI: [10.1016/j.compstruct.2020.111983](https://doi.org/10.1016/j.compstruct.2020.111983).
- [57] L. Kachanov. “Time of the rupture process under creep conditions”. In: *Izvestiia Akademii Nauk SSSR, Otdelenie Tekhnicheskikh Nauk* 8 (1958), pp. 26–31.
- [58] Y. N. Rabotnov, F. A. Leckie, and W. Prager. “Creep problems in structural members”. In: *Journal of Applied Mechanics* 37 (1 1970), pp. 249–249. ISSN: 0021-8936. DOI: [10.1115/1.3408479](https://doi.org/10.1115/1.3408479).
- [59] J. L. Chaboche. “Continuum damage mechanics: Present state and future trends”. In: *Nuclear Engineering and Design* 105 (1 1987), pp. 19–33. ISSN: 0029-5493. DOI: [https://doi.org/10.1016/0029-5493\(87\)90225-1](https://doi.org/10.1016/0029-5493(87)90225-1). URL: <https://www.sciencedirect.com/science/article/pii/0029549387902251>.
- [60] D. Krajcinovic. *Continuum damage mechanics: theory and applications*. Ed. by D. Krajcinovic and J. Lemaitre. Springer Vienna, 1983. ISBN: 0444867007. DOI: [10.1007/978-3-7091-2806-0](https://doi.org/10.1007/978-3-7091-2806-0).
- [61] J. Serra, C. Bouvet, B. Castanié, and C. Petiot. “Scaling effect in notched composites: The Discrete Ply Model approach”. In: *Composite Structures* 148 (July 2016), pp. 127–143. ISSN: 02638223. DOI: [10.1016/j.compstruct.2016.03.062](https://doi.org/10.1016/j.compstruct.2016.03.062).
- [62] P. D. Soden, A. S. Kaddour, and M. J. Hinton. “Recommendations for designers and researchers resulting from the world-wide failure exercise”. In: *Composites Science and Technology* 64 (3-4 2004), pp. 589–604. ISSN: 02663538. DOI: [10.1016/S0266-3538\(03\)00228-8](https://doi.org/10.1016/S0266-3538(03)00228-8).
- [63] M. J. Hinton and P. D. Soden. “Predicting failure in composite laminates: The background to the exercise”. In: *Composites Science and Technology* 58 (7 1998), pp. 1001–1010. ISSN: 0266-3538. DOI: [10.1016/S0266-3538\(98\)00074-8](https://doi.org/10.1016/S0266-3538(98)00074-8).

- [64] M. J. Hinton, A. S. Kaddour, and P. D. Soden. “Evaluation of failure prediction in composite laminates: Background to ‘part C’ of the exercise”. In: *Composites Science and Technology* 64 (3-4 2004), pp. 321–327. ISSN: 02663538. DOI: [10.1016/S0266-3538\(03\)00216-1](https://doi.org/10.1016/S0266-3538(03)00216-1).
- [65] R. M. Christensen. “The world wide failure exercise II examination of results”. In: *Journal of Reinforced Plastics and Composites* 32 (21 Nov. 2013), pp. 1668–1672. ISSN: 07316844. DOI: [10.1177/0731684413498634](https://doi.org/10.1177/0731684413498634).
- [66] A. S. Kaddour and M. J. Hinton. “Maturity of 3D failure criteria for fibre-reinforced composites: Comparison between theories and experiments: Part B of WWFE-II”. In: *Journal of Composite Materials* 47 (6-7 Mar. 2013), pp. 925–966. ISSN: 00219983. DOI: [10.1177/0021998313478710](https://doi.org/10.1177/0021998313478710).
- [67] A. S. Kaddour, M. J. Hinton, P. A. Smith, and S. Li. “The background to the third world-wide failure exercise”. In: *Journal of Composite Materials* 47 (20-21 Sept. 2013), pp. 2417–2426. ISSN: 00219983. DOI: [10.1177/0021998313499475](https://doi.org/10.1177/0021998313499475).
- [68] A. S. Kaddour, M. J. Hinton, P. A. Smith, and S. Li. “A comparison between the predictive capability of matrix cracking, damage and failure criteria for fibre reinforced composite laminates: Part A of the third world-wide failure exercise”. In: *Journal of Composite Materials* 47 (20-21 Sept. 2013), pp. 2749–2779. ISSN: 00219983. DOI: [10.1177/0021998313499476](https://doi.org/10.1177/0021998313499476).
- [69] R. Olsson. *A survey of test methods for multiaxial and out-of-plane strength of composite laminates*. Apr. 2011. DOI: [10.1016/j.compscitech.2011.01.022](https://doi.org/10.1016/j.compscitech.2011.01.022).
- [70] S. Daghighi and P. M. Weaver. “Three-dimensional effects influencing failure in bend-free, variable stiffness composite pressure vessels”. In: *Composite Structures* 262 (Apr. 2021). ISSN: 02638223. DOI: [10.1016/j.compstruct.2020.113346](https://doi.org/10.1016/j.compstruct.2020.113346).
- [71] E. Hara, T. Yokozeki, H. Hatta, Y. Iwahori, T. Ogasawara, and T. Ishikawa. “Comparison of out-of-plane tensile strengths of aligned CFRP obtained by 3-point bending and direct loading tests”. In: *Composites Part A: Applied Science and Manufacturing* 43 (11 Nov. 2012), pp. 1828–1836. ISSN: 1359835X. DOI: [10.1016/j.compositesa.2012.06.016](https://doi.org/10.1016/j.compositesa.2012.06.016).
- [72] J. F. Chen, E. V. Morozov, and K. Shankar. “A combined elastoplastic damage model for progressive failure analysis of composite materials and structures”. In: *Composite Structures* 94 (12 Dec. 2012), pp. 3478–3489. ISSN: 02638223. DOI: [10.1016/j.compstruct.2012.04.021](https://doi.org/10.1016/j.compstruct.2012.04.021).

- [73] C. T. Sun and J. L. Chen. “A simple flow rule for characterizing nonlinear behavior of fiber composites”. In: *Journal of Composite Materials* 23 (10 1989), pp. 1009–1020. ISSN: 1530793x. DOI: [10.1177/002199838902301004](https://doi.org/10.1177/002199838902301004).
- [74] C. Hoffarth, B. Khaled, L. Shyamsunder, S. Rajan, R. Goldberg, K. S. Carney, P. DuBois, and G. Blankenhorn. “Verification and validation of a three-dimensional Orthotropic Plasticity constitutive model using a unidirectional composite”. In: *Fibers* 5 (1 Mar. 2017). ISSN: 20796439. DOI: [10.3390/fib5010012](https://doi.org/10.3390/fib5010012).
- [75] S. W. Tsai, W.-P. Afb, E. M. Wu, and S. Louis. “A general theory of strength for anisotropic materials”. In: *Journal of Composite Materials* 5 (1 1971), pp. 58–80. DOI: [10.1177/002199837100500106](https://doi.org/10.1177/002199837100500106).
- [76] A Matzenmiller, J Lubliner, and R. L. Taylor. “A constitutive model for anisotropic damage in fiber-composites”. In: *Mechanics of Materials* 20 (2 1995), pp. 125–152. ISSN: 0167-6636. DOI: [10.1016/0167-6636\(94\)00053-0](https://doi.org/10.1016/0167-6636(94)00053-0).
- [77] J. Xie, G. Fang, Z. Chen, and J. Liang. “An anisotropic elastoplastic damage constitutive model for 3D needled C/C-SiC composites”. In: *Composite Structures* 176 (Sept. 2017), pp. 164–177. ISSN: 02638223. DOI: [10.1016/j.compstruct.2017.04.043](https://doi.org/10.1016/j.compstruct.2017.04.043).
- [78] H. Holthusen, T. Brepols, S. Reese, and J. W. Simon. “An anisotropic constitutive model for fiber-reinforced materials including gradient-extended damage and plasticity at finite strains”. In: *Theoretical and Applied Fracture Mechanics* 108 (Aug. 2020). ISSN: 01678442. DOI: [10.1016/j.tafmec.2020.102642](https://doi.org/10.1016/j.tafmec.2020.102642).
- [79] J. Cho, J. Fenner, B. Werner, and I. M. Daniel. “A constitutive model for fiber-reinforced polymer composites”. In: *Journal of Composite Materials* 44 (26 Dec. 2010), pp. 3133–3150. ISSN: 00219983. DOI: [10.1177/0021998310371547](https://doi.org/10.1177/0021998310371547).
- [80] I. M. Daniel. “Yield and failure criteria for composite materials under static and dynamic loading”. In: *Progress in Aerospace Sciences* 81 (Feb. 2016), pp. 18–25. ISSN: 03760421. DOI: [10.1016/j.paerosci.2015.11.003](https://doi.org/10.1016/j.paerosci.2015.11.003).
- [81] A Puck and H Schürmann. “Failure analysis of FRP laminates by means of physically based phenomenological models”. In: *Composites Science and Technology* 58 (7 1998), pp. 1045–1067. ISSN: 0266-3538. DOI: [10.1016/S0266-3538\(96\)00140-6](https://doi.org/10.1016/S0266-3538(96)00140-6).
- [82] A Puck and H Schürmann. “Failure analysis of FRP laminates by means of physically based phenomenological models”. In: *Composites Science and Technology* 62 (12 2002), pp. 1633–1662. ISSN: 0266-3538. DOI: [10.1016/S0266-3538\(01\)00208-1](https://doi.org/10.1016/S0266-3538(01)00208-1).
- [83] Z Hashin. “Failure criteria for unidirectional fiber composites”. In: *Journal of Applied Mechanics* 47 (2 1980), pp. 329–334. ISSN: 0021-8936. DOI: [10.1115/1.3153664](https://doi.org/10.1115/1.3153664).

- [84] C. G. Dávila, P. P. Camanho, and C. A. Rose. “Failure criteria for FRP laminates”. In: *Journal of Composite Materials* 39 (4 2005), pp. 323–345. ISSN: 00219983. DOI: [10.1177/0021998305046452](https://doi.org/10.1177/0021998305046452).
- [85] S. T. Pinho, C. G. Dávila, P. P. Camanho, L. Iannucci, and P. Robinson. *Failure models and criteria for FRP under in-plane or three-dimensional stress states including shear non-linearity*. NASA Washington, DC, 2005.
- [86] A. Quintanas-Corominas, P. Maimí, E. Casoni, A. Turon, J. A. Mayugo, G. Guillamet, and M. Vázquez. “A 3D transversally isotropic constitutive model for advanced composites implemented in a high performance computing code”. In: *European Journal of Mechanics, A/Solids* 71 (Sept. 2018), pp. 278–291. ISSN: 09977538. DOI: [10.1016/j.euromechsol.2018.03.021](https://doi.org/10.1016/j.euromechsol.2018.03.021).
- [87] J. E. Marsden and T. J. R. Hughes. *Mathematical foundations of elasticity*. Courier Corporation, 1994.
- [88] J. C. Simo and T. J. R. H. Springer. *Computational inelasticity*. Ed. by J. Marsden, L. Sirovich, and S. Wiggins. Vol. 7. Springer New York, NY, 1998. DOI: [10.1007/b98904](https://doi.org/10.1007/b98904).
- [89] Z. P. Bažant and B. H. Oh. “Crack band theory for fracture of concrete”. In: *Matériaux et Construction* 16 (3 1983), pp. 155–177. DOI: [10.1007/BF02486267](https://doi.org/10.1007/BF02486267).
- [90] J. Lemaitre. “A continuous damage mechanics model for ductile fracture”. In: *Journal of Engineering Materials and Technology* 107 (1 1985), pp. 83–89. ISSN: 0094-4289. DOI: [10.1115/1.3225775](https://doi.org/10.1115/1.3225775).
- [91] J. Lemaitre. *A course on damage mechanics*. Springer Berlin, Heidelberg, 1996. DOI: [10.1007/978-3-642-18255-6](https://doi.org/10.1007/978-3-642-18255-6).
- [92] I. Shahid and F.-K. Chang. “An accumulative damage model for tensile and shear failures of laminated composite plates”. In: *Journal of Composite Materials* 29 (7 1995), pp. 926–981. DOI: [10.1177/002199839502900705](https://doi.org/10.1177/002199839502900705).
- [93] S. Zenia, L. B. Ayed, M. Nouari, and A. Delamézière. “Numerical prediction of the chip formation process and induced damage during the machining of carbon/epoxy composites”. In: *International Journal of Mechanical Sciences* 90 (2015), pp. 89–101. ISSN: 00207403. DOI: [10.1016/j.ijmecsci.2014.10.018](https://doi.org/10.1016/j.ijmecsci.2014.10.018).
- [94] J. Reinoso, G. Catalanotti, A. Blázquez, P. Areias, P. P. Camanho, and F. París. “A consistent anisotropic damage model for laminated fiber-reinforced composites using the 3D-version of the Puck failure criterion”. In: *International Journal of Solids and Structures* 126-127 (Nov. 2017), pp. 37–53. ISSN: 00207683. DOI: [10.1016/j.ijsolstr.2017.07.023](https://doi.org/10.1016/j.ijsolstr.2017.07.023).

- [95] I. U. Din, P. Hao, G. Franz, and S. Panier. “Elastoplastic CDM model based on Puck’s theory for the prediction of mechanical behavior of Fiber Reinforced Polymer (FRP) composites”. In: *Composite Structures* 201 (Oct. 2018), pp. 291–302. ISSN: 02638223. DOI: [10.1016/j.compstruct.2018.06.010](https://doi.org/10.1016/j.compstruct.2018.06.010).
- [96] J. S. Welsh, A. C. Biskner, and E. E. Nelson. “Experimental and numerical failure predictions of biaxially-loaded unidirectional carbon composite laminates”. In: 2009, pp. 87117–5776.
- [97] P. D. Soden, M. J. Hinton, and A. S. Kaddour. “Chapter 2.2 - Biaxial test results for strength and deformation of a range of E-glass and carbon fibre reinforced composite laminates: Failure exercise benchmark data”. In: ed. by M. Hinton, A. Kaddour, and P. Soden. Elsevier, 2004, pp. 52–96. ISBN: 978-0-08-044475-8. DOI: [10.1016/B978-008044475-8/50004-4](https://doi.org/10.1016/B978-008044475-8/50004-4).
- [98] ASTM. *Standard test method for tensile properties of polymer matrix composite materials. ASTM D3039/D3039M*. 2017. DOI: [10.1520/D3039_D3039M-17](https://doi.org/10.1520/D3039_D3039M-17).
- [99] ASTM. *Standard test method for compressive properties of polymer matrix composite materials using a Combined Loading Compression (CLC) test fixture. ASTM D6641/D6641M*. 2018. DOI: [10.1520/D6641_D6641M-16](https://doi.org/10.1520/D6641_D6641M-16).
- [100] A. Ortega, P. Maimí, E. V. González, J. R. S. de Aja, F. M. de la Escalera, and P. Cruz. “Translaminar fracture toughness of interply hybrid laminates under tensile and compressive loads”. In: *Composites Science and Technology* 143 (May 2017), pp. 1–12. ISSN: 02663538. DOI: [10.1016/j.compscitech.2017.02.029](https://doi.org/10.1016/j.compscitech.2017.02.029).
- [101] E. V. González, P. Maimí, E. Martín-Santos, A. Soto, P. Cruz, F. M. de la Escalera, and J. R. S. de Aja. “Simulating drop-weight impact and compression after impact tests on composite laminates using conventional shell finite elements”. In: *International Journal of Solids and Structures* 144-145 (July 2018), pp. 230–247. ISSN: 00207683. DOI: [10.1016/j.ijsolstr.2018.05.005](https://doi.org/10.1016/j.ijsolstr.2018.05.005).
- [102] A. Soto, E. V. González, P. Maimí, F. M. de la Escalera, J. R. S. de Aja, and E. Alvarez. “Low velocity impact and compression after impact simulation of thin ply laminates”. In: *Composites Part A: Applied Science and Manufacturing* 109 (June 2018), pp. 413–427. ISSN: 1359835X. DOI: [10.1016/j.compositesa.2018.03.017](https://doi.org/10.1016/j.compositesa.2018.03.017).
- [103] ISO. *Fibre-reinforced plastic composites - Determination of mode I interlaminar fracture toughness for unidirectionally reinforced materials. ISO 15024:2023*. 2023. URL: www.iso.org.

- [104] ASTM. *Standard test method for in-plane shear response of polymer matrix composite materials by tensile test of a $\pm 45^\circ$ laminate. ASTM D3518/D3518M-18*. 2018. DOI: [10.1520/D3518_D3518M-18](https://doi.org/10.1520/D3518_D3518M-18).
- [105] ASTM. *Standard test method for shear properties of composite materials by v-notched rail shear method. ASTM D7078/D7078M-20*. 2020. DOI: [10.1520/D7078_D7078M-20](https://doi.org/10.1520/D7078_D7078M-20).
- [106] ISO. *Determination of the mode II fracture resistance for unidirectionally reinforced materials using the calibrated end-loaded split (C-ELS) test and an effective crack length approach. ISO 15114:2014*. 2014. URL: www.iso.org.
- [107] G. Catalanotti, A. Arteiro, M. Hayati, and P. P. Camanho. “Determination of the mode I crack resistance curve of polymer composites using the size-effect law”. In: *Engineering Fracture Mechanics* 118 (2014), pp. 49–65. ISSN: 00137944. DOI: [10.1016/j.engfracmech.2013.10.021](https://doi.org/10.1016/j.engfracmech.2013.10.021).
- [108] G. Catalanotti, J. Xavier, and P. P. Camanho. “Measurement of the compressive crack resistance curve of composites using the size effect law”. In: *Composites Part A: Applied Science and Manufacturing* 56 (2014), pp. 300–307. ISSN: 1359835X. DOI: [10.1016/j.compositesa.2013.10.017](https://doi.org/10.1016/j.compositesa.2013.10.017).
- [109] ASTM. *Standard test method for mode I interlaminar fracture toughness of unidirectional fiber-reinforced polymer matrix composites. ASTM D5528/D5528M*. 2022. DOI: [10.1520/D5528_D5528M-21](https://doi.org/10.1520/D5528_D5528M-21).
- [110] ASTM. *Standard test method for determination of the mode II interlaminar fracture toughness of unidirectional fiber-reinforced polymer matrix composites. ASTM D7905/D7905M*. 2019. DOI: [10.1520/D7905_D7905M-19E01](https://doi.org/10.1520/D7905_D7905M-19E01).
- [111] SIMULIA. *ABAQUS User’s Manual, Version 2020*. Dassault Systèmes Simulia Corp, 2020. URL: www.3ds.com.
- [112] ASME. *Standard for verification and validation in computational solid mechanics. ASME V&V 10-2019*. 2019. URL: <https://www.asme.org/>.
- [113] W. R. Cowell and T. P. Christopher. “Transforming Fortran DO loops to improve performance on vector architectures”. In: *Association for Computing Machinery* 12 (1986). ISSN: 0098-3500. DOI: [10.1145/22721.24035](https://doi.org/10.1145/22721.24035).
- [114] P. P. Camanho, P. Maimí, and C. G. Dávila. “Prediction of size effects in notched laminates using continuum damage mechanics”. In: *Composites Science and Technology* 67 (13 Oct. 2007), pp. 2715–2727. ISSN: 02663538. DOI: [10.1016/j.compscitech.2007.02.005](https://doi.org/10.1016/j.compscitech.2007.02.005).

- [115] A. P. Joseph, P. Davidson, and A. M. Waas. “Open hole and filled hole progressive damage and failure analysis of composite laminates with a countersunk hole”. In: *Composite Structures* 203 (Nov. 2018), pp. 523–538. ISSN: 02638223. DOI: [10.1016/j.compstruct.2018.06.120](https://doi.org/10.1016/j.compstruct.2018.06.120).
- [116] W. Tan, B. G. Falzon, L. N. Chiu, and M. Price. “Predicting low velocity impact damage and Compression-After-Impact (CAI) behaviour of composite laminates”. In: *Composites Part A: Applied Science and Manufacturing* 71 (2015), pp. 212–226. ISSN: 1359835X. DOI: [10.1016/j.compositesa.2015.01.025](https://doi.org/10.1016/j.compositesa.2015.01.025).
- [117] B. Egan, M. A. McCarthy, R. M. Frizzell, P. J. Gray, and C. T. McCarthy. “Modelling bearing failure in countersunk composite joints under quasi-static loading using 3D explicit finite element analysis”. In: *Composite Structures* 108 (1 2014), pp. 963–977. ISSN: 02638223. DOI: [10.1016/j.compstruct.2013.10.033](https://doi.org/10.1016/j.compstruct.2013.10.033).
- [118] P. Liu, X. Cheng, S. Wang, S. Liu, and Y. Cheng. “Numerical analysis of bearing failure in countersunk composite joints using 3D explicit simulation method”. In: *Composite Structures* 138 (Mar. 2016), pp. 30–39. ISSN: 02638223. DOI: [10.1016/j.compstruct.2015.11.058](https://doi.org/10.1016/j.compstruct.2015.11.058).
- [119] J. Hu, K. Zhang, Y. Xu, H. Cheng, G. Xu, and H. Li. “Modeling on bearing behavior and damage evolution of single-lap bolted composite interference-fit joints”. In: *Composite Structures* 212 (Mar. 2019), pp. 452–464. ISSN: 02638223. DOI: [10.1016/j.compstruct.2019.01.044](https://doi.org/10.1016/j.compstruct.2019.01.044).
- [120] M. Nebe, A. Soriano, C. Braun, P. Middendorf, and F. Walther. “Analysis on the mechanical response of composite pressure vessels during internal pressure loading: FE modeling and experimental correlation”. In: *Composites Part B: Engineering* 212 (May 2021). ISSN: 13598368. DOI: [10.1016/j.compositesb.2020.108550](https://doi.org/10.1016/j.compositesb.2020.108550).
- [121] P. P. Camanho and F. L. Matthews. “Delamination onset prediction in mechanically fastened joints in composite laminates”. In: *Journal of Composite Materials* 33 (10 1999), pp. 906–927. DOI: [10.1177/002199839903301002](https://doi.org/10.1177/002199839903301002).
- [122] P. P. Camanho, C. G. Dávila, S. T. Pinho, L. Iannucci, and P. Robinson. “Prediction of in situ strengths and matrix cracking in composites under transverse tension and in-plane shear”. In: *Composites Part A: Applied Science and Manufacturing* 37 (2 Feb. 2006), pp. 165–176. ISSN: 1359835X. DOI: [10.1016/j.compositesa.2005.04.023](https://doi.org/10.1016/j.compositesa.2005.04.023).
- [123] P. P. Camanho, A. Arteiro, A. R. Melro, G. Catalanotti, and M. Vogler. “Three-dimensional invariant-based failure criteria for fibre-reinforced composites”. In: *International Journal of Solids and Structures* 55 (Mar. 2015), pp. 92–107. ISSN: 00207683. DOI: [10.1016/j.ijsolstr.2014.03.038](https://doi.org/10.1016/j.ijsolstr.2014.03.038).

- [124] M. Vogler, R. Rolfs, and P. P. Camanho. “Modeling the inelastic deformation and fracture of polymer composites-Part I: Plasticity model”. In: *Mechanics of Materials* 59 (2013), pp. 50–64. ISSN: 01676636. DOI: [10.1016/j.mechmat.2012.12.002](https://doi.org/10.1016/j.mechmat.2012.12.002).
- [125] G. Catalanotti, P. P. Camanho, and A. T. Marques. “Three-dimensional failure criteria for fiber-reinforced laminates”. In: *Composite Structures* 95 (Jan. 2013), pp. 63–79. ISSN: 02638223. DOI: [10.1016/j.compstruct.2012.07.016](https://doi.org/10.1016/j.compstruct.2012.07.016).
- [126] R. Gutkin and S. Pinho. “Practical application of failure models to predict the response of composite structures”. In: Mar. 2011.
- [127] E. V. González, P. Maimí, P. P. Camanho, A. Turon, and J. A. Mayugo. “Simulation of drop-weight impact and compression after impact tests on composite laminates”. In: *Composite Structures* 94 (11 Nov. 2012), pp. 3364–3378. ISSN: 02638223. DOI: [10.1016/j.compstruct.2012.05.015](https://doi.org/10.1016/j.compstruct.2012.05.015).
- [128] J. L. Tsai and C. T. Sun. “Strain rate effect on in-plane shear strength of unidirectional polymeric composites”. In: *Composites Science and Technology* 65 (13 Oct. 2005), pp. 1941–1947. ISSN: 02663538. DOI: [10.1016/j.compscitech.2005.01.013](https://doi.org/10.1016/j.compscitech.2005.01.013).
- [129] M. Bessa. “Meso-mechanical model of the structural integrity of advanced composite laminates”. PhD thesis. University of Porto, 2010.
- [130] F. K. Chang and K. Y. Chang. “A progressive damage model for laminated composites containing stress concentrations”. In: *Journal of Composite Materials* 21 (9 1987), pp. 834–855. ISSN: 1530793X. DOI: [10.1177/002199838702100904](https://doi.org/10.1177/002199838702100904).
- [131] F.-K. Chatig and L. B. Lessard. “Damage tolerance of laminated composites containing an open hole and subjected to compressive loadings: Part I-Analysis”. In: *Journal of Composite Materials* 25 (1 1991), pp. 2–43. DOI: [10.1177/002199839102500303](https://doi.org/10.1177/002199839102500303).
- [132] F. A. Leone. “Deformation gradient tensor decomposition for representing matrix cracks in fiber-reinforced materials”. In: *Composites Part A: Applied Science and Manufacturing* 76 (July 2015), pp. 334–341. ISSN: 1359835X. DOI: [10.1016/j.compositesa.2015.06.014](https://doi.org/10.1016/j.compositesa.2015.06.014).
- [133] J. Llobet, P. Maimí, A. Turon, B. L. Bak, E. Lindgaard, L. Carreras, Y. Essa, and F. M. de la Escalera. “A continuum damage model for composite laminates: Part IV- Experimental and numerical tests”. In: *Mechanics of Materials* 154 (Mar. 2021). ISSN: 01676636. DOI: [10.1016/j.mechmat.2020.103686](https://doi.org/10.1016/j.mechmat.2020.103686).

- [134] I. Lapczyk and J. A. Hurtado. “Progressive damage modeling in fiber-reinforced materials”. In: *Composites Part A: Applied Science and Manufacturing* 38 (11 Nov. 2007), pp. 2333–2341. ISSN: 1359835X. DOI: [10.1016/j.compositesa.2007.01.017](https://doi.org/10.1016/j.compositesa.2007.01.017).
- [135] C Soutis. “Measurement of the static compressive strength of carbon-fibre/epoxy laminates”. In: *Composites Science and Technology* 42 (2 1991), pp. 373–392. ISSN: 02663538. DOI: [10.1016/0266-3538\(91\)90064-V](https://doi.org/10.1016/0266-3538(91)90064-V).
- [136] S. T. Pinho, L. Iannucci, and P. Robinson. “Physically-based failure models and criteria for laminated fibre-reinforced composites with emphasis on fibre kinking: Part I: Development”. In: *Composites Part A: Applied Science and Manufacturing* 37 (1 Jan. 2006), pp. 63–73. ISSN: 1359835X. DOI: [10.1016/j.compositesa.2005.04.016](https://doi.org/10.1016/j.compositesa.2005.04.016).
- [137] SIMULIA. *ABAQUS User's Manual, Version 2022*. Dassault Systèmes Simulia Corp, 2022. URL: www.3ds.com.
- [138] G. Seon, A. Makeev, J. D. Schaefer, and B. Justusson. “Measurement of interlaminar tensile strength and elastic properties of composites using open-hole compression testing and digital image correlation”. In: *Applied Sciences (Switzerland)* 9 (13 July 2019). ISSN: 20763417. DOI: [10.3390/app9132647](https://doi.org/10.3390/app9132647).
- [139] M. R. Wisnom, S. R. Hallett, and C. Soutis. “Scaling effects in notched composites”. In: *Journal of Composite Materials* 44 (2 Jan. 2010), pp. 195–210. ISSN: 00219983. DOI: [10.1177/0021998309339865](https://doi.org/10.1177/0021998309339865).
- [140] C. Soutis and N. A. Fleck. “Static compression failure of carbon fibre T800/924C composite plate with a single hole”. In: *Journal of Composite Materials* 24 (5 1990), pp. 536–558. DOI: [10.1177/002199839002400505](https://doi.org/10.1177/002199839002400505).
- [141] C Soutis, N. A. Fleck, and P. A. Smith. “Failure prediction technique for compression loaded carbon fibre-epoxy laminate with open holes”. In: *Journal of Composite Materials* 25 (11 1991), pp. 1476–1498. DOI: [10.1177/002199839102501106](https://doi.org/10.1177/002199839102501106).
- [142] C Soutis, N. A. Fleck, and P. T. Curtis. “Hole-hole interaction in carbon fibre/epoxy laminates under uniaxial compression”. In: *Composites* 22 (1 1991), p. 31. ISSN: 0010-4361. DOI: [10.1016/0010-4361\(91\)90100-U](https://doi.org/10.1016/0010-4361(91)90100-U).
- [143] C. Soutis, P. T. Curtis, and N. A. Fleck. “Compressive failure of notched carbon fibre composites”. In: *Proceedings of the Royal Society of London. Series A: Mathematical and Physical Sciences* 440 (Feb. 1993), pp. 241–256. ISSN: 0962-8444. DOI: [10.1098/rspa.1993.0014](https://doi.org/10.1098/rspa.1993.0014).

- [144] C Soutis and P. T. Curtis. “A method for predicting the fracture toughness of CFRP laminates failing by fibre microbuckling”. In: *Composites Part A: Applied Science and Manufacturing* 31 (7 2000), pp. 733–740. ISSN: 1359-835X. DOI: [10.1016/S1359-835X\(00\)00003-8](https://doi.org/10.1016/S1359-835X(00)00003-8).
- [145] J. Ahn and A. M. Waas. “Prediction of compressive failure in laminated composites at room and elevated temperature”. In: *AIAA Journal* 40 (2 2002), pp. 346–358. ISSN: 00011452. DOI: [10.2514/2.1652](https://doi.org/10.2514/2.1652).
- [146] C Bouvet and S Rivallant. “Damage tolerance of composite structures under low-velocity impact”. In: ed. by V. V. Silberschmidt. Woodhead Publishing, 2016, pp. 7–33. ISBN: 9780081008706. DOI: [10.1016/B978-0-08-100870-6.00002-X](https://doi.org/10.1016/B978-0-08-100870-6.00002-X).
- [147] Y. Liv. “A contribution to the understanding of compression after impact of composite laminates”. PhD thesis. University of Girona, 2017. URL: <http://hdl.handle.net/10803/461500>.
- [148] I. R. Cázar, A. Turon, E. V. González, O. Vallmajó, and A. Sasikumar. “A methodology to obtain material design allowables from high-fidelity compression after impact simulations on composite laminates”. In: *Composites Part A: Applied Science and Manufacturing* 139 (Dec. 2020). ISSN: 1359835X. DOI: [10.1016/j.compositesa.2020.106069](https://doi.org/10.1016/j.compositesa.2020.106069).
- [149] X. C. Sun and S. R. Hallett. “Failure mechanisms and damage evolution of laminated composites under compression after impact (CAI): Experimental and numerical study”. In: *Composites Part A: Applied Science and Manufacturing* 104 (Jan. 2018), pp. 41–59. ISSN: 1359835X. DOI: [10.1016/j.compositesa.2017.10.026](https://doi.org/10.1016/j.compositesa.2017.10.026).
- [150] C. Wang, Z. Liu, B. Xia, S. Duan, X. Nie, and Z. Zhuang. “Development of a new constitutive model considering the shearing effect for anisotropic progressive damage in fiber-reinforced composites”. In: *Composites Part B: Engineering* 75 (June 2015), pp. 288–297. ISSN: 13598368. DOI: [10.1016/j.compositesb.2015.01.048](https://doi.org/10.1016/j.compositesb.2015.01.048).
- [151] C. Zhang, N. Li, W. Wang, W. K. Binienda, and H. Fang. “Progressive damage simulation of triaxially braided composite using a 3D meso-scale finite element model”. In: *Composite Structures* 125 (July 2015), pp. 104–116. ISSN: 02638223. DOI: [10.1016/j.compstruct.2015.01.034](https://doi.org/10.1016/j.compstruct.2015.01.034).
- [152] A. Tullu and B. S. Kang. “Elastic deformation of fiber-reinforced multi-layered composite cylindrical shells of variable stiffness”. In: *Composites Part B: Engineering* 100 (Sept. 2016), pp. 44–55. ISSN: 13598368. DOI: [10.1016/j.compositesb.2016.06.010](https://doi.org/10.1016/j.compositesb.2016.06.010).

- [153] S. K. Chakrapani, D. J. Barnard, and V. Dayal. “Nonlinear forced vibration of carbon fiber/epoxy prepreg composite beams: Theory and experiment”. In: *Composites Part B: Engineering* 91 (Apr. 2016), pp. 513–521. ISSN: 13598368. DOI: [10.1016/j.compositesb.2016.02.009](https://doi.org/10.1016/j.compositesb.2016.02.009).
- [154] ASTM. *Standard test method for shear properties of composite materials by the V-notched beam method. ASTM D5379/D5379M*. 2019. DOI: [10.1520/D5379_D5379M-19E01](https://doi.org/10.1520/D5379_D5379M-19E01).
- [155] C. T. Sun and Y. Rui. “Orthotropic elasto-plastic behavior of AS4/PEEK thermoplastic composite in compression”. In: *Mechanics of Materials* 10 (1 1990), pp. 117–125. ISSN: 0167-6636. DOI: [10.1016/0167-6636\(90\)90022-8](https://doi.org/10.1016/0167-6636(90)90022-8).
- [156] B. Vieille, W. Albouy, L. Chevalier, and L. Taleb. “About the influence of stamping on thermoplastic-based composites for aeronautical applications”. In: *Composites Part B: Engineering* 45 (1 Feb. 2013), pp. 821–834. ISSN: 13598368. DOI: [10.1016/j.compositesb.2012.07.047](https://doi.org/10.1016/j.compositesb.2012.07.047).
- [157] G. M. Vyas, S. T. Pinho, and P. Robinson. “Constitutive modelling of fibre-reinforced composites with unidirectional plies using a plasticity-based approach”. In: *Composites Science and Technology* 71 (8 May 2011), pp. 1068–1074. ISSN: 02663538. DOI: [10.1016/j.compscitech.2011.03.009](https://doi.org/10.1016/j.compscitech.2011.03.009).
- [158] A. Dean, S. Sahraee, J. Reinoso, and R. Rolfes. “A new invariant-based thermoplastic model for finite deformation analysis of short fibre reinforced composites: Development and numerical aspects”. In: *Composites Part B: Engineering* 125 (Sept. 2017), pp. 241–258. ISSN: 13598368. DOI: [10.1016/j.compositesb.2017.05.043](https://doi.org/10.1016/j.compositesb.2017.05.043).
- [159] I. R. Cózar, F. Otero, P. Maimí, E. V. González, S. Miot, A. Turon, and P. P. Camanho. “A three-dimensional plastic-damage model for polymer composite materials”. In: *Composites Part A: Applied Science and Manufacturing* 163 (Dec. 2022). ISSN: 1359835X. DOI: [10.1016/j.compositesa.2022.107198](https://doi.org/10.1016/j.compositesa.2022.107198).
- [160] I. R. Cózar, F. Otero, P. Maimí, E. V. González, A. Turon, and P. P. Camanho. “An enhanced constitutive model to predict plastic deformation and multiple failure mechanisms in fibre-reinforced polymer composite materials”. In: *Composite Structures* 330 (Feb. 2024). ISSN: 02638223. DOI: [10.1016/j.compstruct.2023.117696](https://doi.org/10.1016/j.compstruct.2023.117696).
- [161] B. Khaled, L. Shyamsunder, C. Hoffarth, S. D. Rajan, R. K. Goldberg, K. S. Carney, P. DuBois, and G. Blankenhorn. “Experimental characterization of composites to support an orthotropic plasticity material model”. In: *Journal of Composite*

Materials 52 (14 June 2018), pp. 1847–1872. ISSN: 1530793X. DOI: [10.1177/0021998317733319](https://doi.org/10.1177/0021998317733319).

- [162] I. Baran, K. Cinar, N. Ersoy, R. Akkerman, and J. H. Hattel. “A review on the mechanical modeling of composite manufacturing processes”. In: *Archives of Computational Methods in Engineering* 24 (2 Apr. 2017), pp. 365–395. ISSN: 18861784. DOI: [10.1007/s11831-016-9167-2](https://doi.org/10.1007/s11831-016-9167-2).
- [163] G. Struzziero, J. J. Teuwen, and A. A. Skordos. “Numerical optimisation of thermoset composites manufacturing processes: A review”. In: *Composites Part A: Applied Science and Manufacturing* 124 (Sept. 2019). ISSN: 1359835X. DOI: [10.1016/j.compositesa.2019.105499](https://doi.org/10.1016/j.compositesa.2019.105499).
- [164] Y. Gao, J. Wang, X. Song, H. Ding, H. Wang, Y. B. Bi, and Y. Ke. “Investigation on the compressive mechanical properties of ultra-thick CFRP laminates”. In: *International Journal of Mechanical Sciences* 241 (Mar. 2023). ISSN: 00207403. DOI: [10.1016/j.ijmecsci.2022.107966](https://doi.org/10.1016/j.ijmecsci.2022.107966).
- [165] P. S. Frederiksen. “Experimental procedure and results for the identification of elastic constants of thick orthotropic plates”. In: *Journal of Composite Materials* 31 (4 1997), pp. 360–382. DOI: [10.1177/002199839703100403](https://doi.org/10.1177/002199839703100403).
- [166] J. N. Reddy. “A simple higher-order theory for laminated composite plates”. In: *Journal of Applied Mechanics* 51 (4 1984), pp. 745–752. ISSN: 0021-8936. DOI: [10.1115/1.3167719](https://doi.org/10.1115/1.3167719).
- [167] C. Kohlhauser and C. Hellmich. “Determination of Poisson’s ratios in isotropic, transversely isotropic, and orthotropic materials by means of combined ultrasonic-mechanical testing of normal stiffnesses: Application to metals and wood”. In: *European Journal of Mechanics, A/Solids* 33 (May 2012), pp. 82–98. ISSN: 09977538. DOI: [10.1016/j.euromechsol.2011.11.009](https://doi.org/10.1016/j.euromechsol.2011.11.009).
- [168] R. Cui and F. L. di Scalea. “On the identification of the elastic properties of composites by ultrasonic guided waves and optimization algorithm”. In: *Composite Structures* 223 (Sept. 2019). ISSN: 02638223. DOI: [10.1016/j.compstruct.2019.110969](https://doi.org/10.1016/j.compstruct.2019.110969).
- [169] I. D. Baere, W. V. Paepegem, and J. Degrieck. “On the nonlinear evolution of the Poisson’s ratio under quasi-static loading for a carbon fabric-reinforced thermoplastic. Part I: Influence of the transverse strain sensor”. In: *Polymer Testing* 28 (2 Apr. 2009), pp. 196–203. ISSN: 01429418. DOI: [10.1016/j.polymertesting.2008.12.002](https://doi.org/10.1016/j.polymertesting.2008.12.002).

- [170] C. Yilmaz, C. Akalin, E. S. Kocaman, A. Suleman, and M. Yildiz. “Monitoring Poisson’s ratio of glass fiber reinforced composites as damage index using biaxial Fiber Bragg Grating sensors”. In: *Polymer Testing* 53 (Aug. 2016), pp. 98–107. ISSN: 01429418. DOI: [10.1016/j.polymertesting.2016.05.009](https://doi.org/10.1016/j.polymertesting.2016.05.009).
- [171] D. Trias, J. Costa, J. A. Mayugo, and J. E. Hurtado. “Random models versus periodic models for fibre reinforced composites”. In: *Computational Materials Science* 38 (2 Dec. 2006), pp. 316–324. ISSN: 09270256. DOI: [10.1016/j.commatsci.2006.03.005](https://doi.org/10.1016/j.commatsci.2006.03.005).
- [172] A. R. Melro, P. P. Camanho, and S. T. Pinho. “Influence of geometrical parameters on the elastic response of unidirectional composite materials”. In: *Composite Structures* 94 (11 Nov. 2012), pp. 3223–3231. ISSN: 02638223. DOI: [10.1016/j.compstruct.2012.05.004](https://doi.org/10.1016/j.compstruct.2012.05.004).
- [173] B. Raju, S. R. Hiremath, and D. R. Mahapatra. “A review of micromechanics based models for effective elastic properties of reinforced polymer matrix composites”. In: *Composite Structures* 204 (Nov. 2018), pp. 607–619. ISSN: 02638223. DOI: [10.1016/j.compstruct.2018.07.125](https://doi.org/10.1016/j.compstruct.2018.07.125).
- [174] J. Brunbauer, C. Gaier, and G. Pinter. “Computational fatigue life prediction of continuously fibre reinforced multiaxial composites”. In: *Composites Part B: Engineering* 80 (June 2015), pp. 269–277. ISSN: 13598368. DOI: [10.1016/j.compositesb.2015.06.002](https://doi.org/10.1016/j.compositesb.2015.06.002).
- [175] I. D. I. C. Society. *A good practices guide for digital image correlation*. Ed. by E. Jones and M. Iadicola. 2018. DOI: [10.32720/idics/gpg.ed1](https://doi.org/10.32720/idics/gpg.ed1).
- [176] C. Solutions. *Vic-2D 2010, testing guide, Technical Report*. 2010.
- [177] K. Hoffmann. *An introduction to stress analysis using strain gauges*. 2012.
- [178] H. Haddadi and S. Belhabib. “Use of rigid-body motion for the investigation and estimation of the measurement errors related to digital image correlation technique”. In: *Optics and Lasers in Engineering* 46 (2 Feb. 2008), pp. 185–196. ISSN: 01438166. DOI: [10.1016/j.optlaseng.2007.05.008](https://doi.org/10.1016/j.optlaseng.2007.05.008).
- [179] B. Pan, K. Qian, H. Xie, and A. Asundi. “Two-dimensional digital image correlation for in-plane displacement and strain measurement: A review”. In: *Measurement Science and Technology* 20 (6 2009). ISSN: 13616501. DOI: [10.1088/0957-0233/20/6/062001](https://doi.org/10.1088/0957-0233/20/6/062001).

- [180] Y. Su, Q. Zhang, X. Xu, and Z. Gao. “Quality assessment of speckle patterns for DIC by consideration of both systematic errors and random errors”. In: *Optics and Lasers in Engineering* 86 (Nov. 2016), pp. 132–142. ISSN: 01438166. DOI: [10.1016/j.optlaseng.2016.05.019](https://doi.org/10.1016/j.optlaseng.2016.05.019).
- [181] J. Holmes, Y. Hafiz, Z. Stachurski, R. Das, and S. Kalyanasundaram. “Surface topography evolution of woven thermoplastic composites under deformation”. In: *Composites Part B: Engineering* 188 (May 2020). ISSN: 13598368. DOI: [10.1016/j.compositesb.2020.107880](https://doi.org/10.1016/j.compositesb.2020.107880).
- [182] J. Holmes, R. Das, Z. Stachurski, P. Compston, and S. Kalyanasundaram. “Development of an S-specimen geometry for shear testing of woven thermoplastic composites”. In: *Composites Part B: Engineering* 203 (Dec. 2020). ISSN: 13598368. DOI: [10.1016/j.compositesb.2020.108485](https://doi.org/10.1016/j.compositesb.2020.108485).
- [183] B. M. Lempriere. “Poisson’s ratio in orthotropic materials”. In: *AIAA Journal* 6 (11 1968), pp. 2226–2227. ISSN: 00011452. DOI: [10.2514/3.4974](https://doi.org/10.2514/3.4974).
- [184] R. Hill. “A theory of the yielding and plastic flow of anisotropic metals”. In: *Proceedings of the Royal Society of London. Series A. Mathematical and Physical Sciences* 193 (1948), pp. 281–297. DOI: [10.1098/rspa.1948.0045](https://doi.org/10.1098/rspa.1948.0045).
- [185] S. W. Tsai. *Strength characteristics of composite materials*. NASA Washington, DC, 1965.
- [186] C. A. Coulomb. “Essai sur une application des regles de maximis et minimis a quelques problemes de statique relatifs a l’architecture”. In: *Mem. Div. Sav. Acad.* 7 (1773), pp. 343–382.
- [187] J. S. Fenner and I. M. Daniel. *Testing the 2-3 shear strength of unidirectional composite*. Springer New York LLC, 2019, pp. 77–84. DOI: [10.1007/978-3-319-95510-0_9](https://doi.org/10.1007/978-3-319-95510-0_9).
- [188] D. Carlos and P. P. Camanho. *Failure criteria for FRP laminates in plane stress*. 2003. ISBN: 2003212663. URL: <https://www.researchgate.net/publication/24323990>.
- [189] A. R. Melro. “Analytical and numerical modelling of damage and fracture of advanced composites”. PhD thesis. University of Porto, 2011.
- [190] G. Lvov, A. Chetverikova, and O. Vodka. “The data-driven approach for prediction of yield function of composites”. In: Institute of Electrical and Electronics Engineers Inc., Oct. 2020, pp. 144–148. ISBN: 9781665405010. DOI: [10.1109/KhPIWeek51551.2020.9250070](https://doi.org/10.1109/KhPIWeek51551.2020.9250070).

- [191] O. Vallmajó, I. R. Cázar, C. Furtado, R. Tavares, A. Arteiro, A. Turon, and P. P. Camanho. “Virtual calculation of the B-value allowables of notched composite laminates”. In: *Composite Structures* 212 (Mar. 2019), pp. 11–21. ISSN: 02638223. DOI: [10.1016/j.compstruct.2018.12.049](https://doi.org/10.1016/j.compstruct.2018.12.049).
- [192] I. R. Cázar, J. J. Arbeláez-Toro, P. Maimí, F. Otero, E. V. González, A. Turon, and P. P. Camanho. “A novel methodology to measure the transverse Poisson’s ratio in the elastic and plastic regions for composite materials”. In: *Composites Part B: Engineering* 272 (Mar. 2024). ISSN: 13598368. DOI: [10.1016/j.compositesb.2023.111098](https://doi.org/10.1016/j.compositesb.2023.111098).
- [193] E. S. (EN). “Aerospace series - Carbon fibre reinforced plastics - Unidirectional laminates - Tensile test parallel to the fibre direction, (EN 2561)”. In: 1995.
- [194] E. S. (EN). “Aerospace series - Carbon fibre reinforced plastics; unidirectional laminates - Tensile test perpendicular to the fibre direction, (EN 2597)”. In: 1999.
- [195] E. S. (EN). “Aerospace series. Carbon fibre thermosetting resin - Unidirectional laminates. Compression test parallel to fibre direction, (EN 2850)”. In: 2017.
- [196] C. T. McCarthy, M. A. McCarthy, W. F. Stanley, and V. P. Lawlor. “Experiences with modeling friction in composite bolted joints”. In: *Journal of Composite Materials* 39 (21 2005), pp. 1881–1908. ISSN: 00219983. DOI: [10.1177/0021998305051805](https://doi.org/10.1177/0021998305051805).
- [197] B. Egan, C. T. McCarthy, M. A. McCarthy, P. J. Gray, and R. M. Frizzell. “Modelling a single-bolt countersunk composite joint using implicit and explicit finite element analysis”. In: *Computational Materials Science* 64 (Nov. 2012), pp. 203–208. ISSN: 09270256. DOI: [10.1016/j.commatsci.2012.02.008](https://doi.org/10.1016/j.commatsci.2012.02.008).
- [198] G. Seon, Y. Nikishkov, and A. Makeev. “Bearing strength and fatigue analysis of tape composites based on continuum damage mechanics methodology”. In: American Institute of Aeronautics and Astronautics Inc, AIAA, 2018. ISBN: 9781624105326. DOI: [10.2514/6.2018-0739](https://doi.org/10.2514/6.2018-0739).
- [199] P. Davidson, A. P. Joseph, and A. M. Waas. “Multi scale progressive damage and failure analysis of bolted joints”. In: American Institute of Aeronautics and Astronautics Inc, AIAA, 2018. ISBN: 9781624105326. DOI: [10.2514/6.2018-0740](https://doi.org/10.2514/6.2018-0740).
- [200] E. V. Larve, K. H. Hoos, Y. Nikishkov, and A. Makeev. “Discrete damage modeling of static bearing failure in laminated composites”. In: *Composites Part A: Applied Science and Manufacturing* 108 (May 2018), pp. 30–40. ISSN: 1359835X. DOI: [10.1016/j.compositesa.2018.02.019](https://doi.org/10.1016/j.compositesa.2018.02.019).

- [201] F. Zhuang, P. Chen, A. Arteiro, and P. P. Camanho. “Mesoscale modelling of damage in half-hole pin bearing composite laminate specimens”. In: *Composite Structures* 214 (Apr. 2019), pp. 191–213. ISSN: 02638223. DOI: [10.1016/j.compstruct.2019.01.062](https://doi.org/10.1016/j.compstruct.2019.01.062).
- [202] K. D. Pae and K. Y. Rhee. “Effects of hydrostatic pressure on the compressive behavior of thick laminated 45° and 90° unidirectional graphite-fiber/epoxy-matrix composites”. In: *Composites Science and Technology* 53 (3 1995), pp. 281–287. DOI: [10.1016/0266-3538\(94\)00080-8](https://doi.org/10.1016/0266-3538(94)00080-8).
- [203] P. D. Soden, M. J. Hinton, and A. S. Kaddour. “Biaxial test results for strength and deformation of a range of E-glass and carbon fibre reinforced composite laminates: failure exercise benchmark data”. In: *Composites Science and Technology* 62 (2002), pp. 1489–1514. URL: <https://api.semanticscholar.org/CorpusID:136614477>.
- [204] P. Maimí, A. Ortega, E. V. González, and J. Costa. “Should the translaminar fracture toughness of laminated composites be represented by the R or the J curve? A comparison of their consistency and predictive capability”. In: *Composites Part A: Applied Science and Manufacturing* 156 (May 2022). ISSN: 1359835X. DOI: [10.1016/j.compositesa.2022.106867](https://doi.org/10.1016/j.compositesa.2022.106867).
- [205] J. Serra, J. E. Pierré, J. C. Passieux, J. N. Périé, C. Bouvet, and B. Castanié. “Validation and modeling of aeronautical composite structures subjected to combined loadings: The VERTEX project. Part 1: Experimental setup, FE-DIC instrumentation and procedures”. In: *Composite Structures* 179 (Nov. 2017), pp. 224–244. ISSN: 02638223. DOI: [10.1016/j.compstruct.2017.07.080](https://doi.org/10.1016/j.compstruct.2017.07.080).
- [206] M. A. Jiménez and A. Miravete. “Application of the finite-element method to predict the onset of delamination growth”. In: *Journal of Composite Materials* 38 (15 2004), pp. 1309–1335. ISSN: 00219983. DOI: [10.1177/0021998304042734](https://doi.org/10.1177/0021998304042734).
- [207] J. M. González-Cantero, E. Graciani, B. López-Romano, and F. París. “Competing mechanisms in the unfolding failure in composite laminates”. In: *Composites Science and Technology* 156 (Mar. 2018), pp. 223–230. ISSN: 02663538. DOI: [10.1016/j.compscitech.2017.12.022](https://doi.org/10.1016/j.compscitech.2017.12.022).
- [208] P. Journoud, C. Bouvet, B. Castanié, F. Laurin, and L. Ratsifandrihana. “Experimental and numerical analysis of unfolding failure of L-shaped CFRP specimens”. In: *Composite Structures* 232 (Jan. 2020). ISSN: 02638223. DOI: [10.1016/j.compstruct.2019.111563](https://doi.org/10.1016/j.compstruct.2019.111563).

- [209] J. S. Charrier, F. Laurin, N. Carrere, and S. Mahdi. “Determination of the out-of-plane tensile strength using four-point bending tests on laminated L-angle specimens with different stacking sequences and total thicknesses”. In: *Composites Part A: Applied Science and Manufacturing* 81 (Feb. 2016), pp. 243–253. ISSN: 1359835X. DOI: [10.1016/j.compositesa.2015.11.018](https://doi.org/10.1016/j.compositesa.2015.11.018).
- [210] J. Xiao, X. Cui, X. Ren, and J. Lua. “A hybrid approach for static progressive damage assessment of a countersunk bolted composite component”. In: American Institute of Aeronautics and Astronautics Inc, AIAA, 2018. ISBN: 9781624105326. DOI: [10.2514/6.2018-0975](https://doi.org/10.2514/6.2018-0975).
- [211] L. J. Hart-Smith. “Mechanically-fastened joints for advanced composites - phenomenological considerations and simple analyses”. In: ed. by E. M. Lenoe, D. W. Oplinger, and J. J. Burke. Springer US, 1980, pp. 543–574. ISBN: 978-1-4684-1033-4. DOI: [10.1007/978-1-4684-1033-4_32](https://doi.org/10.1007/978-1-4684-1033-4_32).
- [212] H. S. Wang, C. L. Hung, and F. K. Chang. “Bearing failure of bolted composite joints. Part I: Experimental characterization”. In: *Journal of Composite Materials* 30 (12 1996), pp. 1284–1313. ISSN: 00219983. DOI: [10.1177/002199839603001201](https://doi.org/10.1177/002199839603001201).
- [213] A. A. Pisano and P. Fuschi. “Mechanically fastened joints in composite laminates: Evaluation of load bearing capacity”. In: *Composites Part B: Engineering* 42 (4 June 2011), pp. 949–961. ISSN: 13598368. DOI: [10.1016/j.compositesb.2010.12.016](https://doi.org/10.1016/j.compositesb.2010.12.016).
- [214] S. D. Thoppul, J. Finegan, and R. F. Gibson. “Mechanics of mechanically fastened joints in polymer-matrix composite structures - A review”. In: *Composites Science and Technology* 69 (3-4 Mar. 2009), pp. 301–329. ISSN: 02663538. DOI: [10.1016/j.compscitech.2008.09.037](https://doi.org/10.1016/j.compscitech.2008.09.037).
- [215] S. Heimbs. “Computational methods for bird strike simulations: A review”. In: *Computers and Structures* 89 (23-24 Dec. 2011), pp. 2093–2112. ISSN: 00457949. DOI: [10.1016/j.compstruc.2011.08.007](https://doi.org/10.1016/j.compstruc.2011.08.007).
- [216] J. Liu, Y. Li, X. Yu, X. Gao, and Z. Liu. “Design of aircraft structures against threat of bird strikes”. In: *Chinese Journal of Aeronautics* 31 (7 July 2018), pp. 1535–1558. ISSN: 10009361. DOI: [10.1016/j.cja.2018.05.004](https://doi.org/10.1016/j.cja.2018.05.004).
- [217] D. H. Kim, S. Y. Kang, H. J. Kim, and H. S. Kim. “Strain rate dependent mechanical behavior of glass fiber reinforced polypropylene composites and its effect on the performance of automotive bumper beam structure”. In: *Composites Part B: Engineering* 166 (June 2019), pp. 483–496. ISSN: 13598368. DOI: [10.1016/j.compositesb.2019.02.053](https://doi.org/10.1016/j.compositesb.2019.02.053).

- [218] Q. Liu, Y. Lu, J. Jiang, X. Yan, and Q. Li. “Experimental and numerical investigation into the dynamic impact responses of CFRP header rail”. In: *Thin-Walled Structures* 181 (Dec. 2022). ISSN: 02638231. DOI: [10.1016/j.tws.2022.110069](https://doi.org/10.1016/j.tws.2022.110069).
- [219] H. M. Hsiao, I. M. Daniel, and R. D. Cordes. “Strain rate effects on the transverse compressive and shear behavior of unidirectional composites”. In: *Journal of Composite Materials* 33 (17 1999), pp. 1620–1642. DOI: [10.1177/002199839903301703](https://doi.org/10.1177/002199839903301703).
- [220] H. Körber. “Mechanical response of advanced composites under high strain rates”. PhD thesis. University of Porto, 2010.
- [221] I. M. Daniel, J. M. Cho, B. T. Werner, and J. S. Fenner. “Characterization and constitutive modeling of composite materials under static and dynamic loading”. In: *AIAA Journal* 49 (8 Aug. 2011), pp. 1658–1664. ISSN: 00011452. DOI: [10.2514/1.J050797](https://doi.org/10.2514/1.J050797).
- [222] J. R. Vinson and E. Woldesenbet. “Fiber orientation effects on high strain rate properties of graphite/epoxy composites”. In: *Journal of Composite Materials* 35 (6 2001), pp. 509–521. ISSN: 00219983. DOI: [10.1106/21E5-2P22-GDWP-VC5C](https://doi.org/10.1106/21E5-2P22-GDWP-VC5C).
- [223] H. Cui, D. Thomson, A. Pellegrino, J. Wiegand, and N. Petrinic. “Effect of strain rate and fibre rotation on the in-plane shear response of $\pm 45^\circ$ laminates in tension and compression tests”. In: *Composites Science and Technology* 135 (Oct. 2016), pp. 106–115. ISSN: 02663538. DOI: [10.1016/j.compscitech.2016.09.016](https://doi.org/10.1016/j.compscitech.2016.09.016).
- [224] F. Weng, Y. Fang, M. Ren, J. Sun, and L. Feng. “Effect of high strain rate on shear properties of carbon fiber reinforced composites”. In: *Composites Science and Technology* 203 (Feb. 2021). ISSN: 02663538. DOI: [10.1016/j.compscitech.2020.108599](https://doi.org/10.1016/j.compscitech.2020.108599).
- [225] M. Ploeckl, P. Kuhn, J. Grosser, M. Wolfahrt, and H. Koerber. “A dynamic test methodology for analyzing the strain-rate effect on the longitudinal compressive behavior of fiber-reinforced composites”. In: *Composite Structures* 180 (Nov. 2017), pp. 429–438. ISSN: 02638223. DOI: [10.1016/j.compstruct.2017.08.048](https://doi.org/10.1016/j.compstruct.2017.08.048).
- [226] M. V. Hosur, J Alexander, U. K. Vaidya, and S Jeelani. “High strain rate compression response of carbon/epoxy laminate composites”. In: *Composite Structures* 52 (3 2001), pp. 405–417. ISSN: 0263-8223. DOI: [10.1016/S0263-8223\(01\)00031-9](https://doi.org/10.1016/S0263-8223(01)00031-9).
- [227] H. Koerber and P. P. Camanho. “High strain rate characterisation of unidirectional carbon-epoxy IM7-8552 in longitudinal compression”. In: *Composites Part A: Applied Science and Manufacturing* 42 (5 May 2011), pp. 462–470. ISSN: 1359835X. DOI: [10.1016/j.compositesa.2011.01.002](https://doi.org/10.1016/j.compositesa.2011.01.002).

- [228] M. Ploeckl, P. Kuhn, and H. Koerber. “Characterization of unidirectional carbon fiber reinforced polyamide-6 thermoplastic composite under longitudinal compression loading at high strain rate”. In: vol. 94. EDP Sciences, Sept. 2015. ISBN: 9782759818174. DOI: [10.1051/epjconf/20159401041](https://doi.org/10.1051/epjconf/20159401041).
- [229] J. I. Perry and S. M. Walley. “Measuring the effect of strain rate on deformation and damage in fibre-reinforced composites: A review”. In: *Journal of Dynamic Behavior of Materials* 8 (2 June 2022), pp. 178–213. ISSN: 21997454. DOI: [10.1007/s40870-022-00331-0](https://doi.org/10.1007/s40870-022-00331-0).
- [230] J Harding and L. M. Welsh. “A tensile testing technique for fibre-reinforced composites at impact rates of strain”. In: *Journal of Materials Science* 18 (6 1983), pp. 1810–1826. ISSN: 1573-4803. DOI: [10.1007/BF00542078](https://doi.org/10.1007/BF00542078).
- [231] N. Taniguchi, T. Nishiwaki, and H. Kawada. “Tensile strength of unidirectional CFRP laminate under high strain rate”. In: *Advanced Composite Materials: The Official Journal of the Japan Society of Composite Materials* 16 (2 Mar. 2007), pp. 167–180. ISSN: 09243046. DOI: [10.1163/156855107780918937](https://doi.org/10.1163/156855107780918937).
- [232] G. C. Jacob, J. M. Starbuck, J. F. Fellers, S. Simunovic, and R. G. Boeman. “Strain rate effects on the mechanical properties of polymer composite materials”. In: *Journal of Applied Polymer Science* 94 (1 Oct. 2004), pp. 296–301. ISSN: 00218995. DOI: [10.1002/app.20901](https://doi.org/10.1002/app.20901).
- [233] L. Cheng, R. He, Y. Gao, H. Cui, and Y. Li. “Determination of fibre tension fracture toughness of composite laminates at high loading rate”. In: *Composites Science and Technology* 228 (Sept. 2022). ISSN: 02663538. DOI: [10.1016/j.compscitech.2022.109619](https://doi.org/10.1016/j.compscitech.2022.109619).
- [234] J. Hoffmann, H. Cui, and N. Petrinic. “Determination of the strain-energy release rate of a composite laminate under high-rate tensile deformation in fibre direction”. In: *Composites Science and Technology* 164 (Aug. 2018), pp. 110–119. ISSN: 02663538. DOI: [10.1016/j.compscitech.2018.05.034](https://doi.org/10.1016/j.compscitech.2018.05.034).
- [235] D. E. Sommer, D. Thomson, J. Hoffmann, and N. Petrinic. “Numerical modelling of quasi-static and dynamic compact tension tests for obtaining the translaminar fracture toughness of CFRP”. In: *Composites Science and Technology* 237 (May 2023). ISSN: 02663538. DOI: [10.1016/j.compscitech.2023.109997](https://doi.org/10.1016/j.compscitech.2023.109997).
- [236] P. Kuhn, G. Catalanotti, J. Xavier, P. P. Camanho, and H. Koerber. “Fracture toughness and crack resistance curves for fiber compressive failure mode in polymer composites under high rate loading”. In: *Composite Structures* 182 (Dec. 2017), pp. 164–175. ISSN: 02638223. DOI: [10.1016/j.compstruct.2017.09.040](https://doi.org/10.1016/j.compstruct.2017.09.040).

- [237] R. O. Ochola, K. Marcus, G. N. Nurick, and T. Franz. “Mechanical behaviour of glass and carbon fibre reinforced composites at varying strain rates”. In: *Composite Structures* 63 (3-4 2004), pp. 455–467. ISSN: 02638223. DOI: [10.1016/S0263-8223\(03\)00194-6](https://doi.org/10.1016/S0263-8223(03)00194-6).
- [238] K. Naresh, K. Shankar, B. S. Rao, and R. Velmurugan. “Effect of high strain rate on glass/carbon/hybrid fiber reinforced epoxy laminated composites”. In: *Composites Part B: Engineering* 100 (Sept. 2016), pp. 125–135. ISSN: 13598368. DOI: [10.1016/j.compositesb.2016.06.007](https://doi.org/10.1016/j.compositesb.2016.06.007).
- [239] P Perzyna. “The constitutive equations for rate sensitive plastic materials”. In: *Quarterly of applied mathematics* 20 (4 1963), pp. 321–332. DOI: [10.1090/qam/144536](https://doi.org/10.1090/qam/144536).
- [240] H. Kang, Y. Li, J. Liang, D. Thomson, H. Cui, and Y. Li. “Failure of short carbon-fiber-reinforced PEEK composites under high strain rate biaxial loading”. In: *Composites Part B: Engineering* 247 (Dec. 2022). ISSN: 13598368. DOI: [10.1016/j.compositesb.2022.110356](https://doi.org/10.1016/j.compositesb.2022.110356).
- [241] S. Eskandari, F. M. A. Pires, P. P. Camanho, H. Cui, N. Petrinic, and A. T. Marques. “Analyzing the failure and damage of FRP composite laminates under high strain rates considering visco-plasticity”. In: *Engineering Failure Analysis* 101 (July 2019), pp. 257–273. ISSN: 13506307. DOI: [10.1016/j.engfailanal.2019.03.008](https://doi.org/10.1016/j.engfailanal.2019.03.008).
- [242] W. Tan and B. Liu. “A physically-based constitutive model for the shear-dominated response and strain rate effect of carbon fibre reinforced composites”. In: *Composites Part B: Engineering* 193 (July 2020). ISSN: 13598368. DOI: [10.1016/j.compositesb.2020.108032](https://doi.org/10.1016/j.compositesb.2020.108032).
- [243] C. Shi, B. Guo, M. Sarıkaya, M. Çelik, P. Chen, and M. Güden. “Determination of the material model and damage parameters of a carbon fiber reinforced laminated epoxy composite for high strain rate planar compression”. In: *International Journal of Impact Engineering* 149 (Mar. 2021). ISSN: 0734743X. DOI: [10.1016/j.ijimpeng.2020.103771](https://doi.org/10.1016/j.ijimpeng.2020.103771).
- [244] W. Jin, Y. Zhang, L. Jiang, G. Yang, J. Chen, and P. Li. “A dynamic constitutive model and simulation of braided CFRP under high-speed tensile loading”. In: *Materials* 15 (18 Sept. 2022). ISSN: 19961944. DOI: [10.3390/ma15186389](https://doi.org/10.3390/ma15186389).
- [245] L. Raimondo, L. Iannucci, P. Robinson, and P. T. Curtis. “Modelling of strain rate effects on matrix dominated elastic and failure properties of unidirectional fibre-reinforced polymer-matrix composites”. In: *Composites Science and Technology*

72 (7 Apr. 2012), pp. 819–827. ISSN: 02663538. DOI: [10.1016/j.compscitech.2012.02.011](https://doi.org/10.1016/j.compscitech.2012.02.011).

- [246] I. M. Daniel. “Constitutive behavior and failure criteria for composites under static and dynamic loading”. In: *Meccanica* 50 (2 Dec. 2015), pp. 429–442. ISSN: 15729648. DOI: [10.1007/s11012-013-9829-1](https://doi.org/10.1007/s11012-013-9829-1).
- [247] D. Ma, A. Manes, S. C. Amico, and M. Giglio. “Ballistic strain-rate-dependent material modelling of glass-fibre woven composite based on the prediction of a meso-heterogeneous approach”. In: *Composite Structures* 216 (May 2019), pp. 187–200. ISSN: 02638223. DOI: [10.1016/j.compstruct.2019.02.102](https://doi.org/10.1016/j.compstruct.2019.02.102).
- [248] B. Chang, X. Wang, Z. Long, Z. Li, J. Gu, S. Ruan, and C. Shen. “Constitutive modeling for the accurate characterization of the tension behavior of PEEK under small strain”. In: *Polymer Testing* 69 (Aug. 2018), pp. 514–521. ISSN: 01429418. DOI: [10.1016/j.polymertesting.2018.06.003](https://doi.org/10.1016/j.polymertesting.2018.06.003).
- [249] P. W. Gerbaud, F. Otero, P. Bussetta, and P. P. Camanho. “An invariant based transversely-isotropic constitutive model for unidirectional fibre reinforced composites considering the matrix viscous effects”. In: *Mechanics of Materials* 138 (Nov. 2019). ISSN: 01676636. DOI: [10.1016/j.mechmat.2019.103146](https://doi.org/10.1016/j.mechmat.2019.103146).
- [250] I. A. R. Lopes, P. P. Camanho, F. M. A. Pires, and A. Arteiro. “An invariant-based elasto-visco-plastic model for unidirectional polymer composites at finite strains”. In: *International Journal of Solids and Structures* 236-237 (Feb. 2022). ISSN: 00207683. DOI: [10.1016/j.ijsolstr.2021.111292](https://doi.org/10.1016/j.ijsolstr.2021.111292).
- [251] M. Hegde and S. S. Mulay. “An approach to model mechanical damage in particulate composites with viscoelastic matrix”. In: *International Journal of Advances in Engineering Sciences and Applied Mathematics* 13 (1 Mar. 2021), pp. 79–88. ISSN: 0975-0770. DOI: [10.1007/s12572-021-00289-7](https://doi.org/10.1007/s12572-021-00289-7).
- [252] S. Oller. *Nonlinear dynamics of structures*. Springer, 2014.
- [253] C. Peyrac, T. Jollivet, N. Leray, F. Lefebvre, O. Westphal, and L. Gornet. “Self-heating method for fatigue limit determination on thermoplastic composites”. In: vol. 133. Elsevier Ltd, 2015, pp. 129–135. DOI: [10.1016/j.proeng.2015.12.639](https://doi.org/10.1016/j.proeng.2015.12.639).
- [254] O. M. Heeres, A. S. J. Suiker, and R. D. Borst. “A comparison between the Perzyna viscoplastic model and the Consistency viscoplastic model”. In: *European Journal of Mechanics A/Solids* 21 (1 2002), pp. 1–12. ISSN: 0997-7538. DOI: [10.1016/S0997-7538\(01\)01188-3](https://doi.org/10.1016/S0997-7538(01)01188-3).

- [255] D. Perić. “On a class of constitutive equations in viscoplasticity: Formulation and computational issues”. In: *International Journal for Numerical Methods in Engineering* 36 (8 1993), pp. 1365–1393. ISSN: 10970207. DOI: [10.1002/nme.1620360807](https://doi.org/10.1002/nme.1620360807).
- [256] C. Miehe and J. Schröder. “Comparative study of stress update algorithms for rate-independent and rate-dependent crystal plasticity”. In: *International Journal for Numerical Methods in Engineering* 50 (2 Jan. 2001), pp. 273–298. ISSN: 00295981. DOI: [10.1002/1097-0207\(20010120\)50:2<273::AID-NME17>3.0.CO;2-Q](https://doi.org/10.1002/1097-0207(20010120)50:2<273::AID-NME17>3.0.CO;2-Q).
- [257] K. Nguyen, V. J. Amores, M. A. Sanz, and F. J. Montáns. “Thermodynamically consistent nonlinear viscoplastic formulation with exact solution for the linear case and well-conditioned recovery of the inviscid one”. In: *Computational Mechanics* 67 (5 May 2021), pp. 1349–1373. ISSN: 14320924. DOI: [10.1007/s00466-021-01991-w](https://doi.org/10.1007/s00466-021-01991-w).
- [258] Y. Bai and T. Wierzbicki. “Application of extended Mohr-Coulomb criterion to ductile fracture”. In: *International Journal of Fracture* 161 (1 Jan. 2010), pp. 1–20. ISSN: 03769429. DOI: [10.1007/s10704-009-9422-8](https://doi.org/10.1007/s10704-009-9422-8).
- [259] D. Mohr and S. J. Marcadet. “Micromechanically-motivated phenomenological Hosford-Coulomb model for predicting ductile fracture initiation at low stress triaxialities”. In: *International Journal of Solids and Structures* 67-68 (Aug. 2015), pp. 40–55. ISSN: 00207683. DOI: [10.1016/j.ijsolstr.2015.02.024](https://doi.org/10.1016/j.ijsolstr.2015.02.024).
- [260] X. Kou, L. Li, X. Du, and X. Zheng. “Elastoplastic dynamic constitutive model of concrete with combined effects of temperature and strain rate”. In: *Case Studies in Construction Materials* 18 (July 2023). ISSN: 22145095. DOI: [10.1016/j.cscm.2023.e01905](https://doi.org/10.1016/j.cscm.2023.e01905).
- [261] R. Panduranga and K. Shivakumar. “Mode-II total fatigue life model for unidirectional IM7/8552 carbon/epoxy composite laminate”. In: *International Journal of Fatigue* 94 (Jan. 2017), pp. 97–109. ISSN: 01421123. DOI: [10.1016/j.ijfatigue.2016.09.014](https://doi.org/10.1016/j.ijfatigue.2016.09.014).
- [262] J. Wiegand. “Constitutive modelling of composite materials under impact loading”. PhD thesis. University of Oxford, 2008.
- [263] X. Oliver and C. A. de Saracibar. *Continuum mechanics for engineers. Theory and problems*. 2nd. 2017. DOI: [10.13140/RG.2.2.25821.20961](https://doi.org/10.13140/RG.2.2.25821.20961).
- [264] W. Tan and B. G. Falzon. “Modelling the crush behaviour of thermoplastic composites”. In: *Composites Science and Technology* 134 (Oct. 2016), pp. 57–71. ISSN: 02663538. DOI: [10.1016/j.compscitech.2016.07.015](https://doi.org/10.1016/j.compscitech.2016.07.015).

- [265] W. Tan, F. Naya, L. Yang, T. Chang, B. G. Falzon, L. Zhan, J. M. Molina-Aldareguía, C. González, and J. Llorca. “The role of interfacial properties on the intralaminar and interlaminar damage behaviour of unidirectional composite laminates: Experimental characterization and multiscale modelling”. In: *Composites Part B: Engineering* 138 (Apr. 2018), pp. 206–221. ISSN: 13598368. DOI: [10.1016/j.compositesb.2017.11.043](https://doi.org/10.1016/j.compositesb.2017.11.043).
- [266] T. Belytschko, W. K. Liu, B. Moran, and K. Elkhodary. *Nonlinear finite elements for continua and structures*. John Wiley & Sons, Inc., 2014. ISBN: 978-1-118-63270-3.
- [267] G. Alfano and E. Sacco. “Combining interface damage and friction in a cohesive-zone model”. In: *International Journal for Numerical Methods in Engineering* 68 (5 Oct. 2006), pp. 542–582. ISSN: 00295981. DOI: [10.1002/nme.1728](https://doi.org/10.1002/nme.1728).
- [268] G. Catalanotti, C. Furtado, T. Scalici, G. Pitarresi, F. P. van der Meer, and P. P. Camanho. “The effect of through-thickness compressive stress on mode II interlaminar fracture toughness”. In: *Composite Structures* 182 (Dec. 2017), pp. 153–163. ISSN: 02638223. DOI: [10.1016/j.compstruct.2017.09.014](https://doi.org/10.1016/j.compstruct.2017.09.014).
- [269] B. Eidel and F. Gruttmann. “Elastoplastic orthotropy at finite strains: Multiplicative formulation and numerical implementation”. In: vol. 28. Nov. 2003, pp. 732–742. DOI: [10.1016/j.commatsci.2003.08.027](https://doi.org/10.1016/j.commatsci.2003.08.027).
- [270] B. Eidel. “Anisotropic inelasticity-modelling, simulation, validation”. PhD thesis. Technical University of Darmstadt, 2004.
- [271] A. Dean, S. Sahraee, J. Reinoso, and R. Rolfes. “Finite deformation model for short fiber reinforced composites: Application to hybrid metal-composite clinching joints”. In: *Composite Structures* 151 (2016), pp. 162–171. ISSN: 02638223. DOI: [10.1016/j.compstruct.2016.02.045](https://doi.org/10.1016/j.compstruct.2016.02.045).
- [272] C. Furtado, G. Catalanotti, A. Arteiro, P. J. Gray, B. L. Wardle, and P. P. Camanho. “Simulation of failure in laminated polymer composites: Building-block validation”. In: *Composite Structures* 226 (Oct. 2019). ISSN: 02638223. DOI: [10.1016/j.compstruct.2019.111168](https://doi.org/10.1016/j.compstruct.2019.111168).
- [273] X. Martinez, S. Oller, F. Rastellini, and A. H. Barbat. “A numerical procedure simulating RC structures reinforced with FRP using the serial/parallel mixing theory”. In: *Computers and Structures* 86 (15-16 Aug. 2008), pp. 1604–1618. ISSN: 00457949. DOI: [10.1016/j.compstruc.2008.01.007](https://doi.org/10.1016/j.compstruc.2008.01.007).
- [274] G. Strang. *Linear algebra and its applications fourth edition*. Thomson, Brooks/Cole, 2006. ISBN: 0030105676 9780030105678 0534422004 9780534422004.

